DrillBit

The Report is Generated by DrillBit Plagiarism Detection Software

Submission Information

Author Name	SHAVETA
Title	Advancing MEMS Gyroscopes: Design, Analysis and Thermal Management for Enhanced Figure of Merit
Paper/Submission ID	5377693
Submitted by	dtuplagcheck@dtu.ac.in
Submission Date	2026-03-23 12:53:50
Total Pages, Total Words	187, 61098
Document type	Thesis

Result Information

Similarity **6 %**

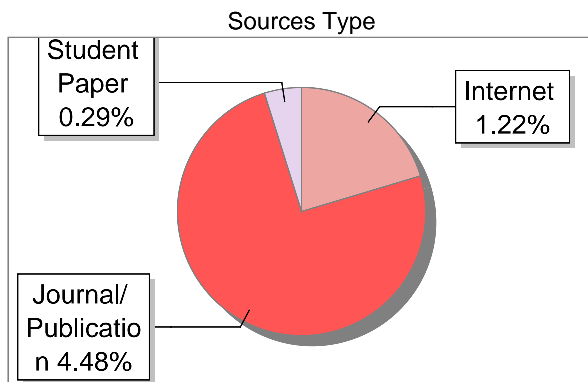

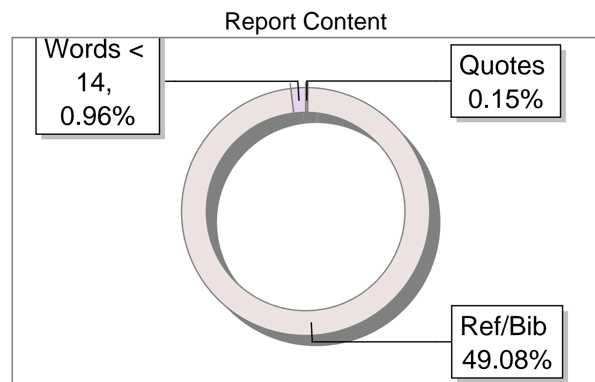

Exclude Information

Quotes	Not Excluded
References/Bibliography	Not Excluded
Source: Excluded < 14 Words	Not Excluded
Excluded Source	**0 %**
Excluded Phrases	Not Excluded

Database Selection

Language	English
Student Papers	Yes
Journals & publishers	Yes
Internet or Web	Yes
Institution Repository	Yes

A Unique QR Code use to View/Download/Share Pdf File

DrillBit Similarity Report

6	150	A	A-Satisfactory (0-10%) B-Upgrade (11-40%) C-Poor (41-60%) D-Unacceptable (61-100%)
SIMILARITY %	MATCHED SOURCES	GRADE	

LOCATION	MATCHED DOMAIN	%	SOURCE TYPE
1	rex.libraries.wsu.edu	<1	Publication
2	Thesis Submitted to Shodhganga Repository	<1	Publication
3	rex.libraries.wsu.edu	<1	Publication
4	rex.libraries.wsu.edu	<1	Publication
5	Thesis Submitted to Shodhganga Repository	<1	Publication
6	rex.libraries.wsu.edu	<1	Publication
7	rex.libraries.wsu.edu	<1	Publication
8	rex.libraries.wsu.edu	<1	Publication
9	rex.libraries.wsu.edu	<1	Publication
10	www.dx.doi.org	<1	Publication
11	rex.libraries.wsu.edu	<1	Publication
12	xplorestaging.ieee.org	<1	Internet Data
13	edisciplinas.usp.br	<1	Publication
14	article.sciencepublishinggroup.com	<1	Publication

	Source	%	Type
15	pdfcookie.com	<1	Internet Data
16	pmc.ncbi.nlm.nih.gov	<1	Internet Data
17	rex.libraries.wsu.edu	<1	Publication
18	digitalrepository.unm.edu	<1	Publication
19	Comparison of different ammonia synthesis loop configurations with the aid of ad by Penkuhn-2017	<1	Publication
20	researchspace.ukzn.ac.za	<1	Publication
21	rex.libraries.wsu.edu	<1	Publication
22	rex.libraries.wsu.edu	<1	Publication
23	Enhanced temperature stability of scale factor in MEMS gyroscope based by Cui-2019	<1	Publication
24	autodocbox.com	<1	Internet Data
25	REPOSITORY - Submitted to VTU Examination 2 on 2026-03-14 10-28 4760515	<1	Student Paper
26	rex.libraries.wsu.edu	<1	Publication
27	moam.info	<1	Internet Data
28	worldwidescience.org	<1	Internet Data
29	Student Archives Data	<1	Student Paper
30	pmc.ncbi.nlm.nih.gov	<1	Internet Data
31	REPOSITORY - Submitted to Awadesh Pratap Singh University, Rewa on 2026-02-25 16-29 5295775	<1	Student Paper

32	Research of a novel stereoscopic symmetrical quadruple hair gyroscope by Guo-2019	<1	Publication
33	rex.libraries.wsu.edu	<1	Publication
34	core.ac.uk	<1	Publication
35	Reconfigurable holograms using VO2-based tunable metasurface by Haimov-2020	<1	Publication
36	rex.libraries.wsu.edu	<1	Publication
37	www.academia.edu	<1	Internet Data
38	Empowering revealed preference survey with a supplementary stated preference survey demonstration, by Tabasi, Maliheh, Yr-2023	<1	Publication
39	ieeexplore.ieee.org	<1	Publication
40	Chalcogenide glass-based Low Loss Graded Index Photonic Crystal Fiber for non-linear applications i, by Chauhan, Jyoti, Yr-2023	<1	Publication
41	REPOSITORY - Submitted to Shri Khushal Das University on 2025-11-20 16-13 4662919	<1	Student Paper
42	Thesis Submitted to Shodhganga Repository	<1	Publication
43	Student Archives Data	<1	Student Paper
44	Thesis submitted to dspace.mit.edu	<1	Publication
45	Report of the WHO technical consultation on the evaluation of respiratory syncytial virus preventio, by Fitzpatrick, Meagan C., Yr-2023	<1	Publication
46	jestec.taylors.edu.my	<1	Publication
47	rex.libraries.wsu.edu	<1	Publication
48	eejournal.ktu.lt	<1	Publication

#	Source	%	Type
49	pdfcookie.com	<1	Internet Data
50	arxiv.org	<1	Publication
51	www.science.gov	<1	Internet Data
52	Carrier transport mechanisms and photovoltaic characteristics of Auto by Zeyada-2017	<1	Publication
53	ieeexplore.ieee.org	<1	Publication
54	Silicon Carbide Converters and MEMS Devices for High-temperature Power Electroni by Guo-2019	<1	Publication
55	nandbox.com	<1	Internet Data
56	Resonance raman studies of oxycytochrome P450cam effect of substrate structure by Hu-1991	<1	Publication
57	ashpublications.org	<1	Internet Data
58	Evaluation of Regional-Scale Receptor Modeling by Lowenthal-2010	<1	Publication
59	IEEE 2020 Symposium on Design, Test, Integration Packaging of MEMS and MOEMS	<1	Publication
60	IEEE 2020 Symposium on Design, Test, Integration Packaging of MEMS and MOEMS	<1	Publication
61	jestec.taylors.edu.my	<1	Publication
62	moam.info	<1	Internet Data
63	Non-uniform, multi-stack solid oxide fuel cell (SOFC) system design f, by Pirasaci, Tolga- 2019	<1	Publication
64	www.freepatentsonline.com	<1	Internet Data
65	www.freepatentsonline.com	<1	Internet Data

66	IEEE 2018 International Conference on Unmanned Aircraft Systems (IC, by Guerout, Gregoire - 2018	<1	Publication
67	In-Run Scale Factor Compensation for MEMS Gyroscope without Calibration and Fitt by Jia-2020	<1	Publication
68	Is higher-quality land developed earlier by Lopez-2019	<1	Publication
69	Recent advances in MEMS-based micro heat pipes by Qu-2017	<1	Publication
70	rex.libraries.wsu.edu	<1	Publication
71	Smurf2 Regulates Inflammation and Collagen Processing in Cutaneous Wound Healing through Transformi, by Stuelten, Christina H., Yr-2022	<1	Publication
72	autodocbox.com	<1	Internet Data
73	A 5-year prospective radiographic evaluation of marginal bone levels adjacent to by Nickenig-2013	<1	Publication
74	A review on cationic lipids with different linkers for gene delivery by Zhi-2017	<1	Publication
75	docplayer.net	<1	Internet Data
76	Hyper fibrinolysis state in COVID 19 and its correlation to lipid parameters, by Sharma, Abhilash, Yr-2024	<1	Publication
77	moam.info	<1	Internet Data
78	REPOSITORY - Submitted to Raffles University on 2026-02-17 10-39 5164242	<1	Student Paper
79	Thesis Submitted to Shodhganga Repository	<1	Publication
80	www-iam.nies.go.jp	<1	Publication
81	connect.biorxiv.org	<1	Internet Data

82	Quantification of carbon nanotube dispersion and its correlation with by Tiwari-2019	<1	Publication
83	rex.libraries.wsu.edu	<1	Publication
84	Thesis Submitted to Shodhganga, shodhganga.inflibnet.ac.in	<1	Publication
85	The design of low frequency underwater acoustic projectors present status and f by Decarpigny-1991	<1	Publication
86	www.dx.doi.org	<1	Publication
87	asbmr.onlinelibrary.wiley.com	<1	Internet Data
88	mdpi.com	<1	Internet Data
89	moam.info	<1	Internet Data
90	www.freepatentsonline.com	<1	Internet Data
91	andthentheresphysics.wordpress.com	<1	Internet Data
92	Carrier transport mechanisms and photovoltaic characteristics of Auto by Zeyada-2017	<1	Publication
93	Cognitive Modeling Effects on Preservice Teachers with Low and Moderate Success by Gorrell-1989	<1	Publication
94	Cross-sectional TEM study of the microstructure of superconducting X-ray detecto by -2002	<1	Publication
95	Effect of Cu content on the shape memory behavior of TiNiCu alloy thin films p by Kosuk-2010	<1	Publication
96	repositorio.uchile.cl	<1	Publication
97	rex.libraries.wsu.edu	<1	Publication
98	Thesis Submitted to Shodhganga Repository	<1	Publication

99	www.atsdr.cdc.gov	<1	Publication
100	www.degruyter.com	<1	Internet Data
101	www.dx.doi.org	<1	Publication
102	eprints.whiterose.ac.uk	<1	Publication
103	moam.info	<1	Internet Data
104	REPOSITORY - Submitted to Rajasthan University of Veterinary Animal Sciences, Bikaner on 2025-10-10 12-37 4358700	<1	Student Paper
105	Synthesis of Anodic Oxide Thin Films on Si Wafers and Their Characte by Ashok-2014	<1	Publication
106	A Computational Study on the Magnetic Resonance Coupling Technique for Wireless by Zakaria-2017	<1	Publication
107	Capacity and energy cost of information in biological and silicon photoreceptors by Abshire-2001	<1	Publication
108	deevybee.blogspot.com.au	<1	Internet Data
109	mdpi.com	<1	Internet Data
110	Sideband Peak Count - a new nonlinear ultrasonic technique for monitoring damag By, Tribikram Kundu,, Guangdon, Yr-2024,6	<1	Publication
111	Thesis Submitted to Shodhganga, shodhganga.inflibnet.ac.in	<1	Publication
112	Thesis Submitted to Shodhganga Repository	<1	Publication
113	www.equisoft.com	<1	Internet Data
114	Air damping of micro bridge resonator vibrating close to a surface with a modera by Qiu-2015	<1	Publication
115	arxiv.org	<1	Publication

	Source	%	Type
116	asmedigitalcollection.asme.org	<1	Internet Data
117	Charactarization of Mechanical Properties of MEMS Materials by Sato-1999	<1	Publication
118	Cold and warmth intensify pain-linked sodium channel gating effects and persist By Sophia Kriegeskorte, Raya Bot, Yr-2023,8,2	<1	Publication
119	cyble.com	<1	Internet Data
120	Design and analysis of hybrid fractal frequency-band reconfigurable metamateria, by Parasher, Rishi, Yr-2025	<1	Publication
121	Determination of 135Cs and 137Cs in environmental samples A review by Russell-2015	<1	Publication
122	economictimes.indiatimes.com	<1	Internet Data
123	eprints.leedsbeckett.ac.uk	<1	Internet Data
124	eprints.sunway.edu.my	<1	Publication
125	etd.ohiolink.edu	<1	Publication
126	forum.effectivealtruism.org	<1	Internet Data
127	frontiersin.org	<1	Internet Data
128	Future Directions Design Meets Neuroscience by Flory-2019	<1	Publication
129	Gate-engineering-based approach to improve the nanoscale DG MOSFET behavior agai by Bentrcia-2013	<1	Publication
130	hepnp.ihep.ac.cn	<1	Internet Data
131	ic4n.org	<1	Publication
132	ieeexplore.ieee.org	<1	Publication

133	ijemnet.com	<1	Publication
134	link.springer.com	<1	Internet Data
135	mdpi.com	<1	Internet Data
136	Modelling of hydrogen transport in silicon solar cell structures under by Hamer-2018	<1	Publication
137	pdfcookie.com	<1	Internet Data
138	pdfcookie.com	<1	Internet Data
139	rex.libraries.wsu.edu	<1	Publication
140	rex.libraries.wsu.edu	<1	Publication
141	Status of Serum Copper and Zinc in Pre-Eclampsia By FZ Muna, ASMM Sirazi, M Majum, Yr-2017,7,23	<1	Publication
142	Thesis submitted to dspace.mit.edu	<1	Publication
143	The Lithium-Ion Battery Modeling Challenge by Docimo-2014	<1	Publication
144	Using Confined Self-Adjusting Carbon Nanotube Arrays as High-Sensitivity Displac by Lee-2014	<1	Publication
145	Vibrational intensities of molecular chains with end groups by J-1969	<1	Publication
146	www.freepatentsonline.com	<1	Internet Data
147	www.mdpi.com	<1	Internet Data
148	www.nature.com	<1	Publication
149	www.ncbi.nlm.nih.gov	<1	Internet Data
150	www.semiconductors.org	<1	Publication

Advancing MEMS Gyroscopes: Design, Analysis and Thermal Management for Enhanced Figure of Merit

A THESIS to be Submitted By

SHAVETA

2K20/PHDAP/506

For the award of the degree of

Doctor of Philosophy

in

Physics

Under the Supervision of

Prof. Rishu Chaujar
Professor
Department of Applied Physics

Dr R. K. Bhan
Sc H & OS (Retd.)
IDST, DRDO

Department of Applied Physics

DELHI TECHNOLOGICAL UNIVERSITY

BAWANA ROAD, NEW DELHI -110042 INDIA

MARCH, 2026

©Delhi Technological University–2024

All rights reserved.

Dedicated

to

My Loving Family

DECLARATION

I declare that the research work presented in this thesis titled "***Advancing MEMS Gyroscopes: Design, Analysis and Thermal Management for Enhanced Figure of Merit***" for the attainment of the degree of Doctor of Philosophy in Physics has been conducted by me, under the guidance of Prof. Rishu Chaujar from the Department of Applied Physics, Delhi Technological University, Delhi, and Dr. R. K. Bhan, Sc 'H' & OS, Institute of Defence Scientists and Technologists (IDST), Timarpur, Delhi. This work has not been previously submitted, either partially or in its entirety, to any other academic institution for any degree or diploma. I declare that this thesis reflects my ideas expressed in my own words. Wherever the ideas or words of others have been incorporated, appropriate citation and referencing have been provided to acknowledge the sources. I also confirm that I have upheld the principles of academic honesty and integrity and that I have not misrepresented, fabricated, or falsified any information, data, facts, or sources in my submission.

Ms. Shaveta
Enrolment No. 2K20/PHDAP/506
Department of Applied Physics
Delhi Technological University

CERTIFICATE

This is to certify that the thesis titled **Advancing MEMS Gyroscopes: Design, Analysis and Thermal Management for Enhanced Figure of Merit,** submitted by **Ms. Shaveta**, to the Delhi Technological University, Delhi, for the award of the degree of **Doctor of Philosophy**, is a bonafide record of the research work done by him under our supervision and guidance. The contents of this thesis, in full or in parts, have not been submitted to any other Institute or University for the award of any degree or diploma.

Prof. Rishu Chaujar Supervisor Department of Applied Physics Delhi Technological University (DTU)	Dr. R.K. Bhan, Sc H & OS (Retd) Co-Supervisor Institute of Defence Scientists and Technologists Defence Research and Development Organisation (DRDO)	Prof. Vinod Singh Head Department of Applied Physics Delhi Technological University (DTU)

New Delhi,

March 2026

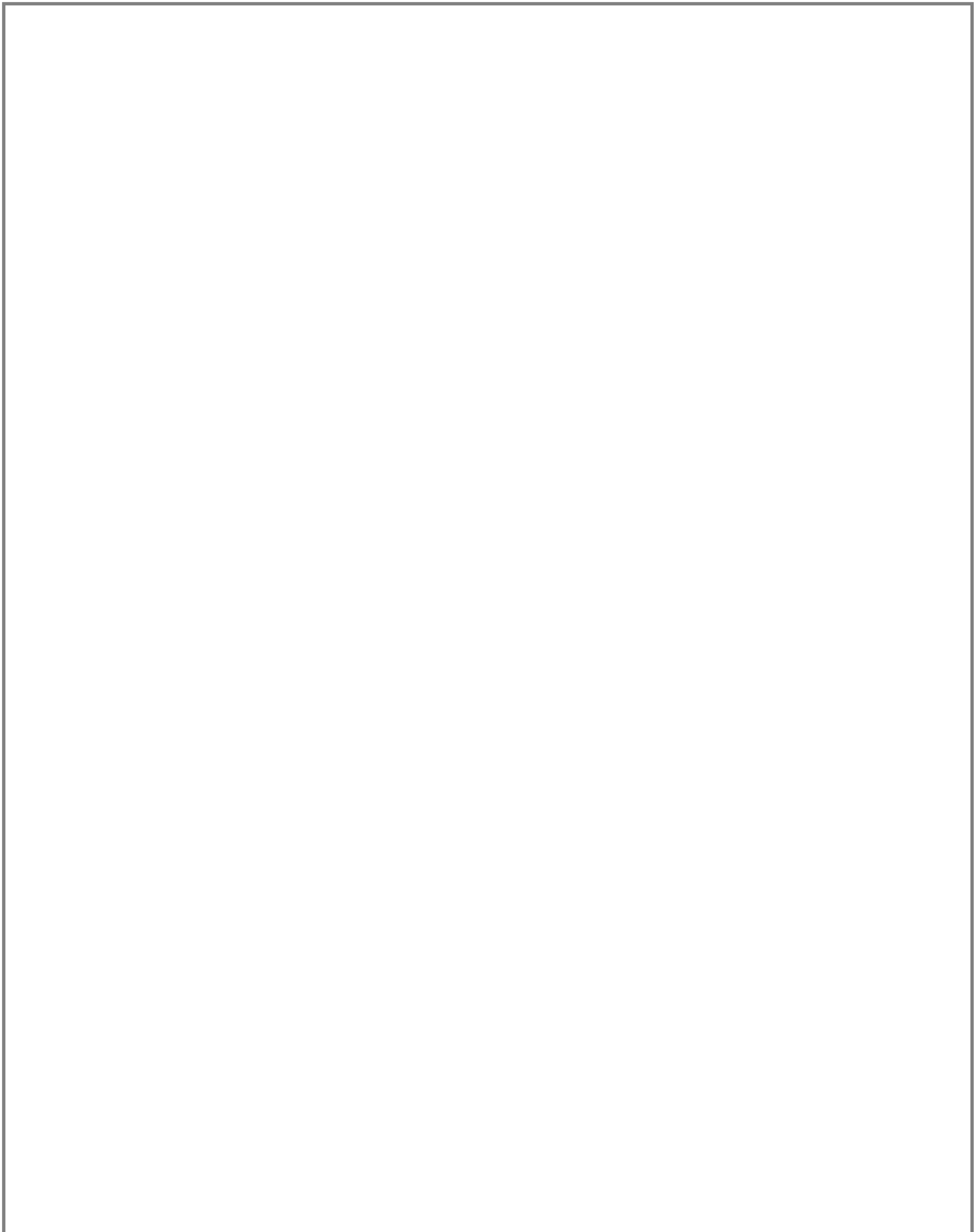

ACKNOWLEDGEMENTS

After many years in research, I began my PhD journey with a strong desire to deepen my understanding and further explore my field of study. I embarked on this path with uncertainty, often questioning whether I would succeed. Today, as I write this thesis, it stands as a testament to perseverance and growth. The journey was filled with challenges, self-doubt, learning, and moments of fulfilment. It taught me patience, resilience, and the importance of consistent effort. Whenever I felt uncertain or directionless, the guidance and encouragement of my mentors and well-wishers helped me move forward. With sincere gratitude, I acknowledge and thank everyone who directly or indirectly supported me in reaching this milestone.

I would like to express my sincere gratitude to my Supervisor, **Prof. Rishu Chaujar**, for her constant guidance, encouragement, and unwavering support throughout my Ph.D. journey. The successful completion of this work would not have been possible without her mentorship and motivation. Her positive attitude and disciplined approach to research have always inspired me to remain focused and consistent. Whenever I faced challenges or felt uncertain, she patiently guided me and helped me find direction. Her timely suggestions and practical solutions ensured steady progress in my work. I am especially thankful for her prompt responses, careful proofreading of manuscripts, thoughtful feedback, and detailed review of the thesis. Despite my professional commitments, she provided full support with administrative processes and ensured timely approvals, greatly facilitating the smooth completion of this work. I feel fortunate to have worked under her guidance and sincerely appreciate her trust and belief in me.

I would like to express my heartfelt gratitude to my Co-Supervisor, **Dr. R.K. Bhan**, for his constant motivation, guidance, and unwavering support throughout my Ph.D. journey. I am sincerely thankful to him for agreeing to guide me and for trusting my abilities. His mentorship extended well beyond technical supervision. From identifying and refining research problems

to conceptualizing ideas, drafting manuscripts, critically reviewing papers, and responding to reviewers' comments, he guided me at every stage. Whenever I felt uncertain, his clarity of vision helped me overcome challenges. During phases when progress was slow, his encouragement and insistence on maintaining rigour kept me focused. His high standards pushed me to improve the quality of my research, leading to publications in reputed journals and strengthening my research maturity. I deeply appreciate his vast knowledge, forward-looking approach, and guidance in adopting emerging technologies. I am truly grateful for his mentorship, patience, and belief in me. It is because of his solid support that I was able to successfully complete my Ph.D.

I sincerely acknowledge **Prof. Vinod Singh**, DRC Chairman and HoD, Applied Physics, DTU, and Prof. Prateek Sharma, Hon'ble Vice Chancellor, DTU, for providing the necessary resources and academic environment that supported my research work. I am grateful to the **members of the SRC and DRC** for their valuable time, constructive feedback, and thoughtful suggestions that strengthened this thesis. I also thank all the faculty members of the department for their encouragement and guidance during my Ph.D. journey. My heartfelt appreciation goes to the departmental staff, especially **Suresh Ji, Krishna Ji, Babita Ji, Deepak Ji, and Naresh Ji**, for their cooperation and support in ensuring that all administrative processes ran smoothly.

I extend my sincere gratitude to **Anshul** for her constant support in handling official matters, including file movements, timely fee submissions, and keeping me informed about important updates. Her assistance made my college journey smooth and comfortable. I would like to sincerely thank my friends **Anurag Bhandari, Shikha Singh, Vishal Deswal, Kajal, Ayushi, Shubhda, Ashish Chopra, Kajal Sharma, Anu, Dedraj, Vipin, and Dr Rahul Kundra** for their constant encouragement and support throughout this journey. I am also deeply appreciative of all the research scholars in the department for their cooperation, discussions, and shared learning experiences

I sincerely acknowledge the **Director, SSPL**, for granting permission to pursue higher studies and publish this work. I am grateful for the guidance, institutional support, and access to laboratory facilities that enabled me to complete my research in a timely manner.

I sincerely thank **Dr Shiv Kumar**, Sc 'G', Ex-Director, ERIPR, DRDO, for his valuable guidance in publishing my research work. I sincerely thank my Division Head, **Dr Shankar Dutta**, for his support and encouragement throughout my PhD journey. I am also grateful to

Dr Isha Yadav and **Ms Yashoda Parmar** for always being there to listen, support, and offer valuable suggestions. I thank **Dr Preety Verma Shah, Sh. Sukhwinder Singh Lamba, Dr Leeladhar, and Vineeta Gond** for their encouragement and support during my PhD work.

On a personal note, I express my heartfelt gratitude to my husband, **Neeraj Kumar**, for his unwavering support, encouragement, and constant belief in me. He has been my pillar of strength throughout this journey.

I dedicate this Ph.D. to my children, **Anshika Kumar** and **Ayaansh Kumar**, whose patience and understanding allowed me to devote long hours to my work. I hope they always remember that learning has no age limit and that family support is a great strength in achieving one's dreams.

I am deeply grateful to my parents, **Sh. J.S. Rajial** and **Smt. Sudershana Kumari**, for their blessings, values, and unwavering faith in me. I also thank my sister, **Dr. Niketa Rajial**, and brother-in-law, **Dr. Amit Kumar**, for their unconditional love and support. I express my sincere gratitude to my father-in-law, **Sh. Sharad Chander**, and mother-in-law, **Smt. Laxmi Devi**, for their blessings and encouragement. I am thankful to my brother-in-law, **Suraj Kumar**, and sister-in-law, **Dr. Priya Butail**, for their constant support, especially Priya for sharing resources and standing by me as we navigated similar academic paths. A special mention to my nephews, **Nivaan Kumar** and **Naksh Kumar**, whose innocence and laughter brought comfort during challenging times.

I would also like to acknowledge all those who may not be mentioned individually but whose encouragement, support, and goodwill contributed to my doctoral journey in meaningful ways.

Above all, I offer my sincere gratitude to God for guiding me with strength and direction throughout this journey and enabling me to successfully complete my doctoral work.

(Shaveta)

New Delhi

March, 2026

ABSTRACT

Advancing MEMS Gyroscopes: Design, Analysis and Thermal Management for Enhanced Figure of Merit

Microelectromechanical systems (MEMS) have become a cornerstone of modern sensing technologies owing to their unique combination of miniaturization, low power consumption, batch fabrication capability, and high sensitivity. This thesis presents a comprehensive investigation of MEMS-based sensors, with a particular emphasis on MEMS gyroscopes as inertial sensors for navigation, intelligent systems, and defence-related applications. The work begins with a broad overview of MEMS sensors, covering pressure, acceleration, and angular rate sensors; bolometers; magnetic sensors; humidity and flow sensors; optical sensors; biosensors; and microphones. The historical evolution of MEMS technology, its biological inspiration, fabrication techniques, and material considerations are discussed in detail. In addition, the emerging role of MEMS in quantum technologies is explored, highlighting their increasing use in quantum sensing, communication, and atomic-scale devices.

Building on this foundation, the thesis focuses on MEMS gyroscopes operating on the Coriolis principle and develops a detailed theoretical framework to describe their dynamic behaviour and performance. Key performance parameters, including sensitivity, bandwidth, noise, and quality factor, are systematically analysed. Rather than optimizing these parameters individually, the work emphasizes the importance of maximizing an integrated performance measure. To this end, a unified design methodology is proposed to enhance an amended Figure of Merit (FOM) that simultaneously accounts for sensitivity, bandwidth, and noise. Analytical models are validated using CoventorWare and MATLAB/Simulink simulations, demonstrating close agreement with theoretical predictions within 5%. Under identical operating conditions, the optimized thick sense mass configuration achieves a 52-fold improvement in FOM, expressed in units of m Hz/dps^2·mm^2. Furthermore, a new empirical relationship between sensitivity and bandwidth is proposed, offering additional insight into design trade-offs. The

effect of temperature on thermomechanical noise is also incorporated to improve the realism of performance prediction.

To further enhance miniaturization without sacrificing performance, a novel Vertical Sense Mass (VSM) MEMS gyroscope architecture is introduced. The proposed VSM design employs deep reactive ion etching (DRIE) to realize thick proof masses in the out-of-plane direction. This approach enables a 30% reduction in sense mass area and a corresponding 36% reduction in overall sensor footprint compared to conventional planar sense mass designs. Despite this reduction in size, the VSM architecture delivers a substantial performance enhancement, with the overall Performance Metric (PM) increasing from 70.7 $mHz/dps^2 \cdot \mu m^2$ for the planar design to 1090 $mHz/dps^2 \cdot \mu m^2$ for the VSM design. Detailed fabrication process flows are presented, and the successful experimental realization of thick proof mass structures using DRIE confirms the practical feasibility of the proposed architecture.

Recognizing damping as a fundamental limitation in miniaturized MEMS gyroscopes, this thesis presents a comprehensive comparative analysis of energy dissipation mechanisms in both PSM and VSM architectures under identical sense mass areas. The study systematically examines air damping, thermoelastic damping, material damping, anchor loss, viscous damping, and acoustic damping. The results indicate that residual air damping remains a dominant loss mechanism even under vacuum packaging. While the overall trends of individual damping mechanisms are similar for both architectures, the net quality factor (Q_{Total}) of the VSM design is approximately eight times higher than that of the planar design. Temperature-dependent analysis further shows that the VSM architecture maintains a 2.7-times higher quality factor across the operating temperature range. In addition, the VSM design exhibits higher sense displacement up to a quality factor of 100, approximately 20 times the bandwidth across all Q values, and a noise reduction factor of 3.3 compared to the planar counterpart. Sensitivity analysis accounting for fabrication imperfections reveals a maximum variation in Q_{Total} of ±12.8%, indicating acceptable robustness. The proposed VSM design is further validated through comparison with state-of-the-art reported designs and available experimental results.

Finally, the thesis addresses thermal robustness, a major challenge that affects the reliability and accuracy of MEMS gyroscopes in real-world operating environments. A novel packaging-level thermal management strategy is proposed through the integration of a thermally optimized substrate that establishes a controlled temperature offset between the sensor and the package base. When combined with a thermally engineered structural design that minimizes heat flow into the sense mass, this approach achieves a device temperature reduction of approximately 25 °C, as confirmed by transient thermal analysis. The improved thermal isolation leads to significant reductions in temperature-dependent variations of sense deflection and scale factor. Specifically, sense deflection variation is reduced from 2.7 × 10 μm/°C to 8.6 × 10 μm/°C, while scale factor temperature sensitivity decreases from 232 ppm/°C to 6 ppm/°C. Additional improvements are observed in noise reduction and bandwidth stabilization. Stress analysis confirms enhanced structural integrity, and etching experiments validate the feasibility of the thermally optimized substrate.

Overall, this thesis presents a holistic, fabrication-aware, and quantitatively validated approach to MEMS gyroscope development, integrating architectural innovation, performance optimization, damping mitigation, and thermal management. The outcomes of this work significantly advance the state of MEMS gyroscope technology and provide robust design guidelines for the development of compact, high-performance, and thermally stable inertial sensors suitable for next-generation navigation, autonomous, and defence systems.

Contents

DECLARATION i

CERTIFICATE ii

ACKNOWLEDGEMENTS iii

ABSTRACT vi

List of figures ix

List of tables xiv

List of publications xv

1. Introduction 1

1.1 MEMS sensors…………………………………………………………… 2

1.1.1 Inertial Sensors: Biological Inspiration to MEMS Inertial Measurement Units……………………………………………... 3

1.2 Market Motivation for MEMS Sensors…………………………………….. 5

1.2.1 Global MEMS and MEMS Sensors Market Scenario…………... 6

1.2.2 Indian Sensors Market and Strategic Importance…………………. 7

1.2.3 MEMS Gyroscope Market and Emerging Trends…………………. 7

1.3 Evolution of Gyroscope Technologies……………………………………… 8

1.3.1 MEMS Gyroscope Architectures………………………………….. 10

1.4 Coriolis Effect………………………………………………………………. 12

1.5 Survey of Prior Work on MEMS Gyroscopes……………………………… 14

1.6 MEMS Fabrication Technologies: An Overview…………………………… 17

1.6.1 Bulk Micromachining……………………………………………... 19

1.6.2 Surface Micromachining………………………………………….. 19

1.6.3 Deep Reactive Ion Etching (DRIE)………………………………. 20

1.6.4 LIGA Process……………………………………………………… 21

1.6.5 Electro-Discharge Micromachining (EDM)………………………. 21

1.6.6 Supporting Microfabrication Processes ……………………. 22

1.7 MEMS Gyroscopes Applications in Navigation and Defence Systems……. 22
1.8 Challenges in MEMS Gyroscopes……………………………………….. 24
1.9 Research Objectives…………………………………………………… 25
1.10 Thesis Organisation…………………………………………………… 25
References……………………………………………………………… 26
2. Fundamental Theory and Operating Principles of MEMS Gyroscope 31
2.1 Introduction…………………………………………………………… 32
2.2 Frame of Reference…………………………………………………… 32
2.2.1 Coriolis force in MEMS Gyroscope……………………………. 34
2.3 Physical Structure of a MEMS Vibratory Gyroscope……………………. 35
2.3.1 Lumped-Parameter Modelling of MEMS Gyroscopes……………. 36
2.3.2 Bandwidth of MEMS gyroscope…………………………………... 41
2.2.3 Thermo-Mechanical Noise……………………………………… 44
2.4 Quadrature Error and Structural Imperfections……………………………... 45
2.5 Assumptions Used in Modelling of the Vibratory MEMS Gyroscope………. 46
2.6 Conclusion…………………………………………………………….. 47
References …………………………………………………………………. 47
3. Structural Parameter Design and Performance Trade-off in Conventional MEMS Gyroscope 49
3.1 Introduction……………………………………………………………. 50
3.2 Gyroscope Structure and Operating Principle………………………………. 51
3.3 Design Assumptions and Modelling Scope………………………………. 52
3.4 Design Parameters and Optimization Variables…………………………….. 52
3.5 Drive and Sense Modal Frequency Analysis……………………………….. 55
3.6 Parametric Analysis of Mass and Stiffness Ratios…………………………. 56
3.6.1 Effect of Mass and Stiffness Ratios on Sensitivity……………….. 56
3.6.1.1 Sensitivity Dependence on Displacement………………… 58
3.6.2 Effect of Mass and Stiffness Ratios on Bandwidth………………… 59
3.6.2.1 Bandwidth dependence on damping……………………… 59
3.6.3 Thermomechanical Noise Analysis……………………………….. 60
3.7 Design Validation Using Simulation…………………………………….. 61
3.7.1 Drive and Sense Displacement Validation………………………… 62
3.7.2 Comparative Performance Evaluation with Literature…………….. 64
3.7.3 Summary of Simulation Validation………………………………… 66
3.8 Figure of Merit–Based Performance Evaluation…………………... 66
3.8.1 Comparison of FOM with Reported Designs……………………… 66

3.8.2 Empirical Relationship Between Sensitivity and Bandwidth………. 68
3.8.3 Effect of Sense-Mass Thickness and Temperature on FOM……….. 68
3.9 Conclusion ………………………………………………………………. 70
References ………………………………………………………………………. 70
4. Miniaturized MEMS Gyroscopes with Thick Vertical Sense Mass Structures for Enhanced Performance 73
4.1 Introduction………………………………………………………………. 74
4.2 Design Methodology of Vertical Sense Mass Gyroscope…………………… 74
4.3 Analytical Performance Evaluation………………………………………… 75
4.4 Optimization of Sense Mass Spring Parameters…………………………… 76
4.4.1 Effect of l_{bs} and t_{bs} on sense $K_{s(vsm)}$ ……………………………… 76
4.4.2 Effect of l_{bs} and t_{bs} on sense resonant frequency f_s………………….. 77
4.5 Comparison of VSM and PSM Design Performance Parameters………….. 78
4.5.1 Sensitivity……………………………………………………… 78
4.5.2 Bandwidth……………………………………………………… 82
4.5.3 Thermomechanical Noise……………………………………… 83
4.6 Comparison Using the Improved Performance Metric…………………….. 84
4.6.1 Comparative Analysis with Reported Designs…………………… 85
4.7 Fabrication Strategy and Experimental Validation………………………… 86
4.7.1 DRIE Experiment on Thick Substrate…………………………... 88
4.8 Conclusion………………………………………………………………. 89
References………………………………………………………………………. 90
5. Damping Mechanisms in MEMS Gyroscope: A Comparative Study of Planar and Vertical Sense Architectures 93
5.1 Introduction………………………………………………………………. 94
5.2 Design Methodology of Vertical Sense Mass Gyroscope…………………... 95
5.3 Damping Analysis of VSM versus PSM…………………………………… 97
5.4 Effect of Damping on Quality Factor……………………………………… 98
5.5 Analytical Modelling of Damping………………………………………….. 99
5.5.1 Air Damping…………………………………………………… 99
5.5.2 Viscous Damping……………………………………………….. 100
5.5.3 Thermoelastic Damping………………………………………… 100
5.5.4 Material (Rayleigh) Damping…………………………………... 100
5.5.5 Anchor Loss…………………………………………………….. 101
5.5.6 Acoustic Damping………………………………………………. 101
5.5.7 Consolidated Damping Considerations…………………………. 101

5.6 Results and Discussion: Effect of Ambient Pressure........................... 102
5.6.1 Air and Viscous Quality Factor Variation.............................. 102
5.6.2 Acoustic Quality Factor Variation...................................... 103
5.6.3 Anchor and Rayleigh Quality Factor Variation......................... 103
5.6.4 Overall Quality Factor Variation with Pressure........................ 105
5.7 Results and Discussion: Effect of Temperature................................. 106
5.7.1 Air and Viscous Quality Factor Variation.............................. 106
5.7.2 Thermoelastic, Rayleigh, and Anchor Quality Factor Variation...... 107
5.7.3 Acoustic Quality Factor Variation...................................... 108
5.7.4 Overall Quality Factor Variation with Temperature................... 108
5.8 Results and Discussion: Frequency-Dependent Damping Characteristics.... 109
5.9 Comparison of VSM and PSM Designs in Terms of Performance Parameters.. 111
5.9.1 Sensitivity Versus Quality Factor...................................... 111
5.9.2 Bandwidth Versus Quality Factor....................................... 112
5.9.3 Thermomechanical Noise versus Quality Factor....................... 112
5.9.4 Overall Performance Trade-Off and Design Implications............ 113
5.10 Sensitivity of Q_{Total} to Key Parameters.. 113
5.10.1 Global Parameter Sensitivity Analysis................................. 113
5.10.2 Local (Fabrication-Induced) Sensitivity Analysis..................... 114
5.10.3 Key Sensitivity Findings.. 114
5.10.4 Interpretation and Design Implications................................. 115
5.11 Design and Experimental Validation.. 116
5.11.1 Comparative Quality Factor–Pressure Behaviour Across State-of-the-Art Architectures.. 116
5.11.2 Experimental Validation... 117
5.12 Mitigating Unwanted Damping Mechanisms in MEMS Gyroscopes.......... 118
5.13 Conclusions... 119
References.. 120
6. Robust Improvement in MEMS Gyroscopes Structure Through Novel Substrate Integration Techniques 122
6.1 Introduction.. 123
6.2 Novel Thermal Design Approach.. 124
6.2.1 Design of Thermal Substrate (TS)...................................... 124
6.2.2 Steady-State Thermal Analysis of Thermal Substrates................ 126
6.2.3 Thermal Resistance Analysis... 127
6.2.4 Thermal Substrate (TS) Temperature Variation........................ 128

6.2.5 Transient Thermal Response…………………………………………….. 129
6.2.6 Stress Analysis…………………………………………………………... 130
6.2.7 Taper Angle Dependence……………………………………………….. 132
6.3 Improved Thermal Design of the MEMS Gyroscope………………………….. 132
6.3.1 Resonant frequency variation with temperature……………………… 134
6.3.2 Heat conduction in Straight and Tapered Sense Beams……………. 136
6.3.3 Sense Displacement with Different Thermal Substrate (TS) Bases... 137
6.4 Scale Factor Temperature Sensitivity………………………………………..... 139
6.5 Noise Temperature Dependence……………………………………………….. 142
6.6 Bandwidth Temperature Dependence………………………………………….. 144
6.7 Results Validation…………………………………………………………… 145
6.8 Fabrication Experiment………………………………………………………... 147
6.9 Conclusion……………………………………………………………………... 148
References…………………………………………………………………………….. 148
7. Summary, Social Impact and Future Scope 151
7.1 Summary……………………………………………………………………….. 152
7.2 Social Impact…………………………………………………………………... 153
7.3 Future Scope………………………………………………………………… 154

List of Figures

1.1 Vestibular system showing otolith organ and semicircular canals.................. 4

1.2 Inertial Measurement Unit 5

1.3 MEMS market forecast 2020-2026.. 6

1.4 Military sensor market trend.. 6

1.5 Indian sensor market (a) Forecast 2024-2033 (b) End user Industry 2024....... 7

1.6 MEMS gyroscope market forecast 2024-2035... 8

1.7 Gyroscope development timeline... 9

1.8 (a)Tuning Fork gyroscope (b) Beam-beam Gyroscope.............................. 10

1.9 (a)Butterfly Gyroscope (b) Quad-mass gyroscope.................................. 10

1.10 (a)Disc (b) Ring resonator gyroscope.. 11

1.11 (a) Hemispherical resonator gyroscope (b) Vertical sense mass gyroscope....... 12

1.12 Coriolis effect due to the Earth's rotation.. 13

1.13 Coriolis effect depiction... 13

1.14 Bulk Micromachining process... 19

1.15 Surface micromachining process.. 20

1.16 Deep Reactive Ion Etching Process.. 21

1.17 Lithographic Galvanoformung Abformung (LIGA process)...................... 21

1.18 Electro-Discharge Micromachining process... 22

1.19 Deployment of MEMS inertial sensors in navigation, guidance, stabilisation, and control systems for civilian, aerospace, and defence applications............ 23

2.1 Inertial frame of reference S' is moving with constant velocity v relative to S.... 33

2.2 Inertial frame of reference M' is accelerating with relative to M.................. 33

2.3 Inertial frame of reference P' is rotating with angular velocity relative to P.... 34

2.4 (a) Coriolis force in gyroscope (b) Gyroscope axis terminology................... 35

2.5 MEMS vibratory gyroscope schematic... 36

2.6 Mass-spring damper system for MEMS gyroscope................................ 36

2.7 Frequency response of drive and sense modes in a typical MEMS vibratory gyroscope.. 43

3.1 (a) Three-dimensional view of the proposed gyroscope structure and the parameter definition. (b) The gyroscope structure is excited in drive mode in the X-direction, with the drive mass displacement shown in red. c) The gyroscope sense mass structure is excited in sense mode along the Z-axis....... 51

3.2 The drive and sense displacement at the drive and sense frequency.............. 55

3.3 Sense displacement variation for the proposed design with (a) M_r at different K_r, (b) Kr at different Mr, and (c) 3D plot showing the variation of sense displacement with Mass ratio (M_r) and Stiffness ratio (K_r)....................... 57

3.4 Variation of Sense displacement as a function of Rotation rate $_y$ for different (a) M_r values for a fixed K_r =6.9. (b) K_r values for a fixed M_r =7.04........... 58

3.5 Normalized displacement with the frequency of the input angular rate at different values of (a) M_r for a fixed K_r =7.04 (b) K_r for a fixed M_r =7.04....... 59

3.6 Bandwidth variation with damping coefficient at different value of (a) M_r for a fixed K_r =7.04 (b) K_r for a fixed M_r =7.04.. 60

3.7 Variation of RMS Thermomechanical noise with sense mass thickness.......... 61

3.8 Comparison of peak drive displacement obtained analytically with MEMS+ and Simulink... 62

3.9 Comparison of sense displacement obtained analytically with MEMS+ and Simulink.. 63

3.10 Drive waveform pattern using MEMS+, Analytical and Simulink simulations... 63

3.11 Sense waveform patterns using MEMS+, Analytical and Simulink simulations. 64

3.12 Sense displacement vs $_y$ for [35] and the proposed design....................... 65

3.13 Change in capacitance vs $_y$ for [35] and proposed design....................... 65

3.14 Comparison of the proposed analytical relation between S vs. BWvis-à-vis experimental result (Ref. Table 3)... 68

3.15 Variation of FOM considering (a) Capacitance (b) Sense displacement.......... 69

3.16 Plot of Thermomechanical Noise variation for the present design and improved thermal design at temperatures ranging from -40 ^{0}C to 125 ^{0}C.................. 70

4.1 Figure 4.1(a) The schematic of Vertical sense mass (VSM) and Planar sense mass. (b) Vertical Sense Mass (VSM) design utilizing depth of 500 µm for sense. (c) Planar Sense Mass (PSM) design that uses a shallow depth of 300 µm for sense mass structure. (d) Vertical Sense Mass (VSM) and Planar Sense Mass (PSM) design structures on the same scale for footprint.................. 75

4.2 (a) Side view of VSM springs attached to sense mass. (b) Modal analysis of sense mass for VSM design for two cases, (i) Low twisting and (ii) High twisting.. 77

4.3 3-D plot showing the variation of sense mass natural frequency with spring length and thickness........ 78

4.4 Modal analysis results: (a) Drive mode in VSM design, (b) Sense mode in VSM design, (c) Drive mode in PSM design, (d) Sense mode in PSM design......... 79

4.5 (a) Drive displacement as a function of frequency showing peak at the resonant frequency f_d (b) Sense displacement as a function of frequency showing peak at the resonant frequency f_s 79

4.6 (a) Sense mass displacement for different M_r at fixed K_r. 80
(b) The plot of sense displacement at different M_r and K_r for VSM and PSM design........ 81

4.7 Sensitivity for VSM design ($M_r = 7.82$, $K_r = 7.80$) and PSM design ($M_r = 7.04$, $K_r = 6.9$) and K_r........ 81

4.8 3d plot of bandwidth variation at diff M_r........ 82

4.9 (a) Normalized displacement for VSM design ($M_r = 7.82$, $K_r = 7.80$) and PSM design ($M_r = 7.04$, $K_r = 6.9$) (b) Bandwidth with normalized damping for VSM design ($M_r = 7.82$, $K_r = 7.80$) and PSM design ($M_r = 7.04$, $K_r = 6.9$) 83

4.10 (a) Thermomechanical noise variation with sense mass thickness 83
(b) 3-D plot for noise variation at different M_r and K_r for PSM design at 500 μm sense mass thickness........ 84

4.11 Experimental results of PM at different sense mass thickness for various designs from literature vis-à-vis our proposed design........ 86

4.12 Fabrication process sequence for the proposed design........ 87

4.13 The SEM image of the released structure........ 89

5.1 (a) Three-dimensional view of the Vertical Sense Mass (VSM) design (b) Planar Sense Mass (PSM) design........ 95

5.2 Drive and sense mode deflection in (a) VSM design and (b) PSM design........ 96

5.3 (a) VSM design: Top view and air motion (b) PSM design: Sense mass Side view, front view and air motion........ 97

5.4 Variation of (a) air-damping and (b) viscous-damping quality factors with ambient pressure for VSM and PSM gyroscope designs........ 103

5.5 Variation of the acoustic damping quality factor with ambient pressure for VSM and PSM gyroscope designs........ 104

5.6 Variation of the anchor-loss quality factor with (a) *w/l* ratio and (b) d/d_p ratio for VSM and PSM gyroscope designs........ 104

5.7 Consolidated quality factors variation with pressure for both the VSM and PSM gyroscope designs........ 105

5.8 Variation of (a) air-damping (b) viscous-damping quality factors with temperature for both VSM and PSM design........ 106

5.9 Variation of (a) thermoelastic-damping and (b) Rayleigh-damping quality factors with temperature for VSM and PSM designs........ 107

5.10 Variation of acoustic-damping quality factor with temperature for VSM and PSM designs........ 108

5.11 Consolidated variation of individual and total quality factors with temperature for VSM and PSM designs at atmospheric pressure........ 109

5.12 Frequency-dependent variation of individual damping-related quality factors for the VSM gyroscope at atmospheric pressure and room temperature........ 110

5.13 Variation of sense-mode displacement with sense-mode quality factor for VSM and PSM gyroscope designs........ 111

5.14 Variation of bandwidth with quality factor for VSM and PSM gyroscope designs........ 112

5.15 Variation of RMS thermomechanical noise with quality factor for VSM and PSM gyroscope designs........ 112

5.16 Figure 5.16 Tornado Plot for 5% fabrication variation sensitivity........ 116

5.17 (a) Quality factor vs pressure showing design validation. (b) Q_{Total} vs pressure plot showing experimental validation........ 118

6.1 Three-dimensional views of various thermal substrates (TS). (a) Planar Silicon with oxide (Type-I). (b) 2-pillar Silicon with oxide (Type-II). (c) 4-pillar Silicon with oxide (Type-III). (d) 4-pillar tapered silicon with oxide (Type-IV).. 125

6.2 Temperature distribution profile for different thermal substrates: (a) Type-I, (b) Type-II, (c) Type-III, (d) Type-IV........ 126

6.3 (a) Temperature variation across TS thickness with and without oxide and base modifications. (b) Temperature variation along the lateral dimension of the TS with and without oxide........ 128

6.4 Transient response of thermal substrates........ 130

6.5 Thermal stress contours in the Type-IV TS at temperatures (a) –40 °C, (b) 100 °C, (c) 125 °C, and (d) stress–temperature plot........ 131

6.6 Thermal stress contours in the Type-IV TS at temperatures (a) –40 °C, (b) 100 °C, (c) 125 °C, and (d) stress–temperature plot........ 132

6.7 MEMS Gyroscope mounted on a Type IV (tapered with four pillars) Thermal substrate (TS) (a) 3D view (b) Side view. The integrated hybrid structure is mounted on the package base........ 133

6.8 Three-dimensional view of the MEMS gyroscope with tapered beam design, showing zoomed-in views of the sense and drive beams........ 134

6.9 (a) drive and sense frequency variation (b) Frequency mismatch variation of the modified beam structure with temperature........ 135

6.10 Typical temperature distribution at temperature other than room temperature... 136

6.11 The heat flow in x, y, z direction at (a)233 K (b) 398K........ 136

6.12 Shows the heat flow in x, y, z directions at (a) 233K (b) 398 K for the tapered beam........ 137

6.13 Sense displacement as a function of temperature for various gyroscope configurations: conventional design without TS, conventional design with TS, tapered beam design without TS, and tapered beam design with TS (Type IV).. 138

6.14 Sense displacement versus temperature for different taper angles…………….. 139

6.15 Sense displacement versus rotation rate at temperatures ranging from –40 °C to 125 °C for (a) conventional design without TS, and (b) tapered beam design with Type IV TS……………………………………………………………….. 140

6.16 Plot of scale factor sensitivity for conventional design without TS and tapered beam design with TS Type IV up to 100 rad/s at temperatures ranging from -40 ^{0}C to 125 ^{0}C………………………………………………………………… 141

6.17 Variation of f_d, f_s, x_d, BW, and Q_s with temperature from –40 °C to 125 °C… 142

6.18 Thermomechanical noise variation for conventional design without TS and tapered beam design with TS from –40 °C to 125 °C………………………….. 144

6.19 Bandwidth variation with temperature for conventional design without TS and tapered beam design with Type IV TS from –40 °C to 125 °C……………….. 144

6.20 SEM images of the fabricated Thermal Substrate (TS): (a) top view of the TS, (b) SEM image showing the channels between adjacent TSs used for dicing, (c) magnified view of one of the channels, and (d) backside view of the TS showing the etched support pillars…………………………………………….. 147

List of Tables

1.1	Classification of MEMS Sensors and Structural Complexity……………………..	3
1.2	Timeline of MEMS Gyroscope Research and Key Developments…………….	18
2.1	Physical Mapping to MEMS Structure………………………………………..	37
2.2	Summary of Noise Impact on Performance Metrics……………………………	45
3.1	The quality factor with pressure………………………………………………..	53
3.2	MEMS vibration gyroscope structure parameters……………………………..	54
3.3	Comparison of FOM for our design vis-à-vis other designs from the literature…………………………………………………………………………	67
4.1	Effect of Sense mass, spring length, and thickness on sense mode frequency and twisting angle of VSM and PSM………………………………………………..	77
4.2	Comparison of PMs for the proposed VSM design vis-à-a-vis from other designs from literature……………………………………………………….	85
5.1	Various type of damping and factors affecting each damping…………………..	102
5.2	The consolidated results of various damping for VSM and PSM design……….	114
5.3	Sensitivity of Q_{Total} to Design and ±5% Fabrication Variation………………….	115
6.1	Thermal resistance values for different Thermal Substrates (Type-I to Type-IV)…………………………………………………………………………….	127
6.2	Von Mises stress values of the gyroscope and Thermal Substrate (TS) due to CTE mismatch………………………………………………………………..	131
6.3	Comparative analysis of temperature compensation techniques reported in the literature and the present study………………………………………...........	148

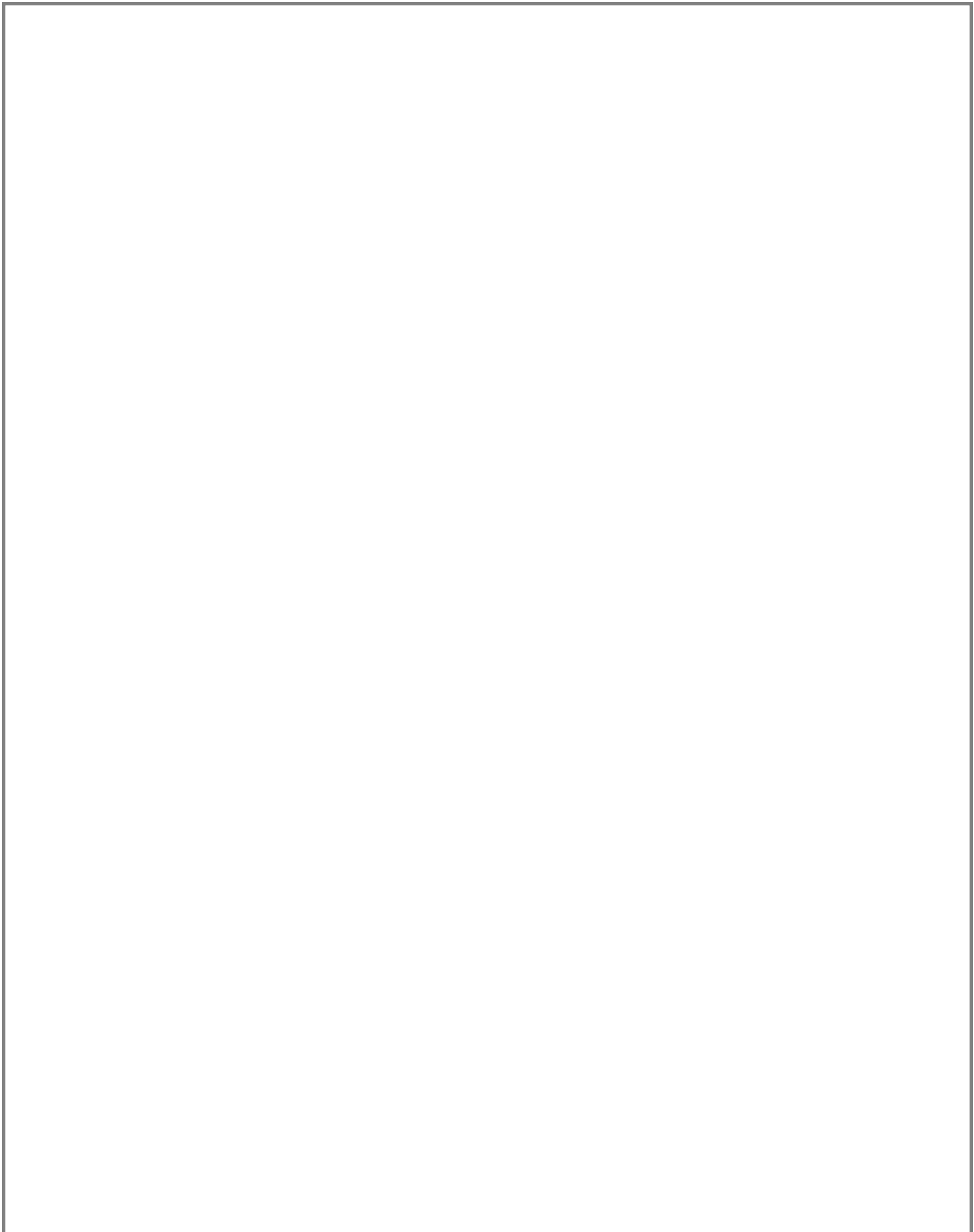

List of publications

Publications Resulted from This Thesis Work

Articles in National and International Refereed Journals (4):

1. **Shaveta**, R.K. Bhan and R. Chaujar, "Design optimization of MEMS gyroscope for enhanced sensitivity, bandwidth and noise reduction", **Micro and Nanostructures** 206 (2025) 208224. **(SCIE index, IF – 3.0).**

2. **Shaveta**, R.K. Bhan and R. Chaujar, "Enhancing MEMS Gyroscope Performance with Vertical Sense Mass Design", **Defence Science Journal,** Vol. 75, No. 6, November 2025, pp. 758-770. **(SCIE index, IF – 1.16).**

3. **Shaveta**, R.K. Bhan and R. Chaujar, "Mitigating thermal effects in MEMS gyroscopes: A novel substrate integration approach", **Sensors & Actuators: A. Physical** 392 (2025) 116733. **(SCIE index, IF – 4.9).**

4. **Shaveta**, R.K. Bhan and R. Chaujar, "Beyond Planar: A Vertical Sense Mass Approach to Overcome Damping Challenge in MEMS Gyroscope", **Micro and Nanostructures** 211(2026) 208539**. (SCIE index, IF – 3.0).**

ARTICLES IN INTERNATIONAL CONFERENCES (2):

1. **Shaveta**, R.K. Bhan and R. Chaujar, "Tapered-based Novel Thermal Compensation Techniques for Enhanced Performance of MEMS-based Gyroscope", in Proc. **IEEE 2024 Second International Conference on Emerging Trends in Information Technology and Engineering (ICETITE)**, pp. 1–4, 2024.

2. **Shaveta**, R.K. Bhan and R. Chaujar, "Effect of pressure on damping for a novel vertical sense mass MEMS gyroscope", in proc. **IEEE International Conference on Recent Smart Technologies in Engineering (DELCON 2025).**

Chapters Contributed in Book (1):

1. **Shaveta**, R.K. Bhan and R. Chaujar "**MEMS Sensors: Journey from Biological Inspiration to Quantum Frontiers**", **Microelectronics: Simulations, Modeling, and Applications, Wiley online library**, Scrivener Publishing. DOI: 10.1002/9781394336487.ch12**.**

CHAPTER 1

INTRODUCTION

- *MEMS Sensors: The Applications in Civilian, Defence & Aerospace.*
- *MEMS Sensors Market Report Notes: Unit and Value Balance of MEMS Gyroscopes.*
- *A Survey on State-of-the-Art MEMS Gyroscope Architectures and Performance Trends.*
- *MEMS Fabrication Technologies (Surface/Bulk Micromachining, DRIE) for Inertial Sensors.*
- *Summary of Key Challenges and Research Needs for Miniaturization, Damping, Noise and Thermal Robustness.*

1.1MEMS sensors

The future demands that technology continue to shrink, become more performance-intensive, and become smarter. Devices are expected to be more compact, respond faster, and consume less power. At the same time, devices should preserve high accuracy and durability under diverse conditions. In 1857, Feynman, in his lecture on “There’s Plenty of Room at the Bottom,” dreamed of how miniaturization could change the world. This gave a glimpse of the paradigm shift that we observe taking form today. This idea would provide the philosophical foundation for micro- and nanoscale engineering, which subsequently has become a fundamental enabler of modern technology. Four decades later, this vision has evolved from theoretical speculation to practical realization, and micro-scale devices are being integrated into virtually every facet of daily life, from smartphones and medical implants to aerospace and defence systems. The miniaturization of systems in practice began with the first integrated circuit fabrication and its demonstration by Texas Instruments (TI) in 1958. Then, with its high mechanical, electrical and thermal properties, silicon became the widely used substrate material. By the mid-1960s, these properties were explored for applications in early micro-scale mechanical devices, thereby beginning solid-state device engineering. These advances ultimately led to microtechnology, enabling mechanical and electrical structures to be fabricated using semiconductor fabrication processes. Combining mechanical, electrical components, and microfabrication technologies gave birth to Micro-Electro-Mechanical Systems (MEMS), also called microsystems in some parts of the world. MEMS technology integrates sensors, actuators, and signal-processing electronics on a shared substrate, enabling compactness, low power consumption, batch manufacturing, and high functional density [1–3].

Sensors are the building blocks in MEMS-based systems. A sensor is a system that responds to the input of physical variables such as temperature, pressure, acceleration, rotation, magnetic fields, or chemical composition. There are many highly efficient sensing mechanisms inherent to nature. For example, when we touch the touch-me-not plant, it reacts by folding its leaflets, while our sensory system utilizes inputs from touch, sight, hearing, taste, and smell to engage in proactive behaviour in response to external stimuli. The human brain serves as an advanced decision-making and control system. MEMS sensors serve a strategically important role in defence and aerospace systems. Owing to their small size, low weight and very high reliability, they reduce system footprint considerably while improving performance, making them indispensable for modern navigation, guidance and control systems [4–13]. Because of the breadth of applications for MEMS technology, there is a wide variety of sensor types, each designed to measure particular physical, chemical or biological parameters. This information is concluded in Table 1, where a summary of the most common MEMS-based sensors is stated with their main functionalities, structure requirements and application within defence.

Inspired by biological systems, engineers have sought to develop artificial sensors that can perceive the environment and respond with high sensitivity and intelligence [6]. This has made MEMS technology a vital part in achieving this objective. MEMS sensors are being developed for applications in pressure, acceleration, gyroscope, microphone, magnetic, biosensor and optical. MEMS fabrication techniques are also being adapted for other advanced applications, like microfabricated cavities and structures for quantum sensors. These trends reflect the importance of MEMS technology across sectors. They are widely used across consumer electronics, automotive systems, biomedical instruments, industrial automation equipment, environmental sensor systems, and personal care products.

Table 1.1 Classification of MEMS Sensors and Structural Complexity

S. No	MEMS Sensor Type	Defence/Strategic Function	Structural Requirement	Relative Structural Complexity	Defence Relevance
1	Accelerometer [14]	Linear acceleration, vibration	Proof mass, springs	Medium	INS aiding, fuze systems
2	Gyroscope [15]	Angular rate sensing (INS core)	Drive & sense masses, resonant structures, electrodes	Very High	Missiles, UAVs, navigation, guidance
3	Pressure Sensor [7]	Altitude sensing, air data systems	Diaphragm, cavity, ports	Low	Aircraft, missiles
4	Bolometer [16]	IR detection, night vision	Thermal isolation, IR absorber	Medium	Surveillance, thermal imaging
5	Magnetic Sensor [17]	Heading, magnetic anomaly	Magnetic layer, suspension	Medium	Navigation aiding
6	Humidity Sensor [4]	Environmental monitoring	Diffusion port, sensing layer	Low	Logistics, storage safety
7	Flow Sensor [8]	Fuel / air flow monitoring	Microchannels, heater	Medium	Propulsion systems
8	Optical Sensor [18]	Target tracking, beam steering	Micromirrors, actuators	High	EO/IR payloads
9	Biosensor [19]	Bio-agent detection	Microchannels, sensing layer	Medium	Nuclear, Biological, and Chemical defence
10	Microphone [20]	Acoustic detection	Diaphragm, cavity	Low	Surveillance
11	Chemical Sensor [13]	Chemical threat detection	Porous layer, heater	Medium	Chemical, Biological, Radiological, Nuclear defence
12	Gas Sensor [6]	Toxic gas monitoring	Microheater, sensing film	Medium	Soldier safety
13	Torque Sensor [21]	Actuation feedback	Torsional springs	Medium	Control systems
14	Strain Gauge[22]	Structural deformation	Strain layer, bridge	Low	Structural Health Monitoring
15	Temperature Sensor [23]	Thermal monitoring	Thermal isolation	Low	System protection

1.1.1 Inertial Sensors: Biological Inspiration to MEMS Inertial Measurement Units

MEMS accelerometers and gyroscopes fall into the category of inertial sensors, because they measure motion by taking advantage of a body's natural tendency to oppose changes in its state

of motion (a property termed inertia). At the heart of these sensors is a tiny micromachined proof mass, suspended mechanically within the device. The surrounding structure of the sensor and proof mass is rigidly attached to the device; as the system undergoes linear acceleration or angular rotation, the proof mass attempts to remain fixed in space due to inertia. The motion between the proof mass and the sensor frame causes a small displacement or rotation, which is converted into an electrical signal by dedicated transduction mechanisms. This means that because this sensing process is based entirely on internal inertial effects and classical mechanics, MEMS inertial sensors can measure motion independently [24–29].

Inertial sensing is not a man-made concept; it is deeply rooted in nature. Long before the development of silicon-based sensors, the human body evolved an efficient inertial measurement system within the inner ear, known as the vestibular system (Figure 1.1). This biological IMU enables humans to perceive linear acceleration, angular motion, gravity, and body orientation without reliance on external references. The otolith organs function as natural accelerometers, where tiny calcium-carbonate crystals act as proof masses that respond to linear acceleration and tilt. Similarly, the three mutually orthogonal semicircular canals function as natural gyroscopes, sensing angular velocity through the inertial lag of fluid during rotational motion. The brain continuously fuses signals from these sensing elements to maintain balance, posture, and spatial awareness [30,31].

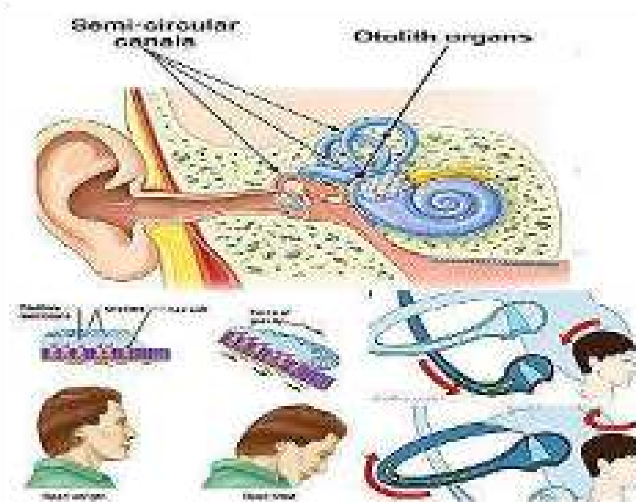

Figure 1.1 Vestibular system showing the otolith organs and semicircular canals [31].

MEMS accelerometers mimic the otolith structure with a suspended silicon proof mass, and MEMS gyroscopes simulate the semi-circular canals by sensing Coriolis-induced motion on vibrating structures. Both sensors together form an Inertial Measurement Unit (IMU), which combines sensor outputs electronically to estimate parameters such as position, velocity, and orientation, as shown in Figure 1.2 [32–34]. This bio-inspired analogy highlights both the fundamental operating principles of inertial sensors and their critical role in navigation and control systems, providing a natural motivation for the study and development of high-performance MEMS gyroscopes discussed in this thesis.

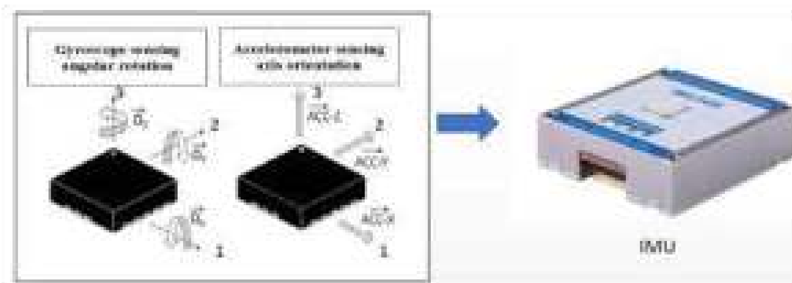

Figure 1.2 Inertial Measurement Unit [35].

Both sensors can run independently, so the electronics can use either accelerometers or gyros. Accelerometers are good for low-frequency motion detection, since they can sense gravity (an accelerometer cannot distinguish between gravity and motion), but in this regard they do not have great capabilities for continuously sensing orientation. Gyros detect rotation around the axes (important in inertial navigation, attitude control, and positioning systems) and compare them with desired angular velocities.

In an IMU, both sensor data are fused to provide full motion and orientation data without a global positioning system (GPS). It is critical in conditions when the GPS signal is unavailable. IMU is positioned at the centre of aerospace and defence navigation systems. A gyroscope is responsible for providing short-term accuracy, fast dynamic response, and reliable attitude determination, while the accelerometer mainly supports long-term correction. Because of this, the overall performance of an IMU is often limited by the gyroscope, particularly due to its noise, drift, accuracy constraints, and sensitivity to environmental conditions. As systems continue to miniaturize, these challenges become even more pronounced, making the MEMS gyroscope the most complex and performance-critical component in an IMU.

In addition, MEMS gyroscopes are highly sensitive to factors such as damping, noise, and temperature variations. Their performance is strongly influenced by parameters such as geometry, structural thickness, material properties, and packaging, all of which play a crucial role in device design and system-level optimization. Although MEMS gyroscope technology has advanced significantly, several key challenges still remain. With continuous scaling down of device dimensions, issues related to accuracy, sensitivity, long-term stability, temperature dependence, noise, and repeatability become increasingly difficult to manage. Structural design constraints, fabrication-induced variations, and environmental effects further limit achievable performance [26,36–40].

Notably, these challenges can also serve as great opportunities for improvement in structural and system-level aspects that are highly relevant to applications seeking tight reliability and robustness guarantees. Thus, this work investigates the design, modelling and simulation of MEMS gyroscopes with emphasis on structural optimization to enhance their performance. By addressing key limitations associated with miniaturization, damping, and thermal effects, this work aims to contribute toward the development of robust, high-precision MEMS gyroscopes suitable for next-generation inertial sensing applications.

1.2 Market Motivation for MEMS Sensors

The MEMS industry's growth and reliance on inertial sensing technologies drive focused research to improve MEMS gyro performance. Commercial MEMS gyroscopes are not only capable of being driven by market trends in nanoscience and precision science, but they also hold strategic importance for navigation, guidance, and stabilization applications.

1.2.1 Global MEMS and MEMS Sensors Market Scenario

The MEMS market is growing steadily, and its technology is maturing. Based on 2024 estimates, total MEMS revenue will be 15.4 billion USD globally; by the end of 2030, it will reach nearly 19.2 billion USD, with a mixed annual growth rate (CAGR) of approximately 3.7% [41]. Because of the high-performance requirements and pricing, the automotive, industrial, and defence MEMS segments generate higher revenues; on the other hand, consumer electronics remains the highest-volume market. A few large manufacturers still control the MEMS sector, especially in emerging Asian markets. Although supply-chain fluctuations and pricing pressures exist, the long-term demand for MEMS-based sensing solutions remains strong, particularly for inertial sensors used in safety-critical and mission-critical applications.

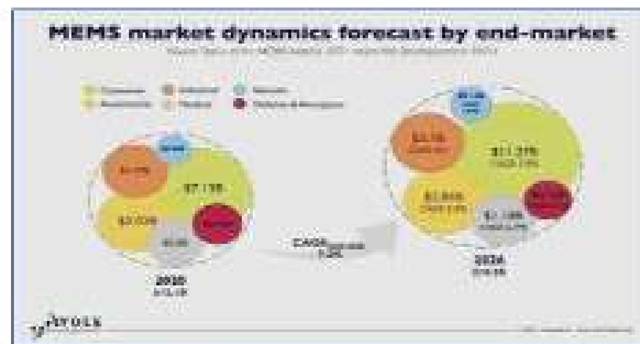

Figure 1.3 MEMS market forecast 2020-2026 [41].

The largest current demand for technologically driven MEMS sensors is in defence. It covers a broad spectrum of applications, from cutting-edge missiles and advanced aircraft to high-tech satellites and UAVs (drones), naval platforms, and heavily armoured ground units. Modern military systems require a miniaturised, robust, and highly accurate sensor. Additionally, these sensors need to operate deterministically and power-efficiently in demanding and even extreme environments with limited or no GPS localizations. For example, the military sensors market was valued at just under 10 billion USD in 2020 and is expected to exceed 17 billion USD by the end of 2030, with a CAGR of ~6% [42]. Among inertial sensors, MEMS accelerometers and gyroscopes are expected to represent significant revenue in this market. Their dominance is driven by the widespread deployment of inertial navigation systems (INS) in military aviation, precision-guided munitions, and autonomous platforms.

Figure 1.4 Military sensor market trend [42].

1.2.2 Indian Sensors Market and Strategic Importance

Growing national-level and subsequent government support, along with the increasing adoption of in-house technologies, are rapidly upgrading the Indian sensors market. Additionally, the IMARC Group projected that approximately 7.9 billion USD was achieved in revenues for the Indian sensors market as of early Year-2024 [43], with potential markets amounting to roughly 15.8 billion USD by Year-2033, resulting in a compound annual growth rate (CAGR) of just under 8 % from Year-2025 until Year-2033, as shown in Figure 1.5. Such MEMS-based sensors capture a large share of this growth, as they can be integrated into automotive systems, consumer electronics, industrial automation, healthcare devices, and aerospace and defence applications. In particular, India's emphasis on Atmanirbhar Bharat (self-reliant India), increased defence indigenisation, and smart infrastructure development have significantly boosted demand for domestically designed and manufactured MEMS sensors. In fact, MEMS gyroscopes are of great importance in Indian defence and aerospace applications, such as navigation, guidance, & stabilization systems for missiles, UAVs, aircraft, and space missions. Indigenous MEMS gyros will additionally reduce import-dependency, thereby allowing the realization of strategic autonomy with national security objectives. Consequently, research efforts to improve the performance and robustness of MEMS gyroscopes align directly with national priorities.

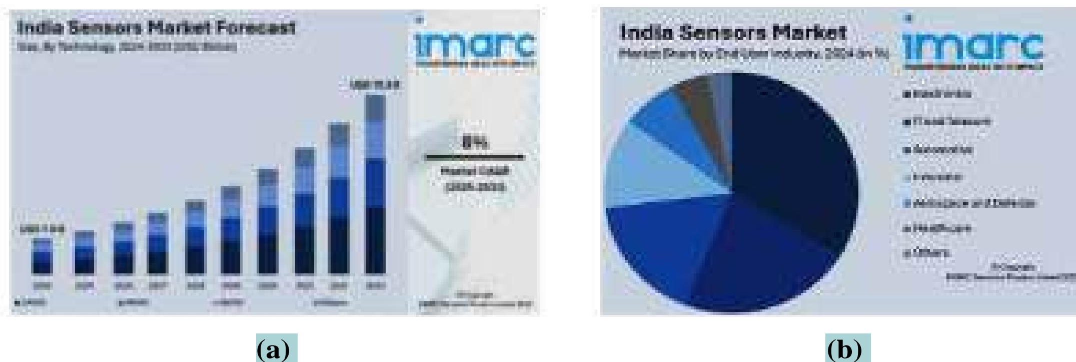

(a) **(b)**

Figure 1.5: Indian sensor market. (a) Forecast for 2024–2033. (b) End-user industry distribution in 2024 [43].

1.2.3 MEMS Gyroscope Market and Emerging Trends

MEMS gyroscopes are among the fastest-growing and most strategically significant segments of the MEMS industry. Figure 1.6 shows that the MEMS gyroscope market is growing from a size of about 3.5 billion USD in 2024 to more than 8.8 billion USD by the year 2035, with an approximate CAGR (Compound Annual Growth Rate) ranging around 9–10% [44]. The use of these sensors in smartphones, automotive stability systems, virtual and augmented reality devices, and inertial navigation systems is increasing rapidly. This is due to the increased demand for miniaturized and, at the same time, high-performance gyroscopes. The consumer applications require low cost and low power consumption. The defence and aerospace industries have much stricter performance and environmental requirements. This difference in requirements highlights the need to improve the performance of the existing technology.

Figure 1.6 MEMS gyroscope market forecast 2024-2035 [44].

By examining the defence, Indian, and global landscape together, MEMS gyroscopes are fundamentally economical at these levels. They are critical from both technological and strategic perspectives. Despite their prevalence, existing MEMS gyroscopes still suffer from several structural non-idealities. Hence, the current thesis is also strongly driven by market needs and outstanding technical problems. The work focuses on the design, modeling, and structural-level improvement of MEMS gyroscopes, with the objective of enhancing performance, robustness, and reliability. The outcomes of this research are expected to contribute toward the development of next-generation MEMS gyroscopes suitable for high-precision inertial navigation applications, particularly in defence and aerospace systems.

1.3 Evolution of Gyroscope Technologies

Gyroscopes are the fundamental inertial sensors used to measure angular rate and orientation, forming the basis of inertial navigation, stabilisation, and guidance systems across the aerospace defence, automotive, and industrial sectors. As seen in Figure 1.7, the history of gyroscope development. Rotational motion and its underlying principles can be traced back to the early 1800s, when spinning tops were observed to resist changes in orientation due to the conservation of angular momentum.

These observations served as the scientific basis for the development of gyroscopes as inertial reference instruments. By the 1850s, experimental gyroscope-like devices, such as those of Johann Bohnenberger, had proven that rotating bodies could serve as a reference for orientation. Initially confined to laboratory studies, gyroscopes gradually transitioned into practical navigation components as the demands of maritime and military engineering became more stringent [24,45,46].

The mechanical gyroscope (including spinning rotors mounted on gimbals) technology matured late in the nineteenth and early twentieth centuries, leading to applications such as gyroscopic compasses for magnetic-independent heading determination. During World War I and World War II, gyros played a crucial role in controlling aircraft attitudes, stabilizing ships, and in torpedo guidance, as well as in initial missile systems. Gyros also allowed for stabilized gun sights and later autopilots, which all significantly improved navigation accuracy and

weapon engagement. But these systems were heavy, costly, and sensitive to shock, vibration, and wear, which constrained their scalability and long-term robustness. To overcome these constraints, solid-state alternatives were investigated, leading to the development of optical gyroscopes exploiting the Sagnac effect. Both types of gyroscopes, i.e., ring laser gyroscope and fiber optic gyroscope, have excellent bias stability, long-term accuracy and are being used in high-end aerospace, submarine and strategic navigation systems. Optical gyros surpassed their mechanical predecessors, but the same physics limitations in micromachining they evolved to overcome kept them too large, expensive, and complex to make sense for smaller, cost-sensitive platforms.

Figure 1.7 Gyroscope development timeline [24,45,46].

Charles Stark Draper's work at the MIT Instrumentation Laboratory in 1930 was a major breakthrough in inertial navigation. Draper and his team were the first to develop complete inertial navigation systems that use gyroscopes, accelerometers, and data from onboard computing chips without needing external references. In the 1960s and 70s, this work during and after World War II gave rise to pioneering systems such as the Polaris missile guidance platform and the Apollo lunar navigation system. Inertial sensors are firmly established as mission-critical components in defence and aerospace applications. The work started in the 1960s with early MEMS technology developing alongside improvements in semiconductor processing. The first MEMS-based devices were demonstrated in 1965, revealing the ability to fabricate mechanical structures at the micro-scale using silicon. During the 1970s and 1980s, research efforts focused on silicon MEMS gyroscopes, leading to experimental prototypes that validated Coriolis-based angular rate sensing. These early devices established the feasibility of micro-scale inertial sensors but were largely confined to laboratory research. The field of MEMS sensors opened commercially during the 1990s, when micro-fabrication improvements combined with advances in packaging and electronics enabled the manufacture of MEMS gyros. By the 2000s, MEMS gyroscopes came to dominate the market due to their small size, low power consumption and cost; they went on to be widely used in cars and electronics such as smartphones and navigation devices, as well as drones and robotics systems. Overall, the

timeline highlights how continuous advances in MEMS technology transformed gyroscopes from experimental devices into indispensable inertial sensors for modern applications [25,47–49].

1.3.1 MEMS Gyroscope Architectures

- **Tuning Fork and Beam-Based MEMS Gyroscopes**

Tuning fork gyros are among the first and most popular MEMS gyroscope architectures [50,51]. The use of two identical proof masses vibrating in antiphase automatically rejects common-mode disturbances like linear acceleration and environmental vibrations, as depicted in Figure 1.8. Beam- and frame-based gyroscopes extend this concept by using flexural elements to anchor vibrating structures. These planar architectures are appealing because they are simple and compatible with standard microfabrication processes. However, their dependence on in-plane motion and thin proof masses results in limited inertial coupling, thereby limiting sensitivity and long-term stability in high-performance navigation applications.

(a) (b)

Figure 1.8 (a)Tuning Fork gyroscope [50] (b) Beam-beam Gyroscope [28].

- **Multi-Mass and Coupled MEMS Gyroscope Architectures**

To address sensitivity and robustness limitations, multi-mass architectures such as butterfly and quad-mass gyroscopes were introduced. Multi-mass structures, e.g., butterfly and quad-mass gyroscopes, were introduced to mitigate sensitivity and robustness limitations [52,53]. By symmetrically arranging multiple coupled masses, these designs enhance effective Coriolis response while suppressing parasitic vibration modes and quadrature errors. Architectural advances are key to achieving MEMS gyroscopes with enhanced performance; more complex structures add challenges in fabrication, tuning and control.

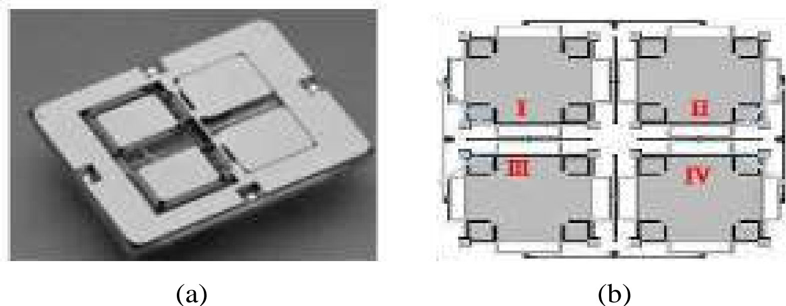

(a) (b)

Figure 1.9 (a)Butterfly Gyroscope [52](b) Quad-mass gyroscope [54].

- **Resonant Disk, Ring, and Wineglass Gyroscopes**

The emergence of disk-and-ring resonator gyroscopes represented a significant advance that leveraged both bulk acoustic and wineglass vibration configurations [55–57]. The intrinsic symmetry of these architectures suppresses anchor loss and fabrication-induced asymmetry, resulting in high-quality factors and enhanced stability. Among them, gyroscopes utilizing the wineglass mode are generally considered to be one of the most promising candidates for MEMS navigation-grade gyroscopes due to their high performance. However, accurate matching of modes and thermal management still remains an important challenge.

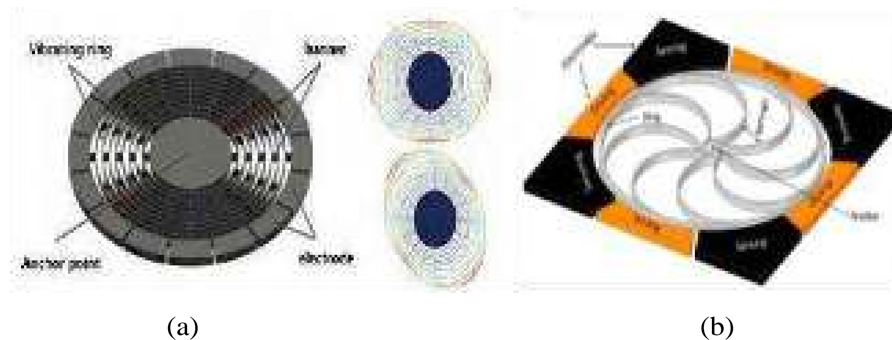

(a) (b)

Figure 1.10 (a)Disc [55] (b) Ring resonator gyroscope [56].

Both the disc and ring resonator gyroscopes presented in Figure 1.10 rely on angular rate sensing through degenerate wine-glass modes; the hollow geometry of the ring resonator minimizes anchor loss and damping, which achieves higher quality factors with better bias stability [57]. This means that ring resonator gyroscopes are chiefly favoured for high-performance and navigation-grade applications, while disc resonator gyroscopes offer a structurally simpler yet more fabrication-sensitive option.

- **Three-Dimensional and Vertical Sense Mass Architectures**

The development of three-dimensional gyroscope architectures with vertical-sense masses, driven by improvements in MEMS fabrication technology, particularly deep reactive-ion etching (DRIE) [58,59]. Figure 1.11a shows the hemispherical resonator gyroscope, which comprises a thin 3D hemispherical shell that vibrates in standing-wave modes. An array of electrodes both excites and senses those vibrations symmetrically. Figure 1.11b shows that by fabricating thick proof masses in the out-of-plane direction, these architectures expand effective inertial mass without enlarging the device footprint. The structural evolution provides improved Coriolis coupling (easier to couple energy into the sensing modes), increased sensitivity and bandwidth, reduced dependence on some damping mechanisms, making it easier to get higher-performance MEMS inertial sensors.

This ongoing research and innovation are motivated by the performance gap between MEMS and optical gyroscopes. Opportunities for improving the performance of MEMS gyroscopes can be found in architectural evolution, advanced fabrication techniques, and system-level optimization. Structural innovations like multi-mass coupling, resonant mode engineering, and vertical sense mass realization show that MEMS gyroscopes have significant untapped potential for further development. This thesis builds upon these developments by systematically exploring design optimization, three-dimensional architectures, damping

mechanisms, and thermal robustness, aiming to advance MEMS gyroscopes toward next-generation inertial navigation systems.

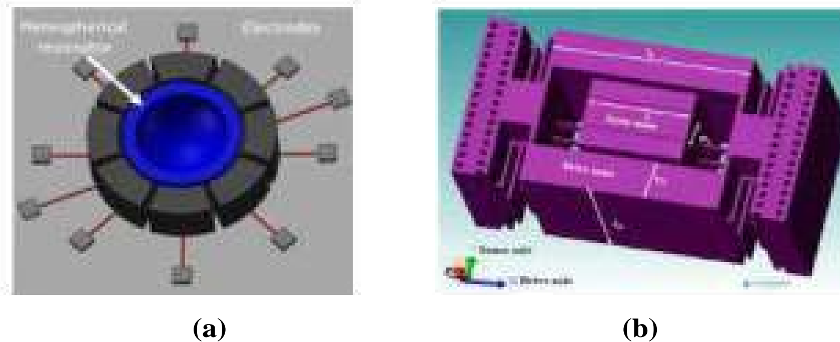

(a) (b)

Figure 1.11 (a) Hemispherical resonator gyroscope [57] (b) Vertical sense mass gyroscope [60].

1.4 Coriolis Effect

MEMS gyroscopes are a transformative technology based on the Coriolis effect, which relates the gyro rate of rotation to vibrating proof masses at the microscale. In contrast to mechanical and optical gyroscopes, MEMS gyroscopes have macroscopic parts, allowing for small, low-power, rugged devices which are compatible with batch fabrication. MEMS gyroscopes were initially adopted by the automotive and consumer electronics industries but quickly proved their applicability to aerospace and defence systems, where size, weight, power, and cost constraints are paramount.

The Coriolis effect is the fundamental physical principle upon which MEMS gyroscope operation relies. It arises from the rotation of reference frames and appears as an apparent deflection of moving objects as viewed from them. The effect, which was initially formally described in 1835 by the French engineer and mathematician Gustave-Gaspard Coriolis while examining the dynamics of motion in rotating mechanical systems, is widely understood today. While the Coriolis effect originated as a concept of mechanical dynamics, its core principles have become directly relevant to geophysics, atmospheric science, oceanography and contemporary inertial sensing technologies [61].

In an inertial reference frame (non-rotating), a particle will travel with constant velocity in a straight line unless an external force acts upon it. However, if that same motion is viewed from a rotating frame of reference, such as a rotating platform or the Earth itself, the trajectory appears as a curve. This apparent deflection is not the action of a real external force on the particle but of the observer's frame rotating. In order to apply Newton's laws in such a rotating frame, extra inertial forces should be added, among which the Coriolis force is one. One of the more familiar examples of the Coriolis effect arises from Earth's rotation, as shown in Figure 1.12. These systematic deflections are seen in the large-scale motions of air and water, such as atmospheric winds and ocean currents: moving air masses move to the right in the Northern Hemisphere but to the left in the Southern Hemisphere. This effect is important in the formation of cyclones, trade winds, and global circulation patterns. Importantly, the Coriolis effect does not create motion but alters the direction of existing motion, with its influence becoming significant over large distances or long-time scales [62].

Figure 1.12 Coriolis effect due to the Earth's rotation [63].

The Coriolis effect can be intuitively understood through a rotating-frame thought experiment shown in Figure 1.13. Consider a particle moving along the x-axis with a linear velocity v. If the reference frame itself begins rotating about the z-axis with an angular rate , an observer located on the rotating frame perceives the particle's trajectory to curve toward the y-direction. To an observer sitting on the z-axis, it appears as though the particle is being pushed sideways, even though no real force is acting on it in the inertial frame. This perceived sideways acceleration is known as the Coriolis acceleration.

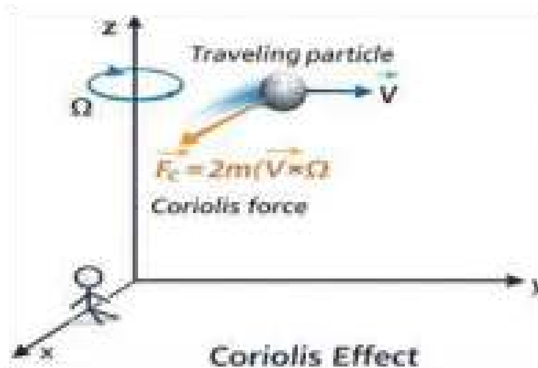

Figure 1.13 Coriolis effect [15].

Mathematically, the Coriolis acceleration is given by

$$= 2 \times \qquad (1)$$

where v is the velocity of the moving particle relative to the rotating frame, and is the angular velocity vector of the rotating frame.

The corresponding Coriolis force acting on a particle of mass m is

$$= 2 \quad \times \qquad (2)$$

This force is always perpendicular to both the particle's velocity and the axis of rotation, resulting in a transverse deflection rather than a change in speed. In MEMS gyroscopes, the Coriolis effect is deliberately exploited to measure angular rotation. A microfabricated proof mass is driven to vibrate along one axis (drive mode). When the device rotates about an orthogonal axis, the vibrating mass experiences a Coriolis acceleration, inducing a secondary motion in a perpendicular direction (sense mode). Angular rate can be estimated by detecting this induced motion.

This mathematical relationship makes the Coriolis effect highly relevant to MEMS gyroscopes, as it manifests itself in physical motion and has broad applicability. However, at the micro-scale, the Coriolis force is very small because it depends on the proof mass, vibration velocity, and angular rate. The resulting displacement is typically at the level of nanometres (or less), making accurate detection extremely difficult. At micro-scale dimensions, the Coriolis force is very small, posing considerable challenges for sensing. The low signal-to-noise ratio and sensitivity to damping, thermal noise, and fabrication imperfections are a few. Therefore, achieving high sensitivity, stability, and robustness in MEMS gyroscopes requires a robust structural design, high-quality factors, and compatible readout electronics. It is these challenges that help explain why, even after three decades of academic exploration and commercial roll-out, new initiatives continue to target further improvements in MEMS gyroscope performance through architectural innovation, material development, and system-level design.

1.5 Survey of Prior Work on MEMS Gyroscopes

Early Foundations and Conceptual Developments (Late 1980s–Early 1990s)

Research on micromachined gyroscopes first appeared towards the end of the 1980s, driven by a demand for small, inexpensive inertial sensors that could replace traditional mechanical and optical gyroscopes. Relative to this linearization of inertial guidance systems and with respect to their angular rate sensitivity, Ref [64] was one of the earliest papers that described a gyroscope as “keeper of direction”. Research in this period generally concentrated on the miniaturization of the traditional inertial sensing paradigms to silicon micromachined components, accepting that early MEMS gyroscopes could not compete with navigation-grade devices immediately.

Reference [65] describes one of the earliest system-level micromechanical inertial devices, noting that although MEMS sensors initially seem to underperform compared to conventional gyroscopes, their small size and compatibility with batch fabrication offer significant advantages. These features have enabled a wide range of commercial applications and hold strong potential for future developments. Overall, this work helped establish a new technological foundation and research direction for MEMS gyroscope development.

Demonstrations of Vibratory MEMS Gyroscopes (Early–Mid 1990s)

The early to mid-1990s marked the first successful demonstrations of functional MEMS vibratory gyroscopes. During this period, comb-drive tuning-fork gyroscopes were experimentally realized, clearly showing the feasibility of electrostatic actuation along with capacitive sensing mechanisms. Around the same time, researchers also demonstrated a surface-micromachined vibrating gyroscope that used a thin polysilicon resonator driven electrostatically and capable of achieving a high quality (Q) factor.

These developments highlighted the importance of high-Q resonant structures, which play a key role in reducing noise and improving the overall sensitivity of the device. Simultaneously, others were investigating different geometries, like vibrating wheels and rings. A vibrating wheel gyroscope with symmetry and mechanical decoupling to suppress common-mode errors was presented. Afterwards, a few described a vibrating ring gyroscope, in which rotation was detected from the precession of nodal lines in an elliptically vibrating ring [28]. These symmetric resonators represented a significant step towards structural methods for bias and noise mitigation.

Process Innovations: Bulk Micromachining and Early DRIE (Mid–Late 1990s)

With device concepts mature, research is most strongly focused on fabrication technologies. Proof masses and suspension structures were immediately defined by anisotropic wet etching, although this method placed crystallographic constraints on both geometry and thickness. In Ref. [66], silicon angular rate sensors were fabricated via anisotropic etching, yielding satisfactory sensitivity but limited structural freedom. The advent of deep reactive ion etching (DRIE) was a huge step forward. Ref [67] reported one of the early uses of DRIE on silicon angular rate sensors, which enabled high-aspect-ratio resonators with thicknesses now approaching 190 µm, highlighting that DRIE could push beyond crystallographic constraints to enable taller proof masses and hence improve signal-to-noise ratio.

Bosch-process DRIE came into widespread use by the late 1990s. Several hundred micrometre etch depths were reported, enabling the fabrication of one-sided suspended tuning-fork structures with higher Q factors and reduced damping. These advancements positioned DRIE as a powerful catalyst for state-of-the-art MEMS gyroscopes.

Toward Integrated and Dual-Axis Gyroscopes (Late 1990s)

In the late 1990s, research broadened to multi-axis sensing and system integration. A quad-symmetric dual-axis micromachined rate gyroscope, which relies on the principle of exploiting quad symmetry in this type of gyroscope to enable simultaneous sensing along two axes. However, mode mismatch and cross-axis sensitivity remained considerable challenges; this work underscored the promise of combining symmetric designs with electrostatic tuning. In fact, Draper Laboratory and other organizations focused on system-level integration, packaging, and electronics co-design in the same time frame. Demonstrations of packaged MEMS gyroscopes were done for space and defence applications, highlighting the need for vacuum packaging and temperature stability.

2000–2003: Shift from Feasibility to Performance Metrics

After 2000, MEMS gyroscope research clearly shifted from proof-of-concept demonstrations to quantitative performance metrics, including bias instability, angle random walk (ARW), scale-factor stability, and temperature robustness. Researchers recognized that while consumer-grade performance had largely been achieved by the late 1990s, navigation-grade performance required fundamental changes in device architecture, material thickness, and fabrication technology. During this period, deep reactive ion etching (DRIE) emerged as a key enabling technology, allowing silicon structures with thicknesses ranging from 50 µm to several hundred micrometres, thereby significantly increasing proof mass and angular momentum. This directly reduced thermomechanical noise, which scales inversely with the square root of the mass, and enabled higher signal-to-noise ratios [68,69].

2003–2006: Thick-Mass and High-Q Resonator Gyroscopes

During early research on MEMS inertial sensors, wet bulk micromachining and traditional plasma deep etching were primarily used [1–3], as bulk micromachining technologies evolved. However, those techniques were limited by anisotropy and depth control, thereby limiting the aspect ratios they could produce. Deep reactive ion etching (DRIE), most commonly inductively coupled plasma (ICP) DRIE, was an extremely effective bulk silicon micromachining technique that could create deep, highly anisotropic features with vertical sidewalls, yielding very high aspect ratios of 20:1 or more for MEMS devices [70]. SOI fabrication using DRIE has produced devices with aspect ratios greater than 20:1, achieving

structural thicknesses of hundreds of microns and resonators with quality factors orders of magnitude higher than those of surface-micromachined equivalents.

This advance stimulated research on bulk-micromachined and thick-mass vibratory gyroscopes, in which high-aspect-ratio structures reduced squeeze-film damping and increased inertial mass, thereby improving both sensitivity and noise performance. During this period, research emphasis centred on (a) vacuum encapsulation to suppress squeeze-film damping, (b) mode-matching to amplify Coriolis response, and (c) structural symmetry to minimise quadrature errors. It also became evident that fabrication tolerances, rather than fundamental physical limits, were the dominant constraint on achieving low-bias drift, prompting the integration of electrostatic tuning mechanisms to compensate for frequency mismatches between the drive and sense modes. While there are techniques in the literature documenting the application of standard Deep DRIE for specific MEMS structures achieving aspect ratios greater than 20:1 [54], and isotropic etchants have been utilised to produce sub-micron trench features with aspect ratios as large as 107:1, but only as part of highly specialised processes [71].In this thesis, we aim to fill this gap by presenting a detailed design and analysis of MEMS gyroscopes that exploit the advantages of Deep DRIE, including high-aspect-ratio fabrication, improved Q factors, and reduced damping, to achieve enhanced inertial performance.

2006–2010: Mode-Matching and Force-Rebalanced Architectures

As MEMS gyros began achieving tactical-grade performance, a distinguishing research focus emerged: mode-matched operation. Similar frequency matching in drive and sense modes is provided in Coriolis gain, but at the cost of lower bandwidth and stability. To overcome these problems, closed-loop or force-rebalanced gyroscopes were designed in which the Coriolis-induced motion is actively nulled, and the feedback force serves as the output signal. This technique resulted in significant improvements in bias stability and scale-factor linearity [72,73].

2010–2015: Toward Navigation-Grade MEMS Gyroscopes

After 2010, research increasingly explored the path to tactical and near-navigation-grade performance for MEMS gyroscopes. Important approaches were: Ultra-thick DRIE resonators (100–500 μm), High-Q (>100,000) operation under ultra-high vacuum, Temperature compensation and material engineering [74]. Due to their inherent symmetry and lower anchor loss [75], disk resonator gyroscopes (DRGs) and ring resonator gyroscopes became the most developed MEMS gyroscope types. But such designs exhibit complex fabrication and are sensitive to process variations, spurring further interest in multi-mass and tuning-fork-based thick-mass architectures.

2015–2020: System-Level Optimization and Reliability

With MEMS gyroscope performance approaching tactical-grade levels, the focus of research shifted to long-term reliability, packaging, and manufacturability. To maintain quality and reduce drift, wafer-level vacuum packaging, integrated getter materials and stress-isolated anchor designs were adopted. Between 2015 and 2020, MEMS gyroscope design progressed significantly thanks to Deep DRIE. Ultra-deep DRIE enabled thick silicon proof masses > 500 μm with enhanced etch uniformity. Silicon etches depths of 600–900 μm were noted in modified Bosch process studies, whereas double-DRIE techniques reported depths of 1–1.4 mm [76–78]. Employing ramped-parameter DRIE, Tang, Najafi, and co-workers achieved 600–800 μm-deep trenches in 1-mm-thick silicon wafers with aspect ratios >40:1, thereby reducing many etching issues. The trends confirmed the viability of thick-mass MEMS gyros where inertial mass, noise and bias must all be minimized to get navigation-grade performance.

Recent Advances in MEMS Gyroscopes (Post-2020)

Starting in 2020, MEMS vibratory gyroscopes research shifted from architectural exploration to improving navigation-grade performance, with particular focus on temperature robustness and long-term stability [79–81], as well as reliability. Notably, while advancements have been made in sensitivity and noise reduction, temperature-driven drift in the bias, scale factor, and resonant frequency remains a critical limitation for high-precision applications. Hence, recent studies have focused on algorithmic and physical mitigation strategies.

Several advanced temperature-compensation techniques can significantly reduce scale factor and bias drift over very large temperature ranges. There has been a clear shift toward a mechanical–thermal approach in improving MEMS gyroscope performance, particularly through active temperature control techniques such as thermoelectric cooling. This approach helps reduce the impact of temperature variations on key parameters like frequency, Q-factor, bias, and scale factor, enabling more stable operation over a wider temperature range and supporting high-precision applications. At the fabrication level, advances in deep reactive ion etching (DRIE) have made it possible to create high-aspect-ratio structures with etch depths reaching several hundred micrometres. However, as these devices have evolved, new challenges have become more evident. Issues related to internal stresses, thermal sensitivity, structural symmetry, and long-term stability are now frequently reported. In many cases, these challenges are addressed through post-fabrication tuning or packaging strategies rather than purely through design modifications. As a result, even though DRIE technology itself is well established, there is still a noticeable gap in design optimisation and performance evaluation, especially for thick-mass MEMS gyroscopes. Table 1.2 summarises the overall development of MEMS gyroscopes along with the key challenges identified over time.

As shown in Table 1.2, MEMS gyroscope performance has advanced to tactical and near navigation-grade levels; however, most studies focus only on fabrication feasibility, architectural symmetry, and compensation techniques [13]. While Deep DRIE etch depth, aspect ratio, and robustness have all advanced over time, Deep DRIE is rarely considered a primary design element in gyroscope modelling or optimisation. Most continue with classical disk, ring, or tuning-fork arrangements and interpret performance changes due to effective mass scaling or high-quality factor without considering noise and bias stability, which are questioned by damping mechanisms, stress gradients, DRIE-induced asymmetries, and mode coupling. Also, higher mass tends to lead to bigger chips rather than taking advantage of vertical space enabled by Deep DRIE. As a result, the potential of thick proof masses to simultaneously enhance mechanical stability, reduce thermo-mechanical sensitivity, and enable footprint reduction through vertical mass utilization has not been sufficiently explored. Limitations arising from thermal sensitivity, fabrication tolerances, and scale-factor instability are therefore commonly mitigated through electronic tuning, control loops, or post-fabrication compensation, rather than being addressed at the structural and design levels without compromising key performance parameters such as sensitivity, bandwidth, and noise floor.

1.6 MEMS Fabrication Technologies: An Overview

MEMS devices are commonly realized using (micro)fabrication techniques adapted from the semiconductor industry, and then extended to build movable micromechanical structures [82–86]. MEMS processing differs from standard IC fabrication in that many of the structures formed will be suspended elements, like beams, proof masses and resonators. MEMS fabrication can be broadly categorized into bulk micromachining, surface micromachining and high-aspect-ratio techniques like DRIE, while highly-focused methods like LIGA and electro-discharge micromachining are only used for specialized applications. Inertial sensor

performance parameters can be directly controlled through the respective fabrication technology, as it defines proof-mass geometry, suspension stiffness, and sensing gaps, which, in turn, impact sensitivity, damping, and noise. Thus, advanced micromachining processes are crucial for scalable, reliable and high-performance MEMS gyroscopes and accelerometers required by many applications.

Table 1.2 Timeline of MEMS Gyroscope Research and Key Developments

Period	**Key Research Focus**	**Major Contributions**	**Key Limitations / Outcomes**
Late 1980s – Early 1990s	Conceptual foundations	Definition of gyroscope as a “keeper of direction”; translation of classical inertial principles to silicon micromachining	Feasibility focus; performance far below navigation-grade
Early–Mid 1990s	First vibratory MEMS gyroscopes	Comb-drive tuning fork gyroscopes; surface-micromachined polysilicon resonators; electrostatic actuation and capacitive sensing	Thin structures, low proof mass, limited robustness
Mid–Late 1990s	Fabrication innovation	Anisotropic wet etching; first application of DRIE to gyroscopes enabling high-aspect-ratio resonators (~190 µm thick)	Crystallographic constraints reduced; DRIE feasibility demonstrated
Late 1990s	Integration and multi-axis sensing	Dual-axis gyroscopes using quad symmetry; system-level packaging and vacuum encapsulation	Mode mismatch and cross-axis sensitivity remained
2000–2003	Shift to performance metrics	Focus on bias instability, ARW, scale-factor stability; DRIE enabled thicker structures (50–300 µm)	Recognition that navigation-grade requires thick mass and high-Q
2003–2006	Thick-mass & high-Q gyroscopes	SOI + DRIE devices; aspect ratios >20:1; vacuum encapsulation; electrostatic tuning	Fabrication tolerances became dominant error source
2006–2010	Mode-matching & force rebalance	Closed-loop force-rebalanced gyroscopes; improved bias stability and linearity	Bandwidth reduction; increased system complexity
2010–2015	Near navigation-grade exploration	Disk and ring resonator gyroscopes; ultra-high Q (>100k); advanced quadrature cancellation	High fabrication complexity; sensitivity to process variation
2015–2020	Reliability & manufacturability	Wafer-level vacuum packaging; getters; stress-isolated anchors; ultra-deep DRIE	Structural thickness increased (>500 µm), but thermal robustness was unresolved.
Post-2015 (DRIE milestone)	Ultra-thick mass feasibility	Modified Bosch and double-DRIE processes achieving 600–900 µm and up to ~1–1.4 mm etch depths; ARDE mitigation	DRIE no longer a bottleneck; stress and thermal effects dominate

Post-2020 – Present	Navigation-grade performance focus	Temperature compensation, active thermal control (TEC), symmetric resonators, FM gyroscopes	Heavy reliance on electronics/control; intrinsic mechanical robustness is still limited
Identified Research Gap	Structural-level optimization	Need for DRIE-enabled thick-mass designs that inherently improve thermal stability and noise	Motivation for the present work

1.6.1 Bulk Micromachining

Bulk micromachining is one of the earliest and most often employed MEMS fabrication methods. In this, the majority of the substrate material (usually single-crystal silicon) is removed over an area to form suspended or free-standing mechanical elements. Etching processes are performed directly onto the substrate to create cavities, membranes, beams or proof masses. Since bulk micromachining can be used to fabricate relatively thick structures, it has good mechanical strength and well-defined material properties [35]. It therefore finds most use in inertial sensors such as accelerometers and gyros. Though this technique may provide less control over devices and layer thickness.

Figure 1.14 Bulk Micromachining process [83]

There is difference between isotropic and anisotropic etching in bulk silicon micromachining. In isotropic etching, the etch rate is uniform in all directions, leading to rounded cavities and excessive undercutting below the masking layer, which results in curved sidewalls in bulk silicon. In contrast, anisotropic etching is orientation-dependent. Typically, {111} planes etch slowly when (100) oriented silicon is etched. Figure 1.14 demonstrates that anisotropic wet etchants (e.g., KOH or TMAH) naturally terminate on {111} planes, allowing the creation of defined V-grooves, membranes, and cavities. A highly boron-doped silicon layer can be used as an etch-stop layer. In general, you can see that isotropic etching produces simple but less controlled profiles, whereas anisotropic etching yields geometrically accurate, self-limiting structures that are critical for MEMS bulk micromachining.

1.6.2 Surface Micromachining

Surface micromachining addresses some of the drawbacks of bulk processing by fabricating MEMS structures from thin films deposited or grown on a substrate. With this method, alternating structural material and sacrificial layers were deposited using chemical vapour deposition, thermal oxidation, etc. Post-patterning, selective etching of the sacrificial layers allows the mechanical structures to be released. Due to precise control over device dimensions, surface micromachining is highly compatible with standard CMOS processes and enables monolithic integration of MEMS devices and electronics. The main limitation of this technique

comes from the relatively thin structural layers, which may limit inertial mass and mechanical robustness.

A MEMS cantilever has been created by utilizing surface micromachining steps shown in Figure 1.15. In a first step, a silicon oxide layer is deposited and patterned on a silicon substrate; this oxide serves as the sacrificial layer that forms the air gap beneath the cantilever. Then, a polycrystalline silicon (poly-Si) layer is deposited and patterned over the oxide to form the structural layer, i.e. the cantilever beam and its anchor region. Lastly, a sacrificial etch neatly removes the underlying silicon oxide on poly-Si, freeing the cantilever as a stand-alone structure while still anchored at the anchor.

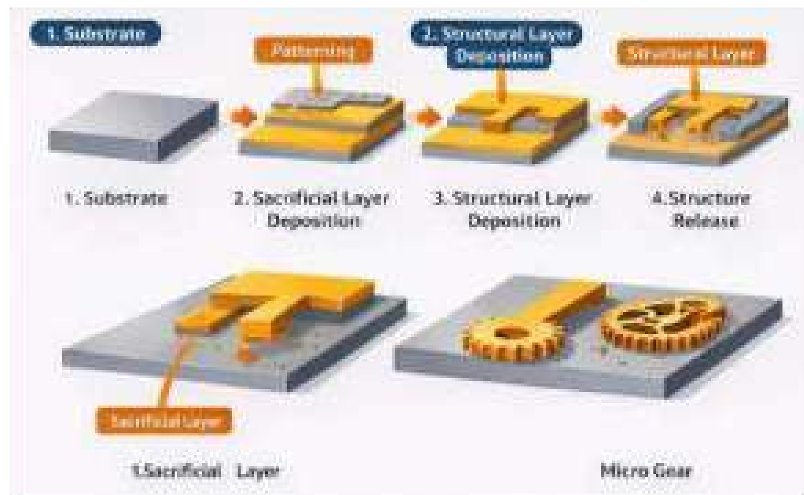

Figure 1.15 Surface micromachining process [83]

1.6.3 Deep Reactive Ion Etching (DRIE)

Deep reactive ion etching is the most significant advancement in MEMS fabrication, enabling high-aspect-ratio, thick silicon structures with nearly vertical sidewalls. DRIE is commonly used to fabricate deep trenches, high-aspect-ratio beams, and heavy proof masses without increasing chip area. This method is especially critical for high-performance MEMS gyros, which rely on increasing the proof mass thickness to improve inertial coupling and sensitivity. DRIE has enabled three-dimensional and vertical-sense mass architectures, providing a link between surface- and bulk-micromachining capabilities.

The DRIE Bosch process shown in Figure 1.16 proceeds through repeated cycles to achieve deep, high-aspect-ratio silicon features. Step 1 (passivation): A fluorocarbon gas (CF) deposits a polymer layer over the trench bottom and sides to inhibit lateral etching. The passivation layer at the trench bottom is preferentially removed by energetic positive ions (phase 2: directional ion bombardment) accelerated toward the ditch, while the sidewalls are protected. In phase 3 (silicon etching), the fluorine radicals react with the exposed silicon at the bottom, generating volatile by-products and resulting in high-aspect-ratio vertical etching. This process is repeated multiple times, which creates nearly vertical sidewalls with the signature scalloping. DRIE has been reported to achieve etch depths of 600 µm with a modified Bosch process [72], whereas standard DRIE processes routinely provide 800–900 µm. For even larger depths, double-DRIE techniques, etching sequentially from both sides of the wafer, have been demonstrated to achieve silicon etch depths of ~1.4 mm, highlighting the capability of DRIE for extreme-depth MEMS and bulk micromachined structures [45].

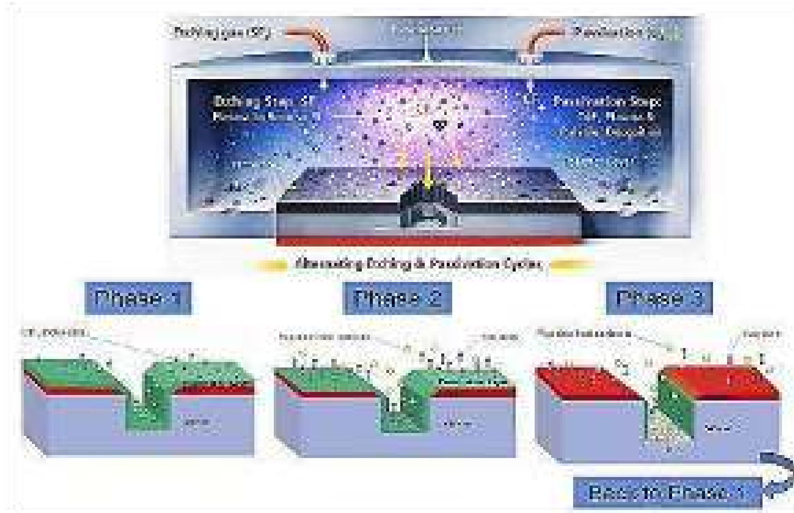

Figure 1.16 Deep Reactive Ion Etching Process [76]

1.6.4 LIGA Process

The LIGA (from the German words for lithography, electroformung, and moulding) process is a supporting microfabrication method used to fabricate thick (up to 1 cm), high-aspect-ratio metal microstructures. Its process uses X-ray lithography to form thick photoresist layers and subsequently patterns them by electroforming to generate metal structures from the moulds, as shown in Figure 1.17. Though LIGA offers high mechanical strength and precision, its complexity, cost, and reliance on synchrotron radiation limit its widespread use in MEMS inertial sensors.

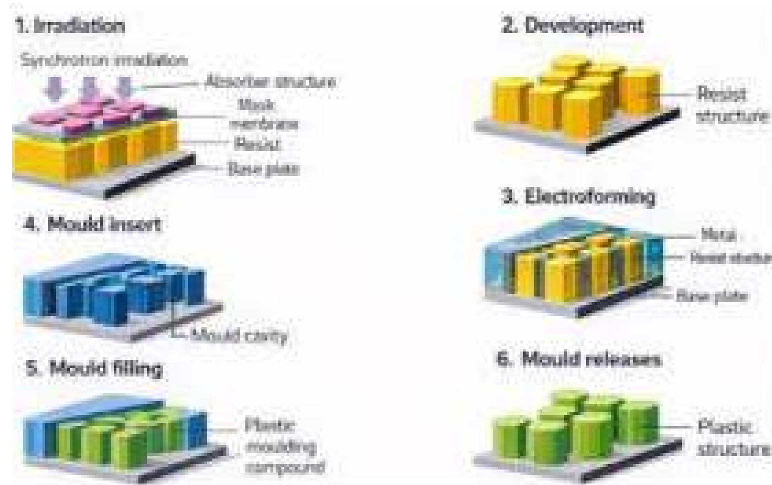

Figure 1.17 Lithographic Galvanoformung Abformung (LIGA process) [87]

1.6.5 Electro-Discharge Micromachining (EDM)

A further specialised fabrication process is electro-discharge micromachining, in which small, controlled electrical discharges are used to etch conductive substrates (Figure 1.14). EDM is used in MEMS applications mainly to machine hard, thick conductive materials that cannot be

processed by lithography. Although EDM offers great freedom for shaping complex geometries, it is typically not well-suited for large-scale MEMS fabrication due to its limited resolution and throughput.

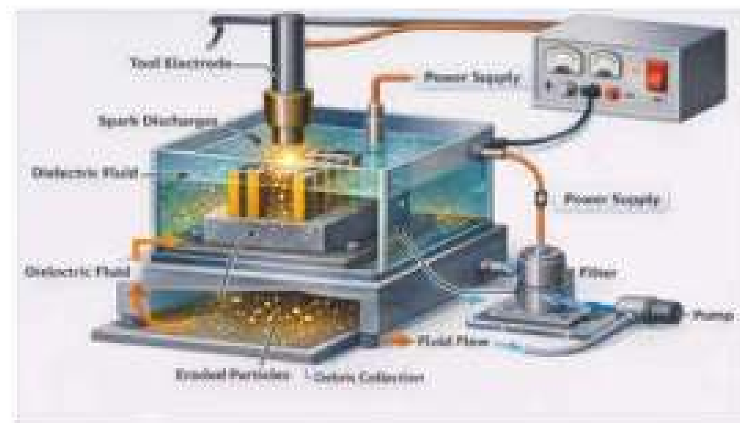

Figure 1.18 Electro-Discharge Micromachining process [88]

Electric Discharge Micromachining (micro-EDM) is illustrated in Figure 1.18. it is a non-contact, high-precision fabrication process for machining electrically conductive materials. Micro-EDM involves a sequence of controlled electrical pulses applied across a very narrow gap between the tool electrode (made out of copper or brass) and the workpiece. These are submerged in a dielectric fluid such as kerosene. The pulsed sparks localized to create very high temperatures cause melting and vaporization of material from the surface of the workpiece by electrostatic action without any mechanical force. Dielectric fluid flushes away the removed material and a micro-EDM power supply/controller regulate pulse energy, gap, and tool position (Z-axis) with precision. This process enables the precise machining of hard and brittle materials, complex micro-features, and deep cavities. Because of this, it is particularly beneficial for MEMS, ceramics and precise micro-manufacturing applications.

1.6.6 Supporting Microfabrication Processes

Apart from the main fabrication methods, MEMS device realisation involves a range of supporting microfabrication processes. Oxidation and diffusion are utilized for property modification, as well as to deposit insulating or doped regions on surfaces. Metallization enables interconnection and electrode formation. Device patterns are defined with high precision using ultraviolet lithography. Both wet and dry etching processes are widely used to define structures and release moving parts. Wafer bonding methods (e.g., anodic, fusion, adhesive) are the basis for device packaging, cavity formation and multi-layer integration. The decision on how to fabricate final devices offers a wide range of options, ultimately dictated by the demands placed on the device with respect to structural thickness, mechanical performance, integration level, and cost. Recent advancements in MEMS fabrication technologies are instrumental both to realizing novel gyro architectures and enhancing performance, so that successful fabrication becomes essential for the development of MEMS sensors.

1.7 MEMS Gyroscopes Applications in Navigation and Defence Systems

MEMS gyros are angular rate sensors, which detect the rotational motion of a body around its principal axes. Here, a MEMS gyroscope is placed on the system to sense angular velocity

along one or more orthogonal axes, which usually correspond to roll, pitch, and yaw. Roll is rotation about the longitudinal axis of the body, pitch is rotation about the lateral axis, and yaw is rotation about the vertical axis. The system would then continuously estimate its orientation by integrating the measured angular rate over time. In practice, MEMS gyroscopes are typically integrated with accelerometers and magnetometers to form inertial measurement units (IMUs) [2,25,47,49,53,89]. A few applications of MEMS gyroscopes are shown in Figure 1.19.

Figure 1.19 MEMS inertial sensors in navigation, guidance, stabilisation, and control systems for civilian, aerospace, and defence applications [2,25,47,49,53,89].

Commercial and Automotive Applications : MEMS gyros were first popularized in the automotive space to improve vehicle safety and stability. Specifically in electronic stability control (ESC) systems, which sense unintended rotation for the corrective braking system. They are also used in rollover detection, anti-lock braking systems and advanced driver assistance systems (ADAS). After automotive applications, they are nowadays used in consumer electronics. They are used in smartphones and tablets for screen orientation, motion-based games, image stabilization (camera), etc. In smart wearables, gyroscopes are combined with accelerometers to accurately monitor the vitals, including gestures, orientation, and the type of activity being performed. These applications demonstrate the maturity and reliability of MEMS gyroscope technology.

Robotics and Industrial Applications: MEMS gyroscopes assist in balancing, orientation holding and trajectory motion of robots. They support the attitude stabilization and trajectory tracking for mobile robot systems, inspiring autonomous vehicles as well as industrial manipulators. In industrial automation, they are used in vibration monitoring, platform levelling, machinery health diagnostics, etc. Other applications include infrastructure monitoring and underground sensing, especially for sewer and pipeline inspections using autonomous robots.

Inertial Navigation Systems (INS): MEMS gyroscopes are key to navigation, providing orientation, velocity, and position by processing motion data over time. They are especially useful where GPS is unavailable. Their compact size and improving accuracy make them suitable for advanced and tactical applications.

Unmanned Aerial Vehicles (UAVs): MEMS gyroscopes enable stable drone flight by providing real-time roll, pitch, and yaw information. Their low weight and power consumption support efficient navigation, autonomous operation, and reliable performance even under high-vibration conditions.

Missiles and Defence Platforms: MEMS gyroscopes are increasingly used in missiles, guided munitions, and tactical navigation systems. Their ability to withstand high shocks and forces during launch makes them well-suited for such environments. They are also used in military vehicles and wearable systems where compact size and durability are essential. While optical gyroscopes remain preferred for highly critical systems such as naval platforms, MEMS gyroscopes have become a practical option for many tactical applications.

Space and Aerospace Applications: In satellites, small spacecraft, and launch vehicles, MEMS gyroscopes support attitude determination and control. They help maintain proper orientation for communication, imaging, and orbital manoeuvres.

Emerging and Non-Traditional Applications: Beyond navigation, MEMS gyroscopes are used for motion sensing in areas like rehabilitation devices and underground sensing. Their growing use in automobiles, smartphones, UAVs, and defence systems highlights their versatility. However, for high-end navigation and defence applications, further improvements in design and performance are still needed.

1.8 Challenges in MEMS Gyroscopes

However, significant progress in MEMS gyroscopes technology can only go so far, and several fundamental challenges persist. Each of which limits their performance, reliability and suitability for high-performance inertial navigation applications, particularly in defence and aerospace.

Most MEMS gyroscope designs we have seen so far focus on improving only one parameter. But all these parameters are connected to each other. There is no system that considers all these parameters together. This is especially true when we try to make the MEMS gyroscope smaller. MEMS gyroscope designs need to be optimized in a way that considers all the parameters, like sensitivity, bandwidth, noise and size, at the same time. The lack of a system to optimise MEMS gyroscope designs is a significant problem that affects their performance.

Miniaturization–Performance Trade-off: The miniaturization of MEMS gyroscopes to fit small size, weight, and power (SWaP) specifications leads to performance degradation. Due to reduced proof mass, there will be a weak Coriolis force, higher thermomechanical noise, and narrower operational bandwidths, which complicate achieving compactness with high precision.

Wafer Thickness underutilization: The standard planar sense-mass architectures generally utilise the lateral dimensions and ignore the available wafer thickness, although there has been progress in deep silicon micromachining (DRIE) [31].

MEMS gyroscopes are highly temperature-sensitive, leading to errors such as frequency and scale-factor drift, bias instability, and reduced reliability. The electronic compensation adds to the system design's complexity, power requirements, and the need for complex calibration efforts. But the structural and packaging-level thermal solutions have not yet been explored. Degradation in gyroscope quality due to limitations, such as uncertainties in material properties and packaging stresses, is a critical issue.

1.9 Research Objectives

1. The design and optimisation of a MEMS gyroscope architecture to simultaneously improve both sensitivity and operational bandwidth, and minimise noise.
2. An architecture is proposed based on a Vertical Sense Mass (VSM) gyroscope that uses wafer thickness to realize the most compact sensor, with the promise of maintaining sensitivity and enhanced bandwidth and noise performance over traditional planar sense mass (PSM) designs.
3. A comparative study of planar and conventional architectures for MEMS gyroscopes to show their effectiveness in optimizing the design to suppress high-order damping modes.
4. To investigate and mitigate thermal effects that influence MEMS gyroscope performance. The design- and substrate-level approaches are proposed to enhance temperature stability, minimised drift, and robustness over wide operating ranges.

1.10 Thesis Organisation

MEMS gyroscopes are among the most widely used MEMS sensors for Inertial Navigation Systems (INS), which provide accurate position and orientation estimation without external references. This makes them critical in defence, aerospace, and autonomous applications where Global Positioning System (GPS) signals are unavailable. However, the miniaturization makes them vulnerable to damping, noise and temperature effects. This thesis addresses these challenges.

The thesis is organized into the following chapters:

In **Chapter 1**, MEMS sensors are discussed in detail. Based on applications, inertial sensors are crucial for navigation and control systems, especially in GPS-denied environments. MEMS gyroscopes were discussed in this chapter for Inertial Navigation Systems (INS). The different fabrication techniques are discussed and the key challenges that degrade MEMS gyro performance are highlighted. It concludes with a discussion of research gaps and objectives, as well as the thesis's scope.

Chapter 2 establishes the theoretical foundation of MEMS gyroscopes. It begins with the basic physics of rotational motion and the Coriolis effect, which form the basis of angular rate sensing. The lumped-mass models for both drive and sense modes are developed to describe the system dynamics. The chapter also covers different gyroscope architectures, actuation and sensing methods, and resonant operation. Key performance parameters—such as sensitivity, bandwidth, quality factor (Q), noise, and scale factor—are defined and analytically linked to structural and material properties. This forms the core framework used throughout the thesis.

Chapter 3 focuses on a conventional planar MEMS gyroscope design. It examines how structural parameters influence performance by modelling the system as a mass–spring–damper. The chapter highlights the trade-offs between different design parameters and introduces a unified Figure of Merit (FOM) to capture their combined effect. This shows that optimizing one parameter alone is not sufficient. The limitations of planar sense-mass designs, particularly under miniaturisation, are discussed, leading to the need for new architectural approaches.

Chapter 4 introduces a Vertical Sense Mass (VSM) architecture that uses a thick wafer to achieve miniaturisation without compromising performance. Both VSM and traditional Planar Sense Mass (PSM) designs are compared in terms of structure, sensing direction, footprint,

frequency response, and sensitivity. Results show improved bandwidth and lower thermomechanical noise while maintaining good sensitivity. The feasibility of fabrication using DRIE is also discussed.

Chapter 5 presents a detailed study of damping, identified as a key factor limiting performance in miniature gyroscopes. Various damping mechanisms—such as air damping, viscous damping, thermoelastic damping, anchor loss, acoustic damping, and material damping—are analysed. The performance of PSM and VSM architectures is compared under different pressures, temperatures, and operating frequencies. The results indicate that the VSM design reduces air and squeeze-film damping, leading to higher Q-factors. The impact of damping on sensitivity, bandwidth, and noise is also quantified.

Chapter 6 addresses thermal robustness, which is critical for operation in harsh and varying environments. A thermally optimised design using tapered beams and a Thermal Substrate (TS) approach is proposed to reduce heat transfer to the sensing elements. Both transient and steady-state thermal analyses, along with thermo-mechanical stress evaluation, are carried out over a wide temperature range. The approach significantly reduces temperature-induced drift, scale-factor variation, and thermomechanical noise, without relying on power-intensive electronic compensation. Fabrication feasibility is also explored using wet etching techniques.

Chapter 7 summarizes the main contributions and findings of this work, with emphasis on the potentials that were achieved through geometry-driven optimization at the architectural level. The thesis describes the impact of the work from both social and strategic perspectives, focusing on self-reliance in defence, aerospace, autonomous systems, and monitoring applications. Finally, future investigations are highlighted, including multi-axis gyroscopes, complete system-level integration, and novel packaging efforts. The exploration of quantum gyroscope principles as a path towards next-generation inertial sensors is also mentioned.

References

[1] Algamili A S, Khir M H M, Dennis J O, Ahmed A Y, Alabsi S S, Ba Hashwan S S and Junaid M M 2021 A Review of Actuation and Sensing Mechanisms in MEMS-Based Sensor Devices Nanoscale Res. Lett. 16

[2] Lyke J C, Michalicek M A and Singaraju B K MEMS in space systems

[3] Hejun H and Bogue R 2007 MEMS sensors: Past, present and future Sensor Review 27 7–13

[4] Rittersma Z M Recent achievements in miniaturised humidity sensorsÐa review of transduction techniques

[5] Khan M A, Sun J, Li B, Przybysz A and Kosel J 2021 Magnetic sensors-A review and recent technologies Engineering Research Express 3

[6] Gardner E L W, Gardner J W and Udrea F 2023 Micromachined Thermal Gas Sensors—A Review Sensors 23

[7] Anon Pressure sensors: The design engineer’s guide

[8] Ejeian F, Azadi S, Razmjou A, Orooji Y, Kottapalli A, Ebrahimi Warkiani M and Asadnia M 2019 Design and applications of MEMS flow sensors: A review Sens. Actuators A Phys. 295 483–502

[9] Ejeian F, Azadi S, Razmjou A, Orooji Y, Kottapalli A, Ebrahimi Warkiani M and Asadnia M 2019 Design and applications of MEMS flow sensors: A review Sens. Actuators A Phys. 295 483–502

[10] Eswaran P and Malarvizhi S 2013 MEMS Capacitive Pressure Sensors: A Review on Recent Development and Prospective

[11] Veena S, Deepika, Hegde V, Nagaraj V S, Suresh H L and Gautham M A 2019 Design and Simulation of Mems based Piezoelectric Acoustic sensor 4th International Conference on Condition Assessment Techniques in Electrical Systems, CATCON 2019 (Institute of Electrical and Electronics Engineers Inc.)

[12] Hossain N, Rimon M I H, Mimona M A, Mobarak M H, Ghosh J, Islam M A and Mahmud M Z Al 2024 Prospects and challenges of sensor materials: A comprehensive review e-Prime - Advances in Electrical Engineering, Electronics and Energy 7

[13] Inobeme A, Natarajan A, Pradhan S, Adetunji C O, Ajai A I, Inobeme J, Tsado M J, Jacob J O, Pandey S S, Singh K R and Singh J 2024 Chemical Sensor Technologies for Sustainable Development: Recent Advances, Classification, and Environmental Monitoring Advanced Sensor Research

[14] Gupta N, Dutta S, Parmar Y, Gond V, Vanjari S R K and Gupta S 2021 Characterization of SOI MEMS capacitive accelerometer under varying acceleration shock pulse durations Microsystem Technologies 27 4319–27

[15] Apostolyuk V 2016 Coriolis vibratory gyroscopes: Theory and design (Springer International Publishing)

[16] Tran V T, Stempitsky V R, Lovshenko I Yu, Korsak K V. and Dao D H 2023 Design and Performance of Amorphous Silicon Based on Uncooled Bolometer-Type Infrared Focal Plane Arrays Doklady BGUIR 21 77–85

[17] Mbarek S Ben, Alcheikh N, Ouakad H M and Younis M I 2021 Highly sensitive low field Lorentz-force MEMS magnetometer Sci. Rep. 11

[18] Li M, Wang M and Li H 2006 Optical MEMS pressure sensor based on Fabry-Perot interferometry Opt. Express 14 1497

[19] Upadhyaya A M, Hasan M K, Abdel-Khalek S, Hassan R, Srivastava M C, Sharan P, Islam S, Saad A M E and Vo N 2021 A Comprehensive Review on the Optical Micro-Electromechanical Sensors for the Biomedical Application Front. Public Health 9

[20] Je C H, Jeon J H, Lee S Q and Yang W S 2017 MEMS Capacitive Microphone with Dual-Anchored Membrane (MDPI AG) p 342

[21] Anon jones-yan-2004-mems-force-and-torque-sensors-a-review

[22] Qin Y, Zhao Y, Li Y, Zhao Y and Wang P 2016 A high performance torque sensor for milling based on a piezoresistive MEMS strain gauge Sensors (Switzerland) 16

[23] Behrmann O, Lisec T and Gojdka B 2022 Towards Robust Thermal MEMS: Demonstration of a Novel Approach for Solid Thermal Isolation by Substrate-Level Integrated Porous Microstructures Micromachines (Basel). 13

[24] Weinberg M S 2015 How to invent (or not invent) the first silicon MEMS gyroscope 2nd IEEE International Symposium on Inertial Sensors and Systems, IEEE ISISS 2015 - Proceedings (Institute of Electrical and Electronics Engineers Inc.)

[25] El-Sheimy N and Youssef A 2020 Inertial sensors technologies for navigation applications: state of the art and future trends Satellite Navigation 1

[26] Applications J W MEMS gyroscopes provide precision inertial sensing Harch, High temperature environments.

[27] Chiu S R, Teng L T, Chao J W, Sue C Y, Lin C H, Chen H R and Su Y K 2014 An integrated thermal compensation system for MEMS inertial sensors Sensors (Switzerland) 14 4290–311

[28] Yazdi N, Ayazi F and Najafi K 1998 Micromachined inertial sensors Proceedings of the IEEE 86 1640–58

[29] Allegato G, Corso L and Valzasina C 2022 Inertial Sensors Silicon Sensors and Actuators: The Feynman Roadmap 439–75

[30] Husseini E, Mohamed S, Ibraheem M and Gad N H Anatomy and physiology of vestibular system: Review Article

[31] Anon Vestibular system, anatomy, function & vestibular system disorders
[32] Zhao W, Cheng Y, Zhao S, Hu X, Rong Y, Duan J and Chen J 2021 Navigation grade mems imu for a satellite Micromachines (Basel). 12 1–12
[33] Harindranath A and Arora M 2024 A systematic review of user - conducted calibration methods for MEMS-based IMUs Measurement (Lond). 225
[34] Khan H, A Rashid A S and Nasir N 2025 Evaluation and calibration of MEMS-IMU sensors for real-time landslide detection and monitoring system Engineering Research Express 7
[35] Johnson B, Albrecht C, Braman T, Christ K, Duffy P, Endean D, Gnerlich M and Reinke J 2021 Development of a Navigation-Grade MEMS IMU INERTIAL 2021 - 8th IEEE International Symposium on Inertial Sensors and Systems, Proceedings (Institute of Electrical and Electronics Engineers Inc.)
[36] Mo Y, Du L, Qu B B, Peng B and Yang J 2018 Squeeze film air damping ratio analysis of a silicon capacitive micromechanical accelerometer Microsystem Technologies 24 1089–95
[37] Wang A, Sahandabadi S, Harrison T, Spicer D and Ahamed M J 2022 Modelling of air damping effect on the performance of encapsulated MEMS resonators Microsystem Technologies 28 2529–39
[38] Judge J A, Photiadis D M, Vignola J F, Houston B H and Jarzynski J 2007 Attachment loss of micromechanical and nanomechanical resonators in the limits of thick and thin support structures J. Appl. Phys. 101
[39] Ferguson M I, Keymeulen D, Peay C and Yee K Effect of Temperature on MEMS Vibratory Rate Gyroscope
[40] Zhang C, Wu Q S, Yin T and Yang H G 2010 A MEMS gyroscope readout circuit with temperature compensation 2010 IEEE 5th International Conference on Nano/Micro Engineered and Molecular Systems, NEMS 2010 pp 458–62
[41] Anon 2024 Global MEMS Sensors market research report forecast to 2034
[42] Anon InvenSense on the evolution of the MEMS market: Think software and use case!
[43] Anon India Sensors Market Size, Share, Growth & Forecast 2034
[44] Anon MEMS Gyroscope Market Size, Share, Report 2024-2032
[45] Wagner J F, Trierenberg A, Wagner J F and Gottlieb Bohnenberger J 2010 The Origin of the Gyroscope: The Machine of Bohnenberger The Machine of Bohnenberger View project Satellite Navigation View project The Origin of the Gyroscope: The Machine of Bohnenberger
[46] Hattis P D How doc draper became the father of inertial guidance
[47] Bhatt G, Manoharan K, Chauhan P S and Bhattacharya S 2019 MEMS Sensors for Automotive Applications: A Review Energy, Environment, and Sustainability (Springer Nature) pp 223–39
[48] Hossain N, Mahmud M Z Al, Hossain A, Rahman M K, Islam M S, Tasnim R and Mobarak M H 2024 Advances of materials science in MEMS applications: A review Results in Engineering 22
[49] Passaro V M N, Cuccovillo A, Vaiani L, De Carlo M and Campanella C E 2017 Gyroscope technology and applications: A review in the industrial perspective Sensors (Switzerland) 17
[50] Zaman M F, Sharma A, Hao Z and Ayazi F 2008 A mode-matched silicon-yaw tuning-fork gyroscope with subdegree-per-hour Allan deviation bias instability Journal of Microelectromechanical Systems 17 1526–36
[51] Ni Y, Li H, Huang L, Ding X and Wang H 2014 On bandwidth characteristics of tuning fork micro-gyroscope with mechanically coupled sense mode Sensors (Switzerland) 14 13024–45

[52] Xu Q, Xiao D, Hou Z, Zhuo M, Li W, Xu X and Wu X 2019 A Novel High-Sensitivity Butterfly Gyroscope Driven by Horizontal Driving Force IEEE Sens. J. 19 2064–71
[53] Laermer F and Urban A 2019 MEMS at Bosch – Si plasma etch success story, history, applications, and products Plasma Processes and Polymers 16
[54] Askari S, Asadian M H and Shkel A M 2021 Performance of quad mass gyroscope in the angular rate mode Micromachines (Basel). 12 1–25
[55] Challoner A D, Ge H H and Liu J Y 2014 Boeing Disc Resonator Gyroscope
[56] Ayazi F and Najafi K 2001 A HARPSS Polysilicon Vibrating Ring Gyroscope vol 10
[57] Rozelle D M, Research Scientist S and Co N G The Hemispherical Resonator Gyro: From Wineglass to the Planets
[58] Marty F, Rousseau L, Saadany B, Mercier B, Français O, Mita Y and Bourouina T 2005 Advanced etching of silicon based on deep reactive ion etching for silicon high aspect ratio microstructures and three-dimensional micro- and nanostructures Microelectronics J. 36 673–7
[59] Funk K, Emmerich H, Schilp A, Offenberg M, Neul R and Laermer F 1999 Surface micromachined silicon gyroscope using a thick polysilicon layer Proceedings of the IEEE Micro Electro Mechanical Systems (MEMS) (IEEE) pp 57–60
[60] Shaveta, Bhan R K and Chaujar R 2025 Enhancing MEMS Gyroscope Performance with Vertical Sense Mass Design Def. Sci. J. 75 758–70
[61] Nasa Planetary Geology pdf
[62] Gerkema T and Gostiaux L 2012 A brief history of the Coriolis force Europhysics News 43 14–7
[63] Kohli Garg R V and Dhawan A Environmental Sciences Atmospheric Processes Winds and Global Circulation of Winds Paper No: 8 Atmospheric Processes Module: 19 Winds and Global Circulation of Winds Development Team Principal Investigator & Co-Principal Investigator
[64] Anon EJN-0805-Science-Wagner-Renz
[65] Elwell J 1991 Progress on micromechanical inertial instruments Conference Proceedings - Symposium Gyro Technology (Publ by Deutsche Gesellschaft fuer Ortung und Navigation)
[66] Maenaka K, Fujita T, Konishi Y and Maeda M 1996 Analysis of a highly sensitive silicon gyroscope with cantilever beam as vibrating mass vol 54
[67] Klaassen E H, Petersen K, Noworolski M, Logan J, Maluf N I, Brown J, Storment C, Mcculley W and Kovacs G T A 1996 s S.ORs ACTWORS A Silicon fusion bonding and deep reactive ion etching: a new technology for microstructures vol 52 (ELSEVIER)
[68] Bao M-H 2000 Handbook of Sensors and Actuators 8 Micro Mechanical Transducers Pressure Sensors, Accelerometers and Gyroscopes
[69] Galiouna Nassiopoulou A and Kaltsas G 2000 Porous Silicon as an Effective Material for Thermal Isolation on Bulk Crystalline Silicon
[70] Painter C C and Shkel A M 2003 Structural and thermal modeling of a z-axis rate integrating gyroscope Structural and thermal modeling of a z-axis rate integrating gyroscope Journal of microelectronics and microengineering vol 13
[71] Marty F, Rousseau L, Saadany B, Mercier B, Français O, Mita Y and Bourouina T 2005 Advanced etching of silicon based on deep reactive ion etching for silicon high aspect ratio microstructures and three-dimensional micro- and nanostructures Microelectronics J. 36 673–7
[72] Marinis T, Soucy J, Marinis T F, Soucy J W and Johansson B D 2007 High Performance MEMS Inertial Instruments Fabricated on LTCC Substrates
[73] Khan N A 2020 Scholarship at UWindsor Scholarship at UWindsor Electronic Theses and Dissertations Theses, Dissertations, and Major Papers Developing highly symmetric

Microelectromechanical systems Developing highly symmetric Microelectromechanical systems (MEMS) based butterfly gyroscopes (MEMS) based butterfly gyroscopes

[74] Waters R, Tally C, Dick B, Jazo H, Fralick M, Kerber M and Wang A 2010 Design and Analysis of a Novel Electro-Optical MEMS Gyroscope for Navigation Applications

[75] Yi H, Fan B, Bu F, Chen F and Luo X Q 2024 Research on Energy Dissipation Mechanism of Cobweb-like Disk Resonator Gyroscope Micromachines (Basel). 15

[76] Herth E, Baranski M, Berlharet D, Edmond S, Bouville D, Calvet L E and Gorecki C 2019 Fast ultra-deep silicon cavities: Toward isotropically etched spherical silicon molds using an ICP-DRIE Journal of Vacuum Science & Technology B 37 021206

[77] Dyer S, Griffin P F, Arnold A S, Mirando F, Burt D P, Riis E and McGilligan J P 2022 Micro-machined deep silicon atomic vapor cells J. Appl. Phys. 132

[78] Tang Y, Sandoughsaz A and Najafi K 2017 Ultra high aspect-ratio and thick deep silicon etching (UDRIE) Proceedings of the IEEE International Conference on Micro Electro Mechanical Systems (MEMS) (Institute of Electrical and Electronics Engineers Inc.) pp 700–3

[79] Abhinav G A A S D K H B and C V 2020Improvements in the sensitivity of MEMS based gyroscope for military applications

[80] Li C, Yang B, Guo X and Chen X 2020 Design, analysis and simulation of a mems-based gyroscope with differential tunneling magnetoresistance sensing structure Sensors (Switzerland) 20 1–17

[81] Oy O, Mervi Paulasto-Krö ckel F, Petzold M, Theuss H and Lindroos V 2020 Handbook of Silicon Based MEMS Materials and Technologies Third Edition Markku Tilli

[82] Han X, Huang M, Wu Z, Gao Y, Xia Y, Yang P, Fan S, Lu X, Yang X, Liang L, Su W, Wang L, Cui Z, Zhao Y, Li Z, Zhao L and Jiang Z 2023 Advances in high-performance MEMS pressure sensors: design, fabrication, and packaging Microsyst. Nanoeng. 9

[83] Pannaga N and Rajesh R P Review: MEMS Fabrication Technology

[84] Hajare R, Reddy V and Srikanth R 2021 MEMS based sensors – A comprehensive review of commonly used fabrication techniques Materials Today: Proceedings vol 49 (Elsevier Ltd) pp 720–30

[85] Xie J, Shen Q, Hao Y, Chang H and Yuan W 2015 Design, fabrication and characterization of a low-noise Z-axis micromachined gyroscope Microsystem Technologies 21 625–30

[86] Bhan R K, Pal R, Dutta S and Yadav I 2016 Development of Unified Fabrication Process and Testing of MEMS Based Comb and Crab Type Capacitive Accelerometers for Navigational Applications vol 203

[87] Anon History of (MEMS) History of MEMS Learning Module LIGA-micromachined gear for a mini electromagnetic motor [Sandia National Labs]

[88] Banu A and Yeakub Ali M 2016 Electrical Discharge Machining (EDM): A Review vol 1

[89] Anon advanced-microsystems-for-automotive-applications-2007-2007

CHAPTER 2

FUNDAMENTAL THEORY AND OPERATING PRINCIPLES OF MEMS GYROSCOPES

- *Introduction to the Frame of reference for inertial and non-inertial motions relevant to MEMS gyroscopes.*
- *Explanation of the Coriolis effect and gyroscope axis and direction terminology.*
- *Derivation of steady-state drive and sense mode responses under harmonic excitation, including magnitude and phase.*
- *Analytical derivation of bandwidth and discussion on drive–sense frequency separation for stable operation. Analysis of dominant noise sources, with derivation of thermomechanical noise.*
- *Sources of quadrature error arising from structural and electrostatic imperfections are identified and discussed.*
- *Key assumptions used in the analytical modelling are discussed.*

2.1 Introduction

This chapter develops the theoretical foundation required to analyze the working principles, performance limits, and design trade-offs of MEMS gyroscopes[1]. The discussion begins with a review of essential concepts in inertial sensing, including frames of reference, rotational kinematics, and the dynamics of motion observed in non-inertial systems. These fundamentals naturally lead to the derivation of the Coriolis force, which underlies vibratory MEMS gyroscopes. Building on this framework, analytical lumped-parameter models are formulated to describe the coupled dynamics of the drive and sense modes [2,3]. The models explicitly account for mass, stiffness, damping, and Coriolis coupling, enabling a clear representation of how mechanical motion is influenced by an applied angular rate. Closed-form steady-state solutions for the drive and sense responses are then derived, with particular attention given to their amplitude and phase behaviour. These results establish a direct relationship between the input rotation rate and the gyroscope's measurable output signal.

The chapter further examines the fundamental factors that govern bandwidth and resolution. Intrinsic mechanical noise sources, especially thermal noise arising from Brownian motion, are discussed in detail, as they impose fundamental limits on gyroscope performance regardless of the electronic readout circuitry. Together, the analyses presented in this chapter provide a coherent theoretical basis for evaluating MEMS gyroscope performance and serve as a foundation for the design optimization and experimental investigations discussed in the subsequent chapters.

Rotational motion requires defining a reference frame to measure position, velocity, and acceleration [4]. In an inertial frame, Newton's laws hold that objects are at rest or persist in motion with uniform velocity unless a force acts on them from outside. In systems such as gyroscopes, we often deal with non-inertial frames, and we need imaginary forces to consider the motion of a frame which is relevant to describing the behaviour of inertial sensors.

2.2 Frame of Reference

The motion of a physical system can only be described with respect to a specified inertial frame of reference, shown in Figure 2.1. Let the position vector of a particle be expressed as:

$$= \hat{} + \hat{} + \hat{} \tag{2.1}$$

where (x, y, z) denote the coordinates of the particle in a three-dimensional Cartesian frame. In inertial frames, a particle not subjected to any external force continues either in a state of rest or uniform linear motion. Mathematically, in an inertial frame, $=$ and for a force-free particle, $= \frac{{}^2}{{}^2} = 0$

Frames moving with constant velocity relative to an inertial frame are also inertial. Consider two inertial frames S and S , where S moves with constant velocity v relative to S as shown in Figure 2.1.

If the origins coincide at t=0, the Galilean transformation relating the two frames is given by:

$$= + \tag{2.2}$$

Differentiating equation (2) with respect to time,

$$= + \quad \text{and} \quad = \tag{2.3}$$

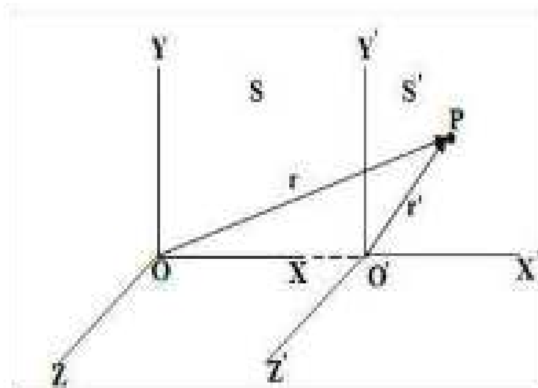

Figure 2.1 Inertial frame of reference S' is moving with constant velocity v relative to S [4].

Thus, acceleration is invariant under Galilean transformations, confirming the equivalence of inertial frames. In a non-inertial frame, Newton's laws do not hold in their original form unless additional forces known as fictitious or inertial forces are introduced. Consider an inertial frame M and a non-inertial frame M accelerating with acceleration a_0 relative to Y, shown in Figure 2.2.

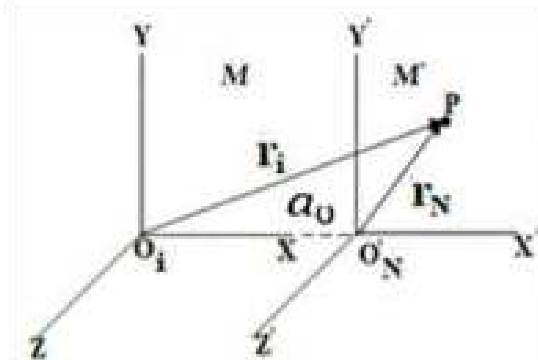

Figure 2.2 Inertial frame of reference M' is accelerating with relative to M [4].

The accelerations measured in the two frames are related by:

$$= \quad + \qquad (2.4)$$

Rewriting Newton's second law in the non-inertial frame:

$$= \quad - \qquad (2.5)$$

where the term $= -$ represents the fictitious force experienced in the accelerating frame. Gyroscopic systems are fundamentally associated with rotating frames of reference. Let an inertial frame, N and a frame N is rotating with angular velocity about a common origin, shown in Figure 2.3.

The time derivative of any vector A in the two frames is related by:

$$\frac{}{} = \frac{}{} + (\times A) \qquad (2.6)$$

Applying this to the position vector r, the velocity relationship becomes:

$$= \quad + \quad \times r \tag{2.7}$$

Differentiating equation (7) again to obtain acceleration:

$$= \quad + 2 \times \quad + \quad \times (\times r) \tag{2.8}$$

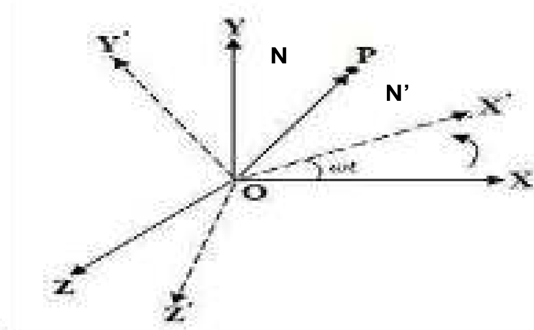

Figure 2.3 Inertial frame of reference P' is rotating with angular velocity relative to P [4].

Multiplying equation (8) by mass m, the force balance in the rotating frame becomes:

$$= \quad - 2 \quad \times \quad - \quad \times (\times r) \tag{2.9}$$

where, $-2 \quad \times$ is the Coriolis force and $- \quad \times (\times r)$ is the centrifugal force. Hence, the Coriolis force exists only when the mass has a velocity relative to the fame which is rotating and is always perpendicular to the velocity vector.

2.2.1 Coriolis force in MEMS Gyroscope

For a gyroscope, A proof mass m is shown moving with a linear velocity v_r along the x-axis (drive direction). Simultaneously, an angular rotation $_y$ is applied about the y-axis, which is in-plane of motion. Due to this rotation, the moving mass experiences an apparent inertial force known as the Coriolis force, given by:

$$= -2 \quad \times \tag{2.10}$$

The cross-product nature of this expression causes the Coriolis force to act perpendicular to both the velocity vector and the rotation axis. In this case, motion along the x-axis combined with rotation about the y-axis produces a Coriolis force along the z-axis, as indicated by the orange arrow. This force induces a small displacement of the mass in the sense direction (z-direction).

In MEMS gyroscopes, this secondary displacement is detected using capacitive-sensing electrodes along the sense axis. The magnitude of the displacement and, hence, the capacitance change are directly proportional to the applied angular rate $_y$. By measuring this capacitance variation, the gyroscope converts rotational motion into an electrical signal, enabling accurate angular rate sensing.

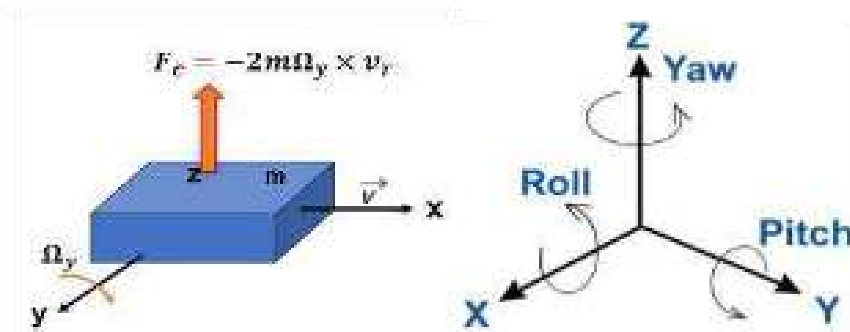

Figure 2.4 (a) Coriolis force in a gyroscope (b) Gyroscope axis terminology [1].

In the gyroscope-axis terminology adopted in this work, the in-plane axes correspond to rotations about axes that lie parallel to the sensor package surface. These axes are identified as the x- and y-axes, associated with roll and pitch rotations, respectively, as shown in Figure 2.4b. Rotations about these axes occur within the plane of the chip surface. The out-of-plane direction (z-axis) is defined as the axis normal to the sensor surface and corresponds to the sense displacement direction in the proposed architecture. Although the mechanical displacement occurs out of plane, the measured angular rate is determined by the axis of applied rotation. In the current configuration, the y-axis rotation corresponds to pitch-rate sensing, while the z-axis rotation corresponds to yaw-rate sensing [5].

Conventional MEMS gyroscopes predominantly employ a tuning-fork architecture in which two proof masses are driven to oscillate with equal amplitude but in opposite directions [6,7]. When the system rotates, the two masses experience Coriolis forces of equal magnitude but opposite direction. This creates a differential change in capacitance, which is directly proportional to the angular rate. The resulting signal is then converted into an electrical output—either as a voltage in analog systems or as digital counts in digital gyroscopes.

On the other hand, when the device undergoes linear acceleration, both masses experience the same inertial force and move together in the same direction. Since there is no difference in their motion, no differential capacitance is generated, and the output remains at the zero-rate level. This behaviour makes such gyroscopes inherently insensitive to linear acceleration effects like shock, vibration, or tilt. In this work, the focus is on a single-mass gyroscope design where the drive and sense motions are achieved through separate structural elements. Unlike traditional tuning-fork designs, multiple sense masses are avoided, as they add significant complexity to both the structure and the fabrication process.

2.3 Physical Structure of a MEMS Vibratory Gyroscope

Vibratory MEMS gyroscopes operate on the principle of Coriolis acceleration, which arises when a vibrating mass experiences angular rotation. Unlike conventional spinning-mass gyroscopes, MEMS gyroscopes employ a micromachined mechanical structure in which a proof mass is deliberately driven into oscillatory motion. When the device is subjected to an external angular rate, energy is transferred from the driven vibration mode to an orthogonal sensing mode through Coriolis coupling [5]. The motion in the sense direction is proportional to the applied angular rate, enabling accurate rotation measurement. In drive mode, a controlled vibration of the proof mass is produced (usually by electrostatic actuation close to resonance for efficient stable operation).

The sense mode, oriented perpendicularly to the drive mode, measures the small oscillation excited by the Coriolis force during rotation. This motion is detected through sensitive techniques like capacitive sensing, and its magnitude is directly proportional to the input angular rate. The generic MEMS gyroscope implementation is shown in Figure 2.5.

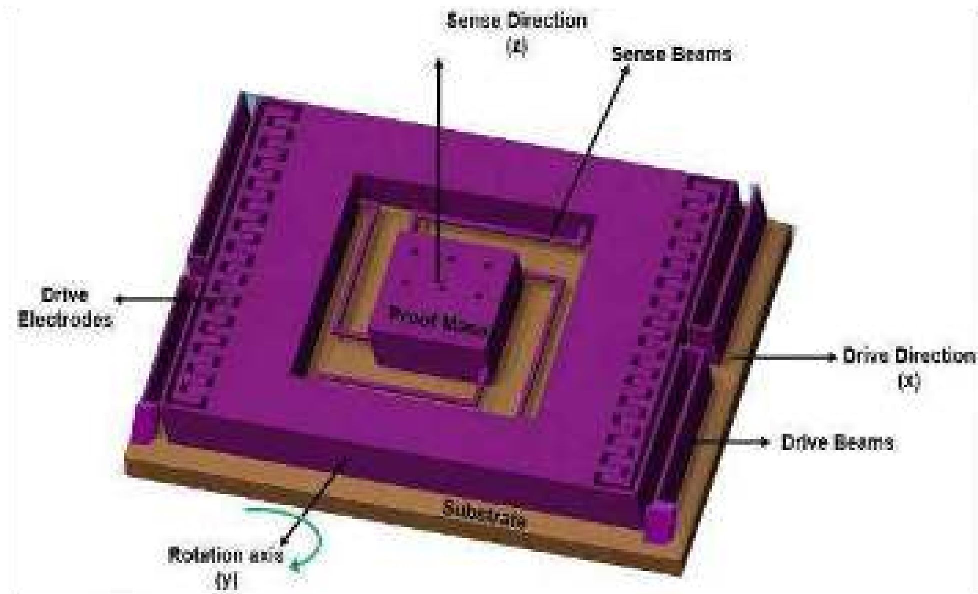

Figure 2.5 MEMS vibratory gyroscope schematic [5].

2.3.1 Lumped-Parameter Modelling of MEMS Gyroscopes

Lumped-parameter modelling is a widely adopted analytical approach for describing the dynamic behaviour of vibratory MEMS gyroscopes. In this framework, the complex distributed structure of the gyroscope, comprising the proof mass, suspension beams, and anchors, is represented by an equivalent mass–spring–damper system. This abstraction enables a compact mathematical description of device dynamics while retaining the dominant physical mechanisms governing gyroscope operation [8].

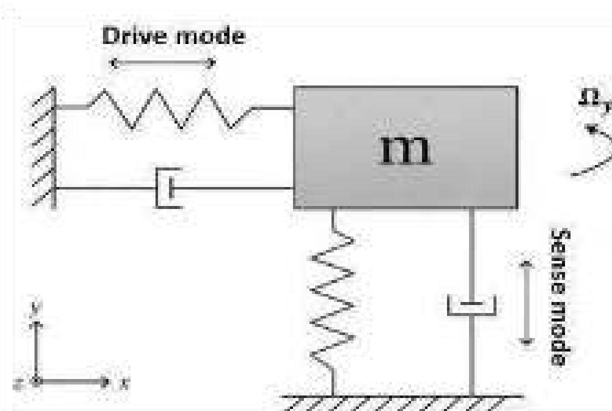

Figure 2.6 Mass-spring damper system for MEMS gyroscope [1].

In a MEMS gyroscope, the proof mass is treated as a rigid body with an effective mass suspended by compliant flexures that provide equivalent stiffness along the drive and sense axes, as shown in Figure 2.6. Energy dissipation mechanisms, including gas damping and structural losses, are collectively represented by viscous damping coefficients. Under this approximation, the distributed elastic and inertial properties of the structure are mapped onto a small set of parameters that characterize the fundamental vibratory modes of interest.

Table 2.1 Physical Mapping to MEMS Structure

Physical MEMS Element	**Lumped-Parameter Equivalent**
Proof mass (plate/frame)	Lumped mass m
Suspension beams/flexures	Springs k_x,k_z
Gas damping	Dampers c_x,c_z
Electrostatic drive	External force $F_d\cos(\ _d t)$
Rotation input	Coriolis coupling term

The primary advantage of the lumped-parameter model is its ability to capture the gyroscope's first-order dynamic response with a minimal set of governing equations. By focusing on the fundamental drive and sense modes, the model allows clear analytical insight into how parameters such as mass, stiffness, damping, and resonance frequency influence sensitivity, bandwidth, and noise performance. This makes the approach particularly suitable for early-stage design exploration and comparative evaluation of different gyroscope architectures.

In the mass–spring–damper abstraction, each vibratory mode is assumed to behave as an independent second-order system in the absence of rotation [9]. Rotation about the sensitive axis causes Coriolis relation between the drive and sense modes, which is incorporated as a velocity-dependent force term. The resulting coupled second-order differential equations form the basis for analytical derivation of steady-state response, sensitivity expressions, and frequency-matching conditions. Although MEMS gyroscopes are inherently distributed mechanical systems, the lumped-parameter representation remains valid when the fundamental modes dominate the response and are well separated from higher-order modes. This condition is typically satisfied in well-designed gyroscopes, where suspension geometry and mass distribution are optimized to maximize modal purity and minimize spurious mode coupling.

From a design perspective, the lumped-parameter model provides valuable insight into scaling relationships. For example, changes in proof-mass thickness directly modify the effective mass and stiffness terms, which, in turn, influence the resonance frequency, quality factor, and Coriolis sensitivity. As a result, the mass–spring–damper abstraction offers a convenient analytical framework for examining the impact of thick-mass implementations enabled by Deep DRIE, including their potential benefits in mechanical robustness and footprint reduction.

Despite its simplifying nature, the lumped-parameter model serves as the theoretical foundation for more detailed finite element simulations and experimental studies. In this thesis, it serves as a baseline analytical tool for understanding the fundamental operation of MEMS gyroscopes and for guiding the design and optimization of thick-mass, Deep-DRIE-enabled gyroscope architectures addressed in subsequent chapters [10].

If x(t) denotes the displacement along the drive axis, z(t) denotes the displacement along the sense axis, $\ _y$ denote the angular rate applied about the y-axis

The proof mass is intentionally driven into harmonic oscillation along the drive axis (x-axis). When the device undergoes rotation about the y-axis, the Coriolis force couples this driven motion to the sense axis (z-axis), producing a measurable displacement proportional to the applied angular rate.

The dynamics of the proof mass are governed by Newton's second law. In an inertial frame, this can be expressed as:

$$= \quad + \quad + \tag{2.11}$$

The individual force components acting along the drive and sense axes are defined as follows:

Elastic restoring forces: $= - \quad , \quad = -$ (2.12)

Damping forces: $, = - \quad , \quad , = -$ (2.13)

External drive force: $= \cos(\quad)$ (2.14)

Where m is the effective proof mass, k_x is the equivalent drive-mode stiffness, and c_x is the equivalent damping coefficient. When the system undergoes rotation about the y-axis, the angular velocity vector is:

$$= \quad \hat{} \tag{2.15}$$

The velocity of the proof mass in the rotating frame is:

$$v = \quad \hat{} + \quad \hat{} \tag{2.16}$$

The Coriolis force acting on the proof mass is therefore given by equation (10). Evaluating the cross product yields the Coriolis force components:

$$, = -2 \quad , \quad , = -2 \tag{2.17}$$

Coupled Equations of Motion: Including elastic, damping, drive, and Coriolis forces, the coupled equations of motion along the drive and sense axes become:

$$+ \quad + \quad = \cos(\quad) - 2 \tag{2.18}$$

$$+ \quad + \quad = 2 \tag{2.19}$$

These equations clearly demonstrate that rotation-induced Coriolis forces introduce coupling between the drive and sense modes. To express the equations in a normalized and physically intuitive form, the following parameters are defined:

$$= \frac{}{}, \quad = \frac{}{} \tag{2.20}$$

$$\frac{}{} = 2 \quad \frac{}{} = 2 \tag{2.21}$$

Dividing the equations of motion by the mass m, the normalized coupled equations become:

$$+ 2 \quad + \quad = \frac{}{} \cos(\quad) - 2 \tag{2.22}$$

$$+ 2 \quad + \quad = 2 \tag{2.23}$$

These equations highlight the dependence of gyroscope behaviour on structural parameters such as stiffness, damping, and modal frequency matching.

Drive Mode Steady-State Response: In practical MEMS gyroscopes, the Coriolis feedback into the drive mode is much smaller than the external actuation force and is therefore neglected. Under this assumption, the drive mode equation (22) simplifies to:

$$+2 \quad + \quad = \text{—}\cos(\quad) \tag{2.24}$$

At steady state, the solution is a harmonic oscillation given by:

$$() = \quad \cos(\quad) \tag{2.25}$$

where the amplitude X_0 is determined by the drive force magnitude, quality factor, and frequency tuning. The corresponding velocity is:

$$() = - \quad \sin(\quad) \tag{2.26}$$

A stable and precisely controlled drive amplitude is essential, as the Coriolis force acting on the sense mode is directly proportional to the drive velocity.

Sense Mode Response Under Coriolis Excitation: Substituting the steady-state drive velocity in equation (26) into the sense mode equation (24) yields:

$$+2 \quad z + \quad = -2 \quad \sin(\quad) \tag{2.27}$$

For algebraic convenience, the excitation can be expressed in cosine form using the identity:

$$\sin(\quad) = \cos(\quad - \text{–}) \tag{2.28}$$

Thus, the sense mode equation becomes:

$$+2 \quad z + \quad = \quad \cos(\quad) \quad \text{where} \quad = 2 \tag{2.29}$$

Steady-State Sense Mode Solution: Assuming a harmonic steady-state response of the form:

$$() = \quad \cos(\quad - \quad) \tag{2.30}$$

The first and second derivatives are:

$$z() = - \quad \sin(\quad - \quad) \tag{2.31}$$

$$() = - \quad \cos(\quad - \quad) \tag{2.32}$$

Substituting equations (30), (31), (32) in equation (29) gives:

$$- \quad \cos(\quad - \quad) - 2 \quad \sin(\quad - \quad) + 2 \quad \sin(\quad - \quad) = \quad \cos(\quad) \tag{2.33}$$

$$[(\quad - \quad) \cos(\quad - \quad) - 2 \quad \sin(\quad - \quad)] = \quad \cos(\quad) \tag{2.34}$$

Using trigonometric identities, the combined cosine–sine term can be expressed as a single cosine with magnitude:

$$A\cos(\quad - \quad) - B\sin(\quad - \quad) = \quad + \quad \cos(\quad - \quad - \quad) \tag{2.35}$$

where, $A = (\quad - \quad) \quad = 2$

Equation (34) can be written as:

$$o \quad \overline{\quad + \quad} \cos(\quad - \quad - \quad) = \quad \cos(\quad - \quad /2) \tag{2.36}$$

$$({}^{2} - {}^{2})^{2} + (\quad)^{2} = \tag{2.37}$$

Equating amplitudes, the steady-state sense displacement amplitude is obtained as:

$$z_0 = \frac{}{(\quad)({}^{2} \quad)} \tag{2.38}$$

$$z_0 = \frac{{}^{2}}{(\quad)({}^{2} \quad)} \tag{2.39}$$

$$(\,) = \tag{2.40}$$

Hence, the phase lag of the sense response is:

$$= \quad {}^{1}\left(\frac{{}^{2}}{(\quad)}\right) \tag{2.41}$$

For ${}_{z} = {}_{d}$, the sense displacement amplitude is:

$$z_0 = \frac{{}^{2}}{} \tag{2.42}$$

where $Q_z = 1/2 \; {}_{z}$ is the quality factor in the sensing vibration mode. However, this result is valid only for a constant (DC) angular rate input and therefore corresponds to zero bandwidth. The derived expression clearly shows that the sense-mode displacement amplitude is linearly proportional to the applied angular rate,

$$z_0 \tag{2.43}$$

This fundamental relationship underpins angular rate measurement in vibratory MEMS gyroscopes and underscores the critical roles of structural parameters, damping, and frequency matching in determining sensitivity and noise performance.

Phase difference: Below resonance, $({}_{d} < {}_{z})$: $0 < \; < 90$

At resonance, $({}_{d} = {}_{z})$: $= 90$

Above resonance, $({}_{d} > {}_{z})$: $90 < \; < 180$

This phase behaviour is crucial for demodulation and quadrature rejection in MEMS gyroscopes.

Sensitivity describes how strongly a gyroscope's output changes in response to an applied angular rate. It is typically expressed as millivolts per degree-per-second (mV/dps) in analog gyroscopes, or least significant bits per degree-per-second (LSB/dps) in digital ones. In simple terms, it represents the gain of the sensor—the ratio of output signal to input angular velocity—and determines how small a rotation the device can detect reliably.

Sensitivity improves with an increase in proof mass, higher drive velocity, and lower damping in the sense mode. In thick-mass MEMS gyroscopes fabricated using Deep DRIE, increasing the structural thickness leads to a higher mass. At the same time, stiffness does not scale in the same way as mass, which allows flexibility in tuning the resonant frequency. The change in geometry also affects damping due to variations in the surface-to-volume ratio. All these factors are captured within the mass–spring–damper model, making it a useful tool for first-order analysis and design optimization of compact, thick-mass gyroscope structures.

2.3.2 Bandwidth of MEMS gyroscope

In practical applications, angular rate signals are time-varying and therefore contain a spectrum of frequency components. To faithfully detect such signals, the gyroscope must possess a finite bandwidth that accommodates these frequency components. Two general approaches commonly employed to achieve non-zero bandwidth are:

1. Intentional frequency separation between the drive and sense modes ($_d$ $_s$), which increases bandwidth at the expense of reduced sensitivity.
2. Closed-loop electro-mechanical feedback using force rebalance or control electronics, which extends bandwidth while preserving high sensitivity.

In the following analysis, only the first approach, frequency separation, is considered.

Let the applied angular rate be a harmonic signal:

$$(\ ) = \ _0\cos(\ ) \tag{2.44}$$

where $_s$ is the signal angular frequency. The sense-mode equation of motion then becomes:

$$+2 \quad + \quad = 2 \ (\ ) \tag{2.45}$$

Substituting equation (26), equation (45) becomes:

$$+2 \quad + \quad = -2 \ _0 \quad \sin(\ )\cos(\ ) \tag{2.46}$$

Using the trigonometric identity,

$$\sin \ \cos \ = \frac{1}{\ }[\sin(\ + \ ) + \sin(\ - \ )] \tag{2.47}$$

The equation (46) can be written as:

$$+2 \quad + \quad = - \ _0 \quad [\sin \quad + \ ) + \quad (\ - \ )) \tag{2.48}$$

Equation (48) shows that the Coriolis force excites the sense mode at two sideband frequencies:

- an upper sideband at $+$
- a lower sideband at $-$

The steady-state response of the sense mode can therefore be written as:

$$(\ ) = \quad \cos[(\ - \ ) + \ ] + \quad \cos[(\ - \ ) + \ ] \tag{2.49}$$

where and are the displacement amplitudes corresponding to the upper and lower sidebands, respectively.

The amplitudes are given by:

$$= \frac{\ }{(\ (\ ))\ (\ (\ ))} \tag{2.50}$$

$$= \frac{\ }{(\ (\ ))\ (\ (\ ))} \tag{2.51}$$

Demodulated Output and Amplitude Response: After synchronous demodulation with respect to the drive frequency $_d$, the output signal can be expressed as:

$$(t) = A(\ )(\cos(\ \ - (\ )) \qquad (2.52)$$

where $A(\ )$ represents the gyroscope's frequency response amplitude. For small signal frequencies ($_s$ $_d$) and drive frequencies close to the sense-mode resonance, the dominant contribution arises from the lower sideband. Under this condition, the amplitude response can be approximated as:

$$A(\ ) = \frac{2\ c}{(\ \ (\ + \ )\ ) + (2\ \ (\ + \ ))} \qquad (2.53)$$

For bandwidth approximation, let the frequency separation between the sense and drive modes is:

$$= \ - \qquad (2.54)$$

For and $_z$ 1, Equation (53) can be approximated as:

$$A(\ ) = \frac{2\ c}{\ } \frac{1}{1\ (\ /\ )} \qquad (2.55)$$

The DC amplitude is therefore expressed as:

$$A(\ ) = \frac{2\ c}{\ } \qquad (2.56)$$

The 3-dB bandwidth $_s$ is defined by:

$$\frac{(\ )}{(\ )} = \frac{1}{2} \qquad (2.57)$$

Substituting equation (56) in (55):

$$= .54 \qquad (2.58)$$

Equation (58) shows that, in an open-loop vibratory MEMS gyroscope, the usable bandwidth is directly proportional to the frequency separation between the drive and sense modes. The 3-dB bandwidth in hertz, f_s, is obtained as:

$$= \frac{\ }{2} = \frac{\dot{\ }}{2} = .54\ \ = .54(\ - \ ) \qquad (2.59)$$

This expression shows that the usable bandwidth of an open-loop vibratory MEMS gyroscope is directly proportional to the frequency separation between the sense and drive modes. In practical terms:

- To achieve 1 Hz of signal bandwidth, the mode separation (f_z–f_d) must be increased by approximately 1.85 Hz.
- Increasing bandwidth, therefore, comes at the cost of reduced sensitivity, since sensitivity is maximised when f_d f_z.

When expressed in hertz, the 3-dB bandwidth of an open-loop MEMS gyroscope is approximately 54% of the drive–sense frequency separation, highlighting the inherent trade-off between sensitivity and bandwidth [11].

The analytical expressions for drive and sense responses show that both modes behave as second-order resonant systems, with their amplitudes governed by the frequency detuning term ($_z^2 -$ $_d^2$) and the damping-dependent term 2 $_z$ $_z$ $_d^2$. In particular, the sense-mode amplitude was shown to be strongly dependent on the proximity between the drive frequency $_d$ and the sense-mode natural frequency $_y$.

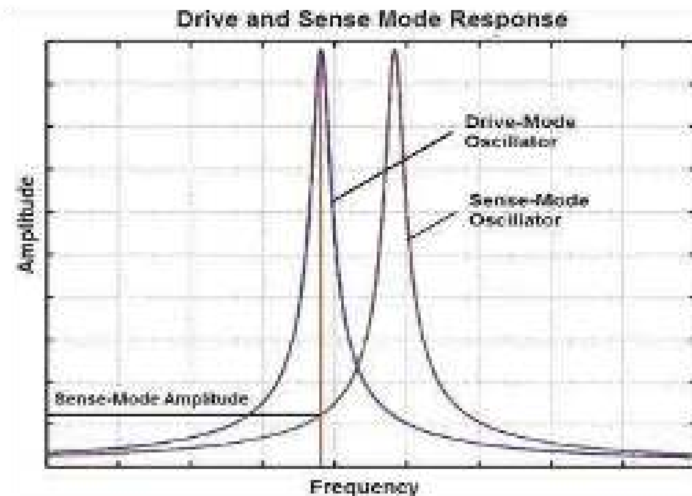

Figure 2.7 Frequency response of drive and sense modes in a typical MEMS vibratory gyroscope.

Figure 2.7 illustrates this frequency-dependent behaviour graphically. The amplitude–frequency curves of both the drive and sense oscillators exhibit sharp resonance peaks characteristic of high-Q second-order systems. The drive-mode oscillator reaches maximum amplitude at its resonance frequency, while the sense-mode oscillator exhibits peak response at its own natural frequency.

The vertical gap between the drive mode and sense mode resonance frequencies represents the frequency detuning f=f –f_d, which was shown in the previous section to govern the bandwidth of the gyroscope. As the two resonance frequencies approach each other, the sense-mode amplitude increases significantly, enhancing sensitivity. However, this also reduces the operational bandwidth, highlighting the inherent sensitivity–bandwidth trade-off derived analytically. The drive and sense resonant frequencies in a MEMS gyroscope are deliberately kept apart to avoid unwanted interaction between the two modes. If the frequencies are too close, energy from the drive motion can leak into the sense axis, increasing quadrature error and making the output unstable. Separating the frequencies also makes the device more tolerant of fabrication variations and temperature changes, and helps ensure that the true Coriolis signal can be clearly identified without interference from the drive motion. This design choice is especially important for achieving stable and reliable performance in high-precision gyroscopes [3].

Increasing the proof-mass thickness enhances inertial mass while allowing stiffness to be independently tailored through flexure design. This structural flexibility supports optimization of sensitivity–bandwidth trade-offs within a compact layout. As a result, thick-mass gyroscopes provide an efficient pathway to meet bandwidth specifications while improving mechanical robustness and maintaining key performance parameters, all within a reduced footprint.

2.3.3 Thermo-Mechanical Noise

Apart from the bandwidth constraints, thermo-mechanical noise arising from random thermal motion of the mechanical structure limits the resolution of a vibratory MEMS gyroscope. Damping mechanisms and mode-coupling noise due to unintended coupling between drive and sense mode, and low-frequency mechanical drift due to slow variations in material properties, residual stress, and environmental conditions are other sources of noise, in addition to electronic noise. In MEMS gyroscopes, it is critical because the Coriolis force acting on the proof mass is typically smaller than the inertial force, as is typically the case in accelerometers. These noise sources directly influence two key performance metrics: angle random walk (ARW), which characterizes short-term noise-driven uncertainty, and bias instability, which governs long-term drift behaviour.

Consequently, thermo-mechanical noise plays a dominant role in determining the minimum detectable angular rate. According to the fluctuation–dissipation theorem, the mean-square value of the thermally induced force acting on a mechanical system over a bandwidth f is given by:

$$^{2} = 4 \qquad (2.60)$$

=1.38×10–23J/K is Boltzmann's constant; T is the absolute temperature.

The noise-equivalent angular rate, $_n$, is defined as the angular rate at which the Coriolis force amplitude equals the root-mean-square thermo-mechanical noise force:

$$_c = \overline{4} \qquad (2.61)$$

Solving for $_n$ equation (61) yields:

$$= \frac{1}{2}\ \overline{4} \qquad (2.62)$$

Using the relation between damping and quality factor:

$$= \qquad (2.63)$$

and noting that $_d$ $_y$, the noise-equivalent angular rate simplifies to:

$$= \quad ( ) \qquad (2.64)$$

$$, \quad = \quad = \quad ( ) \qquad (2.65)$$

$$o, \quad = \frac{180}{} \quad ( ) \qquad (2.66)$$

Equation (66) shows that the thermo-mechanical noise-limited resolution of a vibratory MEMS gyroscope can be improved by increasing m, $_d$ and X_0 and minimizing f.

Increasing the proof-mass thickness can significantly enhance the effective mass without increasing the footprint. The reduced surface-to-volume ratio and improved structural rigidity can lead to higher achievable quality factors. Hence, for high-performance applications, thick-mass gyroscopes are well-suited because they offer a structurally efficient pathway.

Table 2.2 Summary of Noise Impact on Performance Metrics

Noise Source	Dominant Effect on ARW	Dominant Effect on Bias Instability
Thermomechanical (Brownian) noise	Primary limitation	Secondary
Damping-related noise	Strong	Moderate
Mode-coupling noise	Moderate to strong	Strong
Low-frequency mechanical drift	Weak	Primary limitation

As shown in Table 2.2, the angle random walk is fundamentally limited by thermomechanical noise associated with damping in the sense mode, whereas bias instability is governed by low-frequency noise processes arising from structural imperfections, mode coupling, and environmentally induced variations in mechanical properties. Therefore, improvements in short-term resolution and long-term stability require distinct design strategies.

2.4 Quadrature Error and Structural Imperfections

For defence-grade and navigation-grade applications, Quadrature error is one of the most critical problems, particularly where long-term bias stability and zero-rate accuracy are of utmost importance. Ideally, the drive and sense modes are perfectly orthogonal, and the sense response is mainly due to the Coriolis Force generated by rotation. In practical devices, however, structural imperfections introduced by fabrication inevitably lead to forged coupling between the drive and sense modes, resulting in quadrature error [12].

The quadrature error arises from unintentional coupling between the drive and sense modes, independent of Coriolis acceleration. Unlike the Coriolis response, which depends on drive velocity and applied angular rate, quadrature is proportional to drive displacement and exists even at zero rotation, appearing as a parasitic sense-axis output with an ideal 90° phase offset from the Coriolis signal. The error affects the zero-output and bias stability, and increases the Coriolis signal by an order of magnitude.

Fabrication-induced structural asymmetries, including stiffness imbalance, mass non-uniformity, flexure misalignment, and residual stress, are the main causes of the quadrature error. Other factors that contribute to coupling include electrostatic effects, such as electrode misalignment and drive-to-sense feedthrough. To eliminate or suppress this error phase-based demodulation, electrostatic tuning, active compensation, etc, can be employed.

An additional displacement-proportional forcing term appears in the sense-mode dynamics, commonly referred to as quadrature forcing. The normalized sense-mode equation can be expressed as:

$$+2 \quad + \quad = 2 \quad x + \frac{}{} \tag{2.67}$$

where represents the effective stiffness coupling between the drive and sense modes. The second term represents the quadrature forcing. For harmonic drive motion, the steady-state sense response can be written as:

$$( ) = \quad \cos \quad - \frac{}{} + \quad \cos(\quad) \tag{2.68}$$

where Z_q denotes the quadrature-induced component. Thus, mathematically, the quadrature error is the sense-axis displacement component that is proportional to the drive displacement and phase-orthogonal to the Coriolis response, and it is there even in the absence of applied rotation.

2.5 Assumptions Used in Modelling of the Vibratory MEMS Gyroscope

The analytical model developed in this chapter is based on a set of assumptions that enable a tractable mathematical formulation while preserving the essential physical behaviour governing MEMS gyroscope operation. These assumptions are consistent with widely adopted modelling practices and are justified by typical operating conditions of vibratory MEMS gyroscopes [13–15].

Linear Elastic Behaviour: The proof mass, suspension beams, and supporting structures are assumed to operate within the linear elastic regime. Consequently, the restoring forces along the drive and sense axes are modelled as linear spring forces proportional to displacement. This assumption is valid because MEMS gyroscopes are designed to operate at small vibration amplitudes, well below the onset of geometric or material nonlinearities.

Small Displacement and Small Angle Motion: The oscillatory displacements of the proof mass are assumed to be small compared to the characteristic device dimensions. Similarly, the applied angular rate is assumed to be sufficiently small such that higher-order rotational effects can be neglected. Under these conditions, only first-order Coriolis coupling terms are retained, while centrifugal and Euler acceleration terms are ignored.

Lumped-Parameter Approximation: The proof mass is treated as a rigid body with equivalent stiffness and damping, and higher-order modes and internal deformation are neglected. This holds true when the main modes dominate.

Linear Viscous Damping: Damping is thus modelled with simple viscous terms, capturing all the key effects such as squeeze-film and slide-film losses while skirting complicated behaviours.

Drive and Sense Modes Were Decoupled: Without rotation, the drive and sense modes are considered independent and any coupling effects between them will be treated separately.

Lumped-Parameter Approximation: The proof mass is treated as a rigid body with its mass concentrated at a single point, while the suspension is represented using equivalent stiffness and damping values. Effects such as distributed mass, higher-order vibration modes, and internal deformation of the structure are not considered. This simplification works well when the main drive and sense modes dominate the response and are clearly separated from higher-order modes.

Linear Viscous Damping: Energy losses in the system are modelled using linear viscous damping, described through damping coefficients or damping ratios for each mode. This approach captures the primary damping mechanisms under normal conditions, such as squeeze-film and slide-film damping, and is commonly used for initial performance estimation. More complex effects like nonlinear damping or rarefied gas behaviour are not included at this stage.

Decoupled Drive and Sense Modes in the Absence of Rotation:When there is no rotation, the drive and sense modes are assumed to be completely independent of each other. Any coupling caused by structural imperfections, fabrication variations, or electrostatic interactions (such as quadrature errors) is ignored in the basic model and can be addressed separately during detailed analysis or compensation.

Negligible Coriolis Feedback into the Drive Mode: The Coriolis force component acting on the drive mode is assumed to be much smaller than the external actuation force and is therefore neglected in the drive-mode equation. This assumption is valid for practical MEMS gyroscopes operating under closed-loop drive control, where the drive amplitude is actively stabilized.

Harmonic Steady-State Operation: The system is assumed to operate under steady-state harmonic conditions, with the drive mode oscillating at a fixed frequency close to its natural resonance. Transient dynamics during start-up, mode switching, or sudden changes in angular rate are not considered in the present analysis.

Constant Structural and Material Properties: Material properties such as Young's modulus, density, and damping coefficients are assumed to remain constant during operation. The temperature dependence of these parameters is neglected in the analytical model and addressed separately in later chapters focusing on thermal effects and long-term stability.

Uniform Angular Rate Input: The angular rate applied to the system is assumed to be constant and uniform over the time period of interest. In this simplified model, any changes in rotation, shocks, or vibration-induced disturbances are not considered.

Ideal Actuation and Sensing: Electrostatic actuation and capacitive sensing are assumed to be linear and ideal, without considering effects like nonlinearity, pull-in, parasitics, or noise.

These simplifications provide a clear analysis framework, with the more complex effects of real-world details addressed down the line through intricate modelling and experiments.

2.6 Conclusions

This chapter focuses on the main parameters that control the dynamic performance of a MEMS gyroscope for such high-performance applications. It starts from analysis of the steady-state responses of the drive and sense modes, with an emphasis on how the device behaves in response to controlled harmonic excitation. The next section discusses bandwidth and the dominant noise sources limiting resolution and stability in the long term. In addition, quadrature errors due to fabrication imperfections and undesired coupling between drive and sense modes are also studied. To maintain the clarity of the analysis and give it physical meaning, a clear overview of the assumptions made is provided through mechanical modelling.

References

[1] Apostolyuk V 2016 Coriolis vibratory gyroscopes: Theory and design (Springer International Publishing)

[2] Zhanshe G, Fucheng C, Boyu L, Le C, Chao L and Ke S 2015 Research development of silicon MEMS gyroscopes: a review Microsystem Technologies 21 2053–66

[3] Cenk Acar and Andrei Shkel 2009 MEMS Vibration Gyroscopes: Structural approach to improve robustness (Springer-Verlag)

[4] Anon First Semester Mechanics and Properties of Matter Unit 1: Frames of Reference and Gravitation: 11 hours

[5] Shaveta, Bhan R K and Chaujar R 2025 Design optimization of MEMS gyroscope for enhanced sensitivity, bandwidth and noise reduction Micro and Nanostructures 206

[6] Zaman M F, Sharma A, Hao Z and Ayazi F 2008 A mode-matched silicon-yaw tuning-fork gyroscope with subdegree-per-hour Allan deviation bias instability Journal of Microelectromechanical Systems 17 1526–36

[7] Nguyen M N, Ha N S, Nguyen L Q, Chu H M and Vu H N 2017 Z-axis micromachined tuning fork gyroscope with low air damping Micromachines (Basel). 8

[8] Acar C and Shkel A M 2005 An approach for increasing drive-mode bandwidth of MEMS vibratory gyroscopes Journal of Microelectromechanical Systems 14 520–8

[9] Anon Handbook of Modern Sensors Physics, Designs, and Applications Fifth Edition

[10] Herth E, Baranski M, Berlharet D, Edmond S, Bouville D, Calvet L E and Gorecki C 2019 Fast ultra-deep silicon cavities: Toward isotropically etched spherical silicon molds using an ICP-DRIE Journal of Vacuum Science & Technology B 37 021206

[11] Bao M-H 2000 Handbook of Sensors and Actuators 8 Micro Mechanical Transducers Pressure Sensors, Accelerometers and Gyroscopes

[12] Colin M, Thomas O, Grondel S and Cattan É 2020 Very large amplitude vibrations of flexible structures: Experimental identification and validation of a quadratic drag damping model J. Fluids Struct. 97

[13] Darvishian A 2018 Design and Analysis of Extremely Low-Noise MEMS Gyroscopes for Navigation

[14] Wang P, Li Q, Zhang Y, Xi X, Wu Y, Wu X and Xiao D 2022 Scale Factor Self-Calibration of MEMS Gyroscopes Based on the High-Order Harmonic Extraction in Nonlinear Detection IEEE Sens. J. 22 21761–8

[15] Awrejcewicz Jan 2012 Theory of Gyroscope Classical Mechanics pp.125-147

CHAPTER 3

STRUCTURAL PARAMETER DESIGN AND PERFORMANCE TRADE-OFFS IN CONVENTIONAL MEMS GYROSCOPES

- *A single-mass MEMS gyroscope with improved figure of merit (FOM)is proposed by jointly improving sensitivity, bandwidth and noise performance, leading to reduced footprints.*
- *To achieve broad applicability instead of design-specific (application-dependent tuning) for each sensor design, an integrated FOM based design optimization framework is proposed.*
- *The improved design demonstrates a 52 times enhancement in FOM ($m \cdot Hz/(dps)^2 \cdot mm^2$) over disclosed designs at similar operating conditions.*
- *Analytical models are validated with CoventorWare MEMS+ and Simulink simulation results within 5% accuracy, proving the validity of the proposed methodology.*
- *An empirical inverse relationship between sensitivity and bandwidth is established, and validated, as a useful measuring approach for MEMS gyroscope designers.*

3.1 Introduction

MEMS gyroscope-based devices have shown promising applications, including navigation [1–3], automotive, and consumer electronics [4], due to their small size, low power consumption, and high performance [5–7]. While significant advancements have been made in MEMS gyroscope technology, the design and optimisation of these devices remain challenging for researchers and engineers.

Moreover, MEMS capacitive gyroscopes offer several benefits, including high sensitivity, low noise, and negligible drift. They have attracted significant interest for multiple applications due to these characteristics and their compatibility with standard microfabrication processes. Since the pioneering work of Charles Draper in the 1990s, numerous innovative designs have been proposed to enhance the performance of MEMS gyroscopes. These include comb-drive tuning fork gyroscopes for automotive applications [8], symmetric and decoupled silicon micro gyroscopes for operation at atmospheric pressure [9], a matched mode design to increase sensitivity, improve SNR and high-sensitivity in butterfly gyroscopes utilising horizontal driving forces [10], high-performance disc resonator gyroscope [11].Ref [12]proposed a novel high-sensitivity butterfly gyroscope using a horizontal driving force and a rectangular vibration beam. Other notable advancements include the use of force rebalancing techniques for high-bandwidth operation[13], calibration references for mechanical bandwidth design [14], efficient simulation techniques using Simulink and signal processing techniques to reduce noise and improve accuracy [15].

However, to our knowledge, most previous research has focused on optimising individual parameters, such as sensitivity, bandwidth, and noise. Some studies have explored tuning the structure for improved sensitivity at the cost of reduced bandwidth [16]. Others have focused on increasing sensitivity and noise performance at the expense of size and complexity [17]. The effect of the increase in different parameters on the thermomechanical noise of the Coriolis vibration gyroscope is summarised in [18].

Recent advancements in MEMS technology have led to novel designs, such as the MEMS resistive sensing gyroscope [19], which offers miniaturisation but requires different fabrication techniques. They have introduced FOM, which considers resolution and area simultaneously to optimise the device structure. High-performance tuning fork gyroscopes have also been demonstrated for navigation-grade applications [20]. Several comprehensive reviews [21–23] provide further insights into the state-of-the-art MEMS gyroscope technology. While dual-mass gyroscopes offer potential performance advantages. They also introduce complexities in design, fabrication, and operation, leading to enhanced manufacturing costs and reliability issues. A single-mass gyroscope has been proposed to overcome the disadvantages of dual-mass gyros by offering straightforward, well-established fabrication techniques and making it ideal for many applications. To further enhance the performance of single-mass gyroscopes, techniques such as vacuum packaging and intelligent electronic circuitry can be employed to improve the quality factor.

To enable more comprehensive design optimisation, a new figure of merit (FOM) is proposed that considers multiple parameters simultaneously. A fundamental performance metric in the proposed approach maximizes signal-to-noise ratio and overall system performance by prioritising mechanical sensitivity. The design optimisation methodology considers critical parameters such as sensitivity, bandwidth, noise, and footprint, resulting in a design that offers a superior trade-off among these metrics. However, to ensure broader applicability and efficient

resource utilisation, the designer should maximise an integrated figure of merit, such as FOM, allowing the sensor to perform well across various applications. Incorporating a thick sense mass, enabled by advanced DRIE etching [24], further enhances the performance of the gyroscope. A comparative analysis with other designs or fabrication methods, as discussed and summarised in Table 3.3, shows that improvements can be achieved with the proposed design using a simple single-thick-sense mass. Our research efforts have provided valuable insights for optimising MEMS gyroscope design and offer a promising approach for future advancements in the field.

A comprehensive investigation into MEMS gyroscopes encompassing theoretical modelling and software simulations, with a fabrication process and a comparative analysis, is presented. A novel figure of merit (FOM) is introduced to evaluate the performance of the devices. The research also proposes a new empirical relationship between sensitivity and bandwidth. Additionally, it demonstrates the feasibility of fabricating thick mass structures using advanced

3.2 Gyroscope Structure and Operating Principle

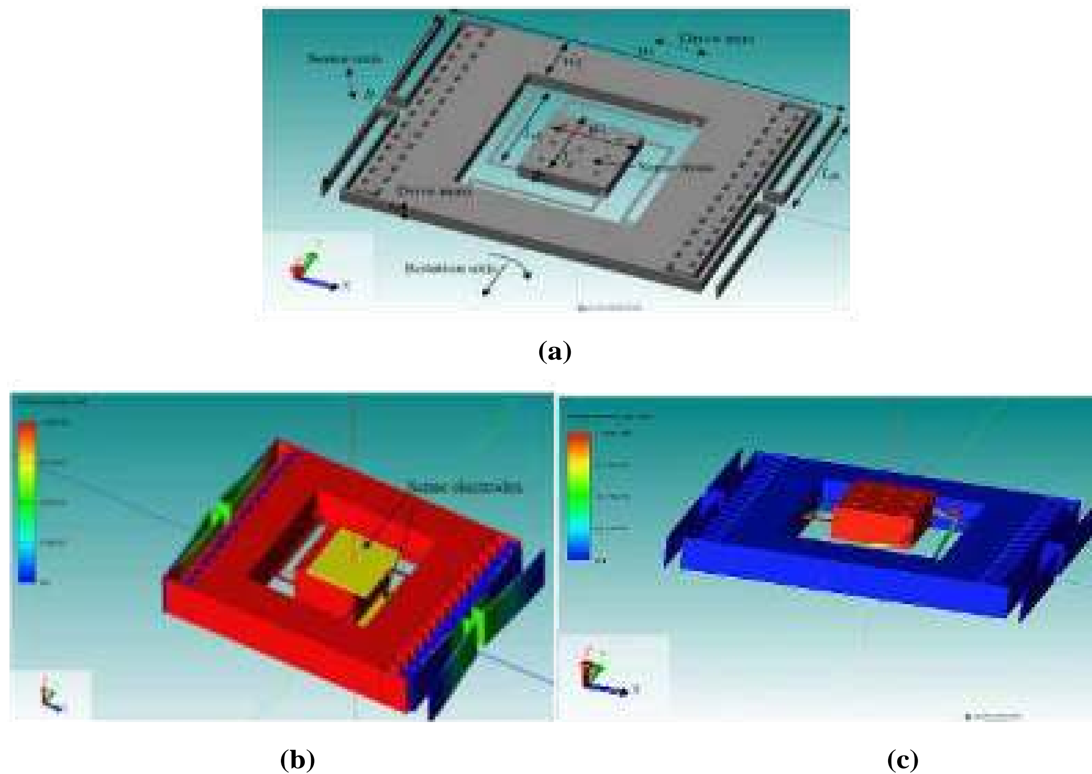

(a)

(b) (c)

Figure 3.1 (a) Three-dimensional view of the proposed gyroscope structure and parameter definition. (b) Drive-mode excitation along the X-direction. (c) Sense-mode excitation along the Z-axis.

In Chapter 2, the theoretical fundamentals governing MEMS vibratory gyroscope operation, such as the generation of Coriolis forces, drive–sense mode coupling, damping mechanisms, and noise sources, were comprehensively derived. This chapter showcases the translation of

those theoretical advances to a typical single-mass MEMS gyroscope design that may be used for design optimization and performance evaluation. The proposed gyroscope structure shown in Figure 3.1a comprises a drive mass with spring-suspended beams that couple to a thick sense mass, forming dynamically decoupled gyroscopic sense and drive modes. The drive mode is excited in the in-plane direction via electrostatic comb-drive actuation (figure 3.1b), while the sense responds to an externally applied angular rotation in the out-of-plane direction via the Coriolis effect (figure 3.1c). The resulting structural layout provides low cross-axis coupling, a reduced quadrature error, and increased bias stability.

The Coriolis-induced displacement of the sense mass is measured by a differential capacitive sensing scheme. The top and bottom electrodes enable the cancellation of common-mode disturbances, such as linear acceleration and parasitic vibrations, thereby improving measurement robustness. Designing the beams independently in the drive and sense directions further enhances mechanical isolation between the two modes. The gyroscope operates by exciting its drive mode at the resonant frequency and detecting the sense mode motion due to the Coriolis effect. The modelling framework described above serves as the foundation for the parametric optimization of mass ratio ($M_r=m_d/m_s$), stiffness ratio ($K_r=k_d/k_s$), and sense-mass thickness discussed in the subsequent sections.

3.3 Design Assumptions and Modelling Scope

The analytical and simulation studies in this chapter are carried out on the basis of a clear set of design assumptions, aligned with the theoretical framework established in Chapter 2.
The gyroscope is modelled as a single-mass system with separate drive and sense modes. The drive mode is assumed to operate at a constant amplitude using electrostatic actuation. The proof mass is treated as rigid, and the mass of suspension beams is neglected. Damping is mainly attributed to squeeze-film, slide-film, and thermoelastic effects. Non-ideal factors such as asymmetry or residual stress are not explicitly included but are handled through design choices like structural symmetry and frequency separation. This chapter focuses on optimizing the mechanical design to reduce noise at the device level, providing a clear basis for further performance analysis.

3.4 Design Parameters and Optimization Variables

A set of mutually dependent design and operation parameters decides the performance of a MEMS gyroscope. The effective mass and stiffness of the drive and sense modes are the key design parameters in this work. These are expressed as the mass ratio ($M_r=m_d/m_s$) and the stiffness ratio ($K_r=k_d/k_s$). The mass ratio influences Coriolis displacement. Its high values improve sensitivity but can affect bandwidth and stability. The stiffness ratio determines the resonant frequencies and strongly impacts frequency response, but is sensitive to fabrication variations. In addition, the thickness of the sense mass is considered an important design factor. Increasing thickness enhances inertial sensitivity and reduces thermomechanical noise, leading to better overall performance.

All this without increasing the overall device footprint. This method exploits advancements made in deep reactive ion etching (DRIE) technology. Also, the other factors related to the environment, packaging, and damping are considered in the optimisation. While these parameters are not considered as design variables directly, their impact on the quality-factor and bandwidth are analyzed to ensure robust performance during realistic operating conditions.

The perforated sense mass structure is optimally designed to operate in vacuum-packaged conditions and hence provides an order-of-magnitude reduction in air damping. This significantly reduces the device's quality factor. The resulting quality factors were achieved in simulated environments using a broad spectrum of ambient pressures and Rayleigh damping to model material losses (data presented in Table 3.1). Results show that vacuum packaging significantly improves quality. This study finds that 1 Torr operating pressure represents a reasonable balance between potential performance and usable form factor.

Table 3.1 The quality factor with pressure

Pressure (Torr)	Damping Coefficient ( )	Damping Coefficient ( )	Drive Quality Factor (Q_d)	Sense Quality Factor (Q_s)
100	-134485.3	3.21e-4	16638	2.5
10	-18948.58	4.535e-5	36401	17.8
1	-1494.043	3.5766e-6	141476	225
0.1	-114.048	2.72967e-7	1022708	2951

We are not trying to maximize an individual figure of merit, rather we are searching a balanced design which simultaneously provides sufficient sensitivity and bandwidth along with low noise. Thus, an integrated figure of merit (FOM) is used as the first estimation criterion. This figure of merit establishes a common language for evaluating trade-offs between conflicting design priorities and identifying optimal parameter configurations. The design variables chosen, along with their respective ranges, serve as the basis for parametric studies in later sections, where trends obtained from analytical expressions, simulations, and experimental considerations are correlated to select an optimum gyroscope configuration.

The MEMS gyroscope's performance is affected by mechanical noise from the structure and by electronic noise from the front-end and feedback circuitry. The system noise is primarily limited by thermomechanical noise of the sense structure, and Johnson and amplifier noise from the readout electronics [25-28]. Thermomechanical noise is equivalent to random molecular motion at finite temperature within the microstructure and serves as a fundamental limit on MEMS gyroscopes. The RMS value of the thermomechanical noise equivalent angular rate is ~6.4×10 dps, which is calculated using the optimized structural parameters listed in Table 3.2. Electronic noise mainly comes from the feedback resistor and amplifier circuit and can generally be measured as [29]:

$$= \overline{2\ (4 \quad + \quad)} \tag{3.1}$$

Where k_g is the amplifier gain, k_b is the Boltzmann constant, R_f is feedback resistance, and I input noise current. The Johnson noise is calculated to be 1.1×10^{-7} V, while the amplifier noise is 1.8×10^{-7} V. The total electronic noise, obtained by combining these noise sources in quadrature, is approximately 2.1×10^{-7} V, which is equivalent to 1.1×10^{-4} dps (calculated by dividing voltage with the overall sensitivity of the structure).

The combined effect of these noise sources can be estimated by combining their individual contributions in quadrature.

$$= \sqrt{\ ^2 + \ ^2} = \sqrt{(64\ 10\ )^2 + (1.1\ 10\ )^2} \tag{3.2}$$

Hence, the total noise is 6.5×10^{-4} dps. However, this paper's primary focus is optimizing the mechanical design of the gyroscope to minimize the dominant noise source, which is the thermomechanical noise. The subsequent sections will delve into the details of the design optimization.

Another important parameter is cross-sensitivity. Ideally, a gyroscope should only register rotation around its designated axis. For example, a gyroscope designed to measure rotation around the "y" axis should only respond to rotations around the y-axis. However, in reality, due to imperfections in manufacturing, design, or external factors, a rotation around the "x" or "z" axis might also generate a small, unwanted signal. This is cross-sensitivity. This error is problematic in applications requiring high precision. A common way to express cross-axis sensitivity is as a percentage, and is as follows:

Cross Sensitivity = (S_{zx} / S_{zy}) * 100% (3.3)

Where S_{zx} is the sensitivity of the sensor to rotation around its intended axis (e.g., the sensitivity of the z-axis sensor to x-axis rotation). S_{zy} is the sensor's sensitivity to rotation around an orthogonal axis. Manufacturing imperfections and environmental factors like temperature and stress can cause cross-sensitivity in MEMS gyroscopes, often mitigated by calibration. However, a key design approach to inherently reduce cross-axis sensitivity in single-drive MEMS gyroscopes is design optimization, primarily by creating highly symmetrical MEMS structures. Symmetry minimizes unwanted responses to rotations on other axes

Table 3.2 MEMS vibration gyroscope structure parameters

Structural parameters	**Value**
Drive and Sense Mass Thickness (t_d & t_s)	300 μm, 300 μm
Drive Mass Frame Width (w_f), Width (w_{db}), Length (w_{dl})	300 μm, 15 μm, 760 μm
Sense Mass Length (l_s) × Width (w_s)	500 μm × 500 μm
Sense beam width (w_{sb}), length (l_{sl}), thickness (t_{sb})	25 μm, 950 μm, 15 μm
Sense gap (d)	5 μm
Comb fingers length (l_{cm}), width (w_{cm}), gap (g_{cm})	100 μm, 50 μm, 2.5 μm
Drive and Sense frequency (f_d)	3253 Hz, 3291 Hz
Drive and Sense stiffness coefficient (k_d)	575.7 N/m, 2.1 N/m
Drive (m_d)and Sense Beam mass (m_s)	1.19×10^{-6} kg, 1.69×10^{-7} kg
Device area ($l_t \times w_t$)	2232 μm × 1610 μm

The cross-coupling sensitivity was evaluated by applying rotations along the x- and z- axes and measuring the resulting sense displacement. The sensitivity to x-axis rotation was found to be

2.53×10^{-13} m/(dps), while the sensitivity to z-axis rotation was 6.82×10^{-16} m/(dps). This translates to cross-coupling sensitivities of 0.002 % for x-axis rotation and 0.0007 % for z-axis rotation in the designed structure.

The resulting mechanical sensitivity is 8.68×10 m/(dps) and bandwidth of 38 HZ, total noise 6.5×10 dps, for the optimized structural parameters shown in Table 3.2. Perforations in sense mass can be introduced to reduce damping; its influence has been considered for the performance estimation. Sense capacitor geometries with gap distances on the order of 5 µm and areas of 500 µm × 500 µm are well within MEMS fabrication capabilities as demonstrated in [30–33], suggesting practical feasibility of the proposed design. Moreover, we have developed in the lab comparable capacitor configurations for micro accelerometers and they are already possible in practice [25,26].

Depending on the specific performance requirements and constraints of the MEMS gyroscope, as well as what resources and expertise are available, designers might choose one optimization method in the design process over another. It is known that (m_c/m_s) is an angular gain of the gyroscope, varying from 0 to 1 [27–29]. Here, it equals 1, but for other symmetric types (e.g., rings, disks, etc.) it is defined as the effective mass, as shown in [10,30–32]. The basic architecture provides a maximum angular rate that must be detected and drives the actuation voltage, which is often hardware dependent.

3.5 Drive and Sense Modal Frequency Analysis

In any MEMS device design, modal analysis is the first and most important simulation step. It highlights the dominant mode shapes of a structure and their corresponding resonant frequencies. The two main modes of interest for the gyroscope are the in-plane drive mode and out-of-plane sense mode. The modal frequencies are computed over a frequency range of 3220 Hz to 3320 Hz, encompassing both resonances.

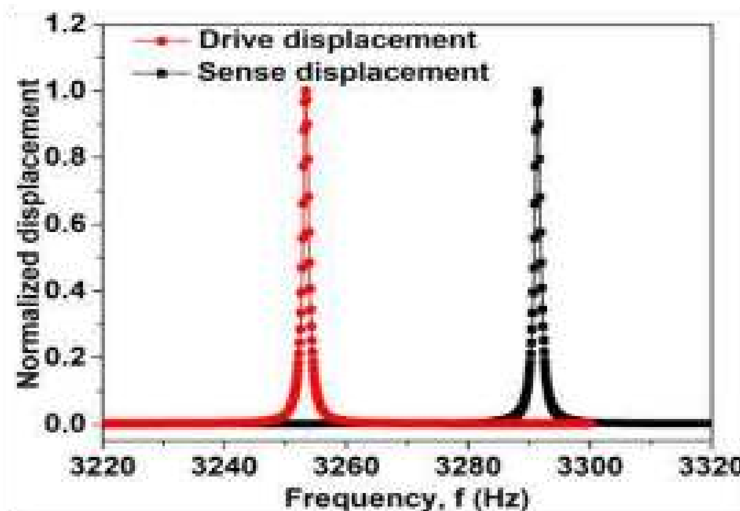

Figure 3.2 The drive and sense displacement at the drive and sense frequency.

The drive-mode resonance is represented by the peak at 3253 Hz, while the sense-mode resonance is shown by the peak at 3291 Hz, as illustrated in Figure 3.2. The sense and drive mode shapes are calculated in simulation, showcasing that the device is operating as intended;

one of the modes (drive) appears purely in-plane, while the other mode appears out-of-plane, which is consistent with how a gyroscope is designed to work. As the drive displacement increases, crosstalk increases due to coupling of flexural modes and quadrature error. The design is minimally coupled in mode and sufficiently strong for a 38 Hz separation to accurately track the state of systems with minimal error. The simulated mode shapes confirm that the device is operating as intended, with the drive mode in-plane and the sense mode out-of-plane. This alignment supports the expected working principle of the gyroscope.

For the case without angular rate, the isolation between the modes is approximately -33 dB in terms of the peak modal amplitude ratio. This degree of isolation indicates that the chosen frequency offset sufficiently suppresses unwanted coupling while preserving sufficient sensitivity. These analytically predicted resonant frequencies and modal behaviour are further validated through finite-element and system-level simulations, as described in the next section.

3.6 Parametric Analysis of Mass and Stiffness Ratios

3.6.1 Effect of Mass and Stiffness Ratios on Sensitivity

To optimize the design of the gyroscope structure, the mass ratio and stiffness ratio are separately varied while keeping the other fixed, and the output is plotted. These ratios vary the sense and drive resonant frequencies and are good guiding factors for determining the sense displacement. Figure 3.3a shows the sense displacement owing to the Coriolis force acting on the structure by varying M_r from 3 to 8 at different K_r values. The ratio of 3.8 for M_r and K_r is considered because it covers most of the design applications. The displacement is plotted on a logarithmic scale to observe the wide deflection range. Here, it is assumed that the structure vibrates in the driving direction with a constant amplitude, and the rotation rate in the plots is 400 °/s. At a stiffness ratio of 5, as the mass ratio varies, the central proof mass deflection rises sharply near an M_r of 5, and then drops rapidly. The same trend was noted at K_r values of 6.0, 6.5, 6.9, and 7.5. Initially, the sensor was designed to lower the drive resonant frequency than the sense resonant frequency. It is observed that at a particular K_r, as Mr increases, the difference between f_d and f_s decreases, increasing the sense deflection. The sense deflection peaks when M_r and K_r are equal or when f_d is equal to f_s. However, at a point in the curve, when K_r becomes higher than M_r, f_d becomes more than f_s, and the trend reverses.

In addition, it can be observed that increasing Mr and Kr does not significantly increase the sense displacement. This fact can be utilized for high-shock sensor applications that require high stiffness for driving and sensing. Furthermore, the sense displacement decreases as the gap between these two parameters or frequencies increases. This will help the designer to determine the structural parameters to optimize the sensitivity and frequency response. A similar behaviour is observed in Figure 3.3b, which shows the sense displacement variation with K_r at different M_r, except that the peak sense displacement is reduced from approximately 1×10^{-2} m to 8×10^{-3} m, which can marginally minimise sensitivity. The overall picture can be viewed simultaneously in a 3D plot that can be used as a reference.

Figure 3.3(c) shows a 3D plot of the log of the sense displacement as a function of the mass and stiffness ratios. Such a plot helps to visualize the combined effects of variations in M_r and K_r on the sensor performance parameters. The plot trend shows that the deflection peaks at approximately 4.3×10^{-3} m. The exact peak value may be slightly different (compared to Figures 3.3a and 3.3b) because of the lower resolution of the X-Y grid values used to clarify the plot. In addition, the sense displacement peaks to the maximum value when M_r is equal to K_r or f_d,

is equal to f_s. If there is a slight deviation from the equal values of M_r and K_r, the deflection amplitude decreases sharply.

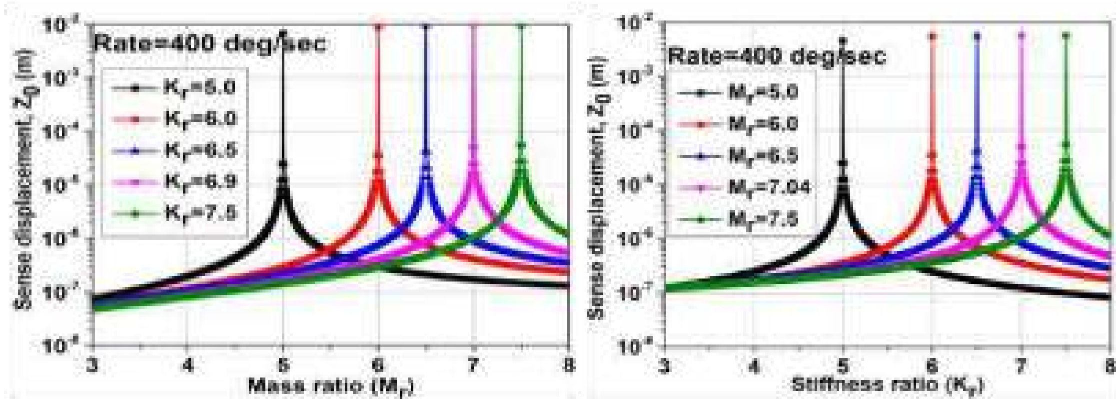

(a) **(b)**

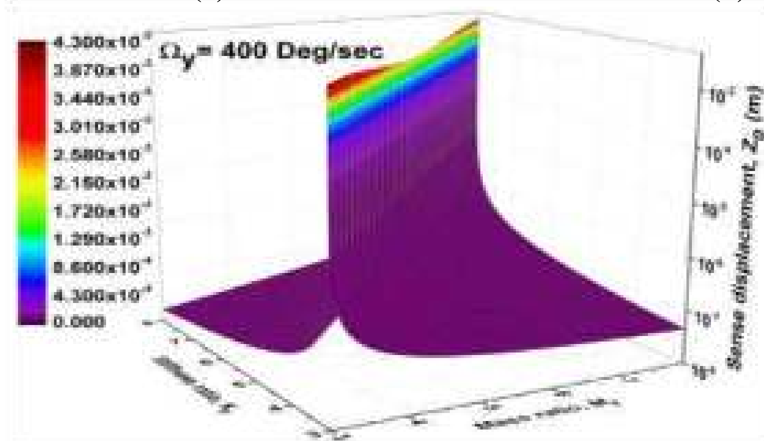

(c)

Figure 3.3 Sense displacement variation for the proposed design with (a) M_r at different K_r, (b) Kr at different Mr, and (c) 3-D plot showing the variation of sense displacement with Mass ratio (M_r) and Stiffness ratio (K_r).

The amplitude drop follows the hyperbolic equation y = P1* x/(P2 + x). For example, for the case of K_r=6.9, P1 is 5.18×10^{-8}, and P2 is -7, and for M_r=7.04, P1 is 1.2×10^{-7} and P2 is -7. As can be seen from the peak of the curve, a slight dip is observed in the middle, which is mainly due to the change in the trend of the frequency from $f_s > f_d$ to $f_d < f_s$ with changing K_r and M_r. This dip in the value at the top is negligible compared with the total variation in the peak-sense deflection. The rotation rate in the displayed curve is 400 °/s. If the rotation rate is increased further, the deflection will increase by the same amount. Further, a trade-off between sensitivity and BW is required to determine which portion of the curve one should choose for the Mr and Kr values. Therefore, the design should be optimized in the peak region but with a poor bandwidth to obtain the maximum sense deflection. In the tail region, the design has the advantage of good bandwidth and is insensitive to all tolerances, but the deflection will be less.

Therefore, a trade-off among the design parameters results in higher sensitivity, greater bandwidth, and lower noise. The design is determined by the type of application and the availability of the fabrication techniques used to realise the structure. As a general design rule, one should work at least one order of magnitude below the peak value to obtain optimal results. In our optimised design, M_r of 7.04 and a K_r of 6.9 are chosen to get an improved FOM, as will be discussed.

3.6.1.1 Sensitivity Dependence on Displacement

Mechanical sensitivity is a key performance metric for MEMS gyroscopes, as it directly determines the magnitude of the output response for a given angular rate input. To evaluate the dependence of sensitivity on structural parameters. Figure 3.4a shows z_o vs. $_y$ and the effect of variation of M_r at a fixed value K_r of 6.9 on the sense displacement of the structure.

These M_r values were obtained to easily visualise the deflection distinctly in the curve. The lowest deflection is at an M_r of 5.0, as this value is much lower than the K_r of 6.9; here, the gap between f_d and f_s is large, as discussed in the subsequent plots. Further, as the M_r value is increased to 6.0, 6.5 and 7.04 the sense deflection rises. The sensitivity, S, was estimated from the slopes of these plots. The mechanical sensitivities at M_r values of 5.0, 6.0, 6.5, 7.04 are 3.23×10^{-10} m/(dps), 9.81×10^{-10} m/(dps), 2.59×10^{-9} m/(dps), 8.68×10^{-9} m/(dps), respectively. However, at a M_r of 7.5, the deflection is less and the sensitivity is reduced to 4.90×10^{-9} m/(dps). This can be attributed to the reversal of the drive and sense frequency trends and an increase in the gap between f_d and f_s.

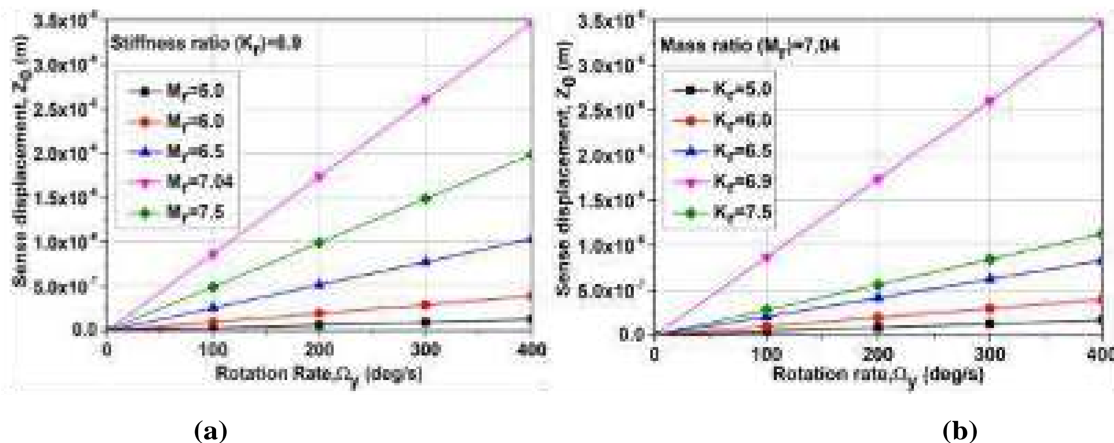

(a) **(b)**

Figure 3.4 Variation of Sense displacement as a function of Rotation rate $_y$ for different (a) M_r values for a fixed K_r =6.9. (b) K_r values for a fixed M_r =7.04.

A similar analysis is performed by varying the stiffness ratio while keeping the mass ratio fixed at 7.04, as shown in Figure 3.4b. The resulting sensitivity values are comparable, confirming that both mass and stiffness ratios influence sensitivity primarily through their effects on frequency separation. These observations reinforce the importance of careful parameter selection to maximise sensitivity while avoiding excessive frequency mismatch that degrades performance.

3.6.2 Effect of Mass and Stiffness Ratios on Bandwidth

In MEMS gyroscopes, bandwidth refers to the range of frequencies over which the sensor can accurately measure the angular velocity. Generally, gyroscopes with a higher bandwidth can measure the angular velocity over a broader range of frequencies, making them more reliable and accurate.

However, gyroscopes with higher bandwidths may also be more sensitive and more prone to noise and other sources of error, so choosing a gyroscope with an appropriate bandwidth for the intended application is essential. Figure 3.5(a) illustrates how the mass ratio (M_r) affects the sense displacement as the input rotation frequency is varied up to 1 kHz, while keeping the stiffness ratio (K_r) fixed at 6.9. The sense displacement is obtained using the bandwidth formulation from Chapter 2 and is normalized with respect to the zero-frequency response . This normalization makes it easier to compare how the frequency response changes for different values of (M_r). The corresponding 3 dB bandwidth values for M_r = 5.0, 6.0, 6.5, 7.04, and 7.5 are 311 Hz, 129 Hz, 54 Hz, 21 Hz, and 73 Hz, respectively. A similar behaviour is observed when stiffness ratio is varied while keeping mass ratio at 7.4, as shown in Figure 3.5(b). This highlights the coupled influence of mass and stiffness ratios on the bandwidth characteristics of the gyroscope.

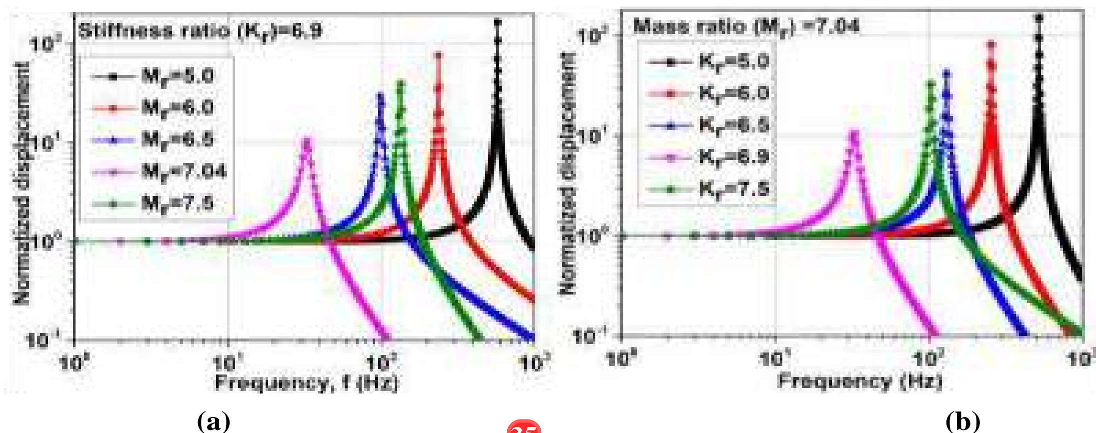

(a) **(b)**

Figure 3.5 Normalized displacement with the frequency of the input angular rate at different values of (a) M_r for a fixed K_r =7.04 (b) K_r for a fixed M_r =7.04.

In short, an increase in M_r will increase the maximum displacement, resulting in higher sensitivity, but at the cost of reduced bandwidth. This was reduced to a minimum at a matched K_r value. A further increase in M_r will increase the BW owing to a more significant mismatch between M_r and K_r or between f_d and f_s. A similar trend is observed in the frequency response for variation in the Kr value at a fixed Mr of 7.04.

3.6.2.1 Bandwidth Dependence on Damping

Packaging and encapsulation affect the structural response by varying the characteristics of the medium. This causes changes in the sense damping coefficient, the sense quality factor, and, hence, the structure's frequency response [28]. Therefore, to explore and optimize the design, the effect of the change in the damping coefficient on the bandwidth of the structure was shown by varying M_r at a fixed K_r of 6.9.

The pressure inside the package is varied to low values, and the damping coefficient C_s is calculated using equations to determine the normalized sense displacement and hence the bandwidth. The pressure inside the package was expected to be one torr. Figure 3.6 shows the variation in bandwidth with the damping coefficient. As seen in the earlier curve in figure 3.5 similar bandwidth trend is observed for different values of M_r. For each curve, the bandwidth continuously increases with an increase in C_s. The increase in the bandwidth is highest with the C_s value when M_r and K_r are apart owing to the larger f_d and f_s difference.

The additional advantage of optimising the structure for higher bandwidths by varying the packaging conditions widely inside the package. At higher values of C_s, the bandwidth saturates, owing to a reduction in the sense amplitude as the practical sense quality factor decreases. The design with M_r of 5.0, 6.0, 6.5, and 7.04 can achieve maximum bandwidths of 550 Hz, 228 Hz, 92 Hz, and 28 Hz, respectively, with increasing C_s. However, this trend is reversed at an M_r of 7.5 Hz and can reach a maximum of 119 Hz. It is worth noting in the figure above that BW shows a slower dependence on C_s than on M_r and K_r. C_s of 1.58×10^{-5} Ns/m at 1 Torr at an M_r of 7.04 and a K_r of 6.9, applied to the sealing and packaging environment expected by the device. Similar bandwidth variation with damping coefficient at different K_r and at a fixed M_r is observed.

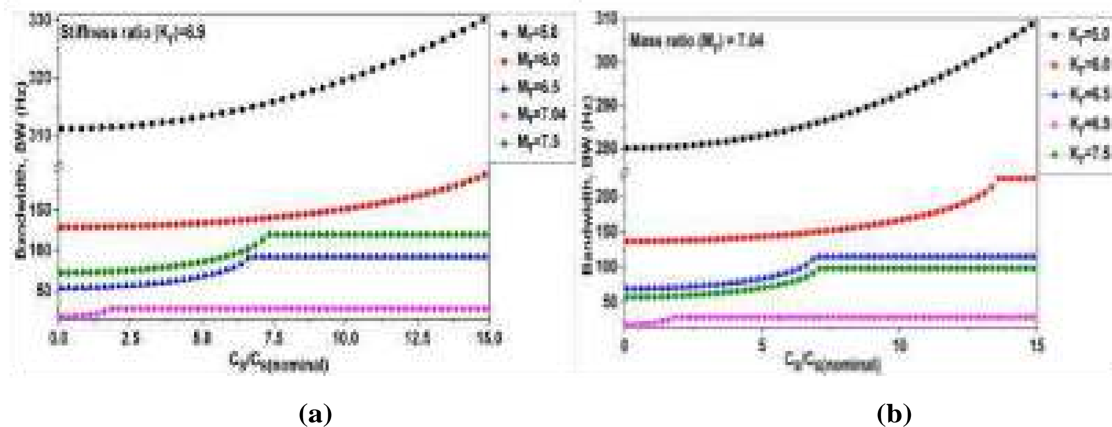

(a) **(b)**

Figure 3.6 Bandwidth variation with damping coefficient at different value of (a) M_r for a fixed K_r =7.04 (b) K_r for a fixed M_r =7.04.

3.6.3 Thermomechanical Noise Analysis

A key factor in determining a sensor's behaviour is its noise performance. A large number of research efforts have focused on reducing noise in MEMS-based sensors, either mechanically or electronically. As a device designer, reducing noise at the structural level is essential. Therefore, electronic noise-reduction techniques can be more efficient. With this aim, we propose a method to reduce noise at the structural level using a thick sense mass.

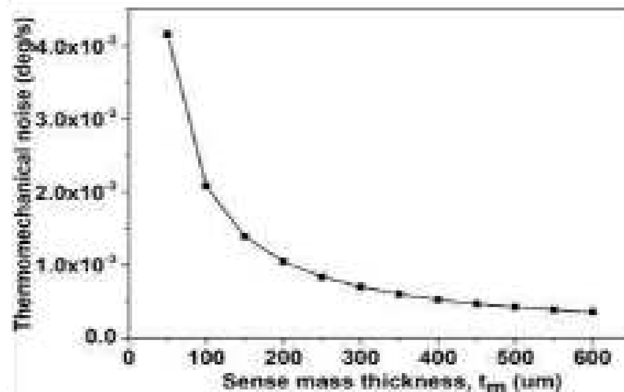

Figure 3.7 Variation of RMS Thermomechanical noise with sense mass thickness.

MEMS gyroscopes are susceptible to acoustic noise. However, this can be easily addressed using proper isolators between the device and the sensing structure[33]. In MEMS gyroscopes, the amplitude of the Coriolis force is minimal; therefore, it is essential to reduce the thermomechanical noise of the structure. As discussed in Chapter 2, the thermomechanical noise equivalent angular rate is inversely proportional to the effective sense mass. The sensing mass can be increased by increasing the proof mass area or thickness.

However, increasing the area increases the device footprint, which will not help us exploit the MEMS-based gyroscope's smaller size advantage. However, if we increase the thickness of the proof mass to reduce the noise, the device footprint will not be increased, but there may be an additional fabrication step, which will be achievable using DRIE [24,34]Working with a thicker sense mass with a reduced area is key to improving the FOM.

Figure 3.7 shows the effect of a change in mass thickness on thermomechanical noise, while keeping the device area fixed. It is observed that the RMS noise is reduced from 4.16×10^{-3} dps at a 50 μm thick wafer to 3.46×10^{-4} dps at a 600 μm thick wafer. For our proposed design, a 300μm wafer thickness (noise is 6.93×10^{-4} dps) was used. This thickness was chosen to be beyond this mass order, and the noise reduction was insignificant. However, this leads to an improved FOM, as will be shown subsequently. The noise did not change with changes in M_r or K_r. Therefore, the effect of changes in M_r and K_r was not considered here.

3.7 Design Validation Using Simulation

In the previous section, the structural parameters were optimized. In this section, using the optimised parameters, a structural model is developed in MEMS simulation software. Through simulation, the device's behaviour was explored under actual environmental conditions without the need for experimentation. Our study validated our analytical results using CoventoWare MEMS+ and Simulink. A process sequence is defined in the MEMS+ software process editor to determine the model.

The structure was visualised, as shown in Figure 3.1a. Then, the structure was further simulated using the appropriate mesher settings to obtain the results. On the other hand, to simulate a structure in Simulink, the model is defined using different components available in the model directory, as shown in Figure 3.8. The structure was then simulated to observe the drive and sense displacement in the desired directions.

3.7.1 Drive and Sense Displacement Validation

In our proposed design, the structure is set to vibrate along the x-axis by applying coupled DC and AC voltages to the comb drives, which is the first step in simulating the MEMS-based gyroscope. The DC voltage varied from 5 to 25 V, while the AC voltage was maintained at 4 V to obtain the maximum displacement along the x-axis. According to our design, the gap between the tip of the comb and the anchor of the fixed comb was 45 µm. According to the thumb rule, one-third of the maximum gap is allowed to work within a safe limit, so the maximum possible displacement is 15 µm. A DC voltage of 20 V was required to achieve this displacement.

Figure 3.8 compares the analytical drive displacements with the simulation. As shown in the curve, the peak deflection occurs nearly at 3253 Hz. The peak drive displacements obtained by MEMS+ and Simulink were within 2% of the analytical value. This validates our analytical calculation used for estimating the drive displacement.

After establishing the drive-mode response, the sense-mode behaviour is analysed by applying an angular rotation about the orthogonal (y) axis while maintaining the same drive excitation conditions. A constant angular rate of 1 rad/s is applied at the drive resonant frequency. Under these conditions, the combined translational and rotational motion generates a Coriolis force, resulting in out-of-plane (z-axis) deflection of the sense mass. Since the Coriolis force is inherently weak, the structure must be designed to maximize sense-mode displacement to achieve adequate sensitivity. Figure 3.9 compares the structure-sense displacement obtained analytically and through simulation. The peak sense displacement obtained at f_d of 3253 Hz by MEMS+, Simulink and analytical are 7.50×10^{-8} m/(dps), 7.34×10^{-8} m/(dps) and 7.15×10^{-8} m/(dps) respectively, and are within 5% of the analytical value. The trend of the output obtained is comparable.

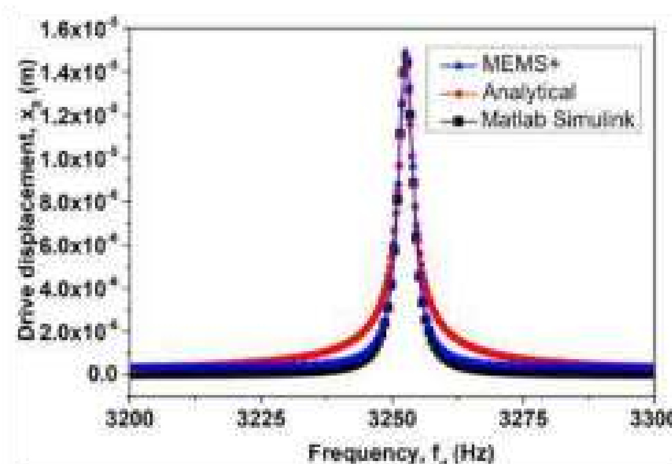

Figure 3.8 Comparison of peak drive displacement obtained analytically with MEMS+ and Simulink.

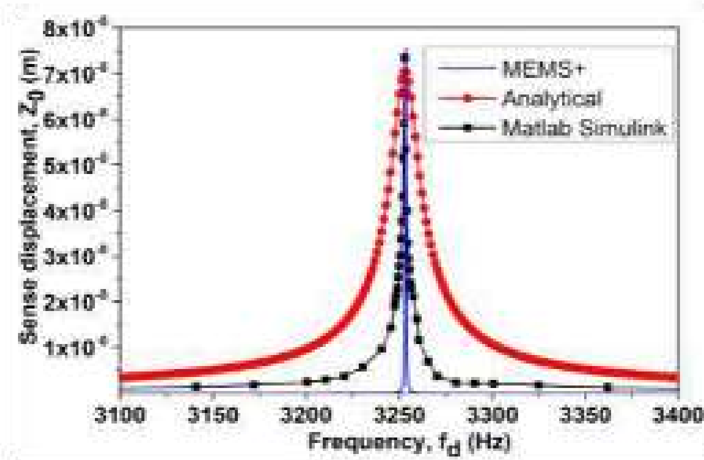

Figure 3.9 Comparison of sense displacement obtained analytically with MEMS+ and Simulink.

Further, we observe the structural behaviour when it oscillates continuously at this constant drive amplitude. Therefore, coupled DC and AC voltages were applied to the structure for longer durations. The same rotation rate of 1 rad/s was used to compare the results. Figure 3.10 shows the drive-displacement waveform obtained analytically and via simulation. A portion of the actual waveform obtained from MEMS+ is shown in the right corner of the graph. The same data from MEMS+ were imported into Origin for comparison. Almost the same amplitude and waveform trend were obtained from MEMS+ and Simulink, as well as analytically.

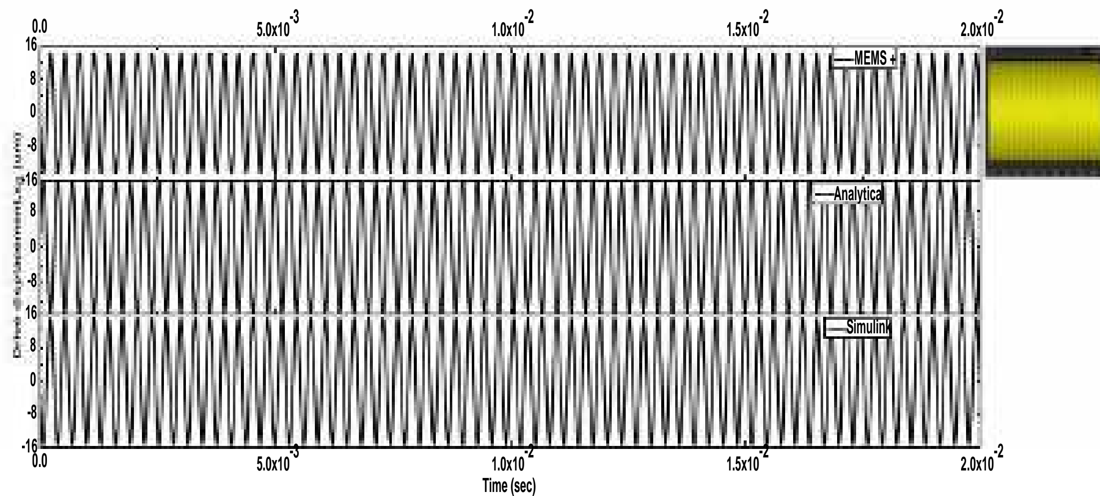

Figure 3.10 Drive waveform pattern using MEMS+, Analytical and Simulink simulations.

This page is extracted due to viral text or high resolution image or graph.

0.0 1.0x10
-2
2.0x10
-2
3.0x10
-2
4.0x10
-2
5.0x10
-2
-1.0
-0.5
0.0
0.5
1.0
-74
-37
0
37
-74
-37
0
37
-74
-37
0
37
74
0.0 1.0x10
-2
2.0x10
-2
3.0x10
-2
4.0x10
-2
5.0x10
-2

Time (sec)

Angular rate (rad/s)

Simulink

Sense displacement, z0 (nm)

Analytical

MEMS+

Figure 3.11 Sense waveform patterns using MEMS+, Analytical and Simulink simulations.

Similarly, Figure 3.11 shows the simulation results for the sense waveform from Simulink and MEMS+, compared with our analytical model, for a unity input rotation signal at 20 Hz. It should be noted here that our analytical model is calibrated using parameters and approaches, as discussed by [33]. The sense displacement is 6.6×10-9 m in Simulink compared to 6.8×10-9 m using our analytical model, and is in good agreement within 3% [33]. As shown in Figure 3.11, our analytical model agrees with Simulink within 3%-5% for MEMS+, validating the proposed design model.

3.7.2 Comparative Performance Evaluation with Literature

To further benchmark the proposed design, a comparative analysis is performed with a representative design from the literature [35], which reports one of the highest mechanical

sensitivities among comparable configurations. Figure 3.12 compares the sense displacement of [35] The design is similar to the proposed design, with an improved FOM. From the curve, it can be seen that the accurate maximum sense displacement at y of 400 °/s for our design is 3.47×10-6 m, which is much higher than the value considered [35]. Owing to the higher sense displacement, the mechanical sensitivity was improved by a factor of 2.5 under accurate formulations. This deflection is read electrically by measuring the change in capacitance between the fixed and moving sense masses.

Figure 3.13 compares the change in capacitance at different rotation rates for our design and the considered design [35]. If the sense gap is kept at 5 µm, the structure may collapse significantly before reaching the maximum deflection. Therefore, the design's working range is reduced. To solve this problem, the sense gap was increased to 11 µm, allowing the structure to operate at up to 400 °/s. The curve shows that the capacitance sensitivity of our proposed design is 0.38 fF/(dps), which is higher than the 0.14 fF/(dps) reported in [35] by a factor of 2.7.

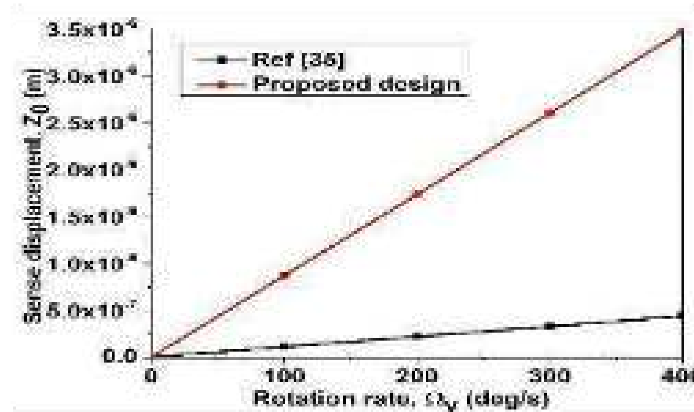

Figure 3.12 Sense displacement vs y for [30] and the proposed design.

Next, we compared the frequency response of our design vis-à-vis [35]. As explained earlier, the more significant the gap between the M_r and K_r values, the lower the sensitivity and the higher the bandwidth. While going deeper into the work, it was observed that the difference between the M_r and K_r ratios is higher than in our proposed work. This resulted in a reduction of 3 dB bandwidth to 18 Hz compared with the bandwidth of 25 Hz in [35]. However, our overall FOM is higher, as discussed in the next section. The effect of variation in the damping coefficient (Cs) on the bandwidth is considered. The tolerable range of damping coefficient variation is greater for our proposed design, and by changing the medium inside the package, the bandwidth can be increased, as explained earlier. It may be stated here that the effect of damping on BW follows the same trends, as shown in figure 3.6a and 3.6b.

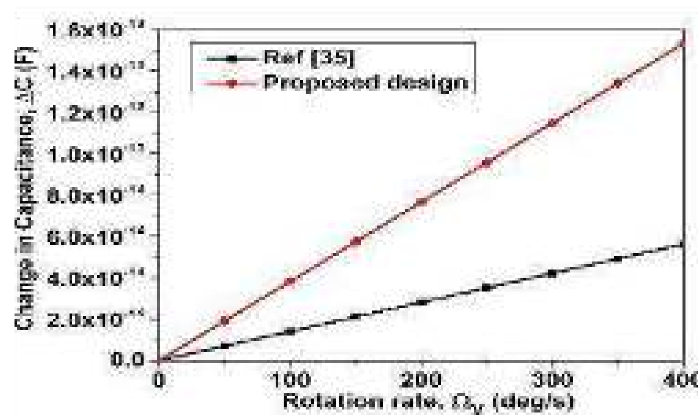

Figure 3.13 Change in capacitance vs y for [30] and proposed design.

Next, the thermomechanical noise equivalent angular velocities were compared. It is proposed to reduce structural noise by increasing the structural sense mass, which is a key feature of our design for achieving a higher FOM [35] . However, with a sense mass thickness of 58 µm, it was found that our proposed design featuring a 300 µm-thick mass achieves a low noise of 0.00064 °/s, which is much lower than the 0.0045 °/s achieved by the considered reference.

After validating and comparing our theoretical results with simulations in MEMS Plus and Simulink, we further validated our improved analytical model against data from the literature. We showed that our design has an improved FOM compared to most designs with configurations similar to ours.

3.7.3 Summary of Simulation Validation

The agreement between analytical predictions, numerical simulations, and comparative literature data confirms the robustness of the proposed design and modelling framework. Simulation results corroborate that high sensitivity was achieved with a controlled bandwidth and lower noise, as specified by the design parameters. These improvements altogether lead to a markedly improved figure of merit, which is explored further in the next section.

3.8 Figure of Merit–Based Performance Evaluation

As previously discussed, various designs have been proposed in the literature to enhance sensitivity, bandwidth, and noise performance. Gyroscope designers typically optimise performance parameters such as sensitivity, noise, and bandwidth for specific applications. However, maximising an integrated figure of merit (FOM) is crucial for broader applicability and resource efficiency, enabling a single sensor to perform well across diverse applications. For instance, MEMS gyroscopes from ST Microelectronics exemplify this versatility, serving in inertial navigation systems (INS) for orientation and movement tracking, image stabilisation in cameras and smartphones to counteract handshakes, and robotics for balance and environmental navigation.

It is important to note that increasing sensing inertia and pickoff area can improve sensitivity, but these are often constrained by device footprint and process limitations. Therefore, the proposed FOM focuses on reducing noise and enhancing sensitivity and considers the device's footprint. Thus, the improved Figure of Merit (FOM) is defined as follows:

$$\text{FOM} = \left[\frac{\quad}{\quad} \right] \tag{3.4}$$

The objective is to maximise the FOM or signal-to-noise ratio of a given design. While different applications may prioritise specific parameters, the proposed FOM provides a comprehensive metric for comparing designs on a common platform [19]. By optimising this FOM, the design can be tailored to various applications by adjusting the thick mass and drive frequency. This approach offers greater flexibility and versatility than designs focused on a single application.

Keeping this in mind, we propose maximising the final FOM's value. This optimisation strategy makes the design versatile and suitable for a wide range of applications beyond the specific target application. By comparing our design with other published designs, we demonstrate the superiority of our approach with respect to the proposed FOM. This comparative analysis highlights the advantages of our design in terms of sensitivity, bandwidth, noise performance and footprint.

3.8.1 Comparison of FOM with Reported Designs

Table 3.3 presents a comparative analysis of various MEMS gyroscope designs, focusing on key performance metrics and a newly proposed figure of merit (FOM). The details of the designs explored for comparing FOM with similar configurations are shown in table. Sensor sensitivity is reported as m/dps or F/dps, depending on the availability of data in the literature.

All the comparisons are presented in Table 3. Our proposed design has a higher FOM of 73 m Hz/dps^2 mm^2 in terms of mechanical sensitivity or 3.24×10^{-6} F Hz/ dps^2 mm^2 with capacitance sensitivity, compared to the majority of existing designs in the literature.

On comparing our proposed design and [35], it can be seen from Table 3.3 that our FOM for the proposed design is 73 m Hz/dps^2 mm^{2,} which is higher than [35] by a factor of 52. Here, it is essential to mention that this improvement is almost comparable for both designs considered for detailed study. Furthermore, [12] have marginally higher FOMs than our case regarding capacitance sensitivity. However, it may be recalled that improving the basic sensitivity parameter at the fundamental level is better by increasing the sense displacement.

Table 3.3 Comparison of FOM for our design vis-à-vis other designs from the literature.

		Sensitivity (S)		**Size (mm x mm)**	**Bandwidth (BW)**	**Noise (N)**	**FOM (S*BW/N*Size)**
	Ref no.	**m/(dps)**	**F/(dps)**		**Hz**	**dps**	
1	Ref. [12]	-	8.08×10^{-15}	5.1×5.1	100	0.0061	5.09×10^{-6}F Hz/ (dps)^2 mm^2 (@20V (V_{dc}) and 4V (V_{ac}))
2	Ref. [30]	1.06×10^{-9}	0.14×10^{-15}	2.3×1.6	25	0.0045	1.5 m Hz/(dps)^2 mm^2 or 1.91×10^{-7} F Hz/(dps)^2
3	Ref. [33]	-	0.47×10^{-18}	3×3	50	0.017	1.54×10^{-10} F Hz/ (dps)^2 mm^2
4	Ref. [34]	4.69×10^{-12}	-	1×1	25	0.0041	0.28 m Hz/(dps)^2 mm^2
5	Ref.[27]	1.74×10^{-11}	-	4.3×4.3	21.6	0.001	2.0×10^{-2} m Hz/(dps)^2 mm^2
6	Ref.[35]	4.02×10^{-10}	-	1.5×1.5	50	0.079	0.11m Hz/(dps)^2 mm^2
7	Ref. [36]	1.75×10^{-9}	-	1×1	5.8	0.00004	25m Hz/(dps)^2 mm^2
8	Ref. [37]	3.8×10^{-9}	-		2.2	0.0002	18m Hz/(dps)^2 mm^2
9	Ref. [38]	-	0.2×10^{-15}	6×6	50	0.1	2.78×10^{-9} F Hz/ (dps)^2 mm^2
10	Ref. [39]	1.40×10^{-10}	-	1.5×1.5	200	0.05	0.25m Hz/(dps)^2 mm^2
	Present work	**8.68×10^{-9}**	**0.38×10^{-15}**	**2.3×1.6**	**18**	**0.0006**	**73 m Hz/(dps)^2 mm^2 or 3.24×10^{-6} F Hz/ (dps)^2 mm^2**

A drive displacement of 30μm was obtained due to a higher drive voltage of 30 V (V_{dc}) and 4 V (V_{ac}) compared to our drive voltage of 20 V (Vdc) and 4 V (V_{ac}). If the drive displacement is estimated at 20 V (V_{dc}) and 4 V (V_{ac}), the capacitance change is 5.38x10^{-15} and consequently, the effective FOM will be 3.0×10^{-6} F Hz/ dps^{2,} which is lower than our proposed value. In summary, the table compares the proposed design (P) with several existing designs from the literature. The proposed single-mass design demonstrates a significantly higher FOM than the other designs, indicating superior performance. This improvement can be attributed to optimized design parameters, advanced fabrication techniques, and effective noise reduction strategies. In short, it is shown that using a simple, thick single-sense mass can achieve a better FOM than other complex approaches, as discussed in the literature, provided a proper design trade-off and optimisation are used.

3.8.2 Empirical Relationship Between Sensitivity and Bandwidth

While sensitivity and bandwidth are both critical performance metrics, no simple analytical relationship between them has been widely reported. Based on the parametric analysis conducted in this chapter, sensitivity and bandwidth are evaluated over a broad range of mass-to-stiffness ratios for a fixed angular rate of 400 dps. The results reveal an inverse relationship between sensitivity and bandwidth, which can be approximated by an empirical expression of the form:

$$= \frac{1}{\ } \tag{3.5}$$

Where K1=2×10^{-8} m/(dps)*Hz is a constant, S is in units of m/(dps), and BW is in hertz, is considered. This relation provides a useful guideline for designers to balance sensitivity and bandwidth during early-stage optimization. Experimental data reported in the literature are used to validate this relationship.

Figure 3.14 shows the data from the literature vis-à-vis the fitted data using Equation 3.5. The point P on the curve corresponds to the proposed design. It can be observed that most of the data from table fit reasonably well with the proposed relation. It can be clearly seen from the figure that the data follows with a different constant of proportionality whose value is estimated as 2×10^{-8} m/dps *Hz because the design utilizes a split frequency method. This implies that the constant K1 is related to the type of design used. Additionally, [31] has a much lower S than our design, possibly because of the low drive displacement on the order of nanometres. In short, our relationship was validated by experimental data and can be utilized directly for the values of our design space.

3.8.3 Effect of Sense-Mass Thickness and Temperature on FOM

Figure 3.15 shows the two plots that illustrate the relationship between the Figure of Merit (FOM)and the mass thickness of a MEMS device. FOM, considering capacitance sensitivity, has units of F Hz/ dps^2 mm^2, and considering sense displacement sensitivity, it has units of m Hz/ dps^2 mm^2. Both plots indicate that increasing the MEMS device's mass thickness can significantly improve its performance, as measured by the FOM. This is due to the increased sensitivity and reduced noise associated with a larger mass.

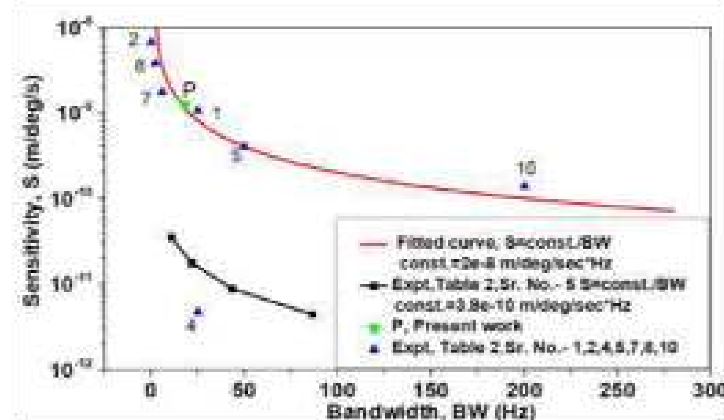

Figure 3.14 Comparison of the proposed analytical relation between S vs. BW vis-à-vis experimental result (Ref. Table 3.3)

Both figures show that FOM vs thickness curves have a low slope and high slope regions have low and high FOMs, suggesting that one should keep thickness consistently above the threshold value to get a high FOM. This threshold thickness, in our case, is above 30 µm. However, it's important to note that there might be limitations to this trend. Increasing the mass thickness too much can increase stress and potential mechanical instability[5–7],[28]. Additionally, fabrication challenges may arise with very thick structures. Therefore, the optimal mass thickness for a particular MEMS device would depend on a balance between performance and practical considerations.

Temperature indeed affects performance parameters. Earlier, we studied this, and the details are discussed in [40], which analyses the impact of temperature change and proposes a new compensation approach for temperature-induced changes at the structural design level. It was suggested that using an improved thermal design for the sense deflection results in a frequency mismatch of 0.18Hz over the entire temperature range and reduces the mechanical sensitivity variation from 232 ppm/K to 4 ppm/K. However, a noise study was not included there. Using a similar methodology, the effect of noise is studied here. Figure 3.16 shows the MEMS gyroscope's overall thermomechanical noise as a function of temperature for the present design and the improved thermal design, spanning -40 ^{0}C to 125 ^{0}C. For both designs, the noise increased almost linearly with temperature. As the temperature increased, thermal agitation became more intense, increasing noise and affecting overall performance stability across temperature changes. For the present design, the noise increases from 5.0×10^{-4} rad/s at -40 ^{0}C to 6.5×10^{-4} rad/s at 125 ^{0}C. But for an improved thermal design, the TM noise is approximately 1.0×10^{-5} rad/s over the entire temperature range. This trend shows that thermomechanical noise can be reduced over a broad temperature range with a suitable design adjustment. Hence structure can be used for applications in which thermal stability and minimal noise are crucial, such as precision navigation and inertial measurement systems.

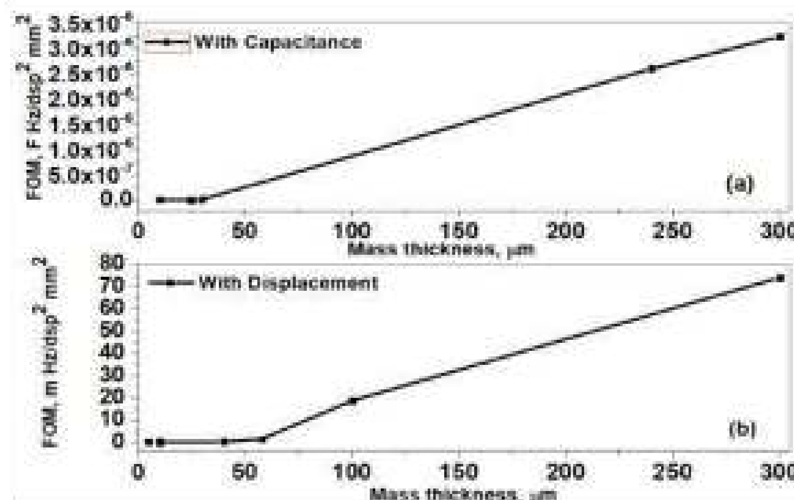

Figure 3.15 Variation of FOM considering (a) Capacitance (b) Sense displacement.

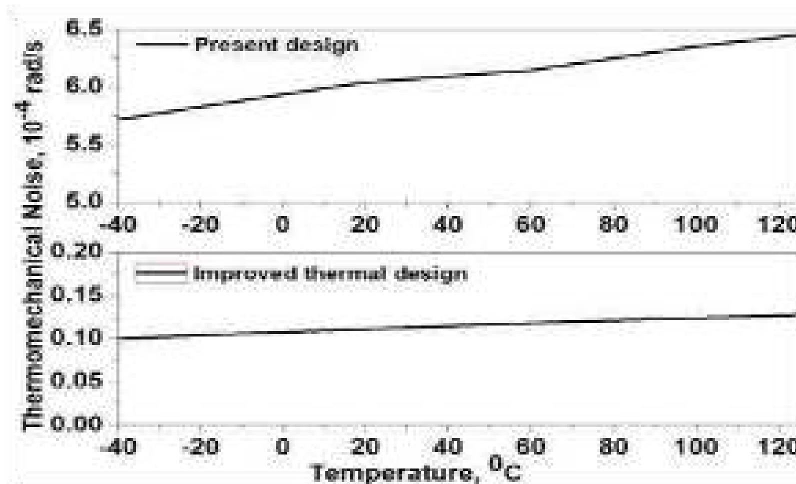

Figure 3.16 Plot of Thermomechanical Noise variation for the present design and improved thermal design at temperatures ranging from -40 ^{0}C to 125 ^{0}C.

3.9 Conclusion

This chapter presented the systematic design optimization and performance evaluation of a single-mass MEMS gyroscope aimed at achieving a high and balanced figure of merit (FOM). Building on the theoretical foundations established in Chapter 2, this chapter presents analytical insights into a practical design framework. It simultaneously enhances sensitivity, bandwidth, and noise performance while reducing footprint. A novel single-mass gyroscope design discussed here utilizes a thick mass structure, which significantly improves the thermomechanical noise and a higher figure of merit (FOM). The fabrication feasibility has been experimentally validated for thick mass using advanced DRIE etching techniques.

A comprehensive design optimisation was conducted across a range of mass and stiffness ratios. A new empirical relationship between sensitivity (S) and bandwidth (BW) was derived and validated through the literature. Simulations were verified with the analytical results. A broader comparison with various designs from the literature demonstrates a 52-fold increase in FOM. An empirical relation between sensitivity and bandwidth is also established. The effect of temperature on thermomechanical noise is simulated and presented. The fabrication process flow is described, and SEM images of the deep-etched structure are presented. This research provides valuable insights and design guidelines for future MEMS gyroscopes. The proposed design and analysis techniques can advance high-performance MEMS gyroscopes for a range of applications.

3.10 References

[1] Passaro V M N, Cuccovillo A, Vaiani L, De Carlo M and Campanella C E 2017 Gyroscope technology and applications: A review in the industrial perspective Sensors (Switzerland) 17

[2] Huang W, Yan X, Zhang S, Li Z, Hassan J N A, Chen D, Wen G, Chen K, Deng G and Huang Y 2023 MEMS and MOEMS gyroscopes: A review Photonic Sensors 13

[3] Xiao Y, Meng J, Yan H, Wang J, Xin K and Tao T 2023 Research on the application of MEMS gyroscope in inspecting the breakage of urban sewerage pipelines Water (Switzerland) 15

[4] Abhinav G A, A S D K H B and C V 2020 Improvements in the sensitivity of MEMS based gyroscope for military applications
[5] Zhang H, Zhang C, Chen J and Li A 2022 A review of symmetric silicon MEMS gyroscope mode-matching technologies Micromachines (Basel) 13
[6] Zhao W, Cheng Y, Zhao S, Hu X, Rong Y, Duan J and Chen J 2021 Navigation grade MEMS IMU for a satellite Micromachines (Basel) 12 1–12
[7] Karimzadehkhouei M, Ali B, Jedari Ghourichaei M and Alaca B E 2023 Silicon nanowires driving miniaturization of microelectromechanical systems physical sensors: A review Adv. Eng. Mater. 25
[8] IEEE Robotics and Automation Society 1999 MEMS '99: Twelfth IEEE International Conference on Micro Electro Mechanical Systems: Technical Digest: Orlando, Florida, USA
[9] Alper S E and Akin T 2005 A single-crystal silicon symmetrical and decoupled MEMS gyroscope on an insulating substrate Journal of Microelectromechanical Systems 14 707–717
[10] Zaman M F, Sharma A, Hao Z and Ayazi F 2008 A mode-matched silicon-yaw tuning-fork gyroscope with subdegree-per-hour Allan deviation bias instability Journal of Microelectromechanical Systems 17 1526–1536
[11] Challoner A D, Ge H H and Liu J Y 2014 Boeing disc resonator gyroscope
[12] Xu Q, Xiao D, Hou Z, Zhuo M, Li W, Xu X and Wu X 2019 A novel high-sensitivity butterfly gyroscope driven by horizontal driving force IEEE Sens. J. 19 2064–2071
[13] Bu F, Fan B, Xu D, Guo S and Zhao H 2021 Bandwidth and noise analysis of high-Q MEMS gyroscope under force rebalance closed-loop control Journal of Micromechanics and Microengineering 31
[14] Ni Y, Li H, Huang L, Ding X and Wang H 2014 On bandwidth characteristics of tuning fork micro-gyroscope with mechanically coupled sense mode Sensors (Switzerland) 14 13024–13045
[15] Patel C and McCluskey P 2012 Modeling and simulation of the MEMS vibratory gyroscope Inter Society Conference on Thermal and Thermomechanical Phenomena in Electronic Systems (ITHERM) 928–933
[16] Maenaka K, Fujita T, Konishi Y and Maeda M 1996 Analysis of a highly sensitive silicon gyroscope with cantilever beam as vibrating mass
[17] Tang T K, Gutierrez R C, Stell C B, Vorperian V, Arakaki G A, Rice J T, Li W J, Chakraborty I, Shcheglov K, Wilcox J Z and Kaiser W J Packaged silicon MEMS vibratory gyroscope for micro spacecraft
[18] Darvishian A 2018 Design and analysis of extremely low-noise MEMS gyroscopes for navigation
[19] Gadola M, Perna M S, Allieri M, Robert P, Verdot T, Berthelot A and Langfelder G 2021 600 µ(dps)/ Hz, 1.2 mm² MEMS pitch gyroscope INERTIAL 2021 IEEE International Symposium on Inertial Sensors and Systems
[20] Johnson B, Albrecht C, Braman T, Christ K, Duffy P, Endean D, Gnerlich M and Reinke J 2021 Development of a navigation-grade MEMS IMU INERTIAL 2021 IEEE International Symposium on Inertial Sensors and Systems
[21] Gill W A, Howard I, Mazhar I and McKee K 2022 A review of MEMS vibrating gyroscopes and their reliability issues in harsh environments Sensors 22 1–36
[22] Zhang H, Zhang C, Chen J and Li A 2022 A review of symmetric silicon MEMS gyroscope mode-matching technologies Micromachines (Basel) 13
[23] Ren X, Zhou X, Yu S, Wu X and Xiao D 2021 Frequency-modulated MEMS gyroscopes: A review IEEE Sens. J. 21 26426–26446

[24] Tang Y, Sandoughsaz A, Owen K J and Najafi K 2018 Ultra deep reactive ion etching of high aspect-ratio and thick silicon using a ramped-parameter process Journal of Microelectromechanical Systems 27 686–697

[25] Apostolyuk V 2016 Coriolis Vibratory Gyroscopes: Theory and Design Springer

[26] Bu F, Fan B, Xu D, Guo S and Zhao H 2021 Bandwidth and noise analysis of high-Q MEMS gyroscope under force rebalance closed-loop control Journal of Micromechanics and Microengineering 31

[27] Acar C and Shkel A M 2009 MEMS Vibration Gyroscopes: Structural Approach to Improve Robustness Springer

[28] Bao M-H 2000 Handbook of Sensors and Actuators 8 Micro Mechanical Transducers Pressure Sensors, Accelerometers and Gyroscopes

[29] Waters R, Tally C, Dick B, Jazo H, Fralick M, Kerber M and Wang A 2010 Design and analysis of a novel electro-optical MEMS gyroscope for navigation applications

[30] Alper S E, Azgin K and Akin T 2007 A high-performance silicon-on-insulator MEMS gyroscope operating at atmospheric pressure Sens. Actuators A Phys. 135 34–42

[31] Khan N A 2020 Developing highly symmetric microelectromechanical systems (MEMS) based butterfly gyroscopes

[32] Bhan R K, Pal R, Dutta S and Yadav I 2016 Development of unified fabrication process and testing of MEMS based comb and crab type capacitive accelerometers for navigational applications

[33] Gupta N, Dutta S, Parmar Y, Gond V, Vanjari S R K and Gupta S 2021 Characterization of SOI MEMS capacitive accelerometer under varying acceleration shock pulse durations Microsystem Technologies 27 4319–4327

[34] Xie J, Shen Q, Hao Y, Chang H and Yuan W 2015 Design, fabrication and characterization of a low-noise Z-axis micromachined gyroscope Microsystem Technologies 21 625–630

[35] Menon P K, Nayak J and Pratap R 2018 Sensitivity analysis of an in-plane MEMS vibratory gyroscope Microsystem Technologies 24 2199–2213

[36] Xiong X and Dong H 2009 Design and analysis of a MEMS vibratory comb gyroscope

[37] Ayazi F and Najafi K 2001 A HARPSS polysilicon vibrating ring gyroscope

[38] Castro S, Dean R, Roth G, Flowers G T and Grantham B 2007 Influence of acoustic noise on the dynamic performance of MEMS gyroscopes

[39] Marty F, Rousseau L, Saadany B, Mercier B, Français O, Mita Y and Bourouina T 2005 Advanced etching of silicon based on deep reactive ion etching for silicon high aspect ratio microstructures and three-dimensional micro- and nanostructures Microelectronics J. 36 673–677

[40] Shaveta, Bhan R K and Chaujar R 2024 Tapered-based novel thermal compensation techniques for enhanced performance of MEMS-based gyroscope 2nd International Conference on Emerging Trends in Information Technology and Engineering (IC-ETITE 2024)

CHAPTER 4

MINIATURIZED MEMS GYROSCOPES WITH THICK VERTICAL SENSE MASS STRUCTURES FOR ENHANCED PERFORMANCE

- *This chapter proposes a novel Vertical Sense Mass (VSM) MEMS gyroscope architecture to address the limitations of conventional planar designs in achieving miniaturization while maintaining high performance.*
- *The VSM design takes advantage of deep reactive ion etching (DRIE) that allows wafer thickness to be exploited, producing a 30% reduction in sense mass area and a overall sensor footprint reduction by 36%.*
- *Analytic models and comparative analysis show that the VSM configuration maintains sensitivity while providing higher bandwidth with lower thermomechanical noise over planar configurations.*
- *An improved performance metric (PM) incorporating sensitivity, bandwidth, noise, and footprint shows that the VSM design achieves 1090 mHz/dps²·µm², which is 15.4 times higher than the planar design.*
- *The fabrication feasibility of the proposed architecture is validated through successful DRIE-based realization of thick proof-mass structures, highlighting the VSM design's suitability for compact, high-performance inertial sensing applications.*

4.1 Introduction

Bohenberger's gyroscopic machine, considered the first gyroscope, finds extensive application in various fields such as platform stabilisation, drone flight control, robotics, airbag rollover detection, smart ammunitions, satellite inertial measurement units (IMUs), and sewerage network monitoring [1–8]. MEMS gyroscopes have significantly impacted inertial sensing due to their miniaturization, cost-effectiveness, and compatibility with integrated circuit technologies [9–15]. Conventional planar MEMS gyroscopes occupy a significant footprint. This motivates research into alternative designs that reduce size while maintaining or improving performance. One such approach is the utilization of nanosensing components [16–18], but they are prone to reliability issues due to stress [19-21]. An alternative approach utilizes the silicon wafer depth for capacitive sensing. While SOI technology enables simple etching, device thickness is currently limited to <200 µm [22–24]. As a result, achieving a larger or similar capacitive plate area in SOI compared to planar Si structures is nearly impossible, making the SOI wafer approach unsuitable for fabricating deep structures [24–28].

Deep silicon etching has become possible owing to recent advancements in deep reactive ion etching (DRIE) technology. Various authors have exploited this deep etching method[29–34]. The Refs. [35,36] reported the use of a deep reactive-ion etching system to etch to a depth of 600 µm by using a modified Bosch process. For even larger etch depths, Refs. [37] reported the use of double DRIE to etch up to 1.4 mm of depth. Additionally, 3D IC technology, which is currently an active topic of research, enables the reduction of the footprint of readout electronics by exploiting the depth of the wafer[38–41]. Therefore, the reduced footprint of both the device and readout IC results in an overall size reduction of the packaged device if the full depth of the Si wafer is exploited. Furthermore, these types of compact devices are required for applications such as mobile devices, the Internet of Things (IoT), and extended reality [3,14].

This study introduces a novel Vertical Sense Mass (VSM) MEMS gyroscope design. Unlike traditional planar sense mass (PSM) designs, the VSM utilizes deep reactive ion etching (DRIE) to create a deep, compact sense mass. The comparative analysis demonstrates the superior performance of the VSM design over planar configurations in terms of scale factor sensitivity, bandwidth, noise, and overall device footprint. The design details, theoretical equations, design trade-offs, comparative study and finally, experimental validation are studied in subsequent sections.

4.2 Design Methodology of Vertical Sense Mass Gyroscope

Figure 4.1a-c illustrates the proposed Vertical Sense Mass (VSM) and conventional Planar Sense Mass (PSM) gyroscope designs. The VSM utilizes a deep DRIE-etched structure with the sense mass oriented perpendicularly to the substrate, enabling a more compact design. In the VSM, rotation induces in-plane sense motion, while in the PSM, it induces out-of-plane motion. Both designs measure rotation by sensing the change in gap between moving and fixed structures. Figure 4.1d compares the footprints of the VSM and PSM designs, demonstrating the significant size reduction achieved by the VSM. The proposed VSM design aims to enhance performance metrics such as sensitivity, bandwidth, and noise while minimizing footprint. Theoretical analysis, including mathematical modeling and simulation, will be used to evaluate the performance advantages of the VSM design.

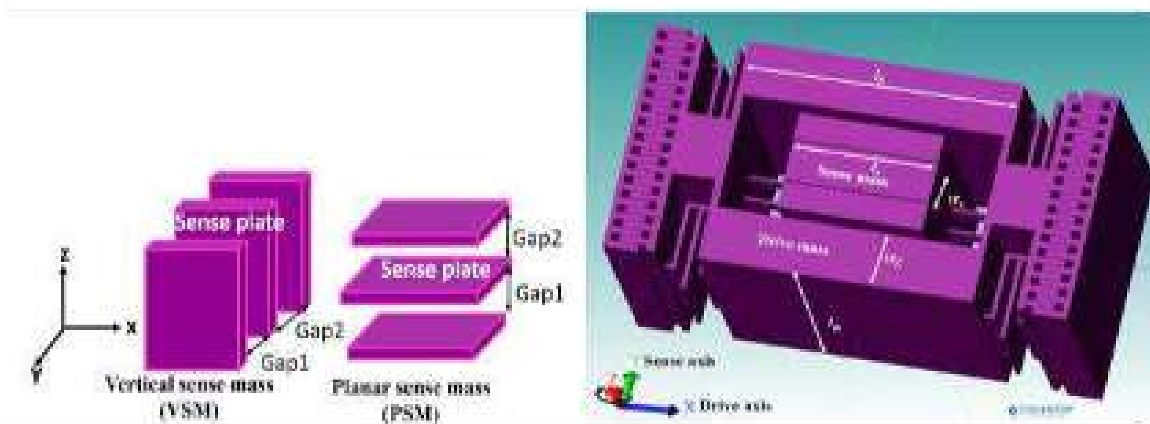

Figure 4.1(a) The schematic of Vertical sense mass (VSM) and Planar sense mass

Figure 4.1(b) Vertical Sense Mass (VSM) design utilizing depth of 500 µm for sense

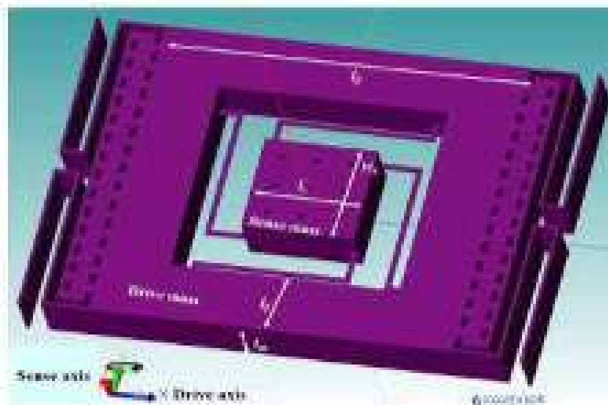

Figure 4.1(c) Planar Sense Mass (PSM) design that uses a shallow depth of 300 µm for sense mass structure.

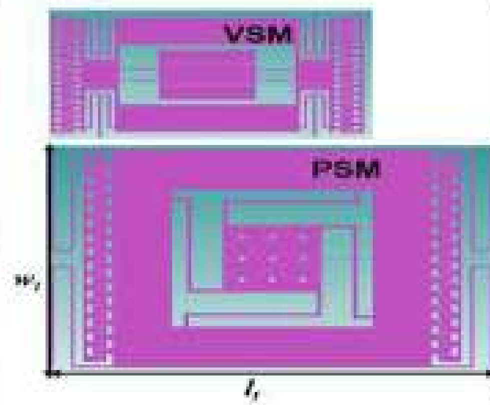

Figure 4.1(d) Vertical Sense Mass (VSM) and Planar Sense Mass (PSM) design structures on the same scale for footprint

4.3 Analytical Performance Evaluation

An analytical performance comparison of the proposed Vertical Sense Mass (VSM) versus conventional Planar Sense Mass (PSM) gyroscope designs is presented. Which is based on four key parameters: sensitivity, bandwidth, thermomechanical noise and device footprint. In order to provide an equitable comparison between the two architectures this analysis also considers a constant input angular rate and fixed drive-mode oscillation amplitude. The mass of the sense springs and damping effects are considered negligible in the analytical formulation, without loss of generality consistent with the assumptions used in previous analytical framework(s).

Although the in-plane sense-mode motion of the VSM and out-of-plane sense-mode operation of PSM have different behaviours with respect to how they displace due to, for example, Coriolis force, motion analysis is performed for both types within a common coordinate system to ease calculation comparison. It facilitates the comparison of the performance metrics of both designs under the same working condition. Advanced microfabrication techniques support the

feasibility for implementing VSM structures, and the analytical results show dramatically better performance metrics with a considerably smaller footprint than with PSM configuration. Here, the MEMS vibratory gyroscope is modelled as a single-degree-of-freedom resonator in drive-mode operation where the drive mass is driven to steady-state oscillation via electrostatic actuation. We mentioned above that the drive displacement amplitude is controlled by the applied electrostatic force, the drive resonance frequency, and quality factor [3,41,42]. In the current comparative study, we use the same value for drive displacement amplitude for both VSM and PSM designs (the only variable translated into performance differences being that of the sense-mode architecture).

When an angular rate is applied, Coriolis force causes the sense mass to move in one of the respective sensing directions based on each architecture [3,41,43].The resulting sense displacement is dependent on the effective sense mass, spring stiffness, damping and frequency separation between drive and sense modes as discussed above in the analytical model.From the sense mode frequency response, the operational bandwidth is defined as the frequency range over which the sensor response is within 3dB of its peak [44,45]. The conventional noise-equivalent angular rate expression derived in the previous section of this thesis has been used for evaluating thermomechanical noise performance. It is demonstrated that the system noise floor depends on the effective mass taking part in generation of Coriolis force, damping, working temperature and bandwidth. The subsequent development of Vertical Sense Mass designs (VSM architecture), by virtue of its vertical structural implementation, can effectively exploit increased sense mass and stiffness offering both a lower thermomechanical noise floor than the planar design but also enhanced bandwidth capabilities [45,46]. In conclusion, the analytical evaluation establishes that the performance sensitivity aspects of the suggested VSM configuration are consistent with the conclusions from prior optimum study while accomplishing increased bandwidth, lower noise and significantly reduced form factor compared to a conventional PSM gyroscope.

4.4 Optimization of Sense Mass Spring Parameters

The optimization of sense mass spring parameters plays a critical role in determining the dynamic performance of both Vertical Sense Mass (VSM) and Planar Sense Mass (PSM) MEMS gyroscopes. The VSM design employs flexure springs to ensure linear, predictable response and appropriate resonant frequencies. To suppress undesired twisting modes, the sense mass is suspended by four beams on either side, optimized for the desired in-plane vibration mode. The spring constant for the straight beam of the VSM is given by [47,48].

$$K_{s(vsm)} = \frac{4Ew_{bs}t_{bs}^{3}}{l_{bs}^{3}} \tag{4.1}$$

is the sense spring width? is the sense spring thickness, is the sense spring length, and E is the Young's modulus of silicon. Hence, the effects of spring thickness and length are studied in detail for a proper trade-off and optimization.

4.4.1 Effect of l_{bs} and t_{bs} on sense ( )

The 3D shape of the sense springs has a direct impact on the twist properties of the VSM structure. The side view of the VSM springs attached to sense mass is presented in Figure 4.2a, and Table 4.1 details how spring dimensions (length, width, thickness) influence important measuring parameter twisting angle. Increasing spring length or thickness increases twisting, while increasing width reduces it.

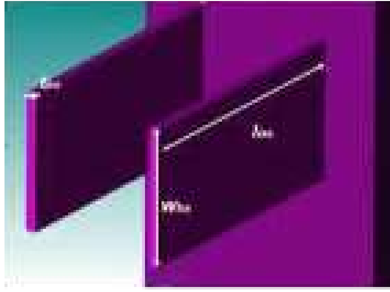

Figure 4.2 (a) Side view of VSM springs attached to sense mass.

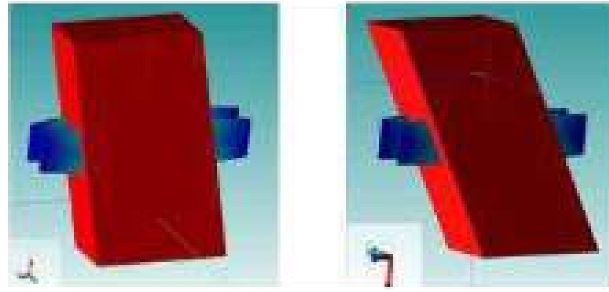

(i) t_{bs}=8 µm (ii) t_{bs}=10 µm

Figure 4.2 (b) Modal analysis of sense mass for VSM design for two cases, (i) Low twisting and (ii) High twisting.

These trends are confirmed by modal analysis (Figure 4.2b). Based on the analysis of spring parameters we obtained the following optimal dimensions for the spring: tbs = 8 µm, lbs = 150 µm, wbs = 75µm; this has resulted in a minimal twisting angle of only 0.05°. This design approach balances between not supporting the unwanted twisting modes and providing in-plane vibration for the VSM, therefore ensuring a stout performance without sacrificing reliability.

Table 4.1. Effect of Sense mass spring length and thickness on sense mode frequency and twisting angle of VSM and PSM

Spring length l_{bs} (µm), spring width w_{bs} (µm)	Spring thickness t_{bs} (µm)	Sense mode1- Frequency f_s of VSM	Sense mode2- Frequency f_s of VSM	Twisting angle of VSM structure (deg)
150 µm, 35 µm	8	32243.5	39202.7	0.86
	10	45052.3	44721.4	2.94
200 µm, 35 µm	8	20937.0	26302.9	2.43
	10	30397.6	29252.2	3.27
150 µm, 50 µm	8	38524.6	65541.0	0.72
	10	53823.7	74141.6	1.35
150 µm, 75 µm	8	47154.8	118875.8	0.05
	10	65871.3	133684.6	0.08

4.4.2 Effect of l_{bs} and t_{bs} on sense resonant frequency f_s

Spring dimensions like stiffness and effective sense mass significantly influence the VSM's resonant frequency (fs). The sense frequency is given by:

$$_s = \sqrt{k_{s(vsm)} / m_{s(vsm)}} \quad (4.2)$$

where k_s is the effective sense-mode spring constant, and m_s is the sense mass, which depends on the sense mass dimensions and material density. Variations in spring length, l_{bs} and thickness, t_{bs} directly affect k_s, thereby altering the gyroscope's sense-mode frequency and bandwidth.

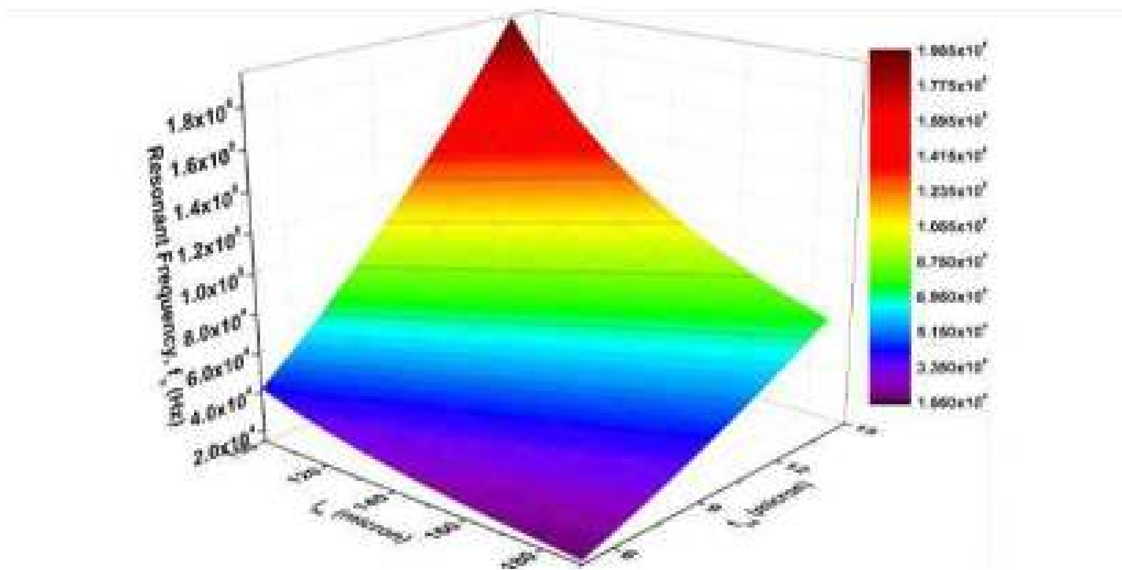

Figure 4.3 3-D plot showing the variation of sense mass natural frequency with spring length (l_{bs})and thickness (t_{bs})

Figure 4.3 illustrates the variation of sense frequency with spring length and thickness. The spring dimensions were optimized to achieve the desired resonant frequency and bandwidth for target applications. The VSM design utilizes a flexure-type spring, while the PSM employs a modified crab-shaped spring, as discussed in Refs.[22,24,28]. Both designs were optimized to minimize unwanted vibration modes. The VSM design significantly reduces the sense mass footprint, achieving a 30% reduction in area compared to the PSM. This translates to a 36% reduction in overall sensor footprint.

Modal analysis results, shown in Figures 4.4a-d, confirm the desired in-plane drive mode and out-of-plane sense mode vibrations for the VSM and PSM designs, respectively. The VSM design, with its reduced footprint and optimized spring design, demonstrates the potential for significant size reduction and improved performance in MEMS gyroscope technology.

4.5 Comparison of VSM and PSM Design Performance Parameters

A systematic comparison of the Vertical Sense Mass (VSM) design with its Planar Sense Mass (PSM) counterpart is conducted, based on performance metrics including sensitivity, bandwidth, and thermomechanical noise. All comparisons are made in the same operating environment for a meaningful evaluation. Simulations are done using CoventorWare 10, and the drive-displacement amplitude is kept constant for both designs.

4.5.1 Sensitivity

The sensitivity of any structure depends on the sense of displacement in response to the produced Coriolis acceleration upon the application of rotation. Figure 4.5a shows the simulated drive displacements (x_0) at resonant frequencies of 47098 Hz and 3253 Hz for the VSM and PSM designs, respectively. Coupled DC and AC were applied along the x-axis to obtain a maximum x_0 of 15μm for both the designs.

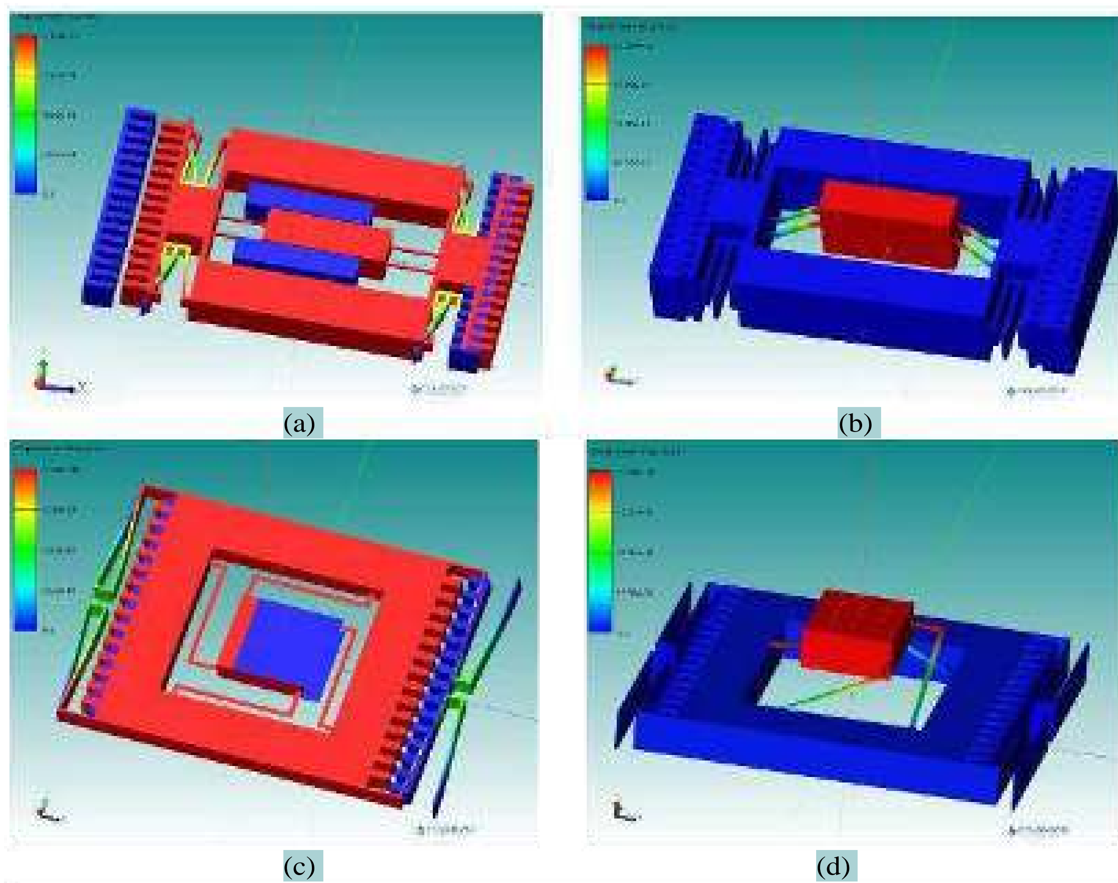

Figure 4.4 Modal analysis results: (a) Drive mode in VSM design, (b) Sense mode in VSM design, (c) Drive mode in PSM design, (d) Sense mode in PSM design.

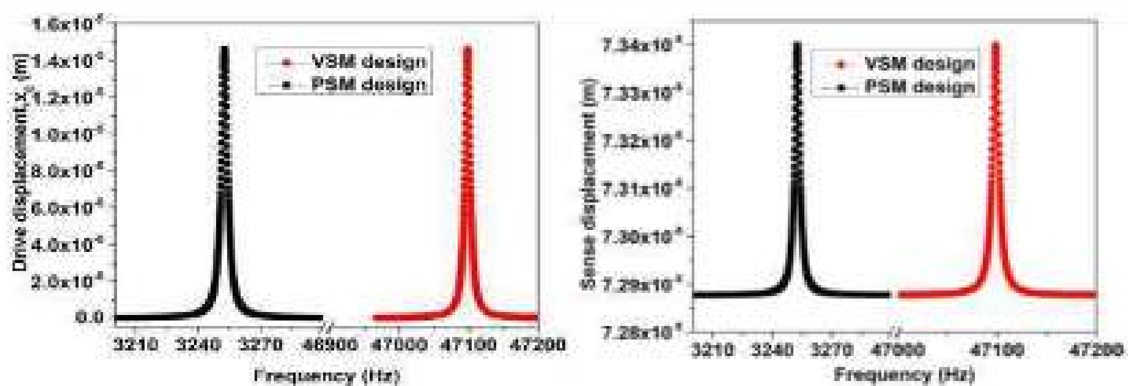

Figure 4.5 (a) Drive displacement as a function of frequency showing peak at the resonant frequency f_d

Figure 4.5 (b) Sense displacement as a function of frequency showing peak at the resonant frequency f_s

After obtaining the peak drive displacement, the structure was subjected to an angular rotation of 1 rad/s along the z-axis for the VSM design and y-axis for the PSM design (Figures 4.1b and4.1c). Owing to the Coriolis effect, the structure deflects along the y-axis in the VSM design and along the z-axis in the PSM design. Figure 4.5b shows the simulated sense deflections for the VSM and PSM design. The peak deflections in the desired axis at 1 rad/s for the VSM and PSM designs are almost identical at 7.34×10^{-8} m and 7.30×10^{-8} m respectively. The peak twisting amplitude and angle for VSM design is 3.21×10^{-18} m and 6.80×10^{-13} deg respectively, which is negligible with respect to the dominating bending mode of vibration of sense mass. Because the results show similar values of sense displacement for the VSM and PSM designs, the performance of the VSM design will be enhanced by utilizing the wafer thickness to reduce the footprint of the device. Furthermore, because the noise has a stronger dependence on $_d$, by shifting f_d to a higher value for the VSM design (compared to PSM) while keeping the same as that of the PSM design, the noise can be reduced in the VSM design and improve the overall PM.

As sense displacement depends on mass ratio $M_r = m_d / m_s$ and spring constant ratio. Optimizing M_r and K_r is crucial for achieving desired resonant frequencies (f_d and f_s) and bandwidth. Drive displacement is kept constant for fair comparison. The VSM and PSM designs are compared at different values of M_r and K_r to assess their impact on performance parameters.

Figure 4.6a illustrates the variation of sense displacement with mass ratio (M_r) at a fixed spring constant ratio (K_r). Here, it is assumed that the structures in both designs vibrate with a constant drive displacement amplitude and rotation rate of 400 °/s. Sense displacement peaks when K_r and M_r are equal, regardless of the design. The VSM design exhibits a maximum sense displacement of 1.15×10^{-2} m at $K_r = 6.9$, while the PSM design achieves a similar value of 1.12×10^{-2} m at $K_r = 7.80$. To comprehensively analyse the influence of both Mr and Kr, a 3D plot depicting sense displacement variation with respect to both parameters is presented in Figure 4.6b. The peak displacement was 1.28×10^{-2} m and 1.18×10^{-2} m for the VSM and PSM designs, respectively. The plot trends for PSM design were similar. For the proposed VSM design, M_r was 7.82, and K_r was 7.80, and for the PSM design M_r was 7.04 and K_r was 6.9 to get the same drive and sense resonant frequencies.

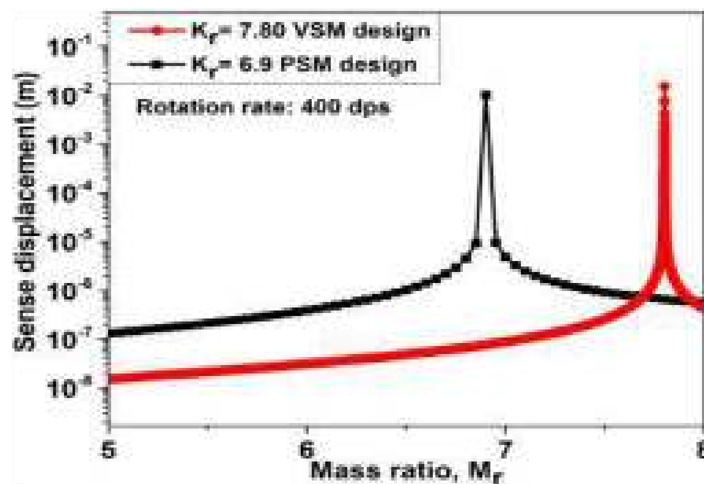

Figure 4.6 (a) Sense mass displacement for different M_r at fixed K_r.

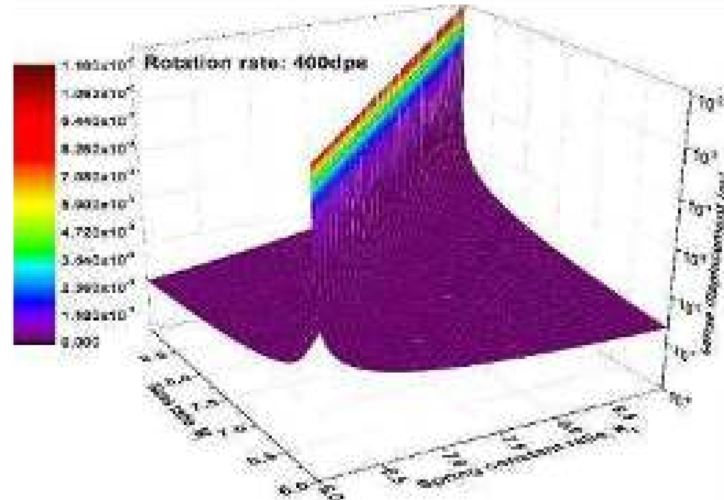

Figure 4.6 (b) The 3-D plot of sense displacement at different M_r and K_r for VSM and PSM design.

Figure 4.7 shows the sense displacement at different rotation rates to determine the mechanical sensitivity of both the designs. The rotation rate was varied from 0 to 400 °/s, and the sense displacement was recorded. From the linear curve fitting, the sensitivities for the VSM and PSM design are 9.63×10^{-9} m/deg/s and 9.60×10^{-9} m/deg/s respectively, which shows that VSM is marginally better than PSM. For any structure, if the mass and spring constant ratios are adjusted such that the gap between the drive and sense frequencies is the same, the sensitivity will remain the same and will be independent of the structural dimensions. Thus, it can be concluded that there may not be any reduction in the sensitivity while optimizing and changing the design from PSM to VSM, but there is a gain in the noise and footprint, and hence in the overall performance metric, as will be shown further.

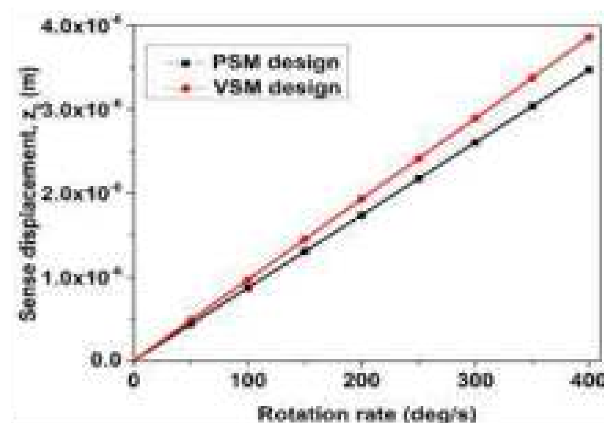

Figure 4.7 Sensitivity for VSM design ($M_r = 7.82$, $K_r = 7.80$) and PSM design ($M_r = 7.04$, $K_r = 6.9$) and K_r.

4.5.2 Bandwidth

Bandwidth is a critical performance parameter for applications requiring accurate angular rate measurement over a wide frequency range. In this section, the bandwidths of these two designs is compared. As discussed earlier, for a given K_r, M_r can be adjusted M_r to obtain the required resonant frequency guided by a particular BW requirement, or vice versa. Figure 4.8 shows the 3d plot of the variation in the 3 dB bandwidth with the mass ratio. As can be seen, a V-shaped curve is observed. The pointed end at the bottom of the V-shaped curve shows almost negligible bandwidth; here, M_r, K_r, f_d and f_s are almost the same. As the M_r and K_r values moved far away from one another, the bandwidth increased and the increase was almost linear along the slanted ends of the V-shaped curve. Generally, the structure will have the highest sensitivity at negligible bandwidth, but to get higher bandwidth to measure angular velocity over a wider range of frequencies, one may have to sacrifice the sensitivity. Therefore, it is important to select a gyroscope with the appropriate bandwidth for the intended application. The trend in this plot is the same for both VSM and PSM designs.

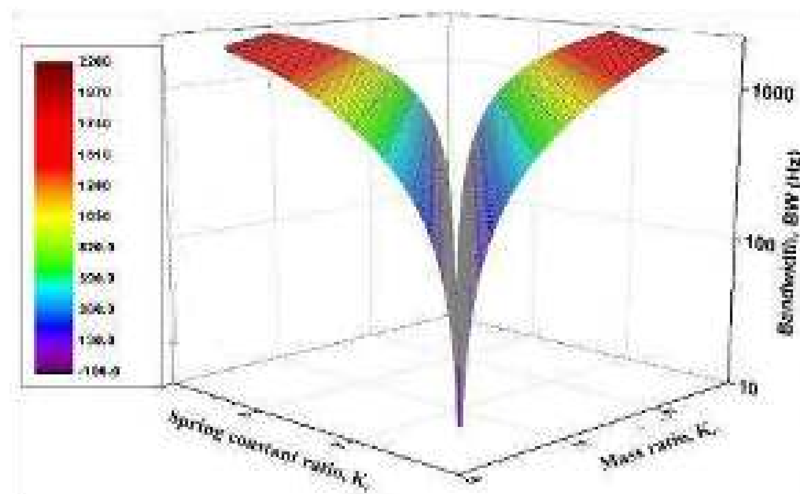

Figure 4.8 3-D plot of bandwidth variation at diff M_r.

Figure 4.9a compares the bandwidths of the VSM and PSM designs. The VSM exhibits wider bandwidths (+3 dB: 25 kHz, -3 dB: 73.75 kHz) compared to the PSM (+3 dB: 18 kHz, -3 dB: 51 kHz). This is attributed to the higher resonant frequency of the VSM design. Both designs have similar sensitivity and drive-sense frequency differences. The VSM design, with optimized spring dimensions and a reduced sense mass footprint (30%), demonstrates improved bandwidth and overall performance.

Figure 4.9b illustrates the impact of damping coefficient (C_s) on bandwidth. For both designs, bandwidth initially increases with C_s but saturates at higher values due to reduced sense amplitude and quality factor. Notably, the VSM design achieves a similar bandwidth (e.g., 29 Hz) at a lower damping coefficient ($C_s = 1.05$) compared to the PSM ($C_s = 1.75$). However, at higher damping ratios, the VSM design exhibits more rapid bandwidth saturation.

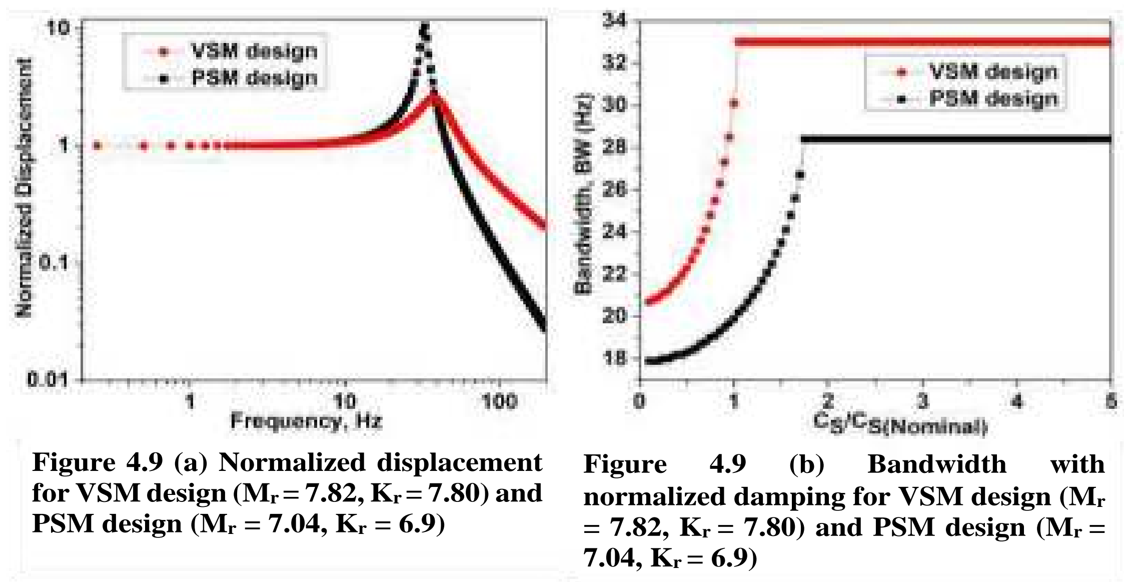

Figure 4.9 (a) Normalized displacement for VSM design (M_r = 7.82, K_r = 7.80) and PSM design (M_r = 7.04, K_r = 6.9)

Figure 4.9 (b) Bandwidth with normalized damping for VSM design (M_r = 7.82, K_r = 7.80) and PSM design (M_r = 7.04, K_r = 6.9)

4.5.3 Thermomechanical Noise

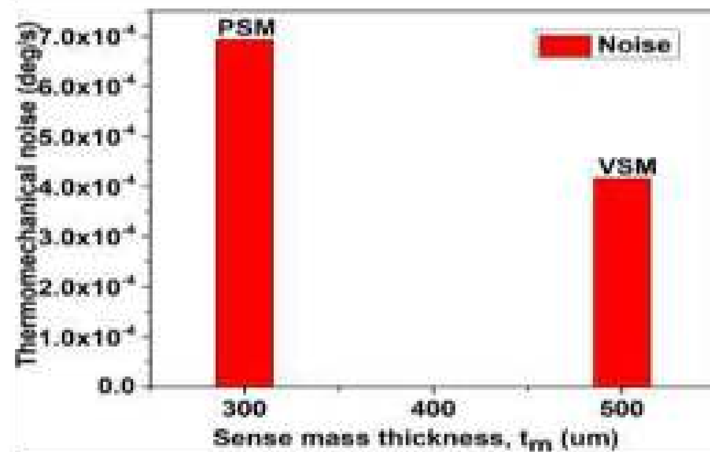

Figure 4.10 (a) Thermomechanical noise variation with sense mass thickness

Thermomechanical noise is a fundamental limiting factor in MEMS gyroscopes. The VSM design exhibits lower thermomechanical noise compared to the PSM. Noise analysis reveals an inverse dependence on sense mass, drive frequency ( ), and drive displacement. The VSM design, with its thicker sense mass (500 µm) and higher resonant frequency to lower the twisting, inherently results in lower noise. Figure 4.10a shows the variation of noise with sense mass thickness, demonstrating lower noise for the VSM compared to the PSM. Furthermore, The noise depends on mass ratio (Mr) and spring constant ratio (Kr), as shown in Figure 4.10b. Although noise differs both Mr and Kr within each design, the VSM has uniformly lower levels of noise. The VSM achieved a noise of 1.7×10^{-4} °/ s for the data indicating that optimized parameters compared with PSM (6.8×10^{-4} °/ s) has similar sensitivities and reduces overall suggested footprint by approximately 36%.

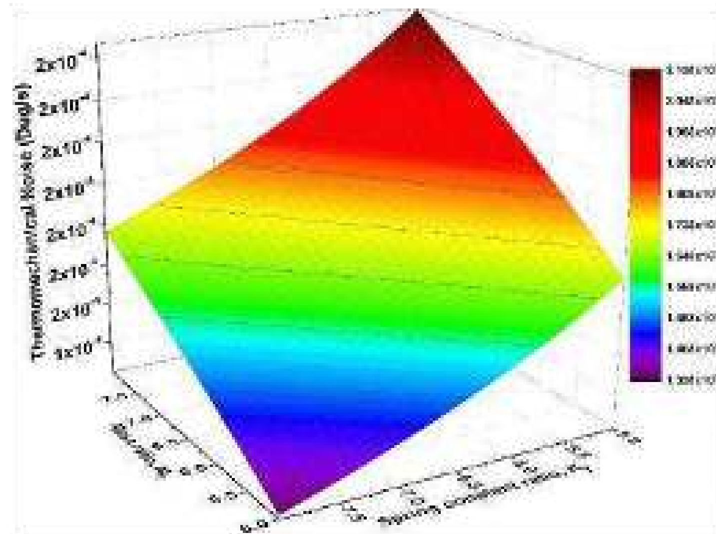

Figure 4.10 (b) 3-D plot for noise variation at different M_r and K_r for PSM design at 500 µm sense mass thickness.

Thus, both VSM- and PSM-based designs can reach a similar sensitivity through the optimisation of structural parameters. The reason behind this is that the higher frequency and less damped nature of the VSM design provides a better response over bandwidth. In addition, the increased proof mass thickness of the VSM reduces thermomechanical noise on a fundamental level. A proven 36% smaller sensor real-estate combined with these performance benefits ultimately make VSM the most scalable and efficient design approach.

4.6 Comparison Using the Improved Performance Metric

New performance metric (PM) is proposed to compare designs, considering sensitivity, bandwidth, noise, and footprint. This metric accounts for the trade-offs inherent in optimizing these parameters. The VSM design, with its reduced footprint and optimized spring dimensions demonstrate superior PM compared to the PSM
The improved performance metrics are defined as:

$$2= \left[\frac{\times}{}\right] \quad (4.3)$$

$$2= \left[\frac{\times}{\times}\right] \quad (4.4)$$

The resultant values of both the performance metrics should be maximized for a particular design. In the literature [27,28,49,50], different parameters are maximized or optimized for a particular design based on specific applications; however, the newly proposed improved performance metric can facilitate the comparison of different designs on the same platform, as discussed in[17].

The objective was to maximize PM to achieve better performance. A comparison of the performance metrics for the VSM and PSM designs is presented in Table 4.2. It is evident that the two designs considered for comparison, shown in the above table, have almost comparable sensitivity; however, the VSM design has a higher bandwidth and lower noise parameters, and both have a reduced footprint. If the PSM design is considered at the same higher resonant frequency or bandwidth as the VSM design, the performance metric for the VSM design is

higher than that of the PSM design. The PM2 for VSM and PSM is 1090 m Hz/dps²µm² and 70.7 m Hz/dps²µm², respectively, which is 15.4 times higher than PSM design.

Table 4.2 Comparison of PMs for the proposed VSM design vis-à-vis from other designs from literature.

Sr. No.	Ref.	Design type	Sensitivity (m/dps)	Bandwidth (BW)	Footprint (mm×mm)	Sense mass thickness (µm)	Mass, m_s (Kg)	Noise (dps)	PM1 (mHz/dps²)	PM2 (mHz/dps²µm²)
1	Ref. [26]	PSM	4.69e-9	25	1×1	10	3.7e-9	0.0041	2.86e-8	0.0286
2	Ref. [48]	PSM	1.74e-11	21.6	4.6×4.6	30	2.1e-7	0.00047	8.00e-7	0.0378
3	Ref. [27]	PSM	1.06e-9	25	2.3×1.3	58	2.3e-8	0.0045	5.89e-6	1.97
4	Ref. [49]	PSM	1.06e-7	7	5.8×6.0	100	2.5e-6	0.0103	7.20e-5	2.07
5	Current study	PSM	9.60e-9	18	2.2×1.6	300	1.0e-7	0.00068	2.54e-4	70.7
6	**Current study**	**VSM**	**9.60e-9**	**25**	**1.51×0.86**	**500**	**9.0e-8**	**0.00017**	**1.41e-3**	**1090**

If the footprint is not considered, that is, PM1 for the VSM and PSM design is 1.42×10^{-3} mHz/dps² and 2.54×10^{-4} mHz/dps², respectively, which is 5.6 times higher than that of the PSM design. Hence, it can be concluded that for VSM, both PM1 and PM2 were higher than those in the PSM design. From a fabrication viewpoint, the VSM design involves a few additional fabrication steps compared to the PSM design. However, these are doable owing to the recent advancements in the silicon fabrication technology of MEMS sensors Refs. [20,22,27]. The VSM design, with its improved performance metric and reduced footprint, enables applications in wearable devices, IoT, AR/VR systems, and UAVs.

4.6.1 Comparative Analysis with Reported Designs

To validate these findings, different MEMS gyroscope designs were obtained from the literature. Various authors have optimized designs to maximize individual parameters, such as sensitivity, bandwidth, noise, and size. The performance metrics of these designs were compared for a meaningful comparison. Table 4.2 presents the designs explored in the literature for comparison [26,27,48,49]. The mechanical sensitivity of the sensor in m/dps was noted from individual references. It can be seen from Table 4.2 that PM1 is 1.41×10^{-3} mHz/dps² (without footprint) and PM2 is 1090 mHz/dps²µm² (with footprint), which is higher among all. The data were analyzed, and trends between the sense mass thickness and PM1 and PM2 was observed. As there is no continuous variation in the sense mass thickness of the performance metric reported in the literature, this trend is shown in the histogram in Figure 4.11.

The plot shows the log of both performance metrics, without a footprint and with a footprint at different sense mass thicknesses. It was observed that both performance metrics improved with an increase in sense mass thickness. When the sense mass thickness was increased from 10 µm to 500 µm, PM1 and PM2 increased by 4.94×10^{4} times and 3.80×10^{4} times, respectively. Furthermore, as discussed in the introduction the area of the VSM and PSM design is 1.29 mm² and 3.59 mm². Hence, the area of VSM design achieved using DRIE in MEMS technology is comparable to the 1.2 mm² area mentioned by Gadola et al. [17] using the NEMS technology. Hence, the data from the literature is presented to support the analysis

considered for comparing the designs, confirming the enhanced performance metric of the proposed VSM design using a thick sense mass.

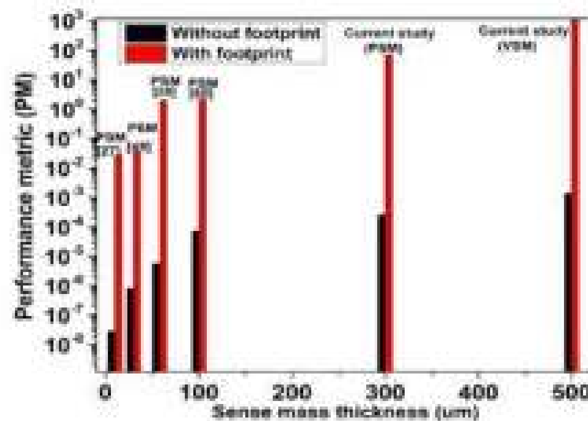

Figure 4.11 Experimental results of PM at different sense mass thickness for various designs from literature vis-à-vis our proposed design.

4.7 Fabrication Strategy and Experimental Validation

Figure 4.12 shows the fabrication sequence for the MEMS gyroscope. Such device is implemented via a three-wafer silicon stack, in which a central structural wafer acting as the active layer is sandwiched by an upper electrode wafer and a lower electrode wafer. To achieve low parasitic resistance and good electrical performance, all wafers are processed using low resistivity silicon (0.01–0.001 ·cm).The fabrication approach leverages deep reactive ion etching (DRIE) to achieve high-aspect-ratio elements and maximizes the use of silicon-wafer thickness for the realization of the Vertical Sense Mass (VSM) architecture.

The fabrication consists of the following steps:

(i) Fabrication of the central wafer
(ii) Fabrication of the bottom wafer
(iii) Fabrication of the top wafer
(iv) Bonding of Wafers and metallization

(i) Fabrication of the central wafer

The fabrication of the central wafer begins with mechanical lapping and polishing, as shown in Figure 4.12, step (a), to achieve the target wafer thickness with high surface planarity. The thickness is optimize using the standard methods described in [51]. Then, a thermal oxide layer with a thickness on the order of 1 µm is grown (see step (b)), which acts as hard mask during DRIE. At step (c), the oxide is patterned using standard photolithography (PLG) [52,53] and DRIE to define the main structural features.The oxide mask is then removed, and the wafer is reoxidized, as shown in steps (d) and (e), to prepare for subsequent etching steps. Finally, step (f) depicts DRIE performed from both the front and back sides of the wafer to precisely define the beams and release the thick sense mass structure. This double-sided etching is critical for achieving high-aspect-ratio vertical features with minimal profile distortion.

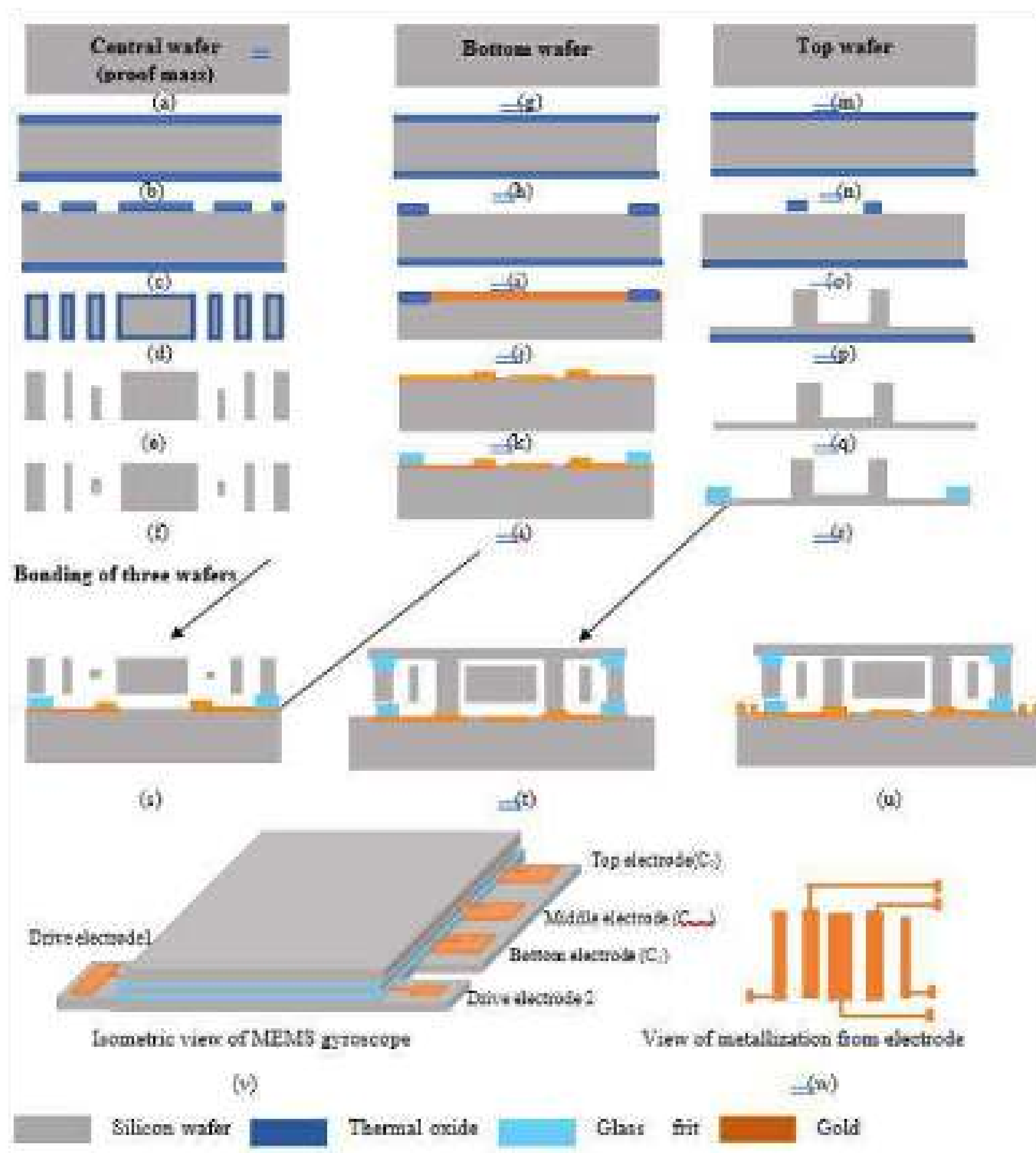

Figure 4.12 Fabrication sequence for the proposed design.

(ii) Fabrication of the bottom wafer

The fabrication of the bottom wafer is illustrated in steps (g–l). As shown in step (g), the wafer is first lapped and polished, and the contact regions corresponding to two drive electrodes and three sense electrodes are defined. Step (h) shows the growth of a thermal oxide layer, which is a masking layer for subsequent processing. Subsequently, the oxide pattern (i) is sputtered followed by metal deposition (j). A second step is used for metal patterning, which selectively increases the metal thickness in certain regions (e.g. to provide thick electrical contacts). A low melting glass frit layer is then spin-coated over the wafer in step (k) as an insulating and

bonding material [54]. The patterned glass frit layer, shown in step (l), precisely defines the bonding gap between the top and bottom wafers, which is a critical parameter for capacitive sensing performance.

(iii) Fabrication of the top wafer

The second wafer is lapped and polished before sense electrode regions are defined. Steps (n) and (o) undergo thermal oxide growth and patterning to ready the wafer for deep etching. Step (p) involves DRIE for obtaining the desired electrode pores. Next, the oxide layer is stripped off and a glass frit layer is deposited (by spin coating) as illustrated with steps (q) and (r); this enables wafer bonding and forms the electrical isolation.

(iv) Bonding of wafers and metallization

The three wafers are directly bonded together according to the process outlined in [55]. In step(s) of Figure 4.12, the central wafer is bonded first to the bottom (outward facing) wafer. Thereafter, in step (t), the top wafer is flipped upside down, accurately aligned and bonded to the accumulated stack. The completed three-wafer assembly is shown at step (u). The electrical interconnections are obtained with a shadow-mask metallization technique.This method allows for reliable electrical accessibility for the drive and sense electrodes without sacrificing device structural integrity. Figure 4.12 Step (v) an isometric view of fully fabricated MEMS gyroscope. The external electrical connections to the device are two for the drive mechanism and three for sensing displacement from top, bottom, and central electrodes. Step (w) gives a close-up view of the metallization coming from the middle electrode.

4.7.1 DRIE Experiment on Thick Substrate

In order to validate the fabrication of thick vertical sense mass structures experimentally, a large range of experimental conditions were explored by optimizing individual steps in the DRIE process. Figure 4.13a-d shows a SEM of a released and representative DRIE structure fabricated based on the optimized process described above. The target thickness of sense mass was 400 µm.

The released structure is shown in Figure 14.3(a). The beam sections connecting to the proof mass are shown in Figure 14.3(b), while the top view of the released device is shown in Figure 14.3(c). Using SEM to analyze the sidewall, Figure 4.13d shows that when the sample was tilted at an angle of 16.40°, its thickness is measured at 396.2 µm. The sidewall thickness was determined to be about 412.1 µm (396.2 / cos (16.40°)), accounting for the tilt angle, and is in good agreement with the design value. At the micrometre or nanometre level, uniform etched structures with nearly vertical sidewalls and high process repeatability were achieved. The excellent etch selectivity and process profile control were realized using a composite masking strategy of thermal oxide, silicon nitride and plasma-enhanced oxide as masks. Additionally, the successful implementation of thick structures by DRIE demonstrates the successful fabrication of VSM devices.

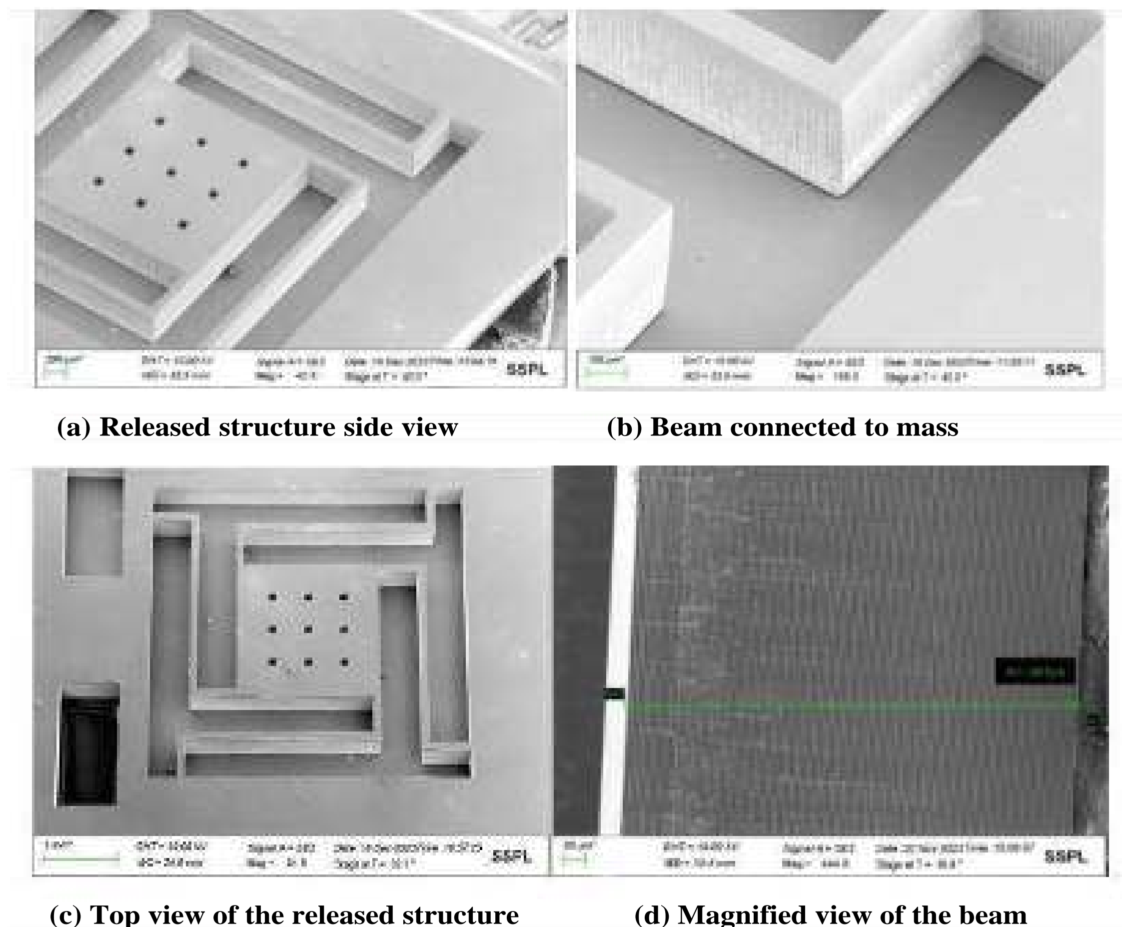

(a) Released structure side view **(b) Beam connected to mass**

(c) Top view of the released structure **(d) Magnified view of the beam**

Figure 4.13 The SEM image of the released structure.

4.8 Conclusion

This chapter described the design, optimization, fabrication strategy and performance assessment of a Vertical Sense Mass (VSM) MEMS gyroscope considered to be an advanced method compared with traditional planar sense mass architecture Through deep reactive ion etching (DRIE, VSM architecture takes advantage of the full thickness of a silicon wafer to achieve a high-aspect-ratio, vertically oriented sense mass, driven by the inability to reach simultaneously wide bandwidths for low noise/read out encumbrance in planar designs.

Theoretical modelling and simulation results show that the optimized VSM design provides clear improvements in both bandwidth and thermomechanical noise. The architecture benefits from a higher effective sense mass and increased resonant frequencies, which help reduce noise while maintaining the same dynamic range. Performance comparison using a defined performance metric (PM) indicates that the proposed VSM design significantly outperforms conventional PSM structures. In particular, the VSM gyroscope achieves a noise figure of merit (FoM) of 1090 $mHz/dps^2 \cdot \mu m^2$, which is about 15.4 times better than the PSM design. It also offers a more compact design, with 30% less sensing mass area and a 36% reduction in overall footprint. The feasibility of implementing thick proof-mass structures was experimentally

supported using optimized DRIE processes. Comparisons with existing designs reported in the literature further confirm that the VSM approach delivers strong overall performance.

In summary, the VSM design emerges as a flexible and high-performance solution for miniaturized gyroscopes. It combines improved sensitivity, wider bandwidth, reduced noise, and compact size, making it well-suited for applications such as body-worn systems, IoT devices, mixed-reality platforms, and UAVs.

References

[1] Passaro V M N, Cuccovillo A, Vaiani L, De Carlo M and Campanella C E 2017 Gyroscope technology and applications: A review in the industrial perspective Sensors 17 2284

[2] Valldorf J and Gessner W 2007 Handbook of advanced microsystems for automotive applications Springer

[3] He Y 2024 Handbook of integrated circuit industry

[4] Gill W A, Howard I, Mazhar I and McKee K 2022 A review of MEMS vibrating gyroscopes and their reliability issues in harsh environments Sensors (Basel) 22 7405

[5] Zhao W, Cheng Y, Zhao S, Hu X, Rong Y, Duan J and Chen J 2021 Navigation-grade MEMS IMU for a satellite Micromachines (Basel) 12 1–12

[6] Weinberg M S 2015 How to invent (or not invent) the first silicon MEMS gyroscope IEEE Int. Symp. on Inertial Sensors and Systems

[7] Xiao Y, Meng J, Yan H, Wang J, Xin K and Tao T 2023 Research on the application of MEMS gyroscope in inspecting the breakage of urban sewerage pipelines Water (Switzerland) 15 2426

[8] Wagner J F, Trierenberg A and Bohnenberger J 2010 The origin of the gyroscope: The machine of Bohnenberger Machines

[9] Gill W A, Howard I, Mazhar I and McKee K 2022 Review of MEMS vibrating gyroscopes and their reliability issues in harsh environments Sensors (Basel) 22 7405

[10] Zhang H, Zhang C, Chen J and Li A 2022 A review of symmetric silicon MEMS gyroscope mode-matching technologies Micromachines (Basel) 13 1255

[11] Zhanshe G, Fucheng C, Boyu L, Le C, Chao L and Ke S 2015 Research development of silicon MEMS gyroscopes: A review Microsystem Technologies 21 2053–2066

[12] Izquierdo A 2024 Pedestrian detection using a MEMS acoustic array mounted on a moving vehicle Sensors and Actuators A: Physical 376 115586

[13] Liu K, Zhang W, Chen W, Li K, Dai F, Cui F, Wu X, Ma G and Xiao Q 2009 The development of micro-gyroscope technology J. Micromech. Microeng. 19 113001

[14] Shaeffer D K 2013 MEMS inertial sensors: A tutorial overview IEEE Communications Magazine 51 100–109

[15] Jones A 1995 Microelectromechanical systems: A DoD dual use technology industrial assessment

[16] Karimzadehkhouei M et al 2023 Silicon nanowires driving miniaturization of microelectromechanical systems physical sensors: A review Adv. Eng. Mater. 25 2300007

[17] Gadola M, Perna M S, Allieri M, Robert P, Verdot T, Berthelot A and Langfelder G 2021 600 μdps/ Hz, 1.2 mm^2 MEMS pitch gyroscope IEEE Int. Symp. on Inertial Sensors and Systems

[18] Dellea S, Rey P and Langfelder G 2017 MEMS gyroscopes based on piezoresistive NEMS detection J. Microelectromech. Syst. 26 1389–1399

[19] Thapliyal T and Melong Study and analysis of MEMS and NEMS based gyroscope 2018 ICISC Proceedings
[20] Larkin K and Ghommem M 2018 A review on vibrating beam-based micro/nano-gyroscope Microsystem Technologies 27 4157–4181
[21] Yang T and Duncan T V 2021 Challenges and potential solutions for nanosensors intended for use with foods Nat. Nanotechnol. 16 251–265
[22] Bhan R K, Pal R, Dutta S and Yadav I 2016 Development of unified fabrication process and testing of MEMS based capacitive accelerometers Sensors and Transducers 203 8–15
[23] Kavitha S, Joseph Daniel R and Sumangala K 2016 Design and analysis of MEMS comb drive capacitive accelerometer Measurement 93 327–339
[24] Gupta N, Dutta S, Parmar Y, Gond V, Vanjari S R K and Gupta S 2021 Characterization of SOI MEMS capacitive accelerometer Microsystem Technologies 27 4319–4327
[25] Kranz M, Hudson T, Ashley P, Ruffin P, Burgett S, Temmen M and Tuck J 2001 Single layer silicon-on-insulator MEMS gyroscope SPIE Proceedings
[26] Acar C and Shkel A M 2005 An approach for increasing drive-mode bandwidth of MEMS vibratory gyroscopes J. Microelectromech. Syst. 14 520–528
[27] Alper S E and Akin T 2005 A single-crystal silicon MEMS gyroscope J. Microelectromech. Syst. 14 707–717
[28] Menon P K, Nayak J and Pratap R 2018 Sensitivity analysis of an in-plane MEMS vibratory gyroscope Microsystem Technologies 24 2199–2213
[29] Owen K J, VanDerElzen B, Peterson R L and Najafi K 2012 High aspect ratio deep silicon etching IEEE MEMS 251–254
[30] Herth E, Baranski M, Berlharet D, Edmond S, Bouville D, Calvet L E and Gorecki C 2019 Fast ultra-deep silicon cavities J. Vac. Sci. Technol. B 37
[31] Klaassen E H, Petersen K et al 1996 Silicon fusion bonding and DRIE technology Sensors and Actuators A 52 132–139
[32] Marty F, Rousseau L, Saadany B, Mercier B, Français O, Mita Y and Bourouina T 2005 Advanced etching of silicon using DRIE Microelectronics J. 36 673–677
[33] Roth S, Staufer U, Stebler C, Thiebaud P and De Rooij N F 1998 Advanced DRIE for MEMS J. Micromech. Microeng. 8 272–278
[34] Xu Q, Xiao D, Hou Z, Zhuo M, Li W, Xu X and Wu X 2019 Butterfly gyroscope IEEE Sens. J. 19 2064–2071
[35] Tang Y, Sandoughsaz A and Najafi K 2017 Ultra high aspect-ratio silicon etching IEEE MEMS 700–703
[36] Tang Y, Sandoughsaz A, Owen K J and Najafi K 2018 Ultra deep reactive ion etching J. Microelectromech. Syst. 27 686–697
[37] Dyer S, Griffin P F, Arnold A S, Mirando F, Burt D P, Riis E and McGilligan J P 2022 Micromachined silicon vapor cells J. Appl. Phys. 132
[38] Panth S, Samadi K and Du Y 2013 Monolithic 3D-IC integration ASP-DAC 681–686
[39] Mii Y J 2022 Semiconductor innovations Symp. on VLSI Technology 276–281
[40] Naeim M, Yang H et al 2023 Design enablement of 3D stacked ICs IEEE 3DIC Conference
[41] Hossam N and Ferguson J 2023 Assembly-level verification of 3DIC packages IEEE 3D Systems Integration Conf. 1–4
[42] Acar C 1979 Handbook of MEMS vibratory gyroscopes Springer
[43] Apostolyuk V 2016 Coriolis vibratory gyroscopes: Theory and design Springer
[44] Patel C and McCluskey P 2012 Modeling and simulation of MEMS gyroscope ITHERM 928–933

[45] Bao M H 2000 Handbook of sensors and actuators: Micro mechanical transducers Elsevier
[46] Ni Y, Li H, Huang L, Ding X and Wang H 2014 Bandwidth characteristics of tuning fork gyroscope Sensors 14 13024–13045
[47] Lishchynska M, Cordero N, Slattery O and O'Mahony C 2006 Spring constant models for MEMS plates Sensors Lett. 4 200–205
[48] Rebeiz G M 2003 RF MEMS: Theory, design, and technology Wiley
[49] Xie J, Shen Q, Hao Y, Chang H and Yuan W 2015 Low-noise Z-axis micromachined gyroscope Microsystem Technologies 21 625–630
[50] Xiong X and Dong H 2009 MEMS vibratory comb gyroscope ASEE Conference
[51] Dutta S, Kumar M, Kumar S, Imran M, Yadav I, Kumar A, Kumar P and Pal R 2015 Lapping assisted dissolved wafer process J. Mater. Sci.: Mater. Electron. 25 1984–1990
[52] Herth E, Baranski M, Berlharet D, Edmond S, Bouville D, Calvet L E and Gorecki C 2016 Ultra-deep silicon cavities J. Vac. Sci. Technol. B 37 021206
[53] Marty F, Rousseau L, Saadany B, Mercier B, Français O, Mita Y and Bourouina T 2005 DRIE silicon microstructures Microelectronics J. 36 673–677
[54] Schnable G L, Kern W and Comizzoli R B 1975 Passivation coatings on silicon devices J. Electrochem. Soc. 122
[55] Moriceau H, Rieutord F, Fournel F, Le Tiec Y, Di Cioccio L, Morales C, Charvet A M and Deguet C 2000 Silicon shadow mask for deposition J. Micromech. Microeng. 10

CHAPTER 5

DAMPING MECHANISMS IN MEMS GYROSCOPES: A COMPARATIVE STUDY OF PLANAR AND VERTICAL SENSE MASS ARCHITECTURES

- *This chapter presents a comprehensive comparative damping analysis of Vertical Sense Mass (VSM) and Planar Sense Mass (PSM) MEMS gyroscopes under identical sense-mass areas.*
- *Despite vacuum packaging, residual air damping remains a dominant loss mechanism. The net quality factor of VSM improves by a factor of 8 as compared to PSM.*
- *Over temperature variation, VSM maintains approx. 2.7 times higher Q with similar trends. Over frequency variation, VSM consistently outperforms PSM.*
- *VSM provides higher sense displacement up to Q   100, with convergence at higher Q. Bandwidth enhancement of approx. 20 times and noise reduction of approx. 3.33 times are achieved.*
- *The fabrication sensitivity analysis shows a maximum Q variation of ±12.8%.*
- *The VSM concept is validated against state-of-the-art designs and experimental data.*

5.1 Introduction

In the rapidly evolving landscape of micro-electro-mechanical systems (MEMS), the continuous drive toward device miniaturization for applications ranging from precision navigation to consumer electronics introduces significant design challenges [1–6]. Achieving optimized performance in MEMS gyroscopes is constrained by several limiting factors, among which damping management is of paramount importance. Damping is an inherent phenomenon that governs energy dissipation in vibrating microstructures and, unlike in macro-scale systems, its impact becomes increasingly pronounced as device dimensions shrink. Miniaturization amplifies multiple damping mechanisms that collectively degrade device performance. Energy dissipation directly influences the quality factor (Q)—a critical performance metric that dictates a gyroscope's sensitivity, noise characteristics, and operational bandwidth [7–9]. In MEMS gyroscopes, damping acts as a double-edged sword: while a controlled level of damping is necessary to ensure stable operation and adequate bandwidth, excessive damping leads to significant energy loss, resulting in degraded Q-factor. A higher Q-factor is theRef ore essential, as it enables the detection of minute input signals, improves sensitivity, suppresses noise, and enhances overall device performance. Consequently, a thorough understanding and precise control of damping mechanisms are vital for advancing MEMS gyroscope technology.

Extensive research efforts have focused on characterizing damping and Q-factors in various MEMS structures; however, performance limitations continue to persist. Ref [10] analyzes and compares the natural frequency, deflection, and Q-factor of a novel hexagonal microcantilever beam with a conventional rectangular beam. Ref [11] presents two theoretical models for predicting viscous damping in perforated MEMS devices with different perforation geometries. Ref [12] reports a comprehensive theoretical, numerical, and experimental investigation of nonlinear damping in flexible structures undergoing large-amplitude vibrations. The dependence of thermoelastic damping (TED) on flexural mode shapes in clamped–clamped MEMS beam-mass structures is numerically studied in Ref [13], while Ref [14] proposes a structure designed to reduce air damping. Despite these advances, controlling and minimizing damping remains an ongoing challenge for MEMS designers [14–16]. To address these challenges, this paper presents an in-depth study of the damping mechanisms in a novel Vertical Sense Mass (VSM) MEMS gyroscope design, recently proposed in Ref [17], and further design innovations reported in Ref s. [18–20]. Building on this foundation, the present work provides a comprehensive comparative analysis of various damping mechanisms and their impact on the quality factor for the VSM design, compared with a conventional Planar Sense Mass (PSM) architecture. The results demonstrate that the VSM design achieves a 30% reduction in sense-mass area, resulting in a 36% smaller sensor footprint, while simultaneously delivering a significant improvement in the overall performance metric compared to the planar design reported in Ref [17].

While the above studies provide valuable insights into individual damping mechanisms and structural configurations, their analyses largely remain focused on isolated effects or specific geometries. In the context of emerging MEMS gyroscope architectures aimed at simultaneously enhancing performance and reducing footprint, a unified understanding of how sense-mass orientation and geometry influence collective damping behaviour remains lacking. In particular, the relationship between architectural innovation and the redistribution of energy dissipation pathways has not been comprehensively explored, motivating a detailed comparative investigation.

5.2 Design Methodology of Vertical Sense Mass Gyroscope

As illustrated in Figure 5.1a and Figure 5.1b, the proposed VSM architecture differs fundamentally from the conventional PSM design in terms of geometry, sensing configuration, and dynamic behaviour. The VSM design employs vertically oriented fixed sensing plates and a deep, compact sense mass fabricated using advanced deep reactive ion etching (DRIE). This vertical orientation allows the sense mass to be positioned perpendicular to the substrate, resulting in a significantly reduced device footprint. In contrast, the PSM configuration consists of three distinct plates: a movable sense mass positioned between fixed top and bottom electrodes. These fixed electrodes are separated from the sense mass by small vertical air gaps that define the capacitive sensing region. For clarity, the fixed top and bottom plates are omitted in Figure 5.1b but are explicitly shown later in Figure 5.3b.

In the VSM design, angular rotation induces an in-plane sense motion, which offers advantages in fabrication simplicity, structural robustness, and system integration, as shown in Figure 5.2a. Conversely, in the PSM design, rotation typically excites an out-of-plane sense motion, as illustrated in Figure 5.2b. In both architectures, the induced sense motion results in a change in differential capacitance between the moving and fixed electrodes, which is subsequently measured to detect the applied angular rate.

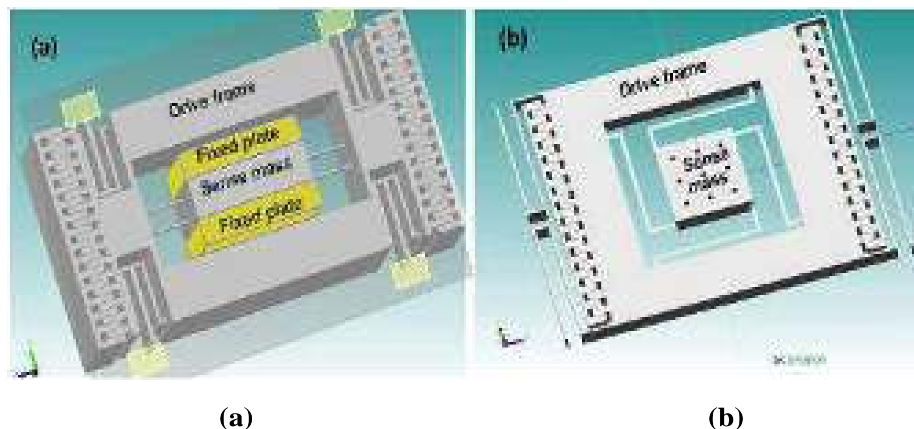

(a) **(b)**

Figure 5.1 (a) Three-dimensional view of the VSM design (b) PSM design.

A key distinction between the two designs lies in their capacitor plate configurations and structural confinement. In the VSM architecture, the differential sensing electrodes are arranged laterally within the same plane, and the critical sensing gap is defined in-plane, independent of the capping wafer. As a result, the sensing gap is not constrained by top or bottom wafers. In contrast, the PSM design relies on a three-wafer stack in which the sensing gap is vertically defined between the movable sense mass and the fixed top and bottom electrodes. This configuration confines the movable structure between two wafers, leading to stronger squeeze-film effects and increased sensitivity to fabrication tolerances. The optimized spring design and increased effective mass in the VSM configuration result in a higher sense-mode resonant frequency, which, as demonstrated in the present analysis, contributes directly to an improved total quality factor. These fundamental differences in sense-mass orientation, gap definition, and structural confinement lead to distinct dynamic characteristics, particularly in resonant behaviour and damping mechanisms. Further design and fabrication details of both architectures are provided in Chapter 4.

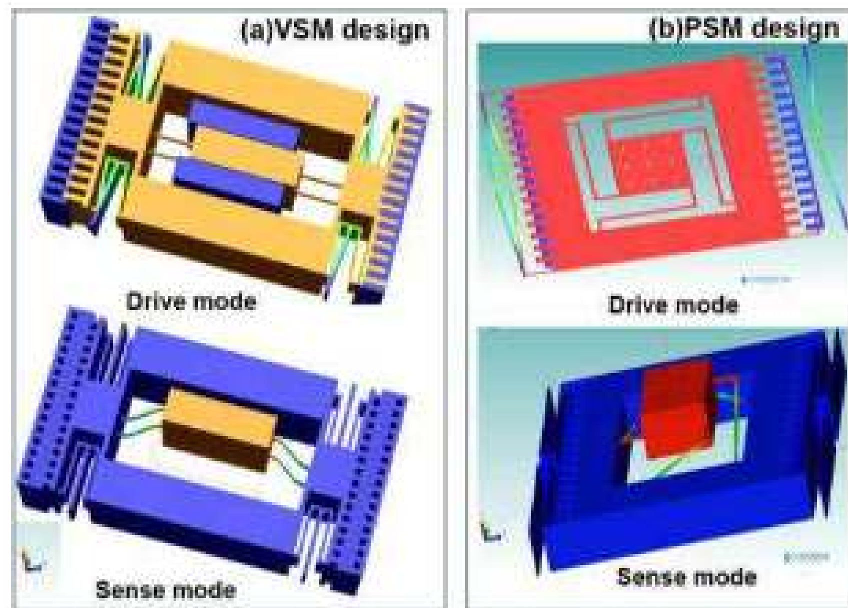

Figure 5.2 Drive and sense mode deflection in (a) VSM design and (b) PSM design.

Both VSM and PSM gyroscopes operate on the same physical principle, wherein Coriolis-induced motion of the sense mass under angular rotation leads to a measurable capacitive change. However, the mechanical implementation differs between the two designs: the VSM employs a flexure-based spring system, while the PSM utilizes a modified crab-shaped spring structure. These differences influence the stiffness distribution, modal characteristics, and energy dissipation behaviour of the devices. The bandwidth of a MEMS gyroscope defines the frequency range over which the sense output accurately responds to an applied angular rate and is closely linked to the sense-mode frequency and quality factor. In addition, the thermomechanical noise, which fundamentally limits sensitivity, is inversely related to the quality factor and is influenced by temperature, sense mass, and operating bandwidth. The design parameters selected for both VSM and PSM configurations are given earlier. Owing to its vertical orientation and efficient utilization of structural volume, the VSM architecture achieves a 30% reduction in sense mass area compared with the PSM design. This reduction translates into an overall 36% decrease in the total sensor footprint, as reported earlier. Detailed discussions of the design methodology and fabrication processes for the VSM and PSM architectures are provided in Ref [17]-[18].

Sensitivity, bandwidth, and noise constitute the primary performance metrics of MEMS gyroscopes, all of which are fundamentally governed by the quality factor (Q). Consequently, precise control of the Q-factor is essential for achieving reliable and high-performance operation. Motivated by this interdependence, the present work undertakes a systematic investigation of the damping mechanisms that influence Q-factor variation as ambient pressure, temperature, and operating frequency change. Understanding how these factors affect energy dissipation provides critical insight into the dynamic behaviour of MEMS gyroscopes and forms the basis for the subsequent damping analysis presented in this chapter.

5.3 Damping Analysis of VSM versus PSM

Damping plays a critical role in determining the performance of MEMS gyroscopes, as it directly influences the quality factor (Q) and, consequently, the device sensitivity, noise floor, operational bandwidth, and power consumption. Excessive damping leads to increased energy dissipation, resulting in degraded performance, while insufficient damping may compromise stability. TheRef ore, a detailed understanding of damping mechanisms is essential for accurate device modeling, performance optimization, and long-term reliability, particularly in the context of aggressive device miniaturization. This analysis is especially important for the VSM and PSM gyroscope architectures, as their fundamentally different geometries and sense-motion directions give rise to distinct energy dissipation behaviours. The VSM design, enabled by deep reactive ion etching (DRIE), employs a vertically oriented sense mass with in-plane sensing motion, whereas the conventional PSM design relies on a horizontally oriented sense mass undergoing out-of-plane motion. These differences significantly affect how various damping mechanisms—such as air damping, thermoelastic damping, anchor loss, viscous damping, and acoustic damping—manifest in each configuration.

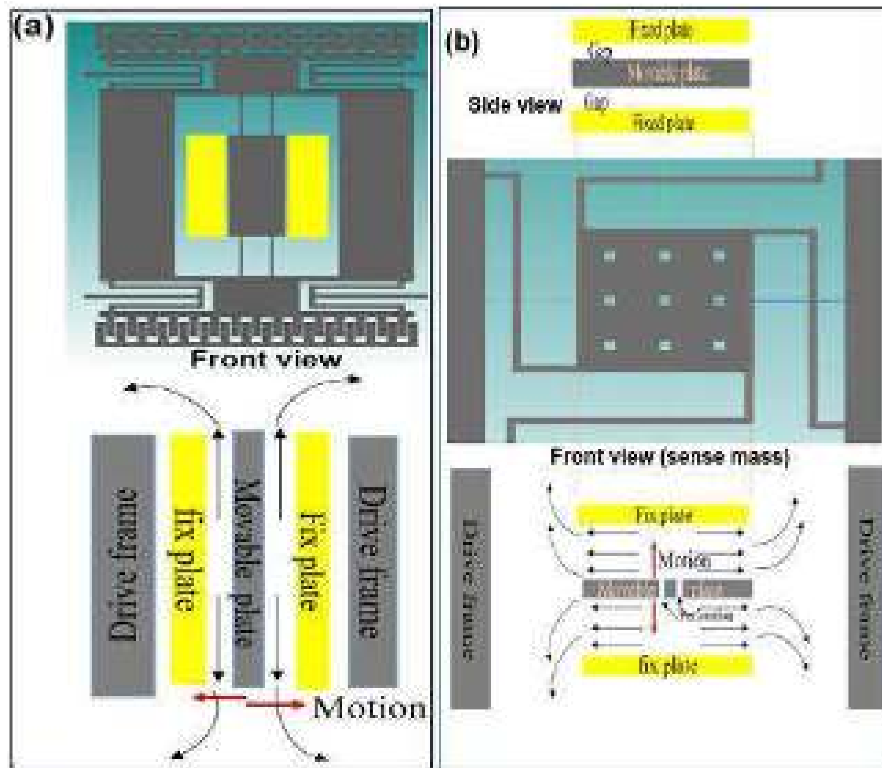

Figure 5.3 (a) VSM design: Top view and air motion (b) PSM design: Sense mass Side view, front view and air motion

Figure 5.3 illustrates the motion of the movable sense mass and the corresponding air movement responsible for energy dissipation in both designs. In the VSM configuration, shown in Figure 5.3a, the movable sense mass is oriented vertically and positioned between two fixed electrodes, while the drive frames are located laterally. The sense mass undergoes horizontal oscillatory motion, moving back and forth perpendicular to the plane of the fixed plates. This

in-plane motion alters the air flow paths and reduces structural confinement, thereby modifying the nature of fluid–structure interaction and associated damping. In contrast, the PSM configuration depicted in Figure 5.3b consists of a horizontally oriented movable sense mass located between fixed top and bottom electrodes, with the drive frames positioned along the vertical direction. For clarity, the central view omits the top and bottom plates, as previously discussed in Figure 5.1b, while these plates are shown explicitly in the corresponding top and bottom subfigures.

In this design, the sense mass undergoes vertical oscillatory motion, moving up and down perpendicular to the plane of the fixed electrodes. This motion results in stronger squeeze-film effects due to the confined air gap between the movable and fixed plates, leading to increased air damping. The contrasting sense-mass orientations, motion directions, and structural confinement in the VSM and PSM designs give rise to markedly different damping characteristics. To fully understand the dominant energy dissipation mechanisms in these two architectures, a detailed examination of the individual damping phenomena relevant to MEMS structures is required. The following sections theRef ore present a systematic analysis of the various damping mechanisms and their respective contributions to the total quality factor in both VSM and PSM gyroscopes.

5.4 Effect of Damping on Quality Factor

Damping phenomena play a decisive role in determining the performance of MEMS gyroscopes, as they directly govern the quality factor (Q) and, consequently, affect sensitivity, noise floor, operational bandwidth, and power consumption. With increasing miniaturization, damping-related energy losses become more pronounced, making their accurate characterization essential for device optimization, reliable modeling, and long-term operational stability. In MEMS gyroscopes, damping is particularly critical due to the strong coupling between mechanical motion and energy-dissipating mechanisms at microscale dimensions.

Damping mechanisms in MEMS structures are broadly classified into two principal categories: fluid damping, arising from interactions between the vibrating structure and the surrounding gas or fluid medium, and solid damping, originating from intrinsic material losses and energy leakage through the supporting structures. The overall performance of a MEMS gyroscope is theRef ore governed by the cumulative contribution of multiple independent loss mechanisms. Energy dissipation in such micro-mechanical sensors can be attributed to several factors, including air damping, viscous damping, thermoelastic damping, material (Rayleigh) damping, anchor loss, and acoustic damping. As these attenuation mechanisms operate independently and vary in extent depending on device geometry and operating conditions, their contributions to total energy loss are effectively uncoupled. Accordingly, the total quality factor of the gyroscope can be expressed as the reciprocal sum of the quality factors associated with the individual loss mechanisms [8]:

$$\frac{1}{\ } = \frac{1}{\ } + \frac{1}{\ } + \frac{1}{\ } + \frac{1}{\ } + \frac{1}{\ } + \frac{1}{\ } \quad (5.1)$$

where Q_{air}, Q_{vis}, Q_{TED}, Q_{Rld}, Q_{anchor} and Q_{acous} represent the quality factors associated with air damping, viscous damping, thermoelastic damping, Rayleigh damping, anchor loss, and acoustic damping, respectively. In this work, the contributions of these dominant damping mechanisms to the total quality factor are systematically analysed and compared for both the VSM and PSM gyroscope architectures. Other secondary damping mechanisms may also exist, such as surface damping arising from interfacial losses, electronic damping associated with charge carrier

motion, and phonon-related losses (Akhiezer damping) due to phonon–phonon interactions. However, for the MEMS gyroscope structures considered in this study, the contribution of these mechanisms is typically negligible compared to the dominant loss processes and is not included in the present analysis.

5.5 Analytical Modelling of Damping

For the purpose of analytical evaluation, a constant angular rate and steady-state drive-mode oscillation are assumed. Although the VSM design undergoes lateral deflection along the y-axis due to Coriolis excitation, while the PSM design experiences perpendicular deflection, a unified coordinate system is employed to simplify the formulation and enable direct comparison between the two architectures.

5.5.1 Air Damping

Air damping Ref ers to the dissipation of vibrational energy due to the presence of a thin gas film within confined gaps between the moving microstructure and adjacent surfaces. This damping mechanism is primarily governed by pressure-driven gas flow effects and manifests in two dominant forms: squeeze-film damping, which occurs during out-of-plane motion that compresses and expands the gas film, and slide-film damping, which arises from in-plane motion that induces shear flow in narrow gaps. The magnitude of air damping depends on parameters such as gap thickness, interacting surface area, operating frequency, and ambient pressure.

Even in vacuum-packaged MEMS gyroscopes, residual gas molecules trapped within micro-scale cavities continue to contribute to pressure-driven flow interactions, making air damping a significant source of energy loss. The damping coefficients associated with slide-film and squeeze-film effects are given by [19,20]:

$$= \frac{c}{(1+2\ \ )} \qquad (5.2)$$

$$= \frac{\quad}{\quad} \frac{c\quad\ ^{3}}{^{3}} \qquad (5.3)$$

where A is the effective sliding area, is the gas viscosity, d is the gap between moving plates, L_{sm} *and* W_{sm} denote the length and width of the sense mass, and, (/) is a geometry-dependent correction factor.

Under reduced pressure conditions, the effective viscosity is modified to account for rarefaction action effects and is expressed as [7]:

$$= \frac{c}{1+9.658\ \cdot} \qquad (5.4a)$$

where the Knudsen number K_n is defined as the ratio of the gas mean free path to the characteristic gap dimension h.The mean free path is given by:

$$= \frac{\quad}{2} \qquad (5.4b)$$

where k_B is Boltzmann's constant, T is the absolute temperature, d is the effective molecular diameter, and P is the absolute pressure. Consequently, air damping is strongly dependent on both pressure and temperature. The quality factor associated with air damping is expressed as:

$$= \frac{\quad}{+} \qquad (5.5)$$

where m is the effective mass and $_s$ is the sense-mode resonant angular frequency.

5.5.2 Viscous Damping

Viscous damping arises from shear friction between the resonating structure and the surrounding bulk fluid. Unlike air damping, which is driven by confined gas flow, viscous damping occurs even in unconfined environments as the moving structure drags adjacent fluid layers, generating shear stresses that dissipate mechanical energy as heat. This damping mechanism depends primarily on fluid viscosity, device geometry, and oscillation velocity.

The quality factor associated with viscous damping is given by [11]:

$$= \frac{\quad}{3} \; \frac{\quad}{2\,c} \qquad (5.6)$$

where $_s$ is the density of the structural material and is the density of the surrounding fluid.

5.5.3 Thermoelastic Damping

Thermoelastic damping (TED) is a fundamental intrinsic loss mechanism in MEMS gyroscopes. It originates from irreversible heat flow induced by cyclic mechanical strain during vibration. As the structure alternately compresses and expands, temperature gradients are generated, leading to heat conduction and associated energy loss. TED is particularly significant in high-frequency and high-Q resonant structures.

The quality factor associated with thermoelastic damping is given by [13]:

$$\frac{1}{\quad} = \frac{\quad}{\quad} \; \frac{\quad}{1\;(\quad)} \qquad (5.7)$$

where E is Young's modulus, is the coefficient of thermal expansion, T_0 is the absolute temperature, C_v is the heat capacity at constant volume, and is the thermal relaxation time.

5.5.4 Material (Rayleigh) Damping

Material damping, also known as intrinsic or Rayleigh damping, is energy dissipation within the structural material itself due to internal friction mechanisms such as viscoelasticity, dislocation motion, and grain boundary effects. Using Rayleigh damping coefficients and , the damping ratio for a vibration mode with angular frequency $_n$ is expressed as [21]:

$$= \frac{\quad}{2} \quad \frac{\quad}{2} \qquad (5.8)$$

The corresponding quality factor is given by:

$$= \frac{\quad}{\quad} \qquad \text{where} \quad = \; 1 \; 2\frac{\; - \;}{-} \qquad = \frac{\; - \;}{-} \qquad (5.9)$$

The Rayleigh coefficients are determined from experimentally measured quality factors at two distinct frequencies.

5.5.5 Anchor Loss

Anchor loss, also known as support loss, arises from the transmission of vibrational energy through the supporting anchors into the substrate. This loss mechanism becomes particularly significant in high-Q vacuum-operated devices, where other damping contributions are minimized. For structures supported by plate-like anchors, the anchor loss is given by [22,23]:

$$^{-1} = -[\ {}_1(-)^{2} + {}_2(-)^{5} + {}_3(-)^{3}\ ] \tag{5.10}$$

where w and l denote the width and length of the attachment region, d and d_p are the characteristic dimensions of the resonating structure and support plate, and A_1, A_2, and A_3 are dimensionless coefficients.

5.5.6 Acoustic Damping

Acoustic damping results from the radiation of elastic waves into the surrounding medium or substrate as the MEMS structure vibrates. This mechanism converts mechanical energy into acoustic energy and depends on vibration mode shape, radiation efficiency, and the acoustic properties of the surrounding medium. The quality factor associated with acoustic damping is given by [24,25]:

$$= \frac{}{2} \tag{5.11}$$

where c is the speed of sound in the surrounding medium and $_r$ is the radiation efficiency.

5.5.7 Consolidated Damping Considerations

The various damping mechanisms discussed above are influenced by a combination of factors, including device geometry, operating frequency, material properties, mode shape, ambient pressure, and temperature. Table 5.1 outlines the various factors that influence the different damping mechanisms relevant to our MEMS gyroscope designs. In the present study, geometry and material parameters are fixed, while the effects of pressure, temperature, and operating frequency are systematically investigated. Air damping, viscous damping, and acoustic damping are analysed primarily as functions of pressure and temperature, whereas thermoelastic damping is examined solely as a function of temperature. Anchor loss is evaluated based on geometric ratios, and the temperature-dependent Rayleigh damping is also accounted for.

The combined effect of all identified damping mechanisms on the total quality factor is evaluated for both VSM and PSM designs. Analytical and empirical models, including those applicable in the high-Knudsen-number regime, are employed [19,23,26,27]. While these models are widely accepted, deviations arising from fabrication tolerances, packaging conditions, and non-continuum gas effects are also discussed. Comparisons with state-of-the-art designs are presented to contextualize the predicted quality factor and sensitivity, thereby clarifying the applicability and limitations of the adopted models and providing a transparent framework for interpreting the damping performance of the proposed gyroscope architecture.

Table 5.1 Various type of damping and factors affecting each damping

Type of damping	Factors affecting the particular damping					
Air damping	Structure geometry, dimensions	Squeeze film/Slide film	Operating frequency	Medium Properties (Viscosity,Density, Molecular Mass)	Pressure	Temperature
Thermoelastic damping	Structure dimensions	-	Operating frequency	Material properties	-	Temperature
Rayleigh/ Material damping	Structure geometry, dimensions	-	Operating frequency	Material properties	-	Temperature
Anchor loss	Anchor geometry, dimensions, thickness	-	-	Material properties	-	-
Viscous damping	Structure geometry, dimensions	-	Operating frequency	Medium Properties	Pressure	Temperature
Acoustic damping	Anchor design, boundary conditions	Size of vibrating structure	Vibration Frequency and modes	Medium Properties (Density, speed of sound, density)	Pressure	Temperature

5.6 Results and Discussion: Effect of Ambient Pressure

Ambient pressure plays a dominant role in determining the magnitude of air damping, viscous damping, and acoustic damping in MEMS gyroscopes. As evident from Equations (5.7)–(5.8), the coefficients governing these damping mechanisms are inherently pressure dependent. This dependence primarily originates from variations in the mean free path of gas molecules, which directly influence the Knudsen number and, consequently, the effective damping coefficients. As pressure decreases, raRef action effects become more pronounced, necessitating the use of pressure-corrected effective viscosity models. In the following subsections, the variation of quality factors associated with air damping, viscous damping, and acoustic damping is systematically analysed as a function of ambient pressure for both VSM and PSM gyroscope designs.

5.6.1 Air and Viscous Quality Factor Variation

Figure 5.4a illustrates the pressure-dependent variation of the air-damping quality factor (Q_{air}) for both VSM and PSM architectures. For both designs, Q_{air} increases monotonically with decreasing pressure, consistent with the reduction in gas-mediated viscous interactions at lower pressures. Across the entire pressure range, the VSM design consistently exhibits a higher Q_{air} compared to the PSM design. This behaviour can primarily be attributed to the VSM's geometric configuration, which provides less confined air-escape paths and mitigates squeeze-film effects. In contrast, the PSM design experiences stronger squeeze-film damping due to the vertical confinement of the sense mass between fixed top and bottom electrodes, resulting in greater resistance to gas flow. A similar trend is observed for the viscous damping quality factor (Q_{vis}), as shown in Figure 5.4b. The VSM design demonstrates a higher Q_{vis} than the PSM across the investigated pressure range. This improvement further enhances the overall quality factor of the VSM gyroscope, particularly in operating environments where viscous damping accounts for a significant portion of total energy loss.

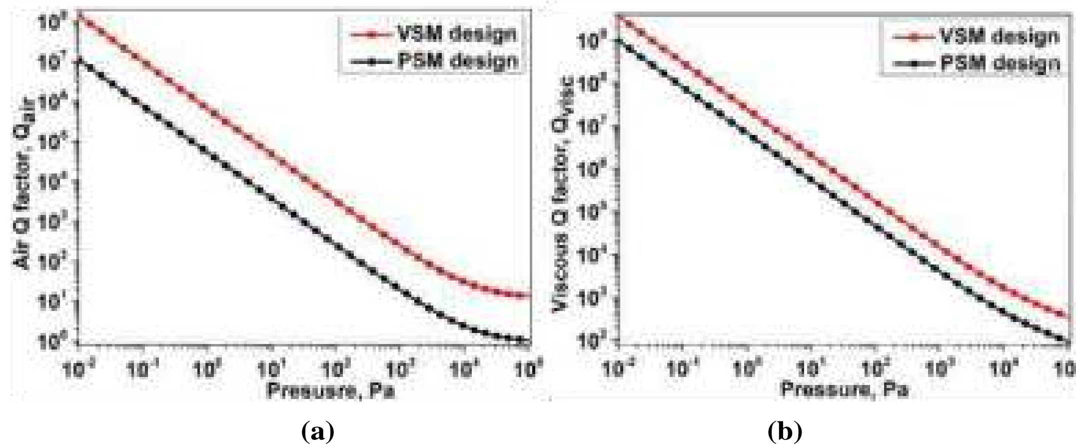

(a) **(b)**

Figure 5.4. Variation of (a) air-damping and (b) viscous-damping quality factors with ambient pressure for VSM and PSM gyroscope designs.

5.6.2 Acoustic Quality Factor Variation

The variation of the acoustic damping quality factor (Q_{acous}) with ambient pressure for both gyroscope designs is presented in Figure 5.5. Acoustic damping originates from the radiation of sound waves into the surrounding medium. As ambient pressure increases, the surrounding medium becomes denser, leading to higher acoustic impedance and increased energy dissipation. Consequently, Q_{acous} decreases with increasing pressure for both VSM and PSM designs. Throughout the entire pressure range, the VSM architecture consistently demonstrates a higher Q_{acous} than the PSM. This advantage is attributed to the vertical orientation of the sense mass and the higher modal frequency associated with the VSM design. These characteristics facilitate more efficient propagation of acoustic waves away from the active sensing region, thereby reducing acoustic energy loss.

5.6.3 Anchor and Rayleigh Quality Factor Variation

Anchor loss represents a geometry-dependent damping mechanism that is largely independent of ambient pressure and temperature. Figure 5.6 presents the variation of the anchor-loss quality factor (Q_{anchor}) for both VSM and PSM designs as a function of the geometric ratios w/l and d/d_p. As shown in Figure 5.6a, increasing the width-to-length ratio (w/l) of the attachment points results in a significant reduction in Q_{anchor}, indicating enhanced energy leakage into the substrate. Anchors with larger widths relative to their lengths are theRef ore more prone to dissipating vibrational energy. Similarly, Figure 5.6b shows that an increase in the characteristic dimension ratio (d/d_p) also leads to a reduction in Q_{anchor}, implying greater transmission of vibrational energy into the support structure.

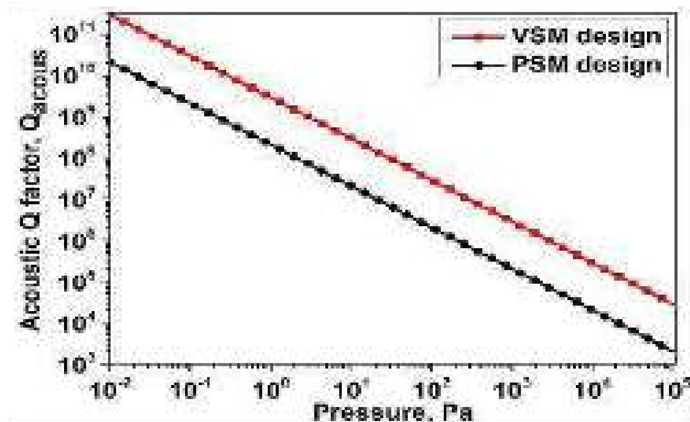

Figure 5.5. Variation of the acoustic damping quality factor with ambient pressure for VSM and PSM gyroscope designs.

Across both geometric ratios, the VSM design consistently exhibits a marginally higher Q_{anchor} than the PSM design. Furthermore, the slope of Q_{anchor} with respect to d/d_p is noticeably steeper than that with respect to *w/l*, highlighting a higher sensitivity of anchor loss to the d/d_p ratio. This observation underscores the critical importance of precise dimensional control particularly of d/d_p, in minimizing anchor-related energy dissipation.

Rayleigh damping models intrinsic material-related energy dissipation and is typically represented using empirical coefficients. Due to its phenomenological nature and the absence of a universally applicable theoretical relationship linking Rayleigh damping to specific geometric or environmental parameters, variations of $Q_{Rayleigh}$ with pressure or structural parameters are not examined in this study. Instead, a constant Rayleigh damping value is assumed to evaluate its relative contribution to the overall damping behaviour.

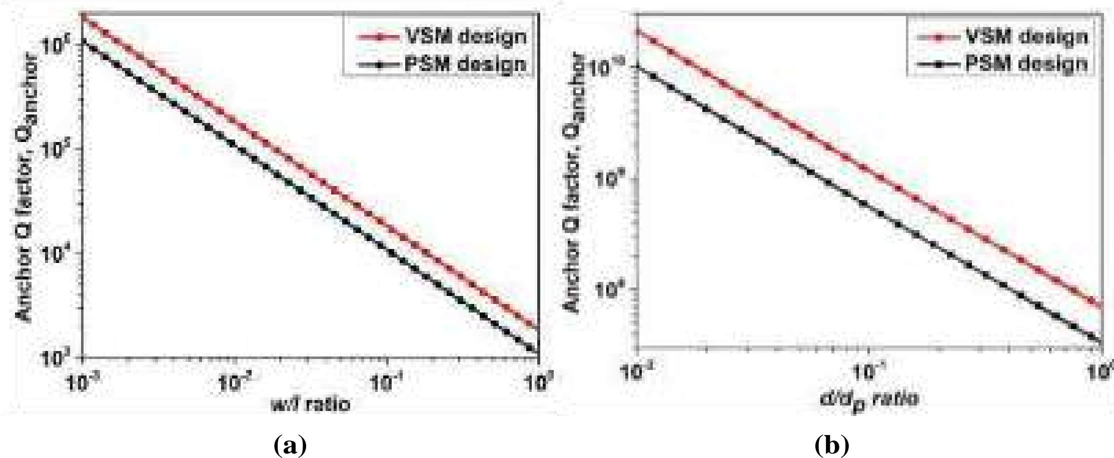

(a) **(b)**

Figure 5.6. Variation of the anchor-loss quality factor with (a) *w/l* ratio and (b) d/d_p ratio for VSM and PSM gyroscope designs.

5.6.4 Overall Quality Factor Variation with Pressure

A comprehensive comparison of all individual quality factors and the resulting total quality factor as a function of ambient pressure is presented in Figure 5.7. The results clearly indicate that the VSM design consistently achieves a higher overall quality factor than the PSM design across the entire pressure range. At low pressures (approximately 10^{-2} to 10 Pa), both designs operate in a vacuum-dominated regime where gas-related damping mechanisms are negligible. In this region, Q_{Total} for the VSM is primarily limited by Rayleigh damping and anchor loss, with values ranging between 10^5 to 10^6. For the PSM design, Q_{Total} is constrained by the same mechanisms but remains lower, typically between 10^4 to 10^5. This indicates that, even in vacuum conditions, the VSM architecture exhibits inherently lower intrinsic energy dissipation.

As ambient pressure increases, viscous and acoustic damping mechanisms become increasingly dominant, leading to a sharp reduction in Q_{Total} for both designs. Although the VSM's deep and compact structure makes it somewhat more susceptible to thermoelastic damping, it remains operational over a significantly wider pressure range. The VSM design demonstrates effective performance from high-vacuum conditions (10^{-2} Pa) up to moderate pressures (10^2–10^3 Pa), with limited operational capability even near atmospheric pressure.

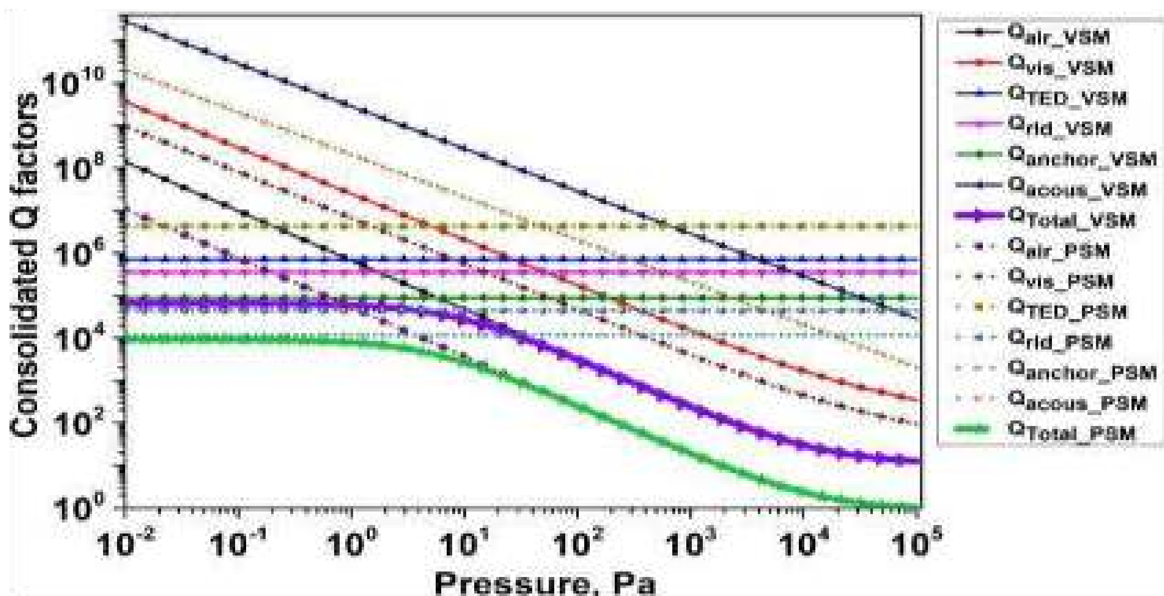

Fig. 5.7 Consolidated quality factors variation with pressure for both the VSM and PSM gyroscope designs

In contrast, the PSM design exhibits optimal performance only under high-vacuum conditions, typically below 10^{-1} Pa. Consequently, for applications requiring high quality factors across a broad range of operating pressures, the VSM architecture emerges as the pRef erred solution. Its superior performance stems from reduced intrinsic damping and more favourable fluid–structure interaction characteristics, making it particularly well suited for high-performance and miniaturized MEMS gyroscope applications.

5.7 Results and Discussion: Effect of Temperature

Temperature variations significantly influence several damping mechanisms in MEMS gyroscopes by altering the thermophysical properties of the surrounding medium and the intrinsic material behaviour of the structure. In this section, the effect of temperature on air damping, viscous damping, thermoelastic damping, Rayleigh damping, acoustic damping, and the resulting total quality factor is systematically analysed for both VSM and PSM designs.

5.7.1 Air and Viscous Quality Factor Variation

Figure 5.8a illustrates the variation of the air-damping quality factor (Q_{air}) with temperature for both VSM and PSM structures. For both designs, a clear decrease in Q_{air} with increasing temperature is observed, indicating enhanced air damping at elevated temperatures. This behaviour is primarily due to the temperature dependence of air's dynamic viscosity. As temperature increases, the dynamic viscosity of air increases according to Sutherland's law (μ $T^{3/2}$) [7]. In squeeze-film damping, this increased viscosity results in greater resistance to gas flow within the device's narrow gaps, thereby increasing energy dissipation and reducing Q_{air}. Across the entire temperature range, the VSM design consistently maintains a significantly higher air-damping quality factor than the PSM design. For example, at lower temperatures and atmospheric pressure, the VSM exhibits a Q_{air} of approximately 14, compared to about 1.7 for the PSM. This substantial difference highlights the inherent effectiveness of the VSM geometry in mitigating squeeze-film damping by reducing confinement and creating more favourable airflow paths.

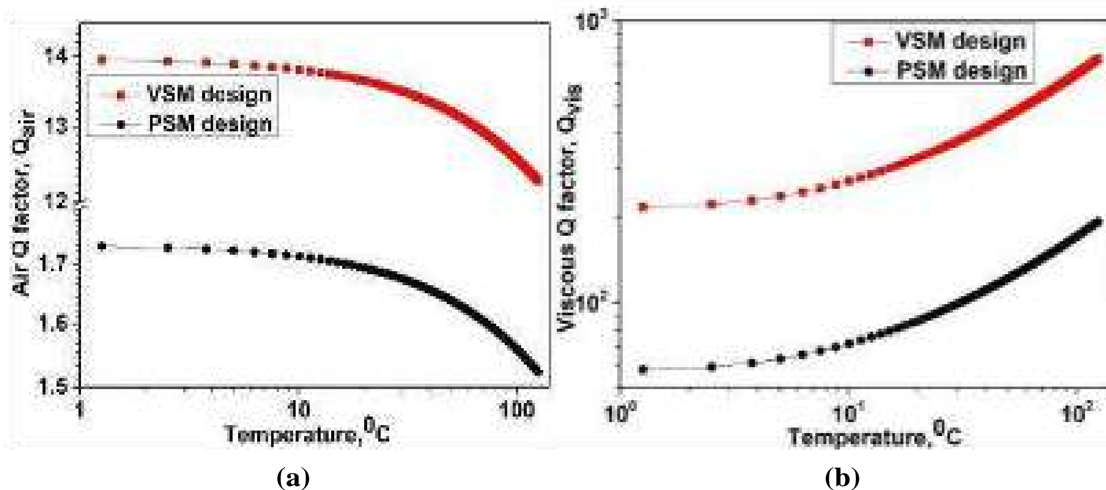

(a) (b)

Fig. 5.8 Variation of (a) air-damping (b) viscous-damping quality factors with temperature for both VSM and PSM design

Figure 5.8b shows the variation in the viscous-damping quality factor (Q_{visc}) with temperature. In contrast to air damping, Q_{visc} increases with increasing temperature for both designs, indicating reduced viscous damping at higher temperatures. This behaviour results from the combined temperature dependence of fluid viscosity, density ($_{flui}$), and raRef action effects. While the bulk dynamic viscosity increases with temperature, the fluid density decreases. Furthermore, at the microscale, higher temperatures increase the mean free path of gas molecules, leading to a higher Knudsen number and a reduction in the effective viscosity (μ_{eff}

) due to raRef action. The net effect is a reduction in the viscous damping coefficient, leading to an increase in Q_{visc}. Across the temperature range, the VSM design consistently exhibits a higher Q_{visc} than the PSM design, reinforcing its superior ability to mitigate fluid-related damping mechanisms.

5.7.2 Thermoelastic, Rayleigh, and Anchor Quality Factor Variation

The effect of temperature on thermoelastic damping is illustrated in Figure 5.9a, which shows a gradual decrease in the thermoelastic-damping quality factor (Q_{TED}) with increasing temperature for both designs. This trend is consistent with thermoelastic damping theory, which predicts that higher temperatures enhance irreversible heat flow associated with cyclic mechanical strain, thereby increasing energy dissipation. Across the investigated temperature range, the PSM design exhibits a higher Q_{TED} than the VSM design, indicating lower thermoelastic damping. This difference is attributed to the distinct geometries and characteristic dimensions of the two architectures. The VSM's deep, compact sense mass results in different thermal diffusion paths and characteristic length scales, which influence the product and may place the VSM closer to the peak-loss regime of thermoelastic damping. Figure 5.9b shows the variation of the Rayleigh-damping quality factor (Q_{rld}) with temperature. For both designs, Q_{rld} decreases with increasing temperature, signifying enhanced intrinsic material damping at elevated temperatures. This behaviour Ref lects increased internal friction and material losses due to temperature-dependent viscoelastic effects. Despite this trend, the VSM design consistently exhibits a significantly higher Q_{rld} (on the order of 5×10^5) than the PSM design (approximately 4×10^4), indicating superior intrinsic energy dissipation characteristics.

Anchor damping is generally considered to be weakly dependent on temperature over typical MEMS operating ranges. Since anchor loss is primarily governed by geometry and elastic properties of the structure and substrate, its temperature dependence is negligible compared to other damping mechanisms such as air or thermoelastic damping. Consequently, anchor loss is treated as a temperature-independent quality factor in this analysis.

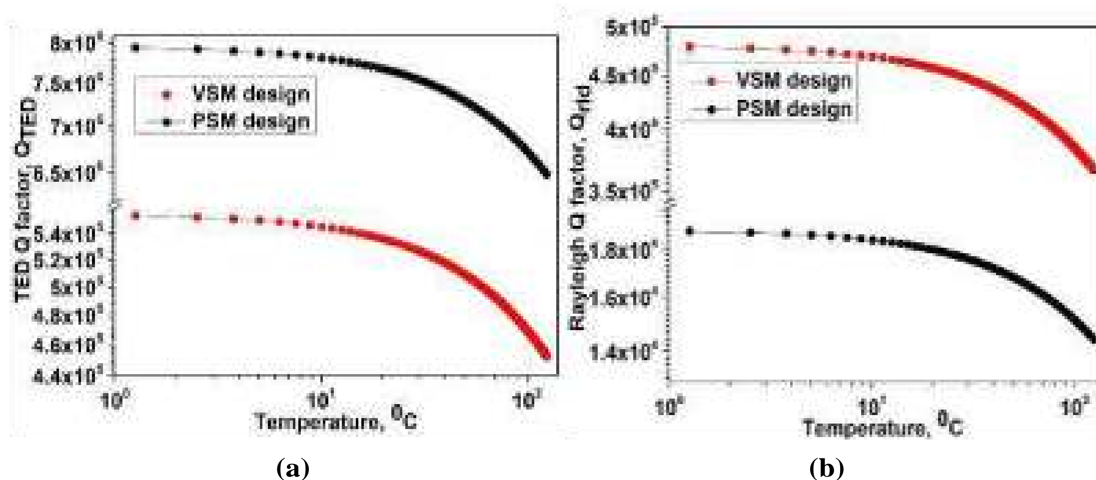

(a) (b)

Figure 5.9 Variation of (a) thermoelastic-damping and (b) Rayleigh-damping quality factors with temperature for VSM and PSM designs.

5.7.3 Acoustic Quality Factor Variation

The variation in the acoustic-damping quality factor (Q_{acous}) with temperature is shown in Figure 5.10. For both VSM and PSM designs, Q_{acous} increases with increasing temperature, indicating reduced acoustic damping at higher temperatures. At constant pressure, an increase in temperature decreases air density and increases the speed of sound. Since the acoustic damping coefficient is proportional to the product $_{fluid}$ c_{sound}, the reduction in density dominates, resulting in lower acoustic energy coupling and reduced damping. Throughout the temperature range, the VSM design consistently exhibits a higher Q_{acous} than the PSM design, further demonstrating its superior ability to suppress acoustic energy losses.

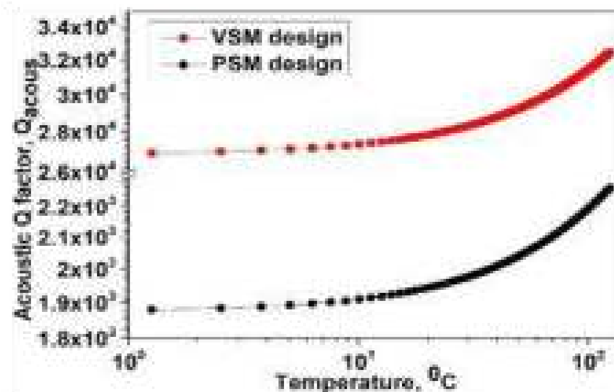

Figure 5.10 Variation of acoustic-damping quality factor with temperature for VSM and PSM designs.

5.7.4 Overall Quality Factor Variation with Temperature

A consolidated comparison of the individual damping-related quality factors and the resulting total quality factor (Q_{Total}) as a function of temperature at atmospheric pressure is presented in Figure 5.11. A key observation is the relatively weak dependence of Q_{Total} on temperature for both designs, in contrast to the strong sensitivity observed with pressure variation. This behaviour indicates that temperature-induced changes in fluid and material properties tend to partially compensate, resulting in a limited net effect on total damping.

At atmospheric pressure, the total quality factor is primarily governed by the lowest air-related damping components. Importantly, the VSM design consistently achieves a substantially higher Q_{Total} than the PSM design by approximately two orders of magnitude—across the entire temperature range. This result highlights the superior robustness of the VSM architecture under ambient operating conditions, driven by its inherently higher quality factors across multiple damping mechanisms, particularly those associated with air interaction. The limited temperature sensitivity of Q_{Total} further suggests that, at atmospheric pressure, intrinsic design features and damping mitigation strategies play a more dominant role than temperature-induced variations in fluid properties. This characteristic makes the VSM design particularly attractive for applications requiring stable performance over a wide temperature range.

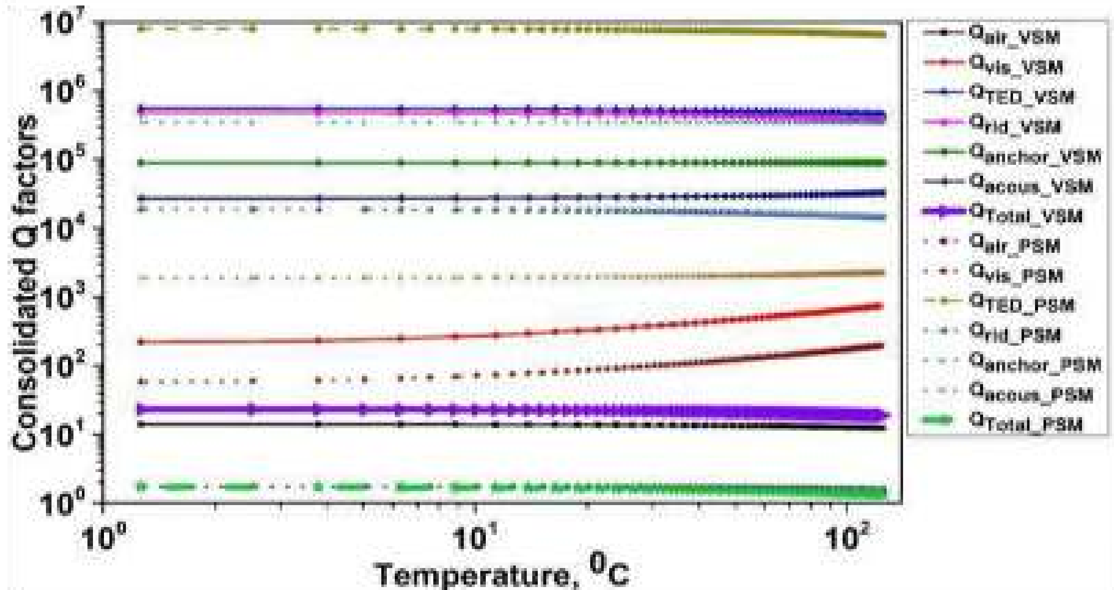

Figure 5.11 Consolidated variation of individual and total quality factors with temperature for VSM and PSM designs at atmospheric pressure.

5.8 Results and Discussion: Frequency-Dependent Damping Characteristics

In addition to environmental factors such as pressure and temperature, the operating frequency of a MEMS gyroscope plays a pivotal role in determining its dynamic response and overall performance. The sense-mode frequency directly influences the relative contributions of various damping mechanisms and, consequently, the achievable quality factor. Since sensitivity, bandwidth, and noise performance are intrinsically coupled to the quality factor, understanding the frequency-dependent damping behaviour is essential for the informed design and optimization of MEMS gyroscopes. In this section, the variation of individual quality factors—including air damping (squeeze-film and slide-film), viscous damping, thermoelastic damping, acoustic damping, anchor loss, and intrinsic (Rayleigh) damping—is systematically analysed as a function of frequency. This comprehensive investigation aims to elucidate the frequency-dependent damping landscape for both VSM and PSM gyroscope architectures and to identify the dominant loss mechanisms governing performance across the operational bandwidth. Figure 5.12 presents the frequency-dependent variation of individual damping-related quality factors for the VSM gyroscope operating at atmospheric pressure and room temperature. Distinct trends are observed for different damping mechanisms, Ref lecting their underlying physical origins. The air-damping quality factor, dominated by squeeze-film effects, exhibits approximately linear frequency dependence. This behaviour indicates that air damping remains strongly coupled to oscillation frequency due to pressure-driven gas flow in confined gaps. Similarly, the acoustic-damping quality factor also shows a near-linear dependence on frequency, Ref lecting the frequency-dependent radiation of acoustic energy into the surrounding medium.

The viscous-damping quality factor increases with the square root of frequency, consistent with shear-dominated energy dissipation in the bulk fluid. Anchor loss remains largely frequency-independent over the investigated range, as it is primarily governed by geometric ratios and

elastic wave transmission into the substrate rather than by oscillation frequency. Thermoelastic damping exhibits a characteristic V-shaped frequency dependence, reaching a minimum when the thermal relaxation time of the structure matches the vibration period. This behaviour is consistent with classical thermoelastic damping theory and highlights the existence of a frequency regime where thermoelastic losses are minimized. In contrast, Rayleigh damping follows a bell-shaped trend, showing approximately linear dependence at lower frequencies and inverse dependence at higher frequencies, Ref lecting its phenomenological nature. Across the entire frequency range, air damping—particularly squeeze-film damping—emerges as the dominant energy dissipation mechanism, effectively limiting the total quality factor under ambient conditions.

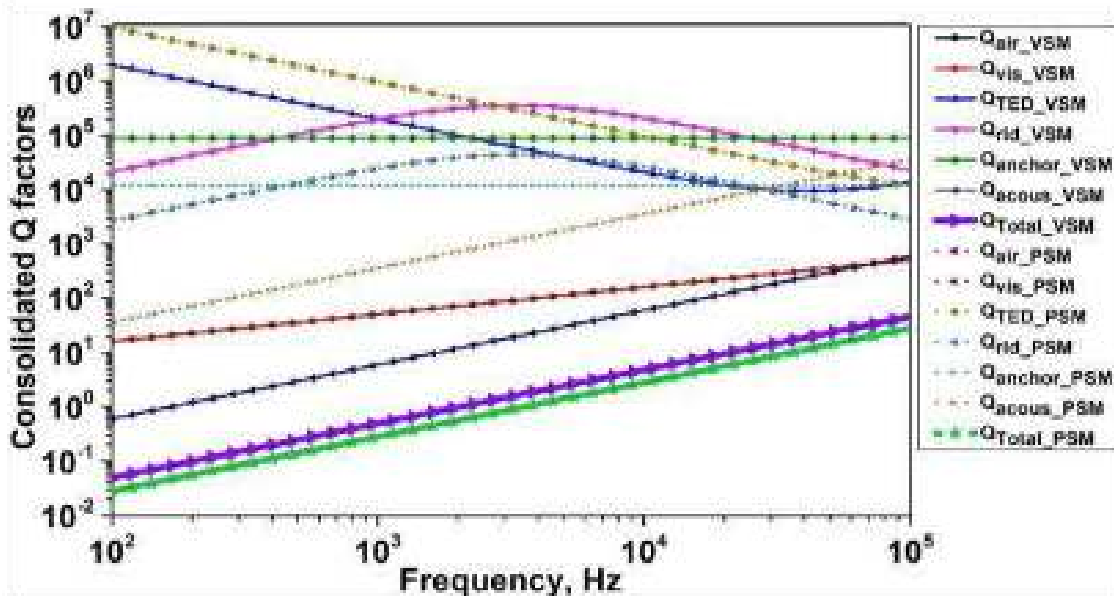

Figure 5.12 Frequency-dependent variation of individual damping-related quality factors for the VSM gyroscope at atmospheric pressure and room temperature.

A comparative evaluation of VSM and PSM gyroscope architectures reveals that the VSM design consistently achieves a higher total quality factor across the frequency spectrum at atmospheric pressure. Despite the PSM design exhibiting a significantly superior thermoelastic quality factor, which initially seems highly advantageous, this advantage is overpowered by its much lower air-related quality factors. These include essential components like air damping, viscous damping or even acoustic damping, all of which have significantly lower values. In addition to this, the PSM design also suffers from lower anchor and Rayleigh quality factors in general, which exacerbate its shortcomings.

The damping characteristics of the VSM design, on the other hand, are entirely air dependent and thus very low in normal environmental conditions. The reduction in damping enables the VSM design to outperform its PSM counterpart by a significant amount in multiple practical applications. It has demonstrated a total quality factor one to two orders of magnitude greater than the PSM design over the frequency span. This is due to its vertical sense mass layout, minimized structural damping and advantageous airflow routes. This makes the VSM

architecture substantially more suitable for high-performance MEMS gyroscopes operating outside ultra-high-vacuum environments.

5.9 Comparison of VSM and PSM Designs in Terms of Performance Parameters

The performance of MEMS gyroscopes is primarily evaluated in terms of bandwidth, sensitivity, noise, and quality factor, all of which are inherently interrelated. In this subsection, a comparative assessment of the VSM and PSM designs is presented to elucidate how architectural differences influence these key performance parameters.

5.9.1 Sensitivity Versus Quality Factor

Figure 5.13 illustrates the dependence of sense-mode displacement (z_0) on the sense-mode quality factor (Q_s) for both architectures. When the drive and sense modes operate at different frequencies, the displacement initially increases linearly with Q_s on a log–log scale. This region corresponds to a damping-limited regime, where increasing the quality factor directly enhances the mechanical response.

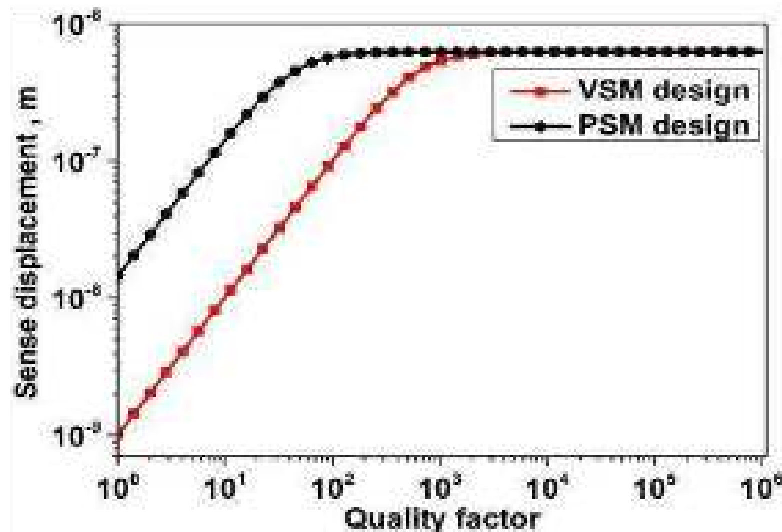

Figure 5.13 Variation of sense-mode displacement with sense-mode quality factor for VSM and PSM gyroscope designs.

As Q_s increases, the displacement eventually saturates, indicating a transition to a regime where the response is no longer limited by damping but by the inherent frequency mismatch between the drive and sense modes. Notably, both VSM and PSM designs achieve comparable maximum displacements at saturation, suggesting that their ultimate sensitivities can be similar under sufficiently high-Q conditions. However, the PSM design reaches this saturation threshold at a substantially lower Q_s than the VSM design under atmospheric pressure and room-temperature operation. This behaviour Ref lects the stronger damping constraints in the PSM architecture and highlights the advantage of the VSM design in sustaining higher effective quality factors before reaching saturation.

5.9.2 Bandwidth Versus Quality Factor

Figure 5.14 depicts the relationship between BW and Q for VSM and PSM gyros. The reverse holds true: high-Q (low-damping) systems have narrower resonance peaks and theRef ore smaller bandwidths, whereas low-Q systems produce broader peaks with greater bandwidth. A notable observation from Figure 5.14 is that the VSM design consistently exhibits a significantly higher bandwidth than the PSM design for any given quality factor. This behaviour is directly attributed to the inherently higher sense-mode resonant frequency of the VSM design (f_s 47 kHz) compared to that of the PSM design (f_s 3 kHz). Although a high Q factor is generally pRef erred to enhance sensitivity, a larger bandwidth—such as that offered by the VSM design—provides improved robustness against frequency drift, fabrication-induced variations, and environmental perturbations.

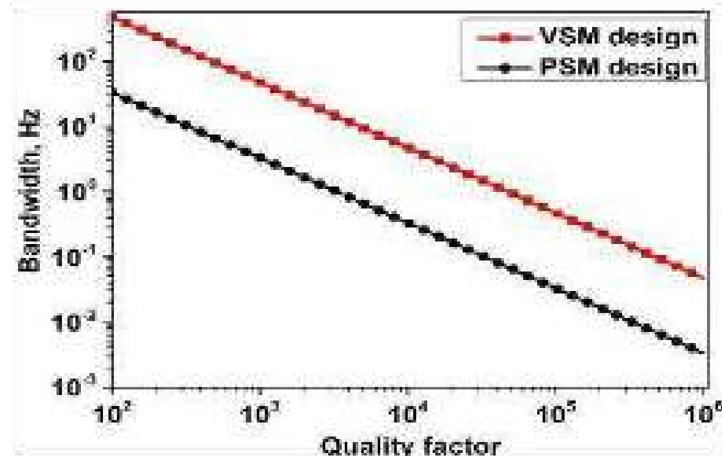

Figure 5.14 Variation of bandwidth with quality factor for VSM and PSM gyroscope designs.

5.9.3 Thermomechanical Noise versus Quality Factor

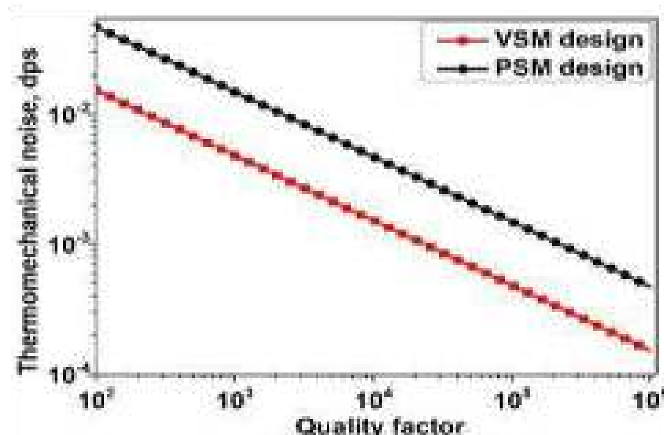

Figure 5.15 Variation of RMS thermomechanical noise with quality factor for VSM and PSM gyroscope designs.

Figure 5.15 shows the thermomechanical noise vs quality for both gyroscope designs. Thermomechanical noise, which is generated by random thermal motion in the resonator and medium, places a limit on achievable resolution. The opposite holds for noise: higher Q values result in lower energy dissipation and less thermal motion. The RMS thermomechanical noise for the VSM design is always lower than that of the PSM design for any Q. As a result, the VSM has optimized parameters such as increased resonant frequency and higher drive-to-sense mode coupling, enabling a lower effective noise floor for higher resolution operation.

5.9.4 Overall Performance Trade-Off and Design Implications

The results show that the peak sense-mode displacement at resonance are comparable for both designs if over quality factors are considered, where the VSM offers performance benefits. Its higher resonant frequency gives it a broader operational bandwidth, which helps in tolerating misalignment and environmental variations.

In addition, the inherently lower thermomechanical noise associated with the VSM design is critical for achieving high-resolution sensing. Using the design parameters, the damping coefficients and corresponding quality factors for both designs were calculated, and the consolidated results are summarized in Table 5.2 at room temperature and a pressure of 1 Pa. The VSM design demonstrates significantly higher quality factors than the PSM design for air damping (both squeeze-film and slide-film), Rayleigh damping, anchor loss, and acoustic damping. The vertical mode (VSM) architecture and small geometry of the VSM drastically reduces energy loss mechanisms for MEMS gyroscopes. However, structure and thermal diffusion characteristics mean it is more susceptible to thermoelastic damping (TED), signalling an important design trade-off in application selection.

A choice of VSM or PSM designs is based on application-specific parameters such as sensitivity, bandwidth, noise performance and stability. The VSM architecture is a stronger and comparatively more balanced MEMS gyroscope solution in high-performance applications. Its ability to simultaneously offer high bandwidth, low noise, and reduced footprint makes it particularly attractive for demanding applications where both performance and integration constraints are critical.

5.10 Sensitivity of Q_{Total} to Key Parameters

To identify the geometric and environmental parameters that most strongly influence the total quality factor (Q_{Total}), a comprehensive sensitivity analysis was performed using the closed-form damping expressions given in Equations (5) – (14), together with the aggregate loss relation in Equation (4). The objective of this analysis was to quantify both design-level sensitivities and fabrication-induced variations, thereby providing practical guidance for robust VSM gyroscope design.

5.10.1 Global Parameter Sensitivity Analysis

As an initial step, a global parameter sweep was conducted across realistic device dimensions and operating conditions representative of MEMS gyroscope fabrication and deployment. The investigated parameter ranges were: sense gap d = 3–10 μm, sense-mass width (w_{sm}) = 30–80 μm, sense-mass length (l_{sm}) = 100–250 μm, beam thickness (t_{bs}) = 6–12 μm, pressure (P) = 10^{2}-10^{4} Pa, and temperature (T) = 250–350 K. Variations in pressure and temperature were propagated through the Knudsen number Kn (P, T) and the effective viscosity μ_{eff}(Kn) using Equations 5.7a–b. The impact of these parameters on performance metrics, such as sensitivity

and the total quality factor, was evaluated, and the resulting trends are summarised in Table 5.3. This global analysis provides an overview of how geometric scaling and environmental conditions collectively shape the damping landscape and limit achievable $Q_{Total.}$

Table 5.2 The consolidated results of various damping for VSM and PSM design

Damping mechanism	Quality factor	VSM Design	PSM Design	Remarks
Air damping	$Q_{squeeze\ film}$	1.46×10^3	1.84×10^2	Less squeeze film and slide film damping due to the unique geometry and perpendicular orientation, making VSM design more effective against this loss mechanism.
	$Q_{slide\ film}$	1.16×10^6	2.54×10^5	
Thermoelastic damping	Q_{TED}	7.09×10^5	4.31×10^6	VSM design experiences more TED damping, this is due to its deeper, more compact structure and different thermal diffusion paths as compared to PSM design.
Rayleigh Damping	Q_{rld}	3.48×10^5	4.40×10^4	VSM design has less material damping as compared to PSM design
Anchor loss	Q_{anchor}	8.96×10^4	1.18×10^4	VSM is more effective in preventing leakage into the substrate through its anchors.
Viscous damping	Q_{vis}	1.92×10^4	1.35×10^4	Q for VSM is comparable to PSM design.
Acoustic damping	Q_{acous}	3.35×10^2	0.23×10^2	VSM design indicates less radiation loss into the surroundings

5.10.2 Local (Fabrication-Induced) Sensitivity Analysis

To assess manufacturability and robustness, a local sensitivity analysis was conducted using realistic lithographic and process-induced dimensional variations. In state-of-the-art MEMS fabrication, critical dimension (CD) variations can be approximated by:

$$= (\quad 1) \quad — \tag{5.15}$$

where is the exposure wavelength, NA is the numerical aperture of the projection lens, and K1 is a process-dependent constant accounting for mask quality, photoresist characteristics, and illumination conditions. As a conservative worst-case scenario, ±5% variations were introduced in key geometric parameters, including sense gap (d), sense-mass width (w_{sm}), sense-mass length (l_{sm}), sense beam thickness (t_{bs}), sense beam width (w_{bs}), and sense beam length (l_{bs}), along with ambient pressure (P) and temperature (T). The resulting shifts in normalized sensitivity (S_p/DeltaS_p) and fractional variation in total quality factor (Q/Q) were evaluated. The consolidated results, including nominal values, design ranges, and fabrication-induced variations, are presented in Table 5.3.

5.10.3 Key Sensitivity Findings

Across both the global parameter sweep and the local ±5% variation analysis, the sense gap (d) consistently emerges as the most influential parameter governing Q_{Total}. This dominant sensitivity arises from the cubic dependence of squeeze-film damping on gap height, yielding a high sensitivity coefficient (S_d +3). The lateral sense-mass dimensions, particularly w_{sm} and l_{sm}, represent the next most influential parameters (Sw_{sm} −3, Sl_{sm} -1), Ref lecting increased gas confinement and enhanced air damping with larger planform areas. In contrast, beam-geometry parameters (t_{bs}, w_{bs}, l_{bs}) primarily affect the resonant frequency and thermoelastic damping and theRef ore exhibit a comparatively weaker influence on Q_{Total}. Environmental

parameters show expected trends: increasing pressure significantly reduces Q_{Total} due to enhanced gas-film damping, while temperature exerts a secondary influence, partially compensating for effects across different damping mechanisms. A ±5% variation in either the sense gap (d) or the sense-mass width (w_{sm}) results in a maximum variation of approximately ±12.8% in Q_{Total}, confirming these parameters as the most fabrication-sensitive design levers. Moderate sensitivity is observed for l_{sm} and ambient pressure, whereas beam parameters and temperature contribute minimally to the overall Q_{Total} variation.

Table 5.3 Sensitivity of Q_{Total} to Design and ±5% Fabrication Variation.

Parameter and Nominal Value	Design parameter sensitivity		Manufacturable design parameter sensitivity (5% of nominal value)		Qualitative Influence	Design Implication
	Variation Range	Normalized Sensitivity (S_p/S_p)	S_p/S_p variation	Normalized Q factor (Q/Q)		
Sense gap (d), 5 µm	3-10 µm	+2.1 to +3.0	±0.05	±12.8 %	Strong Positive	Increasing the gap reduces squeeze-film damping and significantly increases the quality factor (Q).
Sense mass width (w_{sm}), 500 µm	300-600 µm	–2.5 to –3.0	±0.04	11.5 %	Strong Negative	A larger width increases squeeze-film damping, while a smaller lateral span improves Q.
Sense mass length (L_{sm}), 500 µm	300-600 µm	–0.8 to –1.2	±0.02	5.0 %	Weak-Moderate Negative	Larger planform increases damping; compact mass improves Q.
Beam thickness (t_{bs}), 8 µm	6-12 µm	+0.1 to +0.3	±0.01	±1.0 %	Weak Positive	Increased stiffness slightly reduces strain-based loss.
Beam width (w_{bs}), 55 µm	30-80 µm	–0.1 to –0.4	±0.01	1.25 %	Weak-Moderate Negative	Beam width affects mode shape and TED, but has limited effect on total Q.
Beam length (l_{bs}), 150 µm	100-250µm	+0.2 to +0.4	±0.01	±1.5 %	Weak Positive	Longer beams alter resonance frequency; minor influence on Q.
Ambient Pressure (P), 1 Pa	10^{2} - 10 Pa	–1.0 to –3.0	±0.03	10 %	Strong Negative	Vacuum operation is critical; pressure directly governs air damping.
Temperature (T), 300 K	250-350 K	–0.1 to –0.4	±0.01	1.25 %	Weak Negative	Temperature affects viscosity and thermal relaxation; secondary effect

5.10.4 Interpretation and Design Implications

The tornado-style plot in Figure 5.16 shows the sensitivity of each parameter towards the normalized change of Q_{Total} with respect to ±5% fabrication uncertainty. The most significantly responsible mechanism to total damping sensitivity is air confinement, which is mainly subject to sense gap and lateral mass dimensions. TheRef ore, maximizing Q_{Total} in VSM gyro is dependent on accurate gap design and a reduction of lateral sense mass; beam geometry can be

tuned for stiffness and frequency with minimal impact on total damping. This decoupling of stiffness design from dominant damping mechanisms provides an important degree of freedom in achieving robust, high-performance VSM gyroscope designs. A tornado plot of worst-case normalized sensitivity Q/Q (%) with ±5% fabrication variation on important parameters is shown in Figure 5.16. The sense gap d and the sense-mass width w_{sm} have the most considerable effect, supporting that squeeze-film confinement is the dominant damping process.

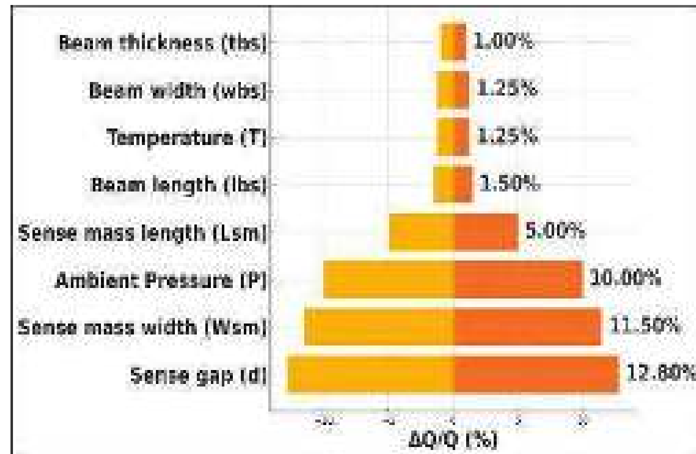

Figure 5.16 Tornado Plot for 5% fabrication variation sensitivity

5.11 Design and Experimental Validation

5.11.1 Comparative Quality Factor–Pressure Behaviour Across State-of-the-Art Architectures

A comparative analysis of the quality factor variation with ambient pressure between various MEMS gyroscope designs, as well as state-of-the-art ones was performed in order to validate the proposed VSM architecture's effectiveness. A comparison of Q-factor versus pressure for three structural categories is shown in Figure 5.17a:
(i) the proposed VSM design,
(ii) a previously reported quasi-VSM comb-type architecture [26], and
(iii) a conventional PSM architecture [27].
The quasi-VSM design described in Ref A lateral capacitance motion system integrated into [26] mimics the sweep dynamics of conventional VSMs, but consciously avoids a significant thick VSM with a complex spring arrangement that is characteristic to those proposed for our design. With the aim of enabling a fair and thorough comparison between these diverse architectures, we have, for the first time, compared all three designs within the same uniform pressure range from 10 ^{2} to 10 Pa, plotting the results on logarithmic axes. Finally, a work [27] deeply accounts for the more complex and synergic effects originating from air damping and viscous damping agents. While the PSM (Plate-Spring Mechanism) is characterized by a unique and dedicated configuration of plate-spring mechanism with quite a small effective vacuum gap, this configuration does not lead to any significant quality factor improvement as the pressure decreases. The significant high inertia effect caused through interaction of slide-film and viscous damping, more prominent because of the low-pressure atmosphere leads to this operation manner. In comparison, this performance of the quasi-VSM comb-type design

is considerably better found in the raRef ied-gas regime, validating the benefits of its lateral motion combined with a smaller confinement induced by squeeze-film effects. The quality factor shows an unequivocal and stable increasing trend when both Ref designs are rigorously normalized to the operation environment parameters unique to the proposed VSM implementation (especially a resonant frequency around 47 kHz and a sensing gap of exactly 5 μm). This is particularly evident that the nature of the damping response is predominantly shaped by geometrics. It is not dictated by spectral elements associated with material loss. This enhancement is from a reduction of squeeze-film stiffness per unit lateral displacement and an earlier onset to the Knudsen-number dominated regime. As a consequence of this, even those architectures which were never intended for VSM behaviour show large improvements as they are operated under conditions similar to VSM. More importantly, the entire quality factor evaluation results reveal that the proposed VSM architecture demonstrates unchanging high-quality factor under all pressure ranges, which further indicates superior robustness of damping performance for this design against typical PSM and quasi-VSM.

5.11.2 Experimental Validation

Experimental validation of the proposed damping-suppression strategy is presented in Figure 5.17b, which re-analyses the quasi-VSM design reported in Ref [28]. Q, the quality factor of MEMS gyroscopes, as defined in practice requires caRef ul experimentation to energize the resonant mode while repressing pressure and thermal perturbances. The quality factor can be extracted through frequency-domain measurements of the bandwidth or in time-domain ring-down analysis. The experimental method described in Ref And [28] represents a widely accepted and well-constituted manner within the field that also just seems to include everything, vacuum packaging, temperature regulation, 3-dB bandwidth analysis to truly effortlessly and appropriately tie down these quite complex devices damping behaviour. The study cited as Ref To evaluate the quality factor, $Q = f_0 /\ \ f$ [28], caRef ul extraction of quality factor was carried out using the full-width-at-half-maximum (FWHM) method. Wherein f_0 is the resonance frequency and f is bandwidth at –3 dB point of resonance peak. The results presented herein show that the quality factor reaches a maximum of around 10 Pa at low pressure and then decreases slowly, monotonically, since the effect of viscosity damping improves with increased pressure.

The simulated trend of the quality factor, as predicted by the current multi-mechanism damping model, shows a remarkable agreement with experimental data and furthermore reaffirms the accuracy and confidence in this analytical framework employed over multiple regimes, such as thermoelastic, anchor-loss and raRef ied-gas. Specifically, when the same structure mentioned in Ref Applying [28] caRef ully, with VSM working parameters, sensing gap of 5 μm and resonant frequency at approximately 47 kHz, can lead to noticeable improvement in the quality factor for the whole scale of pressure conditions. This is marked by a lift of the quality-factor floor, rising an entire order of magnitude, up and to the right in gas-damping regime dominance onset delays to much higher pressures, this marks a significant improvement in performance.

These results demonstrate that:

- The performance enhancement achieved through VSM implementation is geometry-driven. They are not material- or mode-specific.
- Existing quasi-VSM or comb-type layouts can be Ref itted into VSM-like operation to achieve immediate quality-factor improvement.
- The damping-mitigation strategy we proposed is scalable and generalizable.

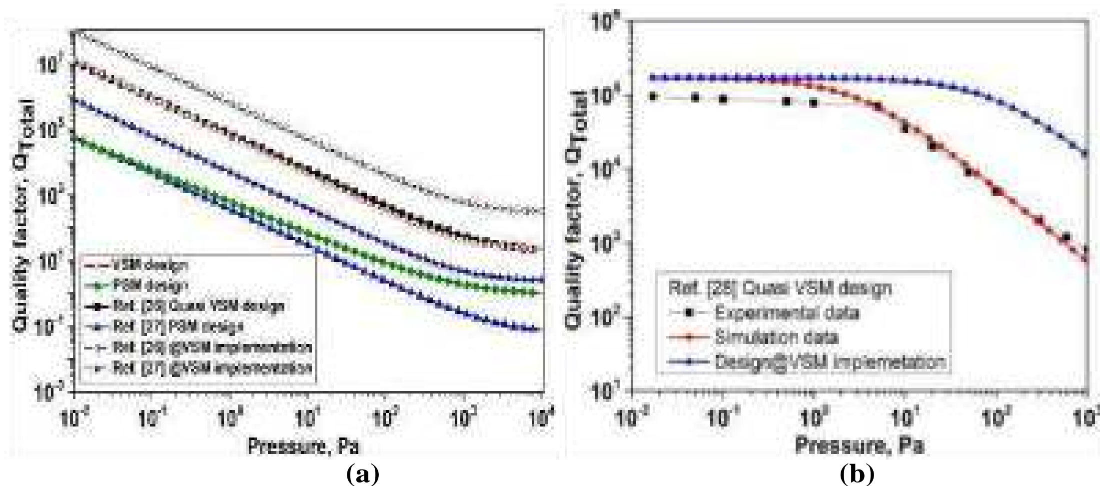

(a) (b)

Figure 5.17 (a) Quality factor vs pressure showing design validation. (b) Q_{Total} vs pressure plot showing experimental validation.

As demonstrated in Figures 5.17a and 5.17b, this extraneous damping suppression process is effective in establishing a vertical spatial modulation of the sense mass that is more optimal than that of traditional PSM and comb-type architectures, as shown in the simulated/comparison behaviour for both measured data.

5.12 Mitigating Unwanted Damping Mechanisms in MEMS Gyroscopes

Despite the advantages of the VSM architecture, it remains difficult to eliminate damping mechanisms in MEMS gyroscopes. Spring suspensions and anchors can be optimised to minimise coupling loss with the support, but elastic wave coupling into the substrate still provides a pathway for anchor loss. To address wave propagation, more advanced isolation methods are being investigated. Gas trapped in vacuum-packaging devices causes fluid damping over time. Although vent holes and gap optimization can aid PSM designs. But controlling passive residual gas dynamics over extended times remains a challenge. Further reducing fluid damping in a VSM design requires novel insights that not only provide more open flow but also maintain structural integrity and performance.

Surface-related phenomena, such as roughness, contamination, or stiction, reduce the energy content of devices with high surface-to-volume ratios. It is hard to optimize them at the atomic or nanometre scale for VSM and PSM architectures. Because the thermodynamic degree of freedom couples with the mechanical motion, it is difficult to isolate damping contributions (e.g. thermoelastic damping and anchor loss). Variations depend on temperature, making stable performance across its operating ranges hard to accomplish. Damping characteristics can be affected by environmental factors, such as ageing, humidity, and vibration, leading to a focus on long-term stability in research. Damping mechanisms must be addressed holistically to not only improve MEMS gyroscope performance but also its reliability. From the analyses in Equations (5.4)–(5.14) and the results in Figures 5.13–5.15, it is concluded that the VSM architecture with geometry-aware damping management significantly improved MEMS gyroscope robustness and performance.

5.13 Conclusions

This chapter provided a detailed exploration of damping mechanisms and performance trade-offs for a VSM MEMS gyroscope, measured against a standard design PSM with the same sense-mass area. This chapter builds on the previous demonstration of improved sensitivity, bandwidth and noise performance of the VSM architecture by selectively damping the specific mechanisms that degrade performance. Here, we aimed to take this a step further and establish the physical origins behind these improvements via a mechanism-wise analysis of damping throughout different axes. All dominant damping mechanisms, including air damping, viscous damping, thermoelastic damping, Rayleigh (material) damping, anchor loss, and acoustic damping, were systematically analysed, and their individual contributions to the total quality factor (Q_{Total}) were quantified for both designs. In addition, the dependence of key performance parameters such as sense displacement, bandwidth, and thermomechanical noise on the quality factor was evaluated to provide a system-level perspective.

The key findings of the chapter are summarized as follows:

- **Pressure-dependent damping:** Both VSM and PSM designs exhibit similar qualitative trends with pressure. However, the VSM architecture maintains a significantly higher overall quality factor, with Q_{Total} being approximately 8× higher than that of the PSM design. For both architectures, the tolerable pressure range without appreciable degradation in Q_{Total} extends up to approximately 1 Pa.

- **Temperature-dependent damping:** The temperature dependence of the quality factor follows similar trends for both designs. Except for thermoelastic damping (Q_{TED}), all other damping mechanisms consistently exhibit higher quality factors in the VSM design. As a result, the net Q_{Total} of the VSM gyroscope is approximately 2.75× higher than that of the PSM across the investigated temperature range.

- **Frequency-dependent behaviour:** The individual damping mechanisms are frequency dependent for both architectures. Due to, superior geometry and elevated operational frequency, the VSM configuration yields a net figure of merit that is approximately 1.6 times greater than that of the PSM across the frequency spectrum.
- **Q(max) at maximum SNR**: The VSM design offers superior sense-mode displacement for quality factors up to Q 100, suggesting that it will respond better in damping-limited regions. For very high Q factors (Q>1000) VSM and PSM designs approach similar displacement levels, revealing frequency-mismatch-limited behaviour.
- **Bandwidth:** The VSM design has a significantly larger operational bandwidth (factor of 20, for all quality-factor values) than that of the PSM design due primarily to its higher sense-mode resonant frequency.
- **Noise performance:** The thermomechanical noise for the VSM gyroscope is consistently lower than for PSM design with a factor of approximately 3.33 reduction, achieving a higher resolution and better signal.
- **Sensitivity to fabrication variations:** A realistic sensitivity analysis accounting for reasonable tolerances in fabrication reveals that the maximum Q_{Total} deviation is between the limits of ±12.8%. One of the parameters, most notable and sensitive to changes in fabrication processes, is that of the sense gap, which emerges as critically important.
- **VSM systems design validation:** The extensively proposed model was thoroughly calibrated with numerous designs and their experimental outputs, leading to an elaborate

report describing the good correlation between predictions based on analytical calculations and extensive computations compared with measured data.

Finally, this chapter lays out precisely how enhanced performance from the VSM gyroscope is fundamentally linked to its geometry and resultant trade-offs among squeeze-film confinement, fluid–structure interactions, and operating frequency. Mainly because they are more susceptible to thermoelastic damping, which must be accounted for, the VSM architecture is repeatedly seen to outperform its PSM counterpart. And this is most effectively realized when there is a proper balance between the key metrics of quality factor, bandwidth, noise, and robustness. These important results confirm that the VSM structure is a more suitable design paradigm for high-performance MEMS gyroscopes, which are holistically analyzed and described in detail in this chapter.

References

[1] Chen Z, Yan K, Wang X, Li R, Zhang A, Wang X, Wang Y, Gao P, Li H, Wang C, Zhang J, Liu M and Lu Q 2025 MEMS gyroscopes in different operation modes: A review Measurement (Lond) 249

[2] Khan H, Rashid A S A and Nasir N 2025 Evaluation and calibration of MEMS-IMU sensors for real-time landslide detection Engineering Research Express 7

[3] Hossain N, Mahmud M Z Al, Hossain A, Rahman M K, Islam M S, Tasnim R and Mobarak M H 2024 Advances of materials science in MEMS applications: A review Results in Engineering 22

[4] Xiao Y, Meng J, Yan H, Wang J, Xin K and Tao T 2023 Research on the application of MEMS gyroscope in inspecting the breakage of urban sewerage pipelines Water (Switzerland) 15

[5] Huang W, Yan X, Zhang S, Li Z, Hassan J N A, Chen D, Wen G, Chen K, Deng G and Huang Y 2023 MEMS and MOEMS gyroscopes: A review Photonic Sensors 13

[6] Shaveta, Bhan R K and Chaujar R 2025 MEMS sensors: Journey from biological inspiration to quantum frontiers Book Chapter 12 331–361

[7] Bao M-H 2000 Handbook of Sensors and Actuators 8 Micro Mechanical Transducers Pressure Sensors, Accelerometers and Gyroscopes

[8] Yi H, Fan B, Bu F, Chen F and Luo X Q 2024 Research on energy dissipation mechanism of cobweb-like disk resonator gyroscope Micromachines (Basel) 15

[9] Bu F, Fan B, Xu D, Guo S and Zhao H 2021 Bandwidth and noise analysis of high-Q MEMS gyroscope under force rebalance closed-loop control Journal of Micromechanics and Microengineering 31

[10] Jujjuvarapu S K, Devsoth L, Akarapu A, Pal P and Pandey A K 2024 Frequency and damping analysis of hexagonal microcantilever beams Sensors and Actuators A Phys 375

[11] Jia Z, Wang Y, Wang X, Xu X, Sun J, Sun M, Bai J, Huang W and Lu Q 2025 Investigation of viscous damping in perforated MEMS devices Microsyst. Nanoeng. 11

[12] Colin M, Thomas O, Grondel S and Cattan E 2020 Very large amplitude vibrations of flexible structures: Experimental identification and validation of a quadratic drag damping model J. Fluids Struct. 97

[13] Odira I, Byiringiro J and Keraita J 2024 Probing multimode thermoelastic damping in MEMS beam mass structure J. Vib. Eng. Technol. 12 4561–4570

[14] Nguyen M N, Ha N S, Nguyen L Q, Chu H M and Vu H N 2017 Z-axis micromachined tuning fork gyroscope with low air damping Micromachines (Basel) 8

[15] Mo Y, Du L, Qu B B, Peng B and Yang J 2018 Squeeze film air damping ratio analysis of a silicon capacitive micromechanical accelerometer Microsystem Technologies 24 1089–1095
[16] Wang A, Sahandabadi S, Harrison T, Spicer D and Ahamed M J 2022 Modelling of air damping effect on MEMS resonators Microsystem Technologies 28 2529–2539
[17] Shaveta, Bhan R K and Chaujar R 2025 Enhancing MEMS gyroscope performance with vertical sense mass design Defence Science Journal 75 758–770
[18] Shaveta, Bhan R K and Chaujar R 2024 Tapered-based novel thermal compensation techniques for enhanced performance of MEMS-based gyroscope Proc. IC-ETITE
[19] Shaveta, Bhan R K and Chaujar R 2025 Design optimization of MEMS gyroscope for enhanced sensitivity, bandwidth and noise reduction Micro and Nanostructures 206
[20] Shaveta, Bhan R K, Lamba S S, Gond V and Chaujar R 2025 Mitigating thermal effects in MEMS gyroscopes: A novel substrate integration approach Sensors and Actuators A Phys 392
[21] Cruz C and Miranda E 2017 A critical review of the Rayleigh damping model 16th World Conference on Earthquake Engineering
[22] Dounkal M K, Bhan R K and Kumar N 2020 Improved vertical comb type capacitive accelerometer using SOI technology J. Micromech. Microeng. 30
[23] Judge J A, Photiadis D M, Vignola J F, Houston B H and Jarzynski J 2007 Attachment loss of micromechanical resonators J. Appl. Phys. 101
[24] Williams E G 1983 Acoustic power radiated from planar sources J. Acoust. Soc. Am. 73 1520–1524
[25] Fahy F and Gardonio P 2007 Sound radiation by vibrating structures Sound and Structural Vibration 135–241
[26] Pistorio F, Saleem M M and Somà A 2021 Dual-mass resonant MEMS gyroscope with electrostatic tuning Applied Sciences 11 1–20
[27] Bao M and Yang H 2007 Squeeze film air damping in MEMS Sens. Actuators A Phys 136 3–27
[28] Zhou J, Shen Q, Xie J B, Cao P P and Yuan W Z 2018 Energy dissipation modelling of silicon micromachined gyroscope Shock and Vibration.

CHAPTER 6

ROBUSTNESS IMPROVEMENT IN MEMS GYROSCOPES STRUCTURE THROUGH NOVEL SUBSTRATE INTEGRATION TECHNIQUES

- *This chapter proposes a novel packaging-level thermal substrate approach. This establishes a controlled temperature offset (~25 °C) between the MEMS gyroscope and the package base, significantly reducing heat transfer to the sensor.*
- *Thermal stability enhancement through synergistic thermal substrate integration and thermally engineered gyroscope design is proposed to minimize heat flow into sensitive regions such as the sense mass.*
- *Reduced sense deflection temperature dependence by approximately 31times, from 2.7 × 10 µm/°C to 8.6 × 10 µm/°C, and lowered scale factor temperature sensitivity from 232 ppm/°C to 6 ppm/°C.*
- *Demonstrated improved noise performance and bandwidth stabilization. This is validated through steady-state and transient thermal analyses.*
- *Confirmed structural reliability and fabrication feasibility via thermal stress analysis and etching experiments, with superior performance validated against existing literature.*

6.1 Introduction

MEMS gyroscopes have become ubiquitous because of their small size, low power consumption, and high accuracy [1–4]. Their critical applications span diverse sectors, including automotive, aerospace, defence, industrial automation, health care, consumer electronics, and virtual and augmented reality [5–8]. The accurate output from the MEMS gyroscope ensures reliable performance of all the systems under varying environmental conditions (temperature, pressure, and humidity). Consequently, understanding and compensating for the behaviour of the device under different conditions is of paramount importance.

The primary focus of this study was to analyze the impact of temperature variations on key performance parameters. Numerous studies have focused on developing effective active temperature compensation and passive thermal isolation techniques to ensure reliable and accurate operation. Common approaches to temperature compensation include integrating external circuits to actively compensate for temperature-induced changes, employing sophisticated algorithms to process sensor data and correct for temperature effects, and adjusting the frequency of the drive and sense modes to mitigate temperature-related variations. Ref. [9] proposed an active temperature compensation method using external electronic hardware integrated with an ASIC and a gyroscope. Ref. [10] employed a multiparameter fusion compensation method with a weighted linear combination of resonant frequency, frequency split, primary mode amplitude, and quadrature error to obtain the stable scale factor temperature coefficient. In addition, Ref. [11] utilized a thermal deformation suppression chip to reduce the thermal out-of-plane deformation for thermal stabilization. Ref. [12] introduced a peripheral monitoring circuit for temperature compensation. Ref. [13] implemented frequency mismatch control to reduce the effect of temperature on the gyroscope structure. Ref. [14] utilised a self-calibration method to control the scale factors by detecting non-linear components. Ref. [15] employed in-run scale-factor error compensation using algorithms for temperature compensation. The other approaches to thermal isolation include utilising materials or structures to isolate the gyroscope from temperature fluctuations and enclosing the gyroscope in a temperature-controlled environment.

For example, Ref. [16] investigated porous silicon as an effective material for thermal isolation Ref. [17] employed a powder MEMS wafer-level process to create porous microstructures. In, Ref. [18], an oven-controlled gyroscope was used for thermal stabilization. Recently, Ref.[19] proposed a thermoelectric-cooler-controlled gyroscope design. These studies collectively demonstrate the diverse strategies available to effectively compensate for the temperature variations in MEMS gyroscopes and ensure their reliable performance in various applications. The difficulty with the above-mentioned approaches is that they may not completely eliminate the temperature dependence of the performance parameters, which may result in residual misalignments, instability, drift, and high-power consumption, particularly at high temperatures.

To address these limitations, a novel thermal-design methodology for MEMS gyroscope sensors was recently proposed in Ref. [20]. Building on this concept, the present work introduces a packaging-level thermal management approach to control heat transfer between the package base and the sensor. This offers a complementary strategy to both compensation and isolation; hence, one may not need the complex hardware or software approaches discussed in the literature for temperature compensation. The proposed approach can be applied to most MEMS sensors and gyroscopes.

This chapter covers the thermal design and analysis of the new advanced thermal substrate (TS), which is verified through finite element analysis, and discusses the integration of the proposed MEMS gyroscope with the thermal substrate. This also analyzes the sensitivity, bandwidth, and noise trends across varying temperatures using thermal substrates, followed by validation with the existing literature.

6.2 Novel Thermal Design Approach

Heat transfer to the device occurs mainly through three mechanisms: conduction, convection, and radiation, with conduction being the most dominant [21]. The heat from the environment and associated electronics is transmitted through the back surface of the device through the package base, which serves as the mounting surface during packaging. Subsequently, this heat was applied to the proof mass of the sensor via the spring beams of the device. Two strategies were proposed to mitigate heat transmission to the device:

a) The device is isolated from the package using an independent Thermal Substrate (TS) that limits heat transmission, thereby reducing the temperature of the sensor. b) Reducing the heat transmitted to the sensor through innovative design modifications of the sensor beams serving as primary heat conduits for heat flow.

The results and analysis demonstrated that these approaches significantly improved the thermal performance of the device at the design level. The device consisted of a MEMS gyroscope integrated with a TS mounted on the package. The TS design was optimized through finite element modeling using the SOLIDWORKS 2024 software, enabling an in-depth analysis of the temperature behaviour within the TS. Second, the novel and improved thermal beam design of the gyroscope and key performance parameters, including sensitivity, noise, and bandwidth, are evaluated under varying temperature conditions using the CoventorWare MEMS+ software. This study culminates in developing a thermally stable MEMS gyroscope, achieved by applying the optimized TS.

6.2.1 Design of Thermal Substrate (TS)

The primary heat transfer mechanism between the MEMS device and the package base is conduction due to their direct thermal contact. The package base attains a steady temperature influenced by the ambient environment and the heated drive electronics. To enhance the sensor's temperature-dependent performance, we propose a novel approach: utilizing an independently optimized thermal substrate (TS). The TS acts as a thermal barrier, effectively reducing heat flow from the package base to the sensor. This thermal isolation improves the sensor's temperature stability and overall performance. Additionally, the TS serves as an electrode, eliminating the need for additional adhesives and reducing potential errors.

Various TS designs are possible, including multiple legs and circular or rectangular shapes. However, the optimal TS design should prioritize the ease of fabrication, mechanical stability, and compatibility with the bonding process. By carefully selecting the TS design, the thermal performance and reliability of MEMS sensors can be further enhanced. The four thermal substrates are:

- Planar silicon with oxide (Type-I)
- Two-pillar silicon with oxide (Type-II)
- Four-pillar silicon with oxide (Type-III)
- Four-pillar tapered silicon with oxide (Type-IV)

These are considered here for comparison based on the fabrication compatibility and mechanical strength. Rectangular and square columns are standard microfabrication features that can be reliably produced with maximum utilisation of Silicon real estate post-dicing of the sensor chips, resulting in higher yields. Figure 6.1 (a, b, c, d) presents isometric views illustrating four distinct TS. Each figure consists of a TS mounted on a package base (mostly ceramic or alumina), with a uniform oxide layer at the bottom. The Type I TS is a planar silicon structure. The Type II TS consists of two rectangular pillars etched on the backside of the silicon. Type III TS is similar to type II TS but with four square pillars instead of two. Type IV TS has four pillars, and the base is tapered along the thickness by an angle. Tapered TS Type IV can be realized using either wet or dry etching. The anisotropic wet etching of (100) silicon resulted in walls with a 54.75^0 sloping angle [22]. Reactive-ion etching results in different taper angles using different etchant gas ratios and RF bias powers [23]. It is assumed that the top surface length L_{TS} and width W_{TS} are 2.2 mm and substrate thickness T_{TS} is 500 μm. These dimensions are the same for all TS.

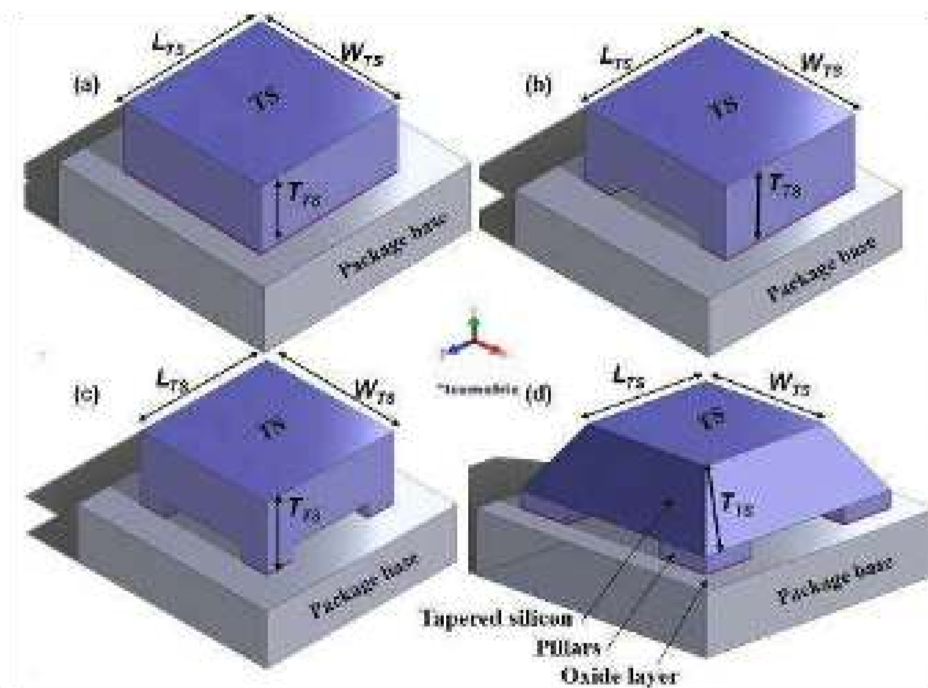

Figure 6.1 Three-dimensional views of various thermal substrates (TS). (a) Planar Silicon with oxide (Type-I). (b) 2-pillar Silicon with oxide (Type-II). (c) 4-pillar Silicon with oxide (Type-III). (d) 4-pillar tapered silicon with oxide (Type-IV).

Further optimization of the structure involves the etching process of the four support columns from the backside, which yielded only a marginal improvement of approximately 1°C in thermal isolation primarily because of large thermal contact area yielding maximum heat transfer. Considering the limited thermal improvement with backside etching optimization and the increased fabrication complexity and mounting difficulties associated with non-standard support shapes, we focused our optimization efforts on the distribution and dimensions of the rectangular support columns, which offer a good trade-off between limited heat transfer and mechanical support and practical implementation. Steady-state thermal simulations of four

distinct Target Structures (TS) were performed utilizing the SOLIDWORKS Simulation software, as depicted in Figure 6.1. Boundary conditions were established as follows: The package base temperature was fixed, the ambient temperature was specified, A uniform heat flux was applied to the model, and contact conditions between the TS and the package base were defined to model heat transfer through conduction accurately. The model was subsequently meshed, and the thermal gradient across the thickness of the TS along the edges was analyzed.

6.2.2 Steady-State Thermal Analysis of Thermal Substrates

It was assumed that the package base was at a temperature of 100^{0}C. Any temperature fluctuations in the base induced changes in the MEMS gyroscope, both across its thickness and along its length. We estimated the amount of heat transmitted across the TS along its thickness.

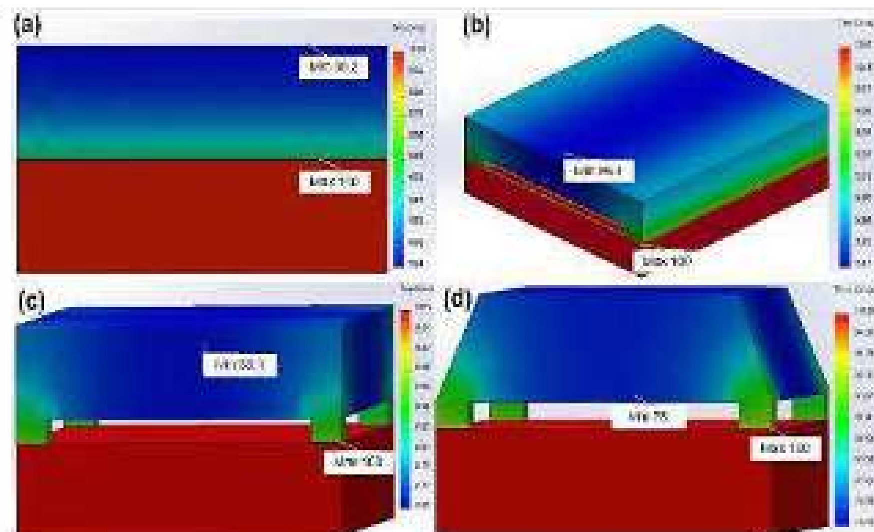

Figure 6.2. Temperature distribution profile for different thermal substrates: (a) Type-I, (b) Type-II, (c) Type-III, (d) Type-IV.

The planar TS (Type-I) exhibits a nearly uniform temperature distribution, indicating minimal thermal isolation. The two-pillar (Type-II) and four-pillar (Type-III) structures show higher temperature concentration near the base, confirming that heat is primarily conducted through the pillars. In contrast, the tapered four-pillar structure (Type-IV) shows a significant reduction in temperature near the substrate surface. For a base temperature of 100 °C, the minimum temperatures observed at the top surface for Types I to IV were approximately 99.2 °C, 96.4 °C, 83.1 °C, and 76 °C, respectively. These results clearly indicate that the TS geometry plays a critical role in governing the temperature distribution. The tapered structure (Type-IV) provides the most effective thermal isolation and is therefore best suited for applications where temperature sensitivity is a major concern.

Figure 6.2 illustrates the simulated temperature distribution within four different TS. The colour gradients represent temperature variations, with blue indicating cooler regions and red indicating hotter regions. The structures are subjected to a uniform heat flux at the base, and the temperature distribution along the thickness of the TS is analyzed. The planar structure in Figure 6.2a exhibits a relatively uniform temperature distribution, with heat spreading evenly

throughout the device. The two-pillar structure in Figure 6.2b shows a higher temperature concentration near the base, indicating that heat is being conducted primarily through the pillars. The four-pillar structure in Figure 6.2c also exhibits a higher temperature concentration near the base. The tapered structure in Figure 6.2d demonstrates a significant reduction in temperature near the top of the device. In Figure 6.2, the maximum temperature value on the scale is 100 °C. The minimum temperature values for Figures 6.2a to 6.2d, as indicated by the temperature distribution scale, are 99.2 °C, 96.4 °C, 83.1 °C, and 76 °C, respectively. The simulation results demonstrate that the geometry of the MEMS structure significantly influences the temperature distribution. Tapered structures, such as Type-IV, can effectively reduce the temperature at the top of the device, which is crucial for applications where temperature sensitivity is a concern. Understanding these thermal characteristics is essential for designing MEMS devices that can operate reliably under various conditions.

6.2.3 Thermal Resistance Analysis

Understanding the thermal resistance characteristics of MEMS structures is essential for designing devices that can effectively manage heat and maintain desired operating conditions. The data presented in Table 6.1 highlight the importance of considering all three heat transfer mechanisms (conduction, convection, and radiation) when analyzing the thermal performance of MEMS devices. The simplified equations for thermal resistance by conduction, convection, and radiation are given by [21]

$$, \quad = \frac{}{}, \quad , \quad = \frac{1}{} \quad , \quad , \quad = \frac{1}{} \qquad (6.1)$$

where L_{TS}, W_{TS}, and T_{TS} represent the length, width, and thickness of the top surface of the thermal substrate, respectively. The parameter k denotes the thermal conductivity of the TS material, h is the convection heat transfer coefficient, and $= (\; + \;)(\;^2 + \;^2)$ is the radiation heat transfer coefficient. Here, is the emissivity, is the Stefan–Boltzmann constant, is the temperature on the surface of the thermal substrate, is ambient temperature. Table 6.1 summarizes the thermal resistance values calculated for all four TS configurations using the above expressions.

Table 6.1. Thermal resistance values for different Thermal Substrates (Type-I to Type-IV).

TS Type	R_{cond} (K/W)	R_{conv} (K/W)	R_{rad} (K/W)
Planar Silicon with oxide (Type-I).	0.8	2.0×10^6	1.2×10^6
2-pillar Silicon with oxide (Type-II).	1.5	1.7×10^6	1.0×10^6
4-pillar Silicon with oxide (Type-III).	5.7	2.0×10^6	1.1×10^6
Tapered with oxide (Type-IV).	33	31×10^6	18×10^6

Table 6.1 shows the consolidated thermal resistances of all four types of TS (Type I to Type IV) after putting TS dimensions and heat transfer coefficients used in the equations. For all four types of MEMS structures, the conductive thermal resistance (R_{cond}) was significantly lower than the convective (R_{conv}) and radiative (R_{rad}) resistances. This indicates that heat transfer occurs primarily through conduction, whereas convection and radiation play less significant roles. The type of MEMS structure (types I to IV) significantly affects the thermal

resistance. The type-IV structures exhibited the highest overall thermal resistance, suggesting better thermal isolation from the surroundings.

6.2.4 Thermal Substrate (TS) Temperature Variation

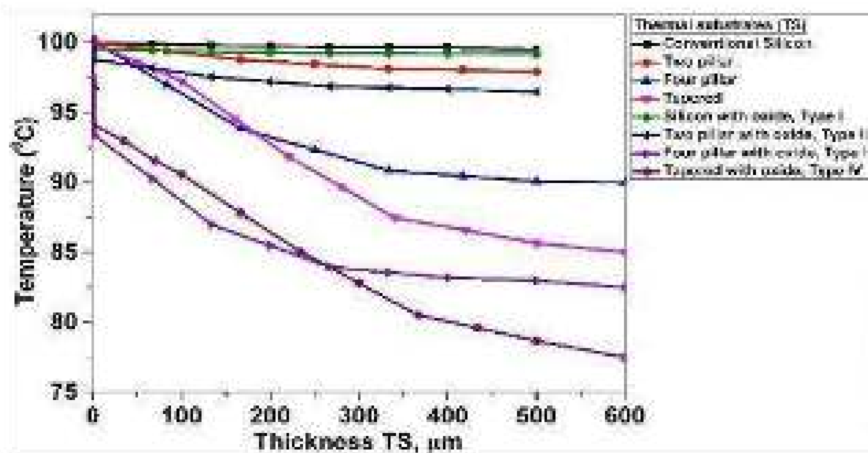

Figure 6.3 (a) Temperature variation across TS thickness with and without oxide and base modifications.

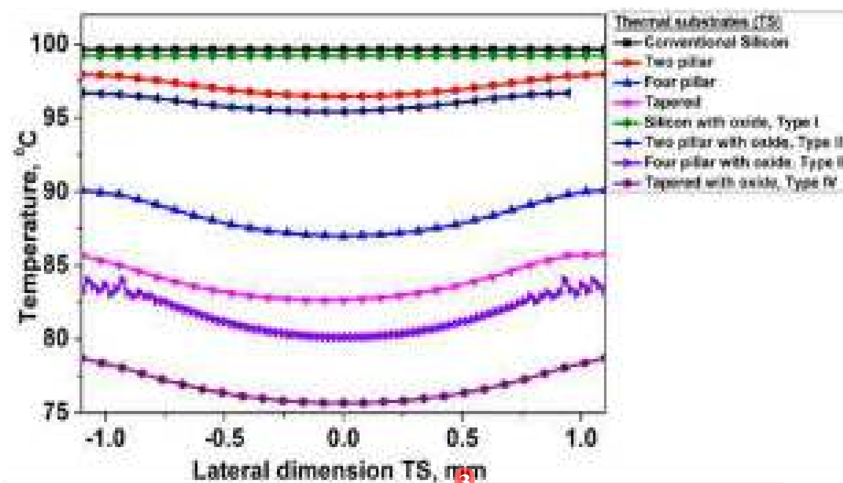

Figure 6.3 (b) Temperature variation along the lateral dimension of the TS with and without oxide.

The simulation results of the Thermal Substrate (TS) temperature variation across the thickness and lateral dimensions are discussed in Figures 6.3a and 6.3b, respectively. For reference, the temperature distribution trends at a typical base temperature of 100 ^{0}C were depicted. The base thickness varied from 0 to 500 µm, while the lateral dimension varied by 1.1 mm left and right from the middle. The analysis also included conventional silicon to demonstrate the temperature drop at a particular thickness for reference. Furthermore, introducing a thermally

grown oxide layer of 1 µm results in a noticeable temperature decrease across the thickness and along the length as the base thickness increases.

Figure 6.3a illustrates the temperature distribution profile among different TS configurations for the thermal management of MEMS devices using SolidWorks software. Here, we mainly consider the contribution of heat conduction from the package's base to the thermal substrate (TS) because the actual sensor will be subsequently mounted on this base, as will be discussed later. Silicon with oxide (Type I) shows a uniform higher temperature near the base and a lower temperature at the top. The presence of an oxide layer offers some thermal isolation; however, the temperature variation is not highly pronounced. Further, by increasing the number of pillars from two to four, the temperature distribution showed a significant reduction from the base to the TS. Tapered TS with oxide (type-IV) provided the most substantial thermal isolation. The temperature distribution profile shows a steep gradient, indicating that the tapered shape combined with the oxide layer effectively minimizes the heat transfer, making it the most effective design for minimizing the temperature-induced performance variation in MEMS gyroscopes. Figure 6.3a shows that incorporating pillars and tapering the base improves thermal isolation by reducing the temperature transfer from the package base. Among all TS, for the 4-pillar tapered silicon with an oxide (Type IV), the temperature is reduced across the thickness by approximately 25 ^{0}C. Hence, this is the most effective method to reduce the temperature as the base thickness increases.

Figure 6.3b shows the temperature variations along the lateral dimensions or length of the base for different thermal substrate (TS) configurations. Regarding the lateral temperature distributions, all TS configurations exhibited the lowest temperature profile in the center. Introducing an oxide layer (Types I, II, III, and IV) consistently led to lower temperatures than the corresponding substrate without an oxide layer. This reinforces the insulating effect of the oxide layer on heat dissipation. A maximum temperature drop of approximately 3 ^{0}C is seen at the center of the structure compared to the outer edge of the tapered structure with four pillars. The different base modifications (two-pillar, four-pillar, and tapered) resulted in varied temperature profiles, but the decreasing trend remained. The type IV configuration exhibits lower temperatures, suggesting potentially better heat dissipation. The conventional silicon substrate showed a relatively stable lateral temperature profile, indicating a consistent heat dissipation behaviour. These results suggest that careful design of the base, including its length and shape, can contribute to improved thermal management. The results indicated that the tapered TS yielded the best thermal management results. We intend to investigate the dependence of the taper angle on the temperature drop in detail for a type IV TS.

6.2.5 Transient Thermal Response

Transient thermal analysis was conducted to evaluate the time-dependent temperature response of the different TS configurations, which is crucial for assessing their behaviour under dynamic operating conditions. The transient responses are shown in Figure 6.4.

The baseline Silicon and Type I structures exhibit near-instantaneous temperature increases to approximately 100°C and 99°C, respectively, indicating minimal thermal isolation. While the Type II (2-pillar silicon with oxide) design demonstrates marginally improved isolation, it rapidly achieves its steady-state temperature of ~96 °C (within ~60 µs, as shown in the inset for the initial 100 µs). In contrast, the Type III (4-pillar) and Type IV (4-pillar tapered) structures display substantially enhanced thermal isolation, requiring significantly longer durations to reach their considerably lower steady-state temperatures of approximately ~83°C and ~76°C, respectively. This behaviour confirms that the increased thermal resistance

engineered into the Type III and, particularly, the Type IV designs effectively lower the final equilibrium temperature and extends the time required to reach it.

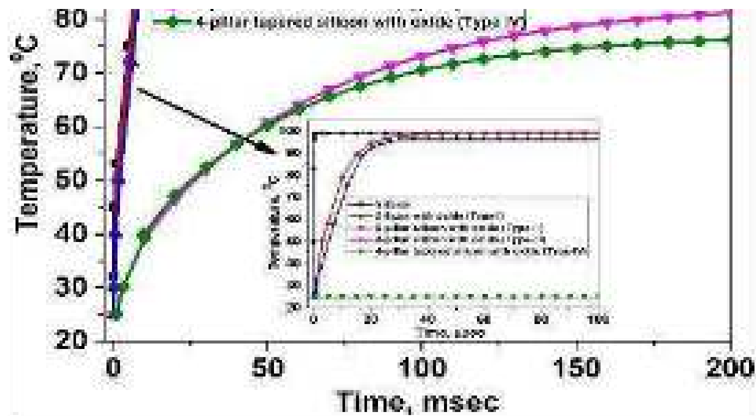

Figure 6.4 Transient response of thermal substrates.

6.2.6 Stress Analysis

A MEMS device's stress tolerance before significant performance degradation happens varies based on several factors. These include the specific material's mechanical properties, the structural design influencing stress distribution, and the types of stress experienced (residual, thermal, or mechanical from external loads). The intended application, such as gyroscopes, also dictates acceptable stress levels. Minimizing internal and external stresses is crucial for ensuring long-term reliability and stable performance, as high or non-uniform stresses can lead to detrimental deformation, fracture, fatigue, and undesirable shifts in critical device parameters like resonant frequencies.

To ensure the structural integrity and prevent permanent deformation or failure of Thermal Substrate (TS) devices, the induced stress within any part should ideally remain well below the ultimate or fracture strength of the constituent materials. In this study, the von Mises stress resulting from Coefficient of Thermal Expansion (CTE) mismatch between Gyroscope sensor and Thermal Substrate (TS) was simulated for four distinct TS designs across a temperature range of -40°C to 125°C.

Figure 6.5 illustrates thermal stress contours in the Type-IV TS, with stress maximally concentrated near Si/SiO interfaces and geometric discontinuities. The arrows depicted at the bottom of the structure in each sub-figure indicate the fixed boundary conditions applied to the substrate during the simulation. This arises from CTE mismatch, Si (2.6 ppm/^{0}C)> SiO (0.5 ppm/^{0}C), leading to compressive stress in SiO after fabrication. Cooling below room temperature typically increases this compression and overall stress. Conversely, heating, while potentially reducing SiO compression, can still elevate the overall von Mises stress in the

composite structure due to complex interactions, as observed. The arrows at the bottom show the fixed boundary applied to the substrate.

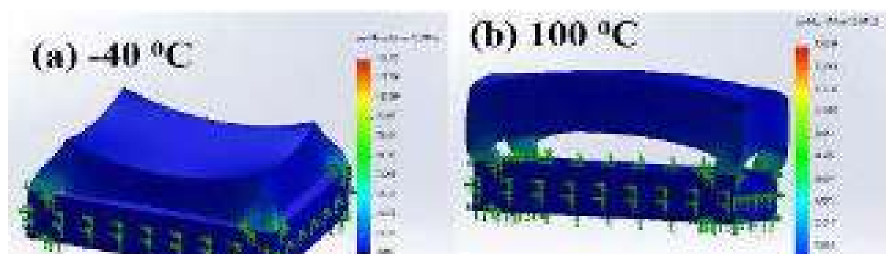

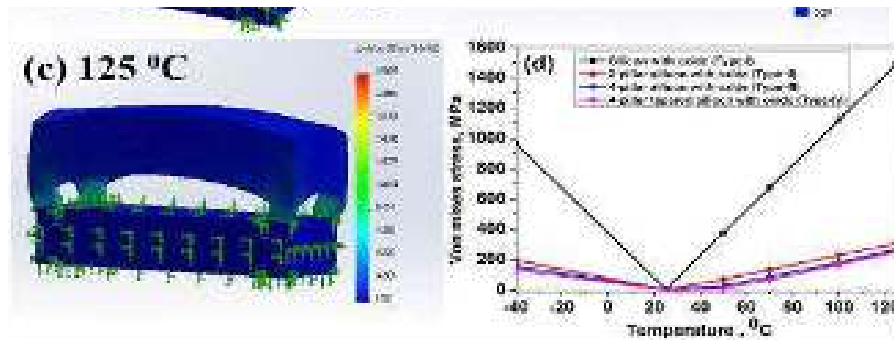

Figure 6.5 Thermal stress contours in the Type-IV TS at temperatures (a) –40 °C, (b) 100 °C, (c) 125 °C, and (d) stress–temperature plot.

Figure 6.5 illustrates thermal stress contours in the Type-IV TS, with stress maximally concentrated near Si/SiO interfaces and geometric discontinuities. The arrows depicted at the bottom of the structure in each sub-figure indicate the fixed boundary conditions applied to the substrate during the simulation. This arises from CTE mismatch, Si (2.6 ppm/^{0}C)> SiO (0.5 ppm/^{0}C), leading to compressive stress in SiO after fabrication. Cooling below room temperature typically increases this compression and overall stress. Conversely, heating, while potentially reducing SiO compression, can still elevate the overall von Mises stress in the composite structure due to complex interactions, as observed. The arrows at the bottom show the fixed boundary applied to the substrate.

Table 6.2 Von Mises stress values of the gyroscope and Thermal Substrate (TS) due to CTE mismatch.

Temperature (^{0}C)	Von Mises stress (MPa)			
	Planar Silicon with oxide (Type-I)	2-pillar Silicon with oxide (Type-II)	4-pillar Silicon with oxide (Type-III)	4-pillar tapered silicon with oxide (Type-IV).
-40	965	195	156	132
25	4	0.48	0.45	0.43
100	1118	228	230	166
125	1489	306	255	249

As shown in Table 6.2 and Figure 6.5d, the maximum von Mises stress increases approximately linearly as the temperature deviates from room temperature in both the heating and cooling directions. Importantly, for all TS configurations, the induced stress levels remain well within tolerable limits and below the fracture strength of the materials used. Overall, these results confirm that incorporating the proposed Thermal Substrate does not compromise structural integrity and is suitable for the reliable operation of MEMS gyroscopes over a wide temperature range.

6.2.7 Taper Angle Dependence

The temperature variation across the Thermal Substrate (TS) is governed by the heat transfer relationship given in [21]:

$$= \overline{} \qquad 6.2$$

where is the taper angle, and Q is the heat flow rate. Figure 6.6 illustrates the simulation

results of the taper angle of the Type IV TS structure and the resulting temperature. As the taper angle of the Type IV TS increased, the temperature consistently decreased. The relationship between the taper angle and temperature appears to be non-linear; for smaller taper angles, the temperature drop is more gradual. Conversely, at larger taper angles, the temperature exhibits a steeper decrease. Tapering effectively reduces the heat conduction pathways, thus maintaining the cooling operating temperature for the MEMS gyroscope. From Equation (2), the temperature change is a trade-off between the TS taper angle and the TS base area. It may be stated here that there is a limit to the taper angle because as the taper angle is increased, the effective area of the sensor will be significantly reduced. However, the bottom of the TS should be compatible with the package where we want to put the sensor, and the top should be approximately 10 % larger than the sensor footprint.

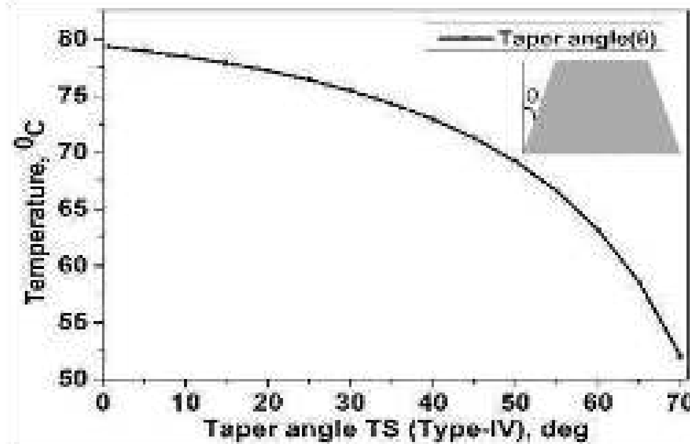

Figure 6.6 Temperature dependence on taper angle for the Type IV Thermal Substrate.

6.3 Improved Thermal Design of the MEMS Gyroscope

Figure 6.7 presents a 3D model and side view of a MEMS gyroscope integrated into a Type IV TS in the CoventorWare MEMS+ software. The central component is a proof or sense mass of the MEMS Gyroscope, responsible for sensing angular velocity. The drive beam anchors are

away from the corners to take advantage of a slightly lower temperature. The thermal Substrate (TS), a tapered structure with four pillars, is designed to dissipate heat, as discussed earlier. Because the material of the TS is silicon, it also acts as the bottom plate to sense the change in the output in response to the input. This prevents the use of additional adhesives to paste the sensor onto the insulator substrate, which has been explored in the literature [11][24][25]. It also avoids the misalignment errors caused by the use of epoxy. In fact, the TS is directly wafer-bonded with the central wafer, in which the sense mass is etched. The foundation on which the entire assembly is mounted is a package base from which heat flows into the sensor and raises the temperature of the sensor.

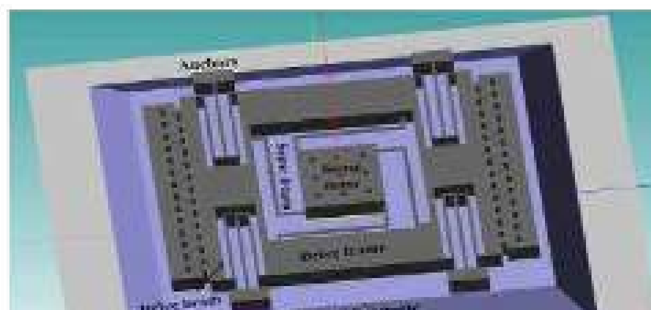

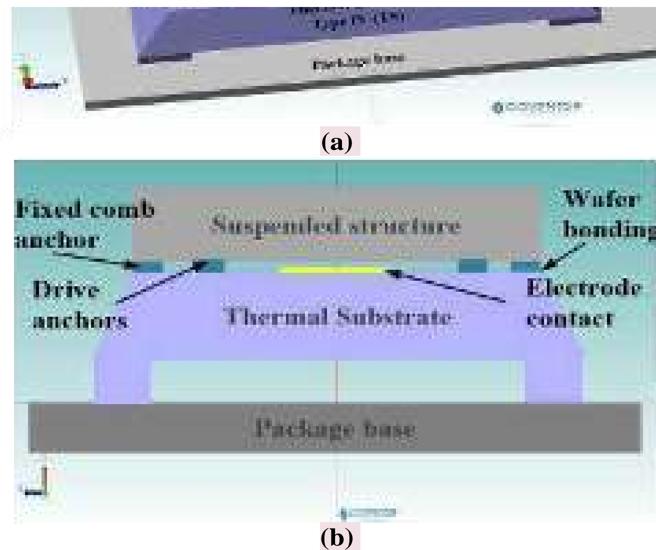

Figure 6.7 MEMS Gyroscope mounted on a Type IV (tapered with four pillars) Thermal substrate (TS) (a) 3D view (b) Side view. The integrated hybrid structure is mounted on the package base

Regarding thermal management, the Type IV TS, which features a tapered design with pillars, will likely be engineered to enhance heat dissipation from the MEMS gyroscope. This is crucial for maintaining optimal performance and preventing device failure owing to overheating. Additionally, the TS and package base offer mechanical support to the gyroscope, shielding it from external shocks and vibrations. The gyroscope integration with the TS is proposed here as a novel design approach to optimize thermal and mechanical performance. The subsequent discussion addresses how integration affects the gyroscope's sensitivity and other performance

parameters.

Previously, a new, improved thermal design of MEMS gyroscopes using modified tapered beams was introduced to reduce the heat flow from the beams to the sensing mass of the gyroscope. The revised gyroscope design featuring these tapered beams is shown in Figure 6.8. A comprehensive analysis was presented in [20]. Heat flow is restricted to the centre of the beam, which prevents temperature rise in the sense mass. In the modified design, the beam thickness is increased to approximately 10 µm at the central region, gradually decreasing toward the anchored ends. This tapering strategy is carefully implemented such that the effective mass of the beam remains unchanged compared to the original rectangular beam design. As a result, the overall sensor mass is preserved, while improving thermal robustness. By introducing this tapered beam geometry for both sense and drive beams, the proposed design effectively reduces temperature-induced stiffness variation and non-uniform deflection, thereby minimizing resonant frequency drift without relying on complex electronic compensation schemes.

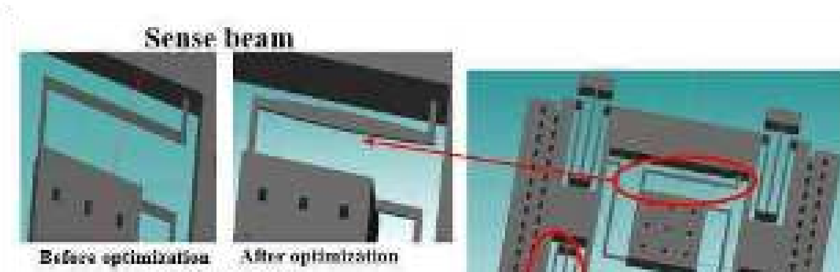

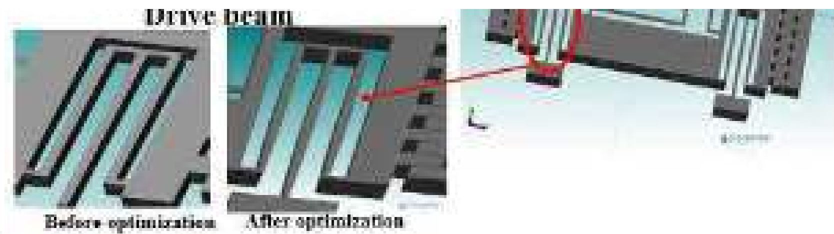

Figure 6.8 Three-dimensional view of the MEMS gyroscope with tapered beam design, showing zoomed-in views of the sense and drive beams.

6.3.1 Resonant frequency variation with temperature

The typical operating temperature range of MEMS gyroscopes used in military and defence applications spans from 233 K to 398 K. Such a wide temperature range can significantly influence device performance and, consequently, its long-term reliability. Temperature variations directly affect the mechanical properties of the structural materials, particularly through changes in Young's modulus and thermally induced deformation. These temperature-dependent variations alter the stiffness of the gyroscope structure, leading to deviations in resonant behaviour and output characteristics.

The dependence of Young's modulus on temperature is commonly expressed as:

$$( ) = (_0)(1 - \quad) \qquad 6.3$$

where E(t) is Young's modulus at the operating temperature, E(t_0) is Young's modulus at the reference temperature, TC_E is the temperature coefficient of Young's modulus, and t represents the change in temperature. As temperature increases, Young's modulus decreases, resulting in reduced structural stiffness. In addition to elastic property variations, other temperature-dependent material properties—such as the coefficient of thermal expansion—also contribute to performance degradation in MEMS gyroscopes. To quantify these effects, modal analysis was performed over a temperature range from 233 K to 398 K in steps of 20 K, as shown in Figure 6.9. The results indicate that both the drive-mode and sense-mode resonant frequencies decrease linearly with increasing temperature. This inverse relationship is primarily attributed to the reduction in Young's modulus of silicon with temperature, as described by Equation 6.3. This behaviour is consistent with both theoretical formulations and simulation results. Linear fitting of the simulated data reveals that the drive-mode and sense-mode resonant frequencies vary with temperature at rates of approximately 0.001 Hz/K and 0.012 Hz/K, respectively. The unequal temperature sensitivities of the drive and sense modes introduce a temperature-dependent frequency mismatch. Over the full operating temperature range from 233 K to 398 K, this mismatch changes by approximately 1.85 Hz, corresponding to a slope of 12 mHz/K. Such variation is undesirable because it directly affects sensor output and contributes to performance drift, as reported in earlier studies. To address this issue, the thermally optimized tapered beam structure was evaluated.

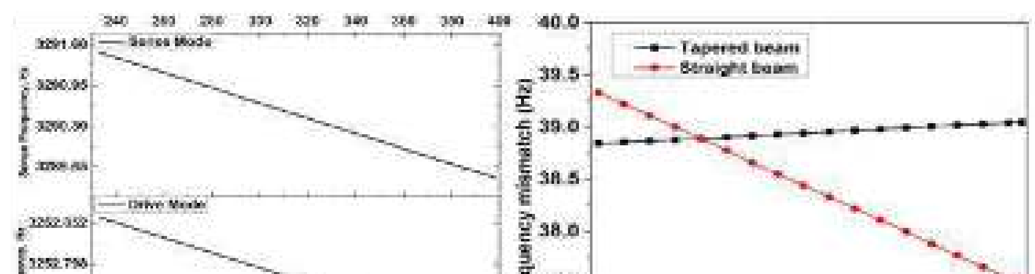

(a) **(b)**

Figure 6.9 (a) drive and sense frequency variation (b) Frequency mismatch variation of modified beam structure with temperature

Figure 6.9b shows the variation of frequency mismatch with temperature for the modified tapered beam design. Compared to the conventional rectangular beam, the total frequency mismatch variation is significantly reduced to approximately 0.18 Hz over the entire temperature range. This substantial reduction in mismatch improves bandwidth stability and enhances the gyroscope's temperature-tolerant operation. Overall, the results demonstrate that the tapered beam design significantly enhances the thermal performance of the MEMS gyroscope. By controlling heat flow through the beam region and reducing thermally induced stiffness variations, temperature effects on resonant frequency and frequency mismatch are minimised to a large extent. This design-based temperature compensation approach is inherently passive and can be extended to other MEMS devices. Furthermore, a variety of tapered beam geometries can be explored to further improve performance, and such tapered structures can be readily fabricated using standard deep reactive ion etching (DRIE) techniques.

6.3.2 Heat conduction in Straight and Tapered Sense Beams

To better understand the influence of temperature on gyroscope performance, a detailed investigation of heat flow patterns within the sense beams was conducted. Figure 6.10 shows the typical temperature distribution within the structure at temperatures other than room temperature, while Figure 6.11 depict the heat flow vectors in the x, y, and z directions at 233 K and 398 K, respectively. These figures present a magnified view of a representative straight-sense beam, which plays a dominant role in determining the gyroscope's stiffness. Along the x-direction, the heat flow within the straight beam is observed to be almost uniformly distributed along the beam length, with slightly higher concentration at the beam bends, indicating localized thermal accumulation at geometric discontinuities. In contrast, for the y- and z-directions, the heat flow is significantly more concentrated within the beam region compared to the sense proof mass. A similar trend—uniform distribution along the beam length with localized intensification at the bends—is consistently observed at both temperature extremes. These observations clearly indicate that the sense beam is the most temperature-sensitive component of the structure and serves as the primary pathway for heat propagation.

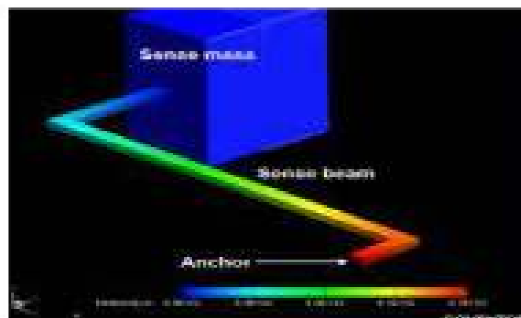

Figure 6.10 Typical temperature distribution at temperature other than room temperature

(a) **(b)**

Figure 6.11 The heat flow in x, y, z direction at (a)233 K (b) 398K

From the heat flow analysis, it is evident that the percentage change in heat flow within the sense mass (m_s) is negligible when compared to the percentage change in the sense spring

constant (k_s). This behaviour arises because the beam dimensions are significantly smaller than the overall size of the sense mass, making the beam more susceptible to temperature-induced variations. Moreover, changes in temperature directly affect Young's modulus (E), which in turn alters the spring constant governed by the beam geometry. As a result, variations in temperature lead to changes in the effective stiffness of each beam, causing beam deformation and, subsequently, non-uniform deflection of the sense mass.

To mitigate this effect, the heat flow behaviour of a tapered sense beam was investigated. Figures 6.12a and 6.12b show the heat flow distribution in the x-, y-, and z-directions for the tapered beam at 233 K and 398 K, respectively. In the tapered beam, heat flow along the x-direction is effectively controlled by gradually tapering the beam thickness from the centre over a longer portion of the beam length. As a result, heat is more concentrated near the centre and reduced toward the beam ends. Compared to the straight rectangular beam, the heat flux in the x-direction is reduced by approximately 10%.

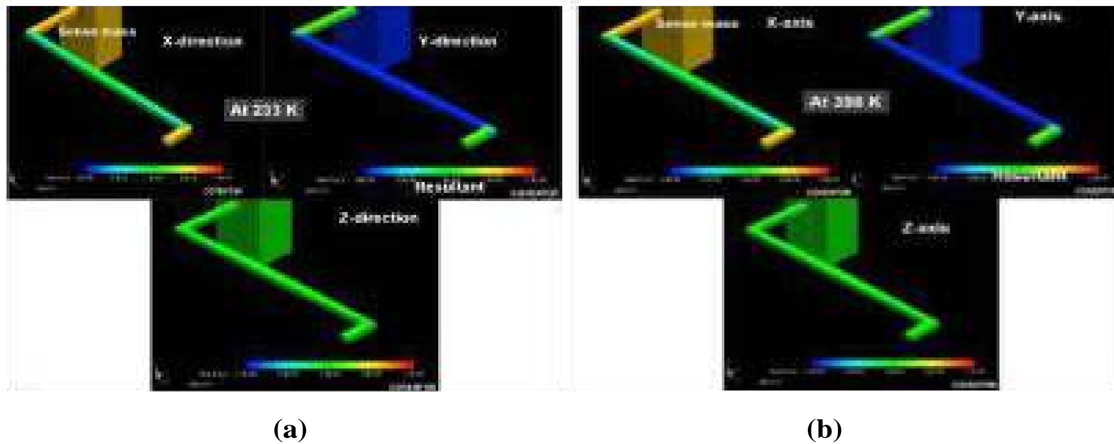

(a) **(b)**

Figure 6.12 Shows the heat flow in x, y, z directions at (a) 233K (b) 398 K for the tapered beam

For the y- and z-directions, the heat flow in the tapered beam is more uniformly distributed along the beam region. Quantitatively, the heat flux reduction is approximately 10% in x-axis, 3% in the y-direction and 15% in the z-direction when compared to the rectangular beam. These results demonstrate that tapering the beam geometry enables effective control of heat flow in all three spatial directions. In addition to improved thermal behaviour, a notable reduction in mechanical stress is also observed. The von Mises stress in the beam decreases from approximately 38 MPa for the rectangular beam to 25 MPa for the tapered beam, indicating enhanced mechanical robustness. Based on these observations, the tapered beam structure's overall performance is further evaluated and compared with earlier results to assess its impact on frequency stability, sensitivity, and temperature tolerance.

6.3.3 Sense Displacement with Different Thermal Substrate (TS) Bases

This section presents the overall enhancement in thermal performance achieved through the combined implementation of the Thermal Substrate (TS) and tapered beam geometry for both the sense and drive directions. The TS reduces heat transfer from the environment and package base, while the tapered beams minimize the temperature sensitivity of key performance parameters, including sense displacement, sensitivity, noise, and bandwidth. To evaluate the effectiveness of this combined approach, four configurations are considered:

(i) conventional gyroscope design without TS,
(ii) conventional design with TS,
(iii) tapered beam design without TS, and
(iv) tapered beam design with TS (Type IV).

Figure 6.13 illustrates the variation of sense displacement with temperature for different gyroscope configurations at a constant rotation rate of 1 rad/s. It is crucial to note that the sense mass is supported by beams from all four sides, resulting in a constrained motion where the beam's centre undergoes rotational motion without significant lateral displacement. This constraint leads to a non-linear dependence of sense displacement on temperature, even under constant rotation.

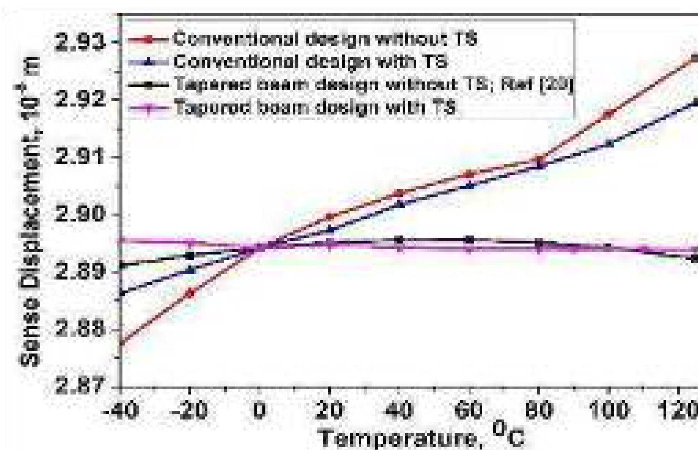

Figure 6.13 Sense displacement as a function of temperature for various gyroscope configurations: conventional design without TS, conventional design with TS, tapered beam design without TS, and tapered beam design with TS (Type IV).

As evident from Figure 6.13, a consistent trend of increasing sense displacement with rising temperature is observed across all gyroscope configurations. There is a positive correlation between temperature and sense displacement. At low temperatures, adding a base to the conventional gyroscope design (original with base) slightly increases the sensed displacement, whereas the trend is opposite at the upper end of temperature. From the slope of conventional design without TS configuration, the change in sense displacement is 2.7×10^{-6} µm/^{0}C. Introducing a TS (Type IV) further amplifies the sense displacement at lower temperatures and reverses this trend at the upper temperature. The crossover point is the ambient temperature of 0 deg (273 K), which is the default setting in the software. All structures are designed to have the same sense displacement at the default temperature value. The Tapered beam design with TS (Type IV) configuration, which likely incorporates additional modifications, exhibits an almost constant sense displacement of 8.6×10^{-8} µm/^{0}C across the entire temperature range. This is highly desirable for the temperature-independent performance of the Gyroscope.

Furthermore, it suggests that one can tailor the deflection slope vs. temperature curve by using our proposed thermal management approaches at the design level. The gyroscope output (sense deflection) is significantly influenced by temperature. This sensitivity could potentially lead to inaccuracies in measurements if not properly accounted for. The tapered base configurations seem to reduce the sensitivity of the gyroscope to temperature. For performance considerations,

the Type IV configuration, with an almost flat temperature dependence, might offer advantages in certain applications.

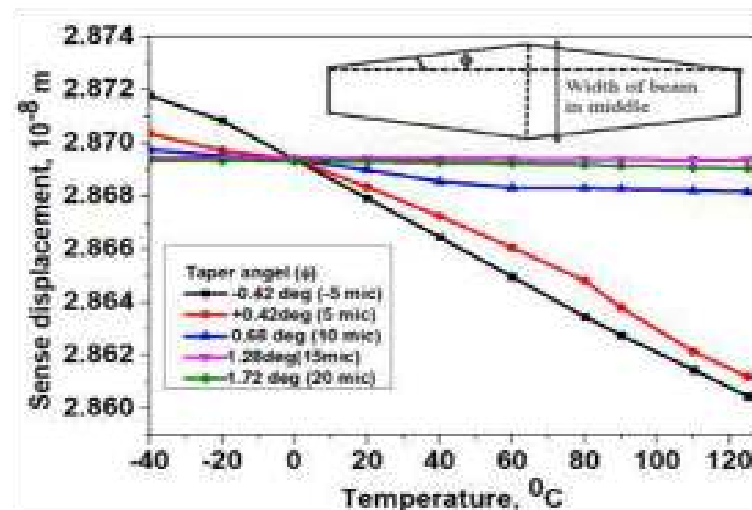

Figure 6.14 Sense displacement versus temperature for different taper angles.

Figure 6.14 illustrates the effect of the taper angle ( ) on the temperature-dependent sensing displacement of the MEMS gyroscope. As shown in the subset, the beams were tapered, varying in width from 5–20 µm from the middle; accordingly, the angle will change. It was observed that the sense displacement consistently decreased with increasing temperature for all taper angles. Taper angles of -0.42° and 0.42° exhibited a more pronounced decrease in sense displacement compared to larger angles (0.68° to 1.72°). Taper angles between 0.68° and 1.72° show minimal or no discernible changes in sense displacement across the temperature range. These findings suggest that the chosen taper angle of 1.28° (15 µm middle portion width) provides a suitable balance between sensitivity and temperature stability, which is considered in the present study.

6.4 Scale Factor Temperature Sensitivity

The scale factor sensitivity (SFS) of a MEMS gyroscope is defined as the slope of the sense-displacement-versus-rotation-rate curve at a given temperature. To investigate the influence of temperature on SFS, simulations were performed over a temperature range of –40 °C to 125 °C for two representative configurations:

(i) A conventional gyroscope design without a Thermal Substrate (TS), and
(ii) A tapered beam design integrated with a Type IV TS.

These two cases were selected to clearly highlight the improvement achieved by the proposed thermal management approach. Figures 6.15a and 6.15b show a plot for different temperatures from -40 to 125 ^{0}C for the conventional design without TS and tapered beam design with TS (Type IV). Only these two cases were considered to show a clear comparison between the designs. For both plots, the data points for each temperature indicated a direct proportionality between the sense displacement and rotation rate. The relationship is nonlinear for each temperature at higher rotation rates. This suggests a positive correlation between the temperature and sense displacement. These results suggest that temperature-compensation

mechanisms may be necessary to account for the varying sensitivities at different temperatures to ensure accurate measurements. The temperature dependence of the sense displacement is attributed to the thermal expansion coefficients or other material properties of the components. The slope for each curve was estimated using a piecewise linear approximation to estimate the scale factor sensitivity. The results up to 100 rad/s were considered first, as the plot was approximately linear up to this rotation. The scale factor sensitivity at each temperature was evaluated and plotted from the slopes of the plots in Figures 6.15a, b.

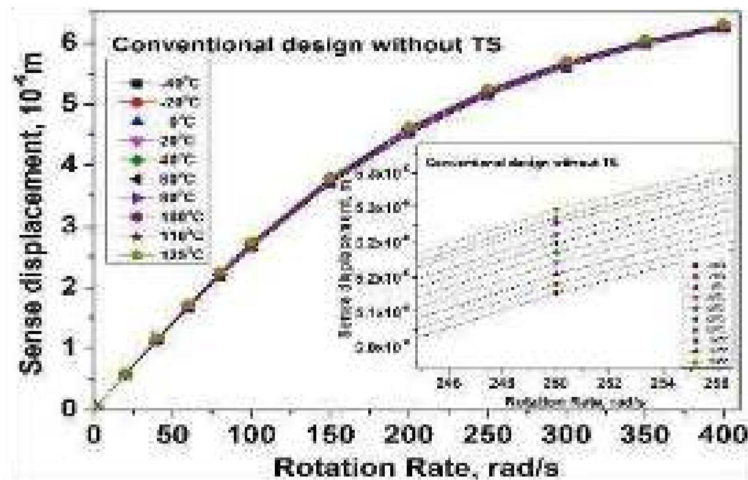

(a)

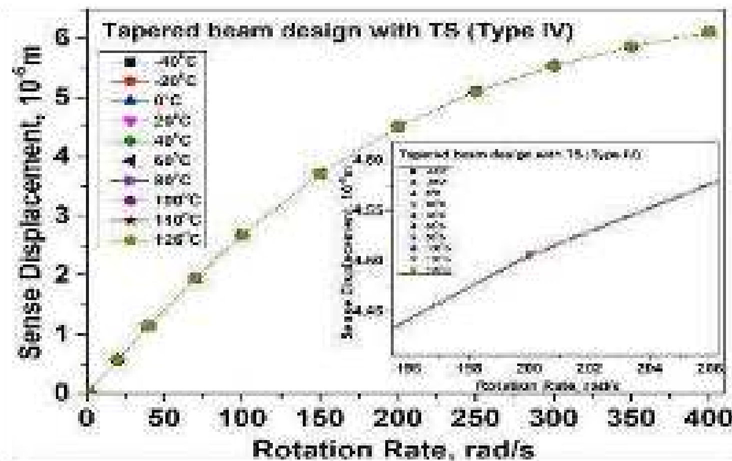

(b)

Figure 6.15 Sense displacement versus rotation rate at temperatures ranging from −40 °C to 125 °C for (a) conventional design without TS, and (b) tapered beam design with Type IV TS.

Figure 6.16 illustrates the effect of temperature on scale factor sensitivity (SFS) for two different MEMS gyroscope designs: a conventional design without TS and a new design using a tapered beam with Type IV TS. For conventional designs without TS, the SFS increases linearly from 2.64×10^{-8} to 2.74×10^{-8} as the temperature rises from -40 ^{0}C to 125 ^{0}C. However, the SFS remained constant for a tapered beam design with Type IV TS across the entire

temperature range. The scale factor temperature coefficient (SFTC) is given by [26].

$$= \frac{1(\quad) - 1(\quad 9}{1(\quad 9} \qquad 6.4$$

Where k_1 is the scale factor, and T is the temperature difference. The Scale factor temperature coefficient (SFTC) for the conventional design without TS is 232 ppm/^{0}C, whereas it is significantly lower at 6 ppm/^{0}C for a tapered beam design with TS. The new tapered beam design demonstrated superior thermal stability compared with the conventional design. Additionally, at higher rotation rates, a three-point linear approximation reveals that the SFTC for the conventional design without TS is 77 ppm/^{0}C, whereas, for the tapered beam design, it is drastically reduced to 1.89 ppm/^{0}C.

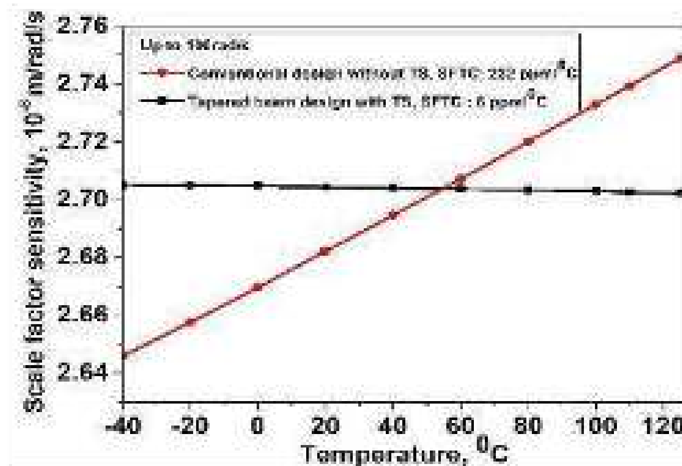

Figure 6.16 Plot of scale factor sensitivity for conventional design without TS and tapered beam design with TS Type IV up to 100 rad/s at temperatures ranging from -40 ^{0}C to 125 ^{0}C.

The non-uniform deformation, driven by differential thermal expansion, results in a net change in capacitance with temperature. Our simulations inherently capture this effect. To quantify this, our simulations indicate an absolute change in capacitance with temperature (C/°C) of 2.8×10^{1} F/°C for the design without the TS, reduced significantly to 1.5×10^{2} F/°C for the design incorporating the TS. The resolution of the proposed readout circuit is 50 zF (50×10^{21} F). The change in capacitance is substantially larger than the readout resolution, confirming that these temperature-induced capacitance changes are indeed resolvable. Here we want to add that the goal of designer is to make C/°C much smaller so that capacitance readout output change due to temperature is much smaller than due to Gyroscope input angular rotation. Hence resolving C/°C is not of primary concern. Only point of concern is that it should not dominate scale factor sensitivity C/ where is input angular rate. However, for further context, if we consider a nominal sense capacitance (C) of 100 fF (1×10^{13} F), the relative change in capacitance per degree Celsius (C/C per °C) is reduced from 2.8×10 /°C without the TS to 1.5×10 /°C with the TS. Using a Thermal Substrate (TS) and tapered beam effectively mitigates the influence of temperature variations on the gyroscope's scale factor sensitivity (SFS) at all rotation rates, making it reliable for applications that require consistent performance across a wide temperature range.

6.5 Noise Temperature Dependence

Thermomechanical (TM) noise is a critical performance metric that reflects the fundamental noise behaviour of MEMS gyroscopes and strongly influences resolution and stability. The thermomechanical noise is expressed as [27]:

$$= \frac{\overline{\quad ( ) \quad ( )}}{{}^{2}( )\ {}^{2} \quad ( )} \tag{6.5}$$

k_B is the Boltzmann constant, T is the absolute temperature, BW is the bandwidth, A_{dm} is the area of the drive mass, $= \overline{\ /\ }$ is the sense mode frequency, $=$ — is the sense resonant frequency, is the sense quality factor, and m_s is the sense mass excited by the Coriolis force. The equation 6.5 clarifies the dependence of noise on temperature. The behaviour of each parameter with respect to temperature was studied to understand the effect of temperature. As mechanical noise has major impact on the structure, hence other sources of noise are neglected as far as the optimum temperature tolerant design of structure is concerned. The variation in the resultant thermomechanical noise with the temperature was studied.

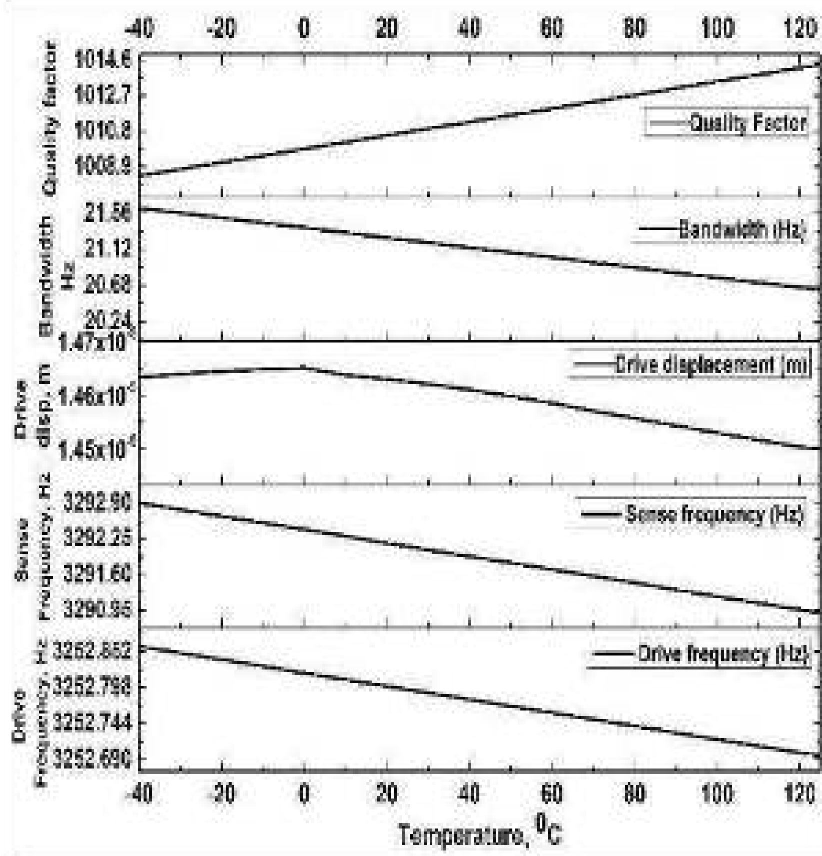

Figure 6.17. Variation of f_d, f_s, x_d, BW, and Q_s with temperature from –40 °C to 125 °C.

Figure 6.17 shows multiple plots depicting the variation of important parameters in Equation 4 with temperature for one of the designs as an example. The parameters analyzed were drive frequency (f_d), sense frequency (f_s), drive displacement (x_d), quality factor (Q_s), and bandwidth (BW). The first two curves from the bottom show a steady decrease in the frequencies with increasing temperature owing to the variation in material properties such as Young's modulus [28]. The sense frequency change rate was more pronounced than the drive frequency. This is because of the different beam shapes; the thermal expansion causes more changes in the dimensions of the sense beam than in the drive beam.

The curve for the drive displacement (x_d) shows a non-linear trend in the drive displacement, with a slight decrease at lower and higher temperatures. This variation indicates a complex interaction between the thermal effects and potential resulting stresses that potentially modify the beam dimensions and critical gaps for the drive beam. The interplay of these factors—primarily the variation in material stiffness, resonant frequency, and damping (Q-factor)—collectively determines the drive displacement achieved under constant drive conditions, leading to the observed non-linear profile. The bandwidth (BW) curve decreased slightly with temperature. Because BW= f×0.54 [27], f represents the drive and sense frequency difference. As seen in the bottom two curves, the drive and sense frequencies decrease with temperature, and a decrease in BW is expected with temperature change.

The quality factor (Q_s) takes into consideration the squeeze film damping variation, thermoelastic dissipation and anchor losses. The curve for the quality factor (Q_s) gradually increased with temperature. This is due to the lower damping losses at higher temperatures. Overall, the plots highlight how temperature variation can significantly affect different parameters. These variations potentially add to the overall noise level of the system. All changes in these parameters lead to a change in the overall thermomechanical noise of the MEMS gyroscope, which is discussed below.

Figure 6.18 shows the MEMS gyroscope's overall thermomechanical noise as a temperature function for the conventional design without TS and tapered beam design with TS at temperatures ranging from -40 ^{0}C to 125 ^{0}C. For both designs, the noise increased almost linearly with temperature. As the temperature increased, the thermal agitation became more intense, leading to an overall increase in noise. Moreover, this type of variation in noise is the commutative effect of the various parameter changes observed in the previous curves in Figure 6.17. These parameter variations collectively contribute to the gyroscope's sensitivity to noise, influencing the overall performance stability across temperature changes. For conventional design, the noise increases from 5.0×10^{-4} rad/s at -40 ^{0}C to 6.5×10^{-4} rad/s at 125 ^{0}C. but for a tapered beam with TS, the TM noise is approximately at 1.0×10^{-5} rad/s for the entire temperature range.

The noise trend in Figure 6.18 appears quasi-linear, differing from the fundamental $T^{0.5}$ thermal noise dependence represented in Equation 6.5. However, the overall noise metric plotted incorporates multiple temperature-dependent parameters from the comprehensive noise model, including Quality factor (Q), resonant frequencies (   ), and bandwidth (BW), whose individual thermal characteristics are presented in Figure 6.17. Fitting the simulation data the effective dependencies approximated by $K_1*T^{0.465}$ (conventional design without TS) and $K_2*T^{0.9}$ (Tapered design with TS), where K_1 and K_2 are proportionality constants. While the $T^{0.9}$ trend appears nearly linear, it represents the combined outcome of multiple factors, consistent with the underlying theory. This trend shows that the tapered beam design with TS is more effective in reducing thermomechanical noise over a broad range of temperatures.

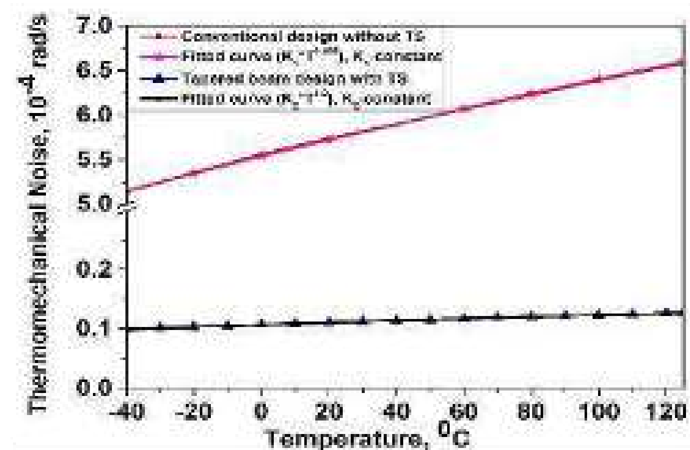

Figure 6.18 Thermomechanical noise variation for conventional design without TS and tapered beam design with TS from –40 °C to 125 °C.

The TS acts as an insulating layer that limits heat transfer from the environment, whereas the tapered beam design enhances mechanical stability and reduces the heat conduction pathway. This makes it a preferred choice for applications in which thermal stability and minimal noise are crucial, such as precision navigation and inertial measurement systems.

6.6 Bandwidth Temperature Dependence

The bandwidth (BW) refers to the frequency at which the MEMS gyroscope can accurately detect the rotational signal. A stable BW is crucial for ensuring performance in various applications.

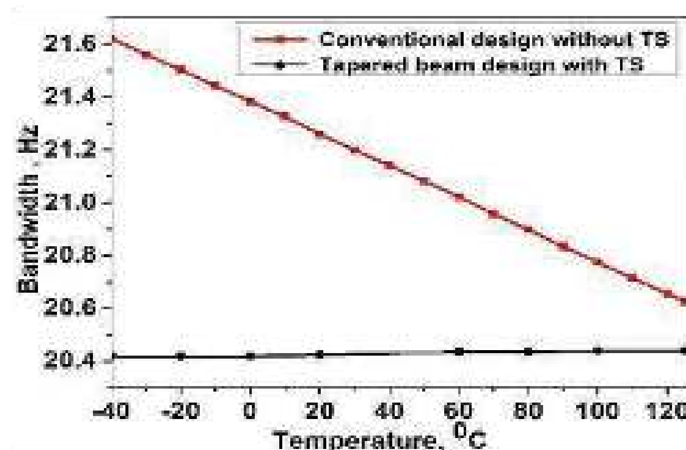

Figure 6.19 Bandwidth variation with temperature for conventional design without TS and tapered beam design with Type IV TS from –40 °C to 125 °C.

Figure 6.19 illustrates the variation in BW for the two designs at different temperatures. For conventional designs without TS, at -40 ^{0}C, the BW is approximately 21.6 HZ and reduces to approximately 20.6 Hz at 125 ^{0}C. This decrease is due to the change in the mechanical properties (such as stiffness) of the gyroscope's structural material, which affects the resonance

frequency and, thus, the overall BW. This makes it less reliable in applications where performance consistency over a wide temperature range is critical. However, for a tapered beam design with TS Type IV, the BW hovers at approximately 20.4 Hz with minimal fluctuation.

The bandwidth (TCB) temperature coefficient was reduced to 158 ppm/^{0}C for the tapered beam with TS from 6060 ppm/^{0}C for the conventional design without TS. The temperature coefficient of frequency (TCF) for the drive and sense structure of a tapered beam with TS is 0.9 mHz/^{0}C and 12 mHz/^{0}C. This is likely due to the combined effect of TS, which acts as a thermal buffer, and tapered beam design, which enhances the structural rigidity and reduces the sensitivity to thermal expansion.

6.7 Results Validation

Table 6.3 presents a comparative analysis of the temperature compensation techniques employed in previous studies and in the current work. The scale factor temperature coefficient and temperature frequency coefficient were considered over a specified temperature range. The main techniques discussed in the literature are frequency mismatch or mode match control, self-calibration, scale factor optimization, fusion compensation, and thermoelectric coolers. Although previous studies have demonstrated effective temperature compensation, the present work offers several advantages.

(a) Wider Operating Temperature Range

The proposed design operates reliably over a wide temperature range of –40 °C to 125 °C, spanning 165 °C. This range is significantly broader than those reported in most previous studies, which typically operate over narrower temperature windows. The ability to maintain stable performance over such an extended range highlights the robustness of the proposed approach and its suitability for harsh, thermally demanding environments, including aerospace, defence, and industrial applications.

(b) Improved Scale Factor Stability

The present study demonstrates a significant improvement in scale factor stability compared to previous studies, achieving a temperature coefficient of 6 ppm/°C. This is notably lower than the majority of the reported values in only two studies [16] and [29], thereby achieving comparable results. [16] and [29] employed scale factor self-calibration techniques involving extensive external hardware and advanced algorithms and are not efficient, in addition to being cost intensive. [29] incorporated two additional error-correction methods. In addition, these approaches generally require higher power consumption owing to the use of external electronics. By contrast, this study focuses on structural modifications at the design level, enabling effective temperature compensation without relying on external hardware and software, with no additional cost. This approach offers a promising avenue for the development of energy-efficient high-performance MEMS gyroscopes.

(c) Improved Frequency Temperature Coefficient

The frequency coefficient data for drive and sense mode are available for only a few references; the present work exhibits superior results with TCF for drive and sense mode of 0.9 mHz/^{0}C and 12 mHz/^{0}C, respectively, which are better than other cases as can be seen from Table 6.3.

Table 6.3 Comparative analysis of temperature compensation techniques reported in the literature and the present study.

Ref.	Technique used or Operation mode	Temperature		Temperature coefficient of frequency (TCF)		Scale factor temperature coefficient (SFTC) (ppm/ ⁰C)
		Range	T (⁰C)	Drive mode (Hz/°C)	Sense mode (Hz/°C)	
Ref. [1]	Fusion compensation method	-30 ⁰C to 70 ⁰C	100	Not available	Not available	8
Ref. [2]	Periphery control circuit	-40 ⁰C to 60 ⁰C	100	Not available	Not available	250
Ref. [3]	Frequency mismatch control	-40 ⁰C to 60 ⁰C	100	Not available	Not available	282.12
Ref. [4]	Scale factor self-calibration	–30 °C to 30 °C	60	Not available	Not available	5.02
Ref. [5]	Coefficient optimization	–20 °C to 40 °C	60	Not available	Not available	10
Ref. [6]	Thermoelectric Cooler	0 ⁰C to 60 ⁰C	60	Not available	Not available	210
Ref. [7]	Scale factor calibration, Dynamic phase error correction, In-phase error calibration	15 ⁰C to 45 ⁰C	30	Not available	Not available	4
Ref. [8]	Split mode	-40 ⁰C to 60 ⁰C	100	Not available	Not available	27
Ref. [9]	Mode matched	-10 ⁰C to 60 ⁰C	70	Not available	Not available	87
Ref. [10]	Mode matched	–40 °C to 80 °C	120	41.5×10^{-3}	16.5×10^{-3}	Not available
Ref. [11]	Frequency mismatch control	–40 °C to 80 °C	120	1.61	1.31	Not available
Present study	**Thermal substrate, beam modification**	**-40 ⁰C to 125 ⁰C**	**165**	**0.9×10^{-3}**	**12×10^{-3}**	**6**

Overall, the results presented in this paper highlight the effectiveness of temperature compensation techniques employed to achieve enhanced sensor performance and reliability. However, Table 6.3 presents a comparative analysis of the temperature compensation techniques employed in previous studies and in the current work. It provides a benchmark of typical performance values for existing MEMS gyroscopes. This context helps to illustrate the potential impact and significance of achieving improved thermal stability through our design approach, even though a direct validation of our specific simulated structure through experimentation is beyond the scope of this initial study. Future work will focus on the

fabrication and experimental verification of the proposed design to directly correlate simulation results with real-world performance.

6.8 Fabrication Experiment

Fabrication experiments were conducted on test structures to evaluate the feasibility of fabricating the proposed thermal substrate (TS) design. Figure 6.20 (a-d) presents scanning electron microscope (SEM) images of the fabricated test structures on Si (110), demonstrating the successful implementation of the design. The wet etching is carried out in 40 wt% KOH solution at 120 °C [30]. Figures 6.20(a) and 6.20(c) provide top-down views of the fabricated TS, revealing an array of square features representing individual thermal elements or heat sinks. This consistent patterning across the substrate indicates reliable and consistent processing. Figures 6.20(b) and 6.20(c) showcase cross-sectional views, highlighting the slanted sidewalls characteristic of wet etching processes with surface roughness of 50.1 nm. Figure 6.20 (d) shows the pillars of the thermal substrate etched on the backside of the TS. These images provide visual evidence of the successful fabrication of the TS design and demonstrate the effectiveness of the wet etching techniques employed. Wet etching's inherent isotropy and crystallographic sensitivity limit uniformity and precision for complex, high-aspect-ratio features. Conversely, while offering superior control, dry etching as an alternative approach typically involves higher costs and slower processing speeds than wet etching. An estimated range for the bonding interface thermal resistance for direct bonding is 0.1 to 10 K mm^2/W.

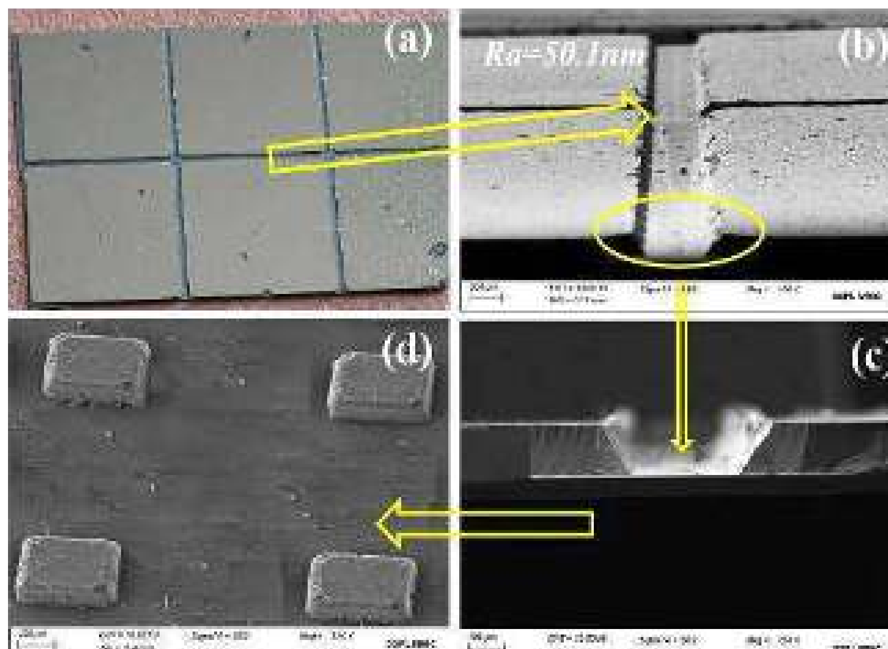

Figure 6.20 SEM images of the fabricated Thermal Substrate (TS): (a) top view of the TS, (b) SEM image showing the channels between adjacent TSs used for dicing, (c) magnified view of one of the channels, and (d) backside view of the TS showing the etched support pillars.

6.9 Conclusion

This chapter presented a novel and effective strategy for enhancing the thermal performance of MEMS gyroscopes. By integrating a thermally optimized Thermal Substrate (TS) and a specifically engineered design, Transient thermal and stress analyses confirmed improved thermo-mechanical characteristics, which directly translated into significantly decreased temperature-dependent variations of parameters. This has significantly reduced the heat transfer to the sensor, resulting in substantial improvements in key performance parameters, including sense deflection, sensitivity, noise, and bandwidth. The case study results confirm a temperature reduction of 25 ^{0}C and a substantial decrease in the temperature-dependent variation of the critical parameters.

The proposed work demonstrates TCF for drive and sense mode as 0.9 mHz/^{0}C and 12 mHz/^{0}C, respectively, and SFTC of 6 ppm/^{0}C up to 100 rad/s and 1.7 ppm/^{0}C at higher rotation rates. The proposed method offers a promising alternative to conventional temperature compensation techniques, eliminating the need for complex external circuitry and algorithms. A comparative analysis with existing literature confirms the exceptional thermal performance of our proposed method. Our results demonstrate a superior temperature coefficient of frequency (TCF) and scale factor temperature coefficient (SFTC) compared to previous studies. The SEM images of the TS show the feasibility of the fabrication using the wet etching technique.

Overall, this chapter establishes the versatility of this approach that makes it applicable to a wide range of MEMS sensors. This is helpful in paving the way for advancements in thermal management and the development of high-performance sensor technologies.

References

[1] Harindranath A and Arora M 2024 A systematic review of user - conducted calibration methods for MEMS-based IMUs Measurement (Lond) 225

[2] Huang W, Yan X, Zhang S, Li Z, Hassan J N A, Chen D, Wen G, Chen K, Deng G and Huang Y 2023 MEMS and MOEMS Gyroscopes: A Review Photonic Sensors 13

[3] Gill W A, Howard I, Mazhar I and McKee K 2022 A Review of MEMS Vibrating Gyroscopes and Their Reliability Issues in Harsh Environments Sensors 22

[4] Zhang H, Zhang C, Chen J and Li A 2022 A Review of Symmetric Silicon MEMS Gyroscope Mode-Matching Technologies Micromachines (Basel) 13

[5] Bhatt G, Manoharan K, Chauhan P S and Bhattacharya S 2019 MEMS Sensors for Automotive Applications: A Review Energy, Environment, and Sustainability (Springer Nature) pp 223–39

[6] Passaro V M N, Cuccovillo A, Vaiani L, De Carlo M and Campanella C E 2017 Gyroscope technology and applications: A review in the industrial perspective Sensors (Switzerland) 17

[7] Xiao Y, Meng J, Yan H, Wang J, Xin K and Tao T 2023 Research on the Application of MEMS Gyroscope in Inspecting the Breakage of Urban Sewerage Pipelines Water (Switzerland) 15

[8] Liechti R 2024 Equivalent electrical circuits for electroacoustic MEMS design: a review Journal of Micromechanics and Microengineering 34

[9] Chiu S R, Teng L T, Chao J W, Sue C Y, Lin C H, Chen H R and Su Y K 2014 An integrated thermal compensation system for MEMS inertial sensors Sensors (Switzerland) 14 4290–311

[10] Cui J, Yan G and Zhao Q 2019 Enhanced temperature stability of scale factor in MEMS gyroscope based on multi parameters fusion compensation method Measurement (Lond) 148

[11] Xing B, Zhou B, Zhang X, Zhang W, Hou B, Wei Q, Zhang T and Zhang R 2020 Thermal Deformation Suppression Chip Based on Material Symmetry Design for Single Center Supported MEMS Devices IEEE Access 8 43314–24

[12] Cao H, Li H, Sheng X, Wang S, Yang B and Huang L 2013 A novel temperature compensation method for a MEMS gyroscope oriented on a periphery circuit Int J Adv Robot Syst 10

[13] Li W, Xiao D, Wu X, Su J, Chen Z, Hou Z and Wang X 2017 Enhanced temperature stability of sensitivity for MEMS gyroscope based on frequency mismatch control Microsystem Technologies 23 3311–7

[14] Wang P, Li Q, Zhang Y, Xi X, Wu Y, Wu X and Xiao D 2022 Scale Factor Self-Calibration of MEMS Gyroscopes Based on the High-Order Harmonic Extraction in Nonlinear Detection IEEE Sens J 22 21761–8

[15] Jia J, Ding X, Qin Z, Ruan Z and Li H 2021 In-Run Scale Factor Compensation for MEMS Gyroscope without Calibration and Fitting IEEE Sens J 21 7316–25

[16] Galiouna Nassiopoulou A and Kaltsas G 2000 Porous Silicon as an Effective Material for Thermal Isolation on Bulk Crystalline Silicon

[17] Behrmann O, Lisec T and Gojdka B 2022 Towards Robust Thermal MEMS: Demonstration of a Novel Approach for Solid Thermal Isolation by Substrate-Level Integrated Porous Microstructures Micromachines (Basel) 13

[18] Wang Y, Cao R, Li C and Dean R N 2021 Concepts, Roadmaps and Challenges of Ovenized MEMS Gyroscopes: A Review IEEE Sens J 21 92–119

[19] Wang Z, Zhou Y, Jiang B, Zhang J, Zhou T and Su Y 2024 A Compact Temperature Controller for MEMS Vibratory Gyroscopes Using Thermoelectric Cooler IEEE Trans Electron Devices 71 3888–94

[20] Shaveta, Bhan R K and Chaujar R 2024 Tapered-Based Novel Thermal Compensation Techniques for Enhanced Performance of MEMS-Based Gyroscope 2nd International Conference on Emerging Trends in Information Technology and Engineering, ic-ETITE 2024 (Institute of Electrical and Electronics Engineers Inc.)

[21] Frank P. et.al. Fundamentals-of-heat-and-mass-transfer-6th-edition JOHN WILEY & SONS

[22] Pannaga N and Rajesh R P Review: MEMS Fabrication Technology

[23] Saffih F, Con C, Alshammari A, Yavuz M and Cui B 2014 Fabrication of silicon nanostructures with large taper angle by reactive ion etching Journal of Vacuum Science & Technology B, Nanotechnology and Microelectronics: Materials, Processing, Measurement, and Phenomena 32

[24] Marinis T, Soucy J, Marinis T F, Soucy J W and Johansson B D 2007 High Performance MEMS Inertial Instruments Fabricated on LTCC Substrates

[25] Allegato G, Corso L and Valzasina C 2022 Inertial Sensors Silicon Sensors and Actuators: The Feynman Roadmap 439–75

[26] He J, Xie J, He X, Du L and Zhou W 2016 Analytical study and compensation for temperature drifts of a bulk silicon MEMS capacitive accelerometer Sens Actuators A Phys 239 174–84

[27] Bao M-H 2000 Handbook of Sensors and Actuators 8 Micro Mechanical Transducers Pressure Sensors, Accelerometers and Gyroscopes

[28] Nandanpawar M L and Rajagopalan S 1978 Wachtman's equation and temperature dependence of bulk moduli in solids J Appl Phys 49 3976–9

[29] Burak Eminoglu, Mitchell H. Kline, Igor Izyumin, Yu-Ching Yeh and Bernhard E. Boser 2014 Background Calibrated MEMS Gyroscope (SENSORS, IEEE)
[30] Dutta S, Imran M, Kumar P, Pal R, Datta P and Chatterjee R 2011 Comparison of etch characteristics of KOH, TMAH and EDP for bulk micromachining of silicon (110) Microsystem Technologies 17 1621–8

CHAPTER 7

SUMMARY, SOCIAL IMPACT AND FUTURE SCOPE

- *This chapter summarizes the research contributions made during the course of the PhD work.*
- *The broader social impact and practical significance of the proposed MEMS gyroscope research are critically discussed.*
- *Potential directions for future research and further development of the present work are also identified in this chapter.*

7.1 Summary

This chapter summarizes the major findings of this work on MEMS gyroscopes focusing more on the design, packaging feasibility and extensive performance analysis of the proposed thick–mass architecture. This work highlights key results on structural optimisation, damping mitigation, and temperature-dependent performance that demonstrate how the thick-sense mass method increases mechanical robustness, stiffens resonant properties, and enhances the quality factor across a wide range of operating regimes. The chapter also appraises the wider physical significance and social impact of this proposed design, especially for defence, aerospace and autonomous systems. Finally, it presents ideas for future work that can further develop the contributions of this work.

Chapter 1 covers the basics of MEMS sensors and inertial gyroscope systems including their utility in aerospace, defence and autonomous navigation platforms. It outlines the demand for small, low-power, high-performance gyroscopes that can operate across a broad spectrum of environmental conditions. This chapter presents the relevant performance figures of merit, including sensitivity, bandwidth, quality factor (Q), and thermomechanical noise, that will serve as the foundation for optimization techniques presented in subsequent chapters.

Chapter 2 addresses the basic theory and working principles of MEMS gyroscopes, including Coriolis force-based sensing, dynamic modelling of drive and sense modes, and resonance behaviour. Analytical formulations that describe the sensitivity–bandwidth trade-off are derived. It also covers noise modelling and demonstrates that thermomechanical noise scales inversely with Q and the resonant frequency, thereby laying the theoretical foundation for passive noise reduction via structural design.

Chapter 3 discusses structural parameter design and performance trade-offs for conventional planar MEMS gyroscopes. Through analytical modelling and simulation, a systematic investigation is conducted on the sensitivity and bandwidth as affected by mass ratio (Mr) and stiffness ratio (Kr). A unified FOM (Figure of Merit) framework to jointly optimize sensitivity, bandwidth, noise, damping and footprint is proposed. Based on this, an optimized configuration has been measured to achieve a ~52 times FOM improvement when compared with the literature. These measurements align with analytical predictions (within 5% accuracy), which were validated using CoventorWare and MATLAB/Simulink simulations.

Chapter 4 introduces a miniaturized MEMS gyroscope architecture based on a thick Vertical Sense Mass (VSM) structure. Utilizing the DRIE fabrication technique to manipulate wafer thickness, the proposed sense structure features a 30% reduction in sense mass area and 36% reduction in overall device footprint while preserving sensitivity (on the order of ~9.6 × 10 m/deg/s). Furthermore, the VSM topology showed enhanced bandwidth and 4 times lower effective thermomechanical noise, consistent with a vertical geometry achieving a size advantage without performance penalties.

Chapter 5 examines damping mechanisms in MEMS gyros and compares PSM and VSM topologies. Finally, through the analysis of the complex motion of micro springs, it identifies air damping and squeeze-film damping as dominant performance-limiting factors in miniaturized devices. With the same operating conditions, the overall quality factor (Q_{Total}) of

the VSM structure is improved by factor of 8 in contrast to planar designs. This leads to up to 20 times higher bandwidth at the same sensitivity and about 3.3 times the noise improvement, suggesting that geometry-based damping mitigation is key for high-performance operation.

Chapter 6 applies a design- and substrate-level mitigation strategy using both tapered thermal substrates and engineered beam structures. The approach provides ~25 °C reduction in temperature rise (effective) and performance of presented gyros attains near constant value throughout –40 °C – 125 °C, with notable drift in scale factor, bandwidth and noise. The solution provides a hardware-efficient, low-power approach to electronic temperature compensation, improving environmental stability with no increase in system complexity.

Chapter 7 concludes the thesis by presenting our main conclusions, demonstrating that geometry-driven and architecture-level innovations can improve bandwidth, noise performance, footprint, damping robustness, and thermal stability. The verified designs demonstrate significant improvements, namely a 52 times increase in FOM, an 8 times reduction in Q-factor, a 4 times noise reduction and footprint shrinkage to confirm scalability and fabrication feasibility. The chapter also discusses social impacts and specifies future directions, including validation of closed-loop systems, multi-axis integration, and investigation of quantum gyroscope concepts for ultra-precise inertial sensing.

7.2 Social Impact

It is unavoidable for today's navigation systems' safety and reliability to be greatly improved with this new generation of MEMS gyroscope. Accurate measuring of orientation and motion becomes crucial for balanced control and accurate positioning in applications like autonomous cars, UAVs, aircraft, emergency response platforms etc. Any drift, bias instability or failure in inertial sensing can directly compromise system performance and safety. As a result, high-end MEMS gyroscopes provide stable and accurate angular rate measurements by enhancing structural design, minimizing quadrature error, and increasing responsiveness to environmental dynamics.

- Improved inertia sensors help both civilian and indigenous defence capabilities. It employs lightweight, scientific-grade multi-sensors and is a key to compact, low-power, high-performance precision sensors for UAVs, guided missiles, and tactical navigation. Indigenous MEMS gyroscopes reduce dependence on imported sensors subject to export controls. This optimization enhances performance and supports national self-reliance in strategic technologies.
- Another important advantage of structural and geometry-based optimization lies in reduced power consumption and overall system cost. Traditional approaches often depend heavily on complex electronic compensation to correct for the errors. By addressing issues at the mechanical design level through improved symmetry, mode decoupling, and structural robustness. The dependence on sophisticated electronic correction circuits can be minimized. This results in lower power requirements, simplified control architecture, and enhanced long-term stability, making the sensor more suitable for battery-operated and resource-constrained systems.

- Furthermore, reliable operation in harsh environmental conditions is essential for real-world deployment. MEMS gyroscopes used in space missions, border surveillance systems, disaster monitoring platforms, and remote installations must withstand wide temperature variations, pressure changes, mechanical shocks, and continuous vibrations. A mechanically optimized structure with improved damping control and stable frequency separation between drive and sense modes ensures consistent performance under such demanding conditions. Consequently, the proposed advancements extend the operational envelope of MEMS gyroscopes, enabling dependable functionality in environments where reliability is not merely desirable but critical.

7.3 Future Scope

The present research establishes a strong structural and thermal foundation for high-performance MEMS gyroscopes. However, several important directions remain for future advancement and practical realization.

- A primary next step is the complete prototyping and experimental validation of the proposed designs for VSM, damping-optimised, and thermally-engineered designs. Although simulations are useful for predicting behaviour, all operations must be tested in the real world to confirm frequency stability, quadrature suppression, bias performance, and long-term reliability at realistic operating conditions. Experimental validation will be necessary to determine whether the simulated advancements yield quantifiable performance benefits.
- Future work should allow integrated pressure–temperature co-design. A unified design framework can be established to ensure stable performance across different pressure and temperature regimes, eliminating the need to treat environmental damping and thermal drift as separate engineering exercises. More specifically, in aerospace, UAV, and severe-environment applications where environmental variations directly affect Q-factor and frequency stability, such a strategy is necessary.
- System-level implementation represents another crucial direction. Closed-loop force-rebalance control, digital signal processing integration, bias stability evaluation, and scale-factor linearity testing must be carried out to assess navigation-grade feasibility. Long-duration drift analysis and environmental testing will further establish the robustness in real-world conditions.
- The proposed structural design and modelling principles can also be extended to multi-axis gyroscopes and integrated inertial measurement units. Addressing cross-axis coupling and packaging challenges enables scalable, compact, and high-precision inertial sensing solutions suitable for advanced autonomous and defence systems.
- Looking forward, understanding the basics of quantum gyroscopes represents a visionary research perspective. Current implementations are still at a laboratory level, but the potential of quantum rotation-sensing technologies promises ultra-high precision beyond classical mechanical limits. Exploring their feasibility and potential integration pathways may unlock new opportunities for next-generation inertial sensing.

In a nutshell, the future scope lies in transitioning from optimized device design to experimentally validated, system-integrated, and scalable inertial platforms, while also exploring emerging quantum technologies for long-term precision enhancement.